

AD-A181 247

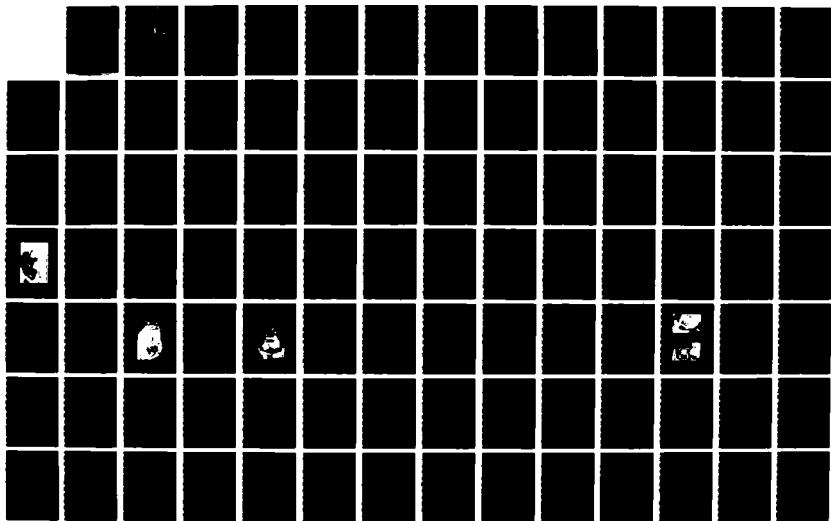
HIGH-RESOLUTION MEASUREMENT OF OH INFRARED AIRGLOW
STRUCTURE(U) UTAH STATE UNIV LOGAN SPACE DYNAMICS LABS
P C NEAL 18 OCT 85 SDL/85-075 AFGL-TR-85-0261
F19618-83-C-0056

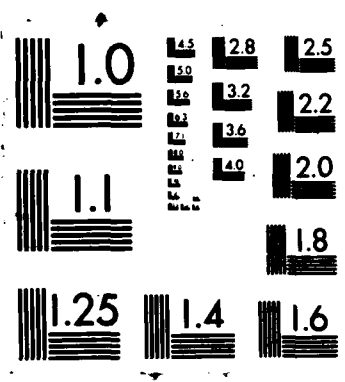
1/3

UNCLASSIFIED

F/G 4/1

NL





AD-A181 247

AFGL-TR-85-0261

HIGH-RESOLUTION MEASUREMENT OF
OH INFRARED AIRGLOW STRUCTURE

by

Parris Cornel Neal

Space Dynamics Laboratories
Utah State University
Logan, Utah 84322-4140

Scientific Report No. 14

18 October 1985

Approved for public release; distribution unlimited.

Prepared for:

Air Force Geophysics Laboratory
Air Force Systems Command
United States Air Force
Hanscom Air Force Base, MA 01731

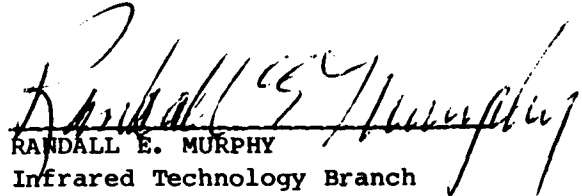
DTIC
ELECTRONIC
JUN 10 1987
S
D

"This technical report has been reviewed and is approved for publication"



FRANCIS X. ROBERT

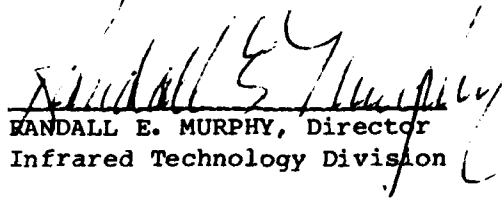
Atmospheric Backgrounds Branch
Infrared Technology Division



RANDALL E. MURPHY

Infrared Technology Branch
Infrared Technology Division

FOR THE COMMANDER



RANDALL E. MURPHY, Director
Infrared Technology Division

This report has been reviewed by the ESD Public Affairs Office (PA) and is releasable to the National Technical Information Service (NTIS).

Qualified requestors may obtain additional copies from the Defense Technical Information Center. All others should apply to the National Technical Information Service.

If your address has changed, or if you wish to be removed from the mailing list, or if the addressee is no longer employed by your organization, please notify AFGL/DAA, Hanscom AFB, MA 01731. This will assist us in maintaining a current mailing list.

Do not return copies of this report unless contractual obligations or notices on a specific document requires that it be returned.

REPORT DOCUMENTATION PAGE

1a. REPORT SECURITY CLASSIFICATION Unclassified		1b. RESTRICTIVE MARKINGS None	
2a. SECURITY CLASSIFICATION AUTHORITY N/A		3. DISTRIBUTION/AVAILABILITY OF REPORT Approved for public release; distribution unlimited.	
2b. DECLASSIFICATION/DOWNGRADING SCHEDULE N/A			
4. PERFORMING ORGANIZATION REPORT NUMBER(S) SDL/85-075		5. MONITORING ORGANIZATION REPORT NUMBER(S) AFGL-TR-85-0261	
6a. NAME OF PERFORMING ORGANIZATION Space Dynamics Labs, USU	6b. OFFICE SYMBOL (If applicable)	7a. NAME OF MONITORING ORGANIZATION Air Force Geophysics Lab	
6c. ADDRESS (City, State and ZIP Code) UMC 41 Logan, UT 84322		7b. ADDRESS (City, State and ZIP Code) Hanscom Air Force Base, MA 01731	
8a. NAME OF FUNDING/SPONSORING ORGANIZATION Air Force Geophysics Lab	8b. OFFICE SYMBOL (If applicable) LSP	9. PROCUREMENT INSTRUMENT IDENTIFICATION NUMBER F19628-83-C-0056	
8c. ADDRESS (City, State and ZIP Code) Hanscom Air Force Base, MA 01731		10. SOURCE OF FUNDING NOS.	
		PROGRAM ELEMENT NO. 62101F	PROJECT NO. 7670
		TASK NO. 10	WORK UNIT NO. AK
11. TITLE (Include Security Classification) High-Resolution Measurement of OH (cont)			
12. PERSONAL AUTHOR(S) Parris Cornel Neal (edited by Bryan Welch)			
13a. TYPE OF REPORT Scientific No. 14	13b. TIME COVERED FROM 2/83 TO 9/85	14. DATE OF REPORT (Yr., Mo., Day) 1985 October 18	15. PAGE COUNT 224
16. SUPPLEMENTARY NOTATION			
17. COSATI CODES		18. SUBJECT TERMS (Continue on reverse if necessary and identify by block number)	
FIELD	GROUP	SUB. GR.	
			MAPSTAR Infrared emissions Airglow
			Laboratory simulation program Gravity waves
19. ABSTRACT (Continue on reverse if necessary and identify by block number)			
<p>Disturbances in the atmospheric airglow layer, which cause bright and dark bands or "stripes" to appear, have been observed by scientists. These disturbances are attributed to "gravity waves" propagating through the atmosphere. An instrument capable of resolving the temporal, spatial and spectral characteristics of OH infrared emissions has been designed and has gathered quantitative data concerning airglow structure.</p> <p>An optically-compensated interferometer-spectrometer was the basic instrument used to measure the phenomena. The instrument is an order of magnitude more sensitive than conventional spectrometers and its high-throughput allows temporal resolution as short as 30 seconds. Spatial data were obtained by matching the interferometer's high-throughput to a unique optical system which includes a 50-cm telescope. The large-diameter telescope maintains the throughput of the interferometer but narrows the instrument's field-of-view to less than a degree. The spatial resolution of (cont)</p>			
20. DISTRIBUTION/AVAILABILITY OF ABSTRACT UNCLASSIFIED/UNLIMITED <input checked="" type="checkbox"/> SAME AS RPT. <input type="checkbox"/> DTIC USERS <input type="checkbox"/>		21. ABSTRACT SECURITY CLASSIFICATION Unclassified	
22a. NAME OF RESPONSIBLE INDIVIDUAL Francis X. Robert/Contract Monitor		22b. TELEPHONE NUMBER (Include Area Code) 617 861-3630	22c. OFFICE SYMBOL AFGL/LSP

11. Title (continued): Infrared Airglow Structure

19. Abstract (continued): the system is 14 milliradians.

The interferometer was operated inconjunction with a low-light-level infrared imaging isocon camera system provided by the University of Southampton, England. The camera was co-aligned with the telescope to provide an infrared video "eye" for the interferometer.

A bright OH airglow structure vent was recorded on June 15, 1983 from an observation site located at Sacramento Peak, New Mexico. The structures were measured at elevation angles near the horizon. Quantitative data concerning wavelength, periods, phase velocities, spectral characteristics and rotational temperature were gathered.



Accession For	
NTIS CRA&I	<input checked="" type="checkbox"/>
DTIC TAB	<input type="checkbox"/>
Unannounced	<input type="checkbox"/>
Justification	
By	
Distribution /	
Availability Codes	
Dist	Avail and/or Special
A-1	

FOREWORD

In January, 1983, the Air Force Geophysics Laboratory (AFGL) awarded contract number F19628-83-C-0056 to the Space Dynamics Laboratories (SDL) at Utah State University (USU) in Logan, Utah, under which SDL assists in the infrared measurement program.

MAPSTAR is part of AFGL's Laboratory Simulation program. The overall goal of the program is to create a controlled-environment data base of infrared emissions resulting from molecular interactions in order to more accurately characterize and identify the sources of infrared radiation in the atmosphere. As a result, our ability to identify and track man-caused disturbances in the atmosphere with infrared instruments will be greatly enhanced.

Laboratory models are being cross-checked with actual atmospheric observations. Based on these findings, nuclear and atmospheric predictive models will be refined so that we may assess the effects of mankind's activities on atmospheric chemistry and more accurately identify artificial sources of infrared radiation, such as rocket plumes.

AFGL has contracted the Laboratory Simulation Program to SDL.

MAPSTAR is part of a ground-based remote sensing program designed to define infrared structure in the OH region of the mesosphere. Several sensors will be employed in the MAPSTAR effort. In the program's first stage, a high-resolution ground-based interferometer equipped with a high-straylight rejection telescope was used to examine the spectral characteristics of

airglow from sources in the mesosphere. Data are also being collected with a Doppler radar and an Isocon optical imager.

The interferometer-telescope sensor was designed to gather quantitative data on the structure of airglow originating in the mesosphere, particularly the structure of alternating bands of airglow attributed to "gravity waves" propagating through the atmosphere. Data gathered in June, 1983, apparently revealed wavelengths, periods and phase velocities for the gravity waves, as well as rotational temperatures in the bright and dark bands of airglow, providing a wealth of new information about the chemical and physical behavior of the mesosphere.

SUMMARY

A bright OH Meinel airglow structure event was recorded on June 15, 1983 from Sacramento Peak, New Mexico. The MAPSTAR interferometer was operated in conjunction with low-light-level infrared imaging isocon camera system provided by the University of Southampton, England. The camera was co-aligned with the telescope to provide an infrared video "eye" for the interferometer.

The structures were measured at elevation angles near the horizon. Apparent wavelengths, periods and phase velocities of 24 ± 1 km, 14 ± 1 minutes, and 28 ± 2 meters/second respectively, were calculated for the recorded structure. The interferometer data show intensity modulations of 20-40 percent within the structure. A mean rotational temperature of 165 degrees Kelvin was calculated using the interferometer spectral data and temperature modulations of 5 to 10 degrees Kelvin were recorded in phase with the intensity modulations.

This report discusses the structure and performance of the MAPSTAR interferometer and telescope, as well as the results obtained using the sensor. Data collected shed new light on the phenomena under investigation and will provide a foundation for studies in the future.

This page intentionally left blank.

LIST OF CONTRIBUTORS

Utah State University
A. J. Steed, Principal Investigator
Doran Baker, Scientific Advisor
Parris Cornel Neal

RELATED CONTRACTS AND PUBLICATIONS

F19628-81-C-0056

This page intentionally left blank.

TABLE OF CONTENTS

	<u>Page</u>
FOREWORD	iii
SUMMARY	v
LIST OF CONTRIBUTORS	vii
TABLE OF CONTENTS	ix
LIST OF TABLES	xi
LIST OF FIGURES	xiii
I. INTRODUCTION	1
Airglow Structure Measurement Background	2
Airglow Structure and the Theory of Atmospheric Gravity Waves	5
Interferometers and Fourier Transform Spectroscopy	7
Isocon Television System	13
Scope and Objectives	16
II. OPTICAL INSTRUMENTATION SYSTEM DESIGN	19
Design Philosophy	19
High-Throughput Interferometer Design	21
Drive System	29
Detector System	32
Telescope Design	34
Instrument Housing	40
III. MEASUREMENT THEORY	43
The Interferogram	43
Calibration Source	46
Instrument Response	48
Phase Correction	50
Apodization and Interpolation	52
Line Amplitude Extraction	59
IV. OH ROTATIONAL TEMPERATURE MODELING	62
Introduction	62
The Excited OH Radical	63
Rotational Temperature Model	64
Error Analysis and Testing of Model	72
V. RESULTS	78
Introduction	78
Background	78

TABLE OF CONTENTS (cont'd)

	<u>Page</u>
Infrared Isocon Camera Results	79
Infrared Radiometer Data	88
Direct Comparison of Interferometer and Radiometer Intensities	91
Rotational Temperatures for Interferometer Zenith Data	94
Rotational Temperature Smoothing Algorithm	95
Interferometer Recorded Structure	96
 VI. DISCUSSION OF RESULTS	 109
Rotational Temperatures	109
Rotational Temperature and Intensity Modulations	111
Temperature Differences Observed Between Bands	115
Temperature and Intensity Phase Relationship	117
 VII. CONCLUSIONS AND RECOMMENDATIONS	 119
Overview	119
Conclusions	119
Recommendations for Future Research	122
 REFERENCES	 126
 APPENDICES	 132
Appendix A. OH Transitions	133
Appendix B. RCA-Limited Germanium Detector Specifications	136
Appendix C. Interferometer Data Catalog	141

LIST OF TABLES

<u>TABLE</u>		<u>Page</u>
2-1	Summary of interferometer-spectrometer specifications	41
4-1	Molecular data for OH $\Delta v=2$, (4,2) band . . .	70
4-2	Molecular data for OH $\Delta v=2$, (3,1) band . . .	70
4-3	Molecular data for OH $\Delta v=3$, (8,5) band . . .	71
4-4	Molecular data for OH $\Delta v=3$, (7,4) band . . .	71
5-1	Summary of OH airglow structure measurement results for June 15, 1983	105
B-1	Germanium detector spectral response	137
B-2	Detailed specifications on RCA detector . . .	140

This page intentionally left blank.

LIST OF FIGURES

Figure		Page
1-1.	Layout of a conventional Michelson interferometer	9
1-2.	Interaction of off-axis rays in a conventional Michelson interferometer [Steed 1978]	11
1-3.	Isocon camera system spectral range including the OH emissions within that range [Taylor 1983-84]	15
1-4.	Image isocon photo of OH airglow structure taken by Taylor et al. [1980] in Switzerland in August of 1980	17
2-1.	Optical layout of interferometer telescope system	20
2-2.	Optical compensation method conceived by Connes [1956]	22
2-3.	Optical compensation with an optical section inserted into one leg of a Michelson interferometer [Steed 1978]	24
2-4.	Plot of aberration limits for Connes [1956] method of optical compensation compared with conventional Michelson interferometer [Steed 1978]	28
2-5.	Cross section of optical wedge in two drive positions a distance X apart [Steed 1978]	30
2-6.	Optically-compensated interferometer showing beamsplitter, wedges, and bearing assemblies	33
2-7.	Picture of RCA Limited liquid-nitrogen cooled germanium detector system	35
2-8.	Interferometer placed inside housing	42

2-9.	Interferometer system equipped with 20-inch diameter telescope. The isocon camera is also mounted on the telescope . . .	42
3-1.	Typical "double sided" interferogram	45
3-2.	Interferometer calibration source	48
3-3.	Real and imaginary parts of a blackbody curve (a.) before and (b.) after phase correction	53
3-4.	Real and imaginary parts of a spectral curve (a.) before and (b.) after phase correction	54
3-5.	Optimal apodization functions, showing resolution vs. sidelobe attenuation [Espy 1984]	58
3-6.	Comparison of normalized instrument functions; sinc(—), sinc ² (- -), and Hamming(· · ·) [Espy 1984]	59
4-1.	Measured OH spectra showing (4,2), (3,1), (8,5), and (7,4) Meinel bands	64
4-2.	Model temperature test results on synthetic spectra vs. signal-to-noise ratio with standard deviation shown as bars [Espy 1984]	76
4-3.	Model intensity test results on synthetic spectra vs. signal-to-noise ratio with standard deviation shown as bars [Espy 1984]	77
5-1.	Large isocon IR camera photo, day 166 8:15 hrs. UT, camera field of view 28° vertical, 37° horizontal, at an elevation of about 10°	80
5-2.	Isocon IR camera photo, day 166, 7:32 hrs. UT, field of view = 13° vertical 15° horizontal, interferometer looking at "X" on a bright band	82
5-3.	Isocon IR camera photo, day 166, 7:40 hrs. UT, field of view = 13° vertical 15° horizontal, interferometer looking at "X" on a dark band	83

5-4.	Isocon IR camera photo, day 166, 7:48 hrs. UT, field of view = 13° vertical 15° horizontal, interferometer looking at "X" on a bright band	84
5-5.	Isocon IR camera photo, day 166, 8:31 hrs. UT, field of view = 13° vertical 15° horizontal, interferometer looking at "X" on a dark band	86
5-6.	Isocon IR camera photo, day 166, 8:42 hrs. UT, field of view = 13° vertical 15° horizontal, interferometer looking at "X" on a bright band	87
5-7.	Radiometer readings for UT days 162, 165, and 166 during 1983. The data is for the 1.53 μ m channel	89
5-8.	OH (3,1) band radiance and rotational temperature, viewing angle = zenith, day 165, 3:30-7:30 hrs. UT	92
5-9.	OH (3,1) band radiance and rotational temperature, viewing angle = zenith, day 166, 3:30-6:45 hrs. UT	93
5-10.	OH (4,2) band rotational temperature and standard deviation before smoothing	97
5-11.	OH (4,2) band rotational temperature and standard deviation after smoothing	98
5-12.	OH (3,1) band relative intensity and standard deviation, viewing angle = 17° El. 328° Az., day 166, 7:30-8:30 hrs. UT	100
5-13.	OH (3,1) band smoothed rotational temperature and standard deviation, viewing angle = 17° El. 328° Az., day 166, 7:30-8:30 hrs. UT	101
5-14.	OH (3,1) band relative intensity and standard deviation, viewing angle = 15.5° El. 340° Az., day 166, 8:30-9:15 hrs. UT	103
5-15.	OH (3,1) band smoothed rotational temperature and standard deviation, viewing angle = 15.5° El. 340° Az., day 166, 8:30-9:15 hrs. UT	104

5-16.	OH (3,1) band relative intensity and standard deviation, viewing angle = 15.5° E1. 309° Az., day 166, 9:15-10:15 hrs. UT	106
5-17.	OH (3,1) band smoothed rotational temperature and standard deviation, viewing angle = 15.5° E1. 309° Az., day 166, 9:15-10:15 hrs. UT	107
5-18.	OH (7,4) band smoothed rotational temperature and standard deviation, viewing angle = 15.5° E1. 340° Az., day 166, 8:30-9:15 hrs. UT	108
6-1.	Expected values for η (vertical axis) based on gravity-wave models and oxygen measurements [Pendleton 1985]	113
B-1.	Typical detector spectral response	137
B-2.	RCA germanium detector liquid-nitrogen dewar outline	138
B-3.	Detector preamplifier circuit	139
C-1.	OH (4,2) band radiance and standard deviation, viewing angle = zenith, day 165, 3:30-7:30 hrs. UT	142
C-2.	OH (4,2) band rotational temperature and standard deviation, viewing angle = zenith, day 165, 3:30-7:30 hrs. UT	143
C-3.	OH (4,2) band smoothed rotational temperature and standard deviation, viewing angle = zenith, day 165, 3:30-7:30 hrs. UT	144
C-4.	OH (3,1) band radiance and standard deviation, viewing angle = zenith, day 165, 3:30-7:30 hrs. UT	145
C-5.	OH (3,1) band rotational temperature and standard deviation, viewing angle = zenith, day 165, 3:30-7:30 hrs. UT	146
C-6.	OH (3,1) band smoothed rotational temperature and standard deviation, viewing angle = zenith, day 165, 3:30-7:30 hrs. UT	147

C-7.	OH (8,5) band radiance and standard deviation, viewing angle = zenith, day 165, 3:30-7:30 hrs. UT	148
C-8.	OH (8,5) band rotational temperature and standard deviation, viewing angle = zenith, day 165, 3:30-7:30 hrs. UT	149
C-9.	OH (8,5) band smoothed rotational temperature and standard deviation, viewing angle = zenith, day 165, 3:30-7:30 hrs. UT	150
C-10.	OH (7,4) band radiance and standard deviation, viewing angle = zenith, day 165, 3:30-7:30 hrs. UT	151
C-11.	OH (7,4) band rotational temperature and standard deviation, viewing angle = zenith, day 165, 3:30-7:30 hrs. UT	152
C-12.	OH (7,4) band smoothed rotational temperature and standard deviation, viewing angle = zenith, day 165, 3:30-7:30 hrs. UT	153
C-13.	OH (4,2) band radiance and standard deviation, viewing angle = zenith, day 166, 3:30-6:45 hrs. UT	154
C-14.	OH (4,2) band rotational temperature and standard deviation, viewing angle = zenith, day 166, 3:30-6:45 hrs. UT	155
C-15.	OH (4,2) band smoothed rotational temperature and standard deviation, viewing angle = zenith, day 166, 3:30-6:45 hrs. UT	156
C-16.	OH (3,1) band radiance and standard deviation, viewing angle = zenith, day 166, 3:30-6:45 hrs. UT	157
C-17.	OH (3,1) band rotational temperature and standard deviation, viewing angle = zenith, day 166, 3:30-6:45 hrs. UT	158
C-18.	OH (3,1) band smoothed rotational temperature and standard deviation, viewing angle = zenith, day 166, 3:30-6:45 hrs. UT	159

C-19.	OH (8,5) band radiance and standard deviation, viewing angle = zenith, day 166, 3:30-6:45 hrs. UT	160
C-20.	OH (8,5) band rotational temperature and standard deviation, viewing angle = zenith, day 166, 3:30-6:45 hrs. UT	161
C-21.	OH (8,5) band smoothed rotational temperature and standard deviation, viewing angle = zenith, day 166, 3:30-6:45 hrs. UT	162
C-22.	OH (7,4) band radiance and standard deviation, viewing angle = zenith, day 166, 3:30-6:45 hrs. UT	163
C-23.	OH (7,4) band rotational temperature and standard deviation, viewing angle = zenith, day 166, 3:30-6:45 hrs. UT	164
C-24.	OH (7,4) band smoothed rotational temperature and standard deviation, viewing angle = zenith, day 166, 3:30-6:45 hrs. UT	165
C-25.	OH (4,2) band relative intensity and standard deviation, viewing angle = 17° El. 328° Az., day 166, 7:30-8:30 hrs. UT	166
C-26.	OH (4,2) band rotational temperature and standard deviation, viewing angle = 17° El. 328° Az., day 166, 7:30-8:30 hrs. UT	167
C-27.	OH (4,2) band smoothed rotational temperature and standard deviation, viewing angle = 17° El. 328° Az., day 166, 7:30-8:30 hrs. UT	168
C-28.	OH (3,1) band relative intensity and standard deviation, viewing angle = 17° El. 328° Az., day 166, 7:30-8:30 hrs. UT	169
C-29.	OH (3,1) band rotational temperature and standard deviation, viewing angle = 17° El. 328° Az., day 166, 7:30-8:30 hrs. UT	170
C-30.	OH (3,1) band smoothed rotational temperature and standard deviation, viewing angle = 17° El. 328° Az., day 166, 7:30-8:30 hrs. UT	171

C-31.	OH (8,5) band relative intensity and standard deviation, viewing angle = 17° El. 328° Az., day 166, 7:30-8:30 hrs. UT	172
C-32.	OH (8,5) band rotational temperature and standard deviation, viewing angle = 17° El. 328° Az., day 166, 7:30-8:30 hrs. UT	173
C-33.	OH (8,5) band smoothed rotational temperature and standard deviation, viewing angle = 17° El. 328° Az., day 166, 7:30-8:30 hrs. UT	174
C-34.	OH (7,4) band relative intensity and standard deviation, viewing angle = 17° El. 328° Az., day 166, 7:30-8:30 hrs. UT	175
C-35.	OH (7,4) band rotational temperature and standard deviation, viewing angle = 17° El. 328° Az., day 166, 7:30-8:30 hrs. UT	176
C-36.	OH (7,4) band smoothed rotational temperature and standard deviation, viewing angle = 17° El. 328° Az., day 166, 7:30-8:30 hrs. UT	177
C-37.	OH (4,2) band relative intensity and standard deviation, viewing angle = 15.5° El. 340° Az., day 166, 8:30-9:15 hrs. UT	178
C-38.	OH (4,2) band rotational temperature and standard deviation, viewing angle = 15.5° El. 340° Az., day 166, 8:30-9:15 hrs. UT	179
C-39.	OH (4,2) band smoothed rotational temperature and standard deviation, viewing angle = 15.5° El. 340° Az., day 166, 8:30-9:15 hrs. UT	180
C-40.	OH (3,1) band relative intensity and standard deviation, viewing angle = 15.5° El. 340° Az., day 166, 8:30-9:15 hrs. UT	181
C-41.	OH (3,1) band rotational temperature and standard deviation, viewing angle = 15.5° El. 340° Az., day 166, 8:30-9:15 hrs. UT	182

C-42.	OH (3,1) band smoothed rotational temperature and standard deviation, viewing angle = 15.5° El. 340° Az., day 166, 8:30-9:15 hrs. UT	183
C-43.	OH (8,5) band relative intensity and standard deviation, viewing angle = 15.5° El. 340° Az., day 166, 8:30-9:15 hrs. UT	184
C-44.	OH (8,5) band rotational temperature and standard deviation, viewing angle = 15.5° El. 340° Az., day 166, 8:30-9:15 hrs. UT	185
C-45.	OH (8,5) band smoothed rotational temperature and standard deviation, viewing angle = 15.5° El. 340° Az., day 166, 8:30-9:15 hrs. UT	186
C-46.	OH (7,4) band relative intensity and standard deviation, viewing angle = 15.5° El. 340° Az., day 166, 8:30-9:15 hrs. UT	187
C-47.	OH (7,4) band rotational temperature and standard deviation, viewing angle = 15.5° El. 340° Az., day 166, 8:30-9:15 hrs. UT	188
C-48.	OH (7,4) band smoothed rotational temperature and standard deviation, viewing angle = 15.5° El. 340° Az., day 166, 8:30-9:15 hrs. UT	189
C-49.	OH (4,2) band relative intensity and standard deviation, viewing angle = 15.5° El. 309° Az., day 166, 9:15-10:15 hrs. UT	190
C-50.	OH (4,2) band rotational temperature and standard deviation, viewing angle = 15.5° El. 309° Az., day 166, 9:15-10:15 hrs. UT	191
C-51.	OH (4,2) band smoothed rotational temperature and standard deviation, viewing angle = 15.5° El. 309° Az., day 166, 9:15-10:15 hrs. UT	192
C-52.	OH (3,1) band relative intensity and standard deviation, viewing angle = 15.5° El. 309° Az., day 166, 9:15-10:15 hrs. UT	193

C-53.	OH (3,1) band rotational temperature and standard deviation, viewing angle = 15.5° El. 309° Az., day 166, 9:15-10:15 hrs. UT	194
C-54.	OH (3,1) band smoothed rotational temperature and standard deviation, viewing angle = 15.5° El. 309° Az., day 166, 9:15-10:15 hrs. UT	195
C-55.	OH (8,5) band relative intensity and standard deviation, viewing angle = 15.5° El. 309° Az., day 166, 9:15-10:15 hrs. UT	196
C-56.	OH (8,5) band rotational temperature and standard deviation, viewing angle = 15.5° El. 309° Az., day 166, 9:15-10:15 hrs. UT	197
C-57.	OH (8,5) band smoothed rotational temperature and standard deviation, viewing angle = 15.5° El. 309° Az., day 166, 9:15-10:15 hrs. UT	198
C-58.	OH (7,4) band relative intensity and standard deviation, viewing angle = 15.5° El. 309° Az., day 166, 9:15-10:15 hrs. UT	199
C-59.	OH (7,4) band rotational temperature and standard deviation, viewing angle = 15.5° El. 309° Az., day 166, 9:15-10:15 hrs. UT	200
C-60.	OH (7,4) band smoothed rotational temperature and standard deviation, viewing angle = 15.5° El. 309° Az., day 166, 9:15-10:15 hrs. UT	201

This page intentionally left blank.

CHAPTER I

INTRODUCTION

The mesosphere is the interface region between the earth's inner and outer atmospheres. Occurrences at the mesopause include: the temperature gradient makes a sign change, the atmospheric pressure, density, and mean molecular weight all have an inflection point in their respective curves [Banks and Kockarts 1973]. The atmosphere makes a transition from a fluid to free molecular flow in this region which accounts for these changes. The unique properties of the mesospheric region are of great interest in understanding the middle atmosphere and its influence on the energy budget of the earth.

The 80 to 100 km region (mesosphere) is a difficult region to study because the altitude is too low for direct satellite observations and too high for direct balloon or airplane measurements. Ground based studies are hampered by the intervening atmosphere. There are some relatively transparent atmospheric "windows" in the near infrared, however. Hydroxyl radicals (OH) reside in this mesospheric region in sufficient concentrations to radiate a large amount of energy at the red and near infrared wavelengths [Baker 1978].

The excitation of OH is caused by various solar and chemical processes. The excited OH radical is a complex vibrational-rotational system which emits radiation spectrally. The spectral radiation distribution is near Maxwell-Boltzmann in nature [Baker 1978]; therefore, the OH spectral radiation can be measured, the Boltzmann distribution determined, and a rotational temperature calculated [Ware 1980]. This temperature can then be used to help understand the chemistry and physics of the entire region. Banks and Kockarts [1973] show that mesospheric temperatures during the summer months at a mid-latitude site can be expected to be between 150 °K and 190 °K.

Recent studies have shown that mesospheric optical radiation called airglow has, at times, exhibited some "wavelike" structure [Taylor et al. 1980]. These waves have been studied using photographic and photometric methods. The object of this study was to develop and utilize an instrument to provide quantitative data of OH rotational temperature and intensity variations during these airglow structure events.

Airglow Structure Measurement Background

The atmospheric airglow layer has been observed and studied for many years using a variety of methods. The studies conducted during the decades from 1930 to 1970, however, failed to recognize the nature of the airglow structure phenomenon. Rayleigh [1931] was among the first

to recognize the difference between airglow and aurora. He referred to the enhanced airglow as "non-polar aurorae." Photographs of the airglow structure were presented in 1952 by Hoffmeister [1952]; but again, neither the identity nor the source of the airglow structure was understood. Chamberlain [1961] briefly outlines the historical efforts in airglow studies up until 1961. During the decade of the 60s the techniques of photometry were perfected and most optical atmospheric study efforts were centered around these methods.

Kieffaber [1973] presented photographic evidence in 1972 of apparent airglow "waves" and "cells" in the 750-900 nm wavelength region using infrared film and a 35-mm camera. She proposed that the airglow stripes originated from a disturbance in the OH layer. Again in late 1972, Peterson and Kieffaber [1973] recorded more occurrences of structure at their mid-latitude site near Albuquerque, New Mexico. The photographically recorded events were also tracked with infrared photometers (1.65 and 2.2 μm) and shown to be moving between 20 and 40 meters/second.

In 1975, Crawford et al. [1975] flew an image intensified isocon television system on board NASA's CV990 aircraft. Peterson and Kieffaber [1975] observed on the same flight with their cameras and photometers. Both groups recorded "cloud-like" airglow structures. Again using 35-mm cameras, Moreels and Herse [1977] measured extensive OH airglow structure over Europe. Their findings were similar

to those of Peterson and Kieffaber. Waves on the order of 40-km spatial wavelength appeared to be traveling at horizontal speeds from 15 to 20 meters/second. Peterson [1979] was able to record numerous occurrences from 1975 through 1978 with some of the events being enhanced enough to see the structure with the naked eye. The University of Southampton Atmospheric Physics group [Taylor et al. 1980 and Taylor 1984] recorded many structure events with the image isocon television cameras from 1975 through 1983. Using radiometric techniques, Huppi and Baker [1976] also recorded OH intensity variations. Takeuchi and Misawa [1981] record some short-period waves of OH intensity and rotational temperature using a tilting filter photometer. This study used a narrow field of view, fast scan rate instrument. The spectral resolution was rather coarse, however, (unable to resolve the base line between adjacent band lines) and the measurements were taken without the aid of any photographic or video equipment making it difficult to identify what was being observed. Airglow structure was also recorded by Peterson and Adams [1983] during a total lunar eclipse in the summer of 1982. In this lunar eclipse study extensive use was made of photographic equipment as well as a vertical sounding radar.

During the decade of the 1970's, interferometric-spectroscopy applied to middle atmospheric research matured as a measurement science. Interferograms processed using computer-based fast Fourier transform (FFT) methods yielded

high-resolution OH airglow spectra from which intensity and rotational temperatures could be extracted. Baker [1978] presents an excellent summary of the studies conducted in this area. However, because the instruments used had wide fields of view (therefore integration over large areas), low throughput (therefore long integration times), or low spectral resolution the small spatial airglow variations were not able to be spectroscopically measured at high resolution.

The references cited and many others have recorded OH airglow structure events. However, none of the researchers were able to provide a measure of high-resolution spectral changes and therefore calculate the differences in OH rotational temperature of the dark and bright band "waves." This dissertation gives the design, development, and operation of a special high-throughput, narrow field of view, fast scan interferometer-spectrometer which can spectrally, spatially, and temporally resolve the OH airglow emission structure.

Airglow Structure and the Theory of Atmospheric Gravity Waves

In a landmark paper, Hines [1960] suggested that under certain conditions the atmosphere could be disturbed by a "gravity wave." Later, Hines [1965] hypothesized that the passage of internal gravity waves (IGW's) through the atmosphere would cause some reversible, adiabatic heating

(temperature fluctuations associated with waves) until the dissipation of the wave became excessive. Along with his gravity wave hypothesis, Hines [1965] gave a simple model to describe his suspected IGW temperature fluctuations. Using some constants from the high-altitude vapor-trail measurements of Kochanski [1964] in the Hines model, a calculated temperature change of ± 6 °K could be expected in conjunction with the passage of an IGW through the atmosphere. Temperature and wind measurements by Rai and Fejer [1971] using rocket-grenade techniques support the IGW hypothesis put forth by Hines.

The atmospheric scientific community in the Soviet Union has done extensive work in the area of an adiabatic-oscillation IGW model similar to the work of Hines [1960]. Krassovsky et al. [1977] summarize much of the modeling and measurement efforts of this group. The basic instrument used is a three-axis diffraction spectrograph, supported by various photometers. The large data base of measurements presented, shows strong correlation between the magnitude of the temperature modulation and the period of the IGW. The observational data presented exhibit, for IGW periods of about 25 minutes, the calculated rotational temperature changes of about 6 °K with the passing of the wave [Krassovsky et al. 1977]. Additionally, the Soviet work indicates that a significant rotational temperature difference can be seen between high level and low level OH vibrational transitions. The observed differences range

from 5 to 25 °K with the high vibrational level transitions appearing hotter.

Interferometers and Fourier

Transform Spectroscopy

The Michelson interferometer was invented in the 1880's by Albert Abraham Michelson [Shankland 1974]. In the Michelson-Morley experiment, the instrument was used in an attempt to measure the earth's movement through an "ether." Michelson also used his interferometer to determine the exact length of the standard meter and to measure the diameter of celestial bodies. He also discovered the spectral fine structure of hydrogen, mercury, and thallium [Shankland 1974]. This pointed out the potential for what would be later be called "Fourier spectroscopy."

Optically-sensitive detectors were subsequently used in conjunction with Michelson interferometers, in which one mirror was mechanically displaced at a constant rate, to produce an electrical interferogram. The interferogram was then inverted using Fourier transform techniques to yield direct spectral data. In 1910, Ruben and Woods [Connes 1963] obtained the first far infrared spectrum using this method. Fellgett [1949] and Jacquinot [1954] independently showed the inherent advantage that the interferometer has over grating and prism spectrometers. This advantage results from measuring all spectral components simultaneously. This improvement was referred to by

Fellgett as "multiplex spectroscopy". Jacquinet [Connes 1963] also showed that absence of slits in Michelson spectrometry also improved system throughput when compared with conventional grating methods.

The advent of large, fast computers and the development of the fast Fourier transform [Forman 1966], which together could calculate a large Fourier transform quickly, spread the use of Fourier transforms for power spectral density analysis into many fields. Notable contributions were made in the field in the 1950's, 1960's, and 1970's by Mertz [1959], Connes [1956], Gebbie and Vanasse [1956], Strong and Vanasse [1959], Forman [1966], Haycock and Baker [1975], and Steed [1978]. Many of the improvements in the field were reported at the 1970 Aspen Conference on Fourier Spectroscopy [Vanasse et al. 1971].

Figure 1-1 shows the typical layout of the Michelson interferometer. The system is comprised of a beamsplitter that divides the incoming light beam into two equal parts, two mirrors (M_1 is stationary and M_2 is mobile), and a condenser lens to focus the light onto a detector.

The incoming light is divided into two portions by the beamsplitter with each portion directed to its respective mirror. The energy is then reflected by the mirrors and is recombined at the beamsplitter and passed onto the detector system. The recombined beam is modulated by differences in the path lengths between the beamsplitter and each of the mirrors. If the mobile mirror M_2 is in a position such

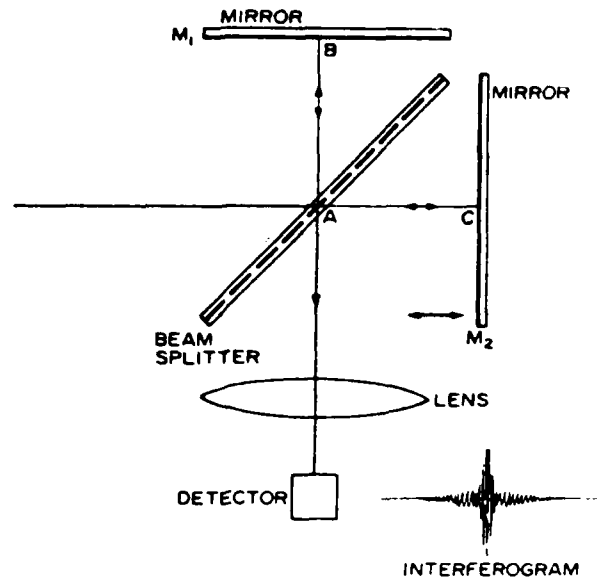


Figure 1-1. Layout of a conventional Michelson interferometer.

that the path length AC is the same as the path length AB, then the recombined signals are in phase and thus add constructively. The same constructive addition occurs when the path length difference $BC-AC$ is any integral number of wavelengths of the incoming signal. On the other hand, if the path length difference is not an integral multiple of the wavelength, then the recombined signal will have varying amounts of destructive interference depending upon the phase difference. As the path length AC is changed in a uniform manner, by moving M_2 at a constant rate, the electrical signal from the detector is the interferogram of the incoming optical signal. The Fourier transformed interferogram yields the spectral content of the incoming light.

The simultaneous measurement of high-resolution spectral, temporal, and spatial characteristics of the OH airglow structure requires an instrument with both a narrow field of view and high throughput. The standard Michelson interferometer, when used for high-resolution measurements, has a narrow field of view but its low throughput would make it an order of magnitude less sensitive.

The narrow field of view limitation of a standard Michelson interferometer is illustrated in Figure 1-2. When incoming energy is allowed to enter the interferometer off-axis ($\theta \neq 0^\circ$) the relationship between the displacement of mirror M_2 and the actual path difference between the two mirrors is altered. The path difference or retardation is no longer $2d$ as it is when light is coming straight into the instrument, but now is $2d\cos\theta$, where θ is the angle of the incoming light with respect to the entry normal. For an instrument with a given resolving power the maximum usable field of view for a standard Michelson interferometer is, according to Vanasse [1977]

$$\Omega_{\max} = 2\pi/R \quad , \quad (1.1)$$

where

Ω_{\max} = maximum field of view in steradians,

R = resolving power of instrument.

To increase the throughput (thus achieving a faster scan rate) an optically-compensated interferometer was chosen for use in this study. There have been many proposed methods

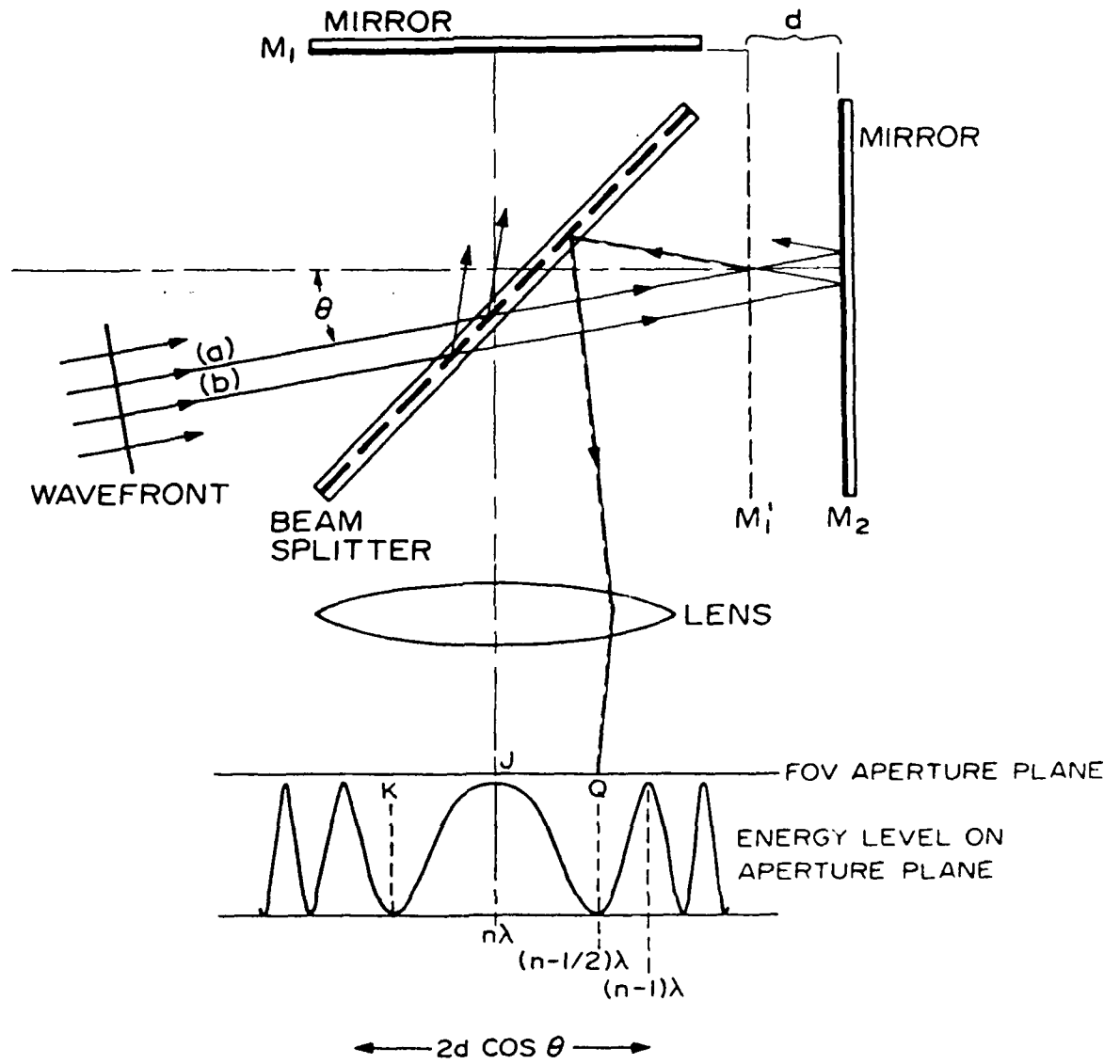


Figure 1-2. Interaction of off-axis rays in conventional Michelson interferometer [Steed 1978].

of field-widening or optical-compensation for increasing the throughput of an interferometer. These techniques are reviewed by Baker [Vanasse 1977]. The method used for the instrument in this study was first proposed by Connes [1956], and uses optical-compensation wedges or prisms in each leg of the interferometer (specific details are discussed in Chapter II). Optical compensation increases the throughput by increasing the usable field of view of the instrument. However, the measurement of OH airglow structure requires a small field of view. The high throughput of the compensated interferometer was matched (maintaining temporal resolution) to a special optical system which included a large-diameter telescope to obtain the desired narrow field of view while maintaining throughput.

The interferometer system was now able to simultaneously resolve the spectral, temporal, and spatial characteristics of the OH airglow structure. However, because the measured radiation was in the infrared it was necessary to locate and measure a structure occurrence and to characterize the total structure into which the interferometer was looking. The video viewing system used is described in the next section.

Isocon Television System

Taylor [1983-84] participated in this research by providing and operating a low light-level infrared television camera used in conjunction with the interferometer-spectrometer. This Southampton University infrared TV camera allowed any airglow structure to be quickly and efficiently identified and permanently recorded as video information. Taylor's system employed an image intensified isocon television system. This isocon television system is briefly described here for completeness.

The isocon tube is different than other scanning image tubes in that it uses a different portion of the scanning electron beam to create the signal. The low-energy electron beam scans a high-resistance target as in other tubes; however, the isocon signal comes from the electrons that are scattered off the target [Soule 1968] rather than the reflected electrons used by conventional equipment (orthicons use the reflected beam). The scattered signal, although small in magnitude, has a high signal-to-noise ratio, and is particularly well suited to the viewing of the low-contrast, faint OH airglow.

The TV system used to image the airglow structures was specially modified to enable clear images of the OH airglow patterns to be obtained in less than a second [Taylor 1984]. The television camera used was an English Electric Valve Miniature Isocon, Type P1477 fitted with a single-stage

image intensifier, optically coupled to a 55-mm image isocon tube. The camera has a signal-to-noise ratio of approximately 40 dB at 10 ft-candles (starlight conditions) and a dynamic range of about 2000:1.

To further enhance the capability of the camera to image very faint airglow structures, it was arranged for the electronic image to be integrated on the target of the TV tube for a period of up to a second (longer integration times allow the image charge on the target to migrate and thus smear the image) before being scanned and recorded onto video tape [Taylor 1984]. This technique is particularly useful as it improves the signal-to-noise ratio of the airglow signal by nearly an order of magnitude (7 times for a 1-second integration period) with no significant loss of temporal resolution.

The camera has an extended red spectral response (S25) with a peak sensitivity at about 500 nm and a long wavelength cut off at 900 nm. Images of the near-infrared OH structure were obtained by placing a Schott RG715 band stop filter in front of the camera lens. The combined response of this filter and the TV camera gave a bandwidth (half maximum) of 715 to 850 nm and a peak sensitivity around 750 nm. This bandwidth is illustrated in Figure 1-3. The location of all the OH emission bands within this spectral range are indicated. The intensity in the zenith of the OH emission within this bandpass is typically 5 to 15 kR; the principal emissions are the OH (9,4) and (5,1)

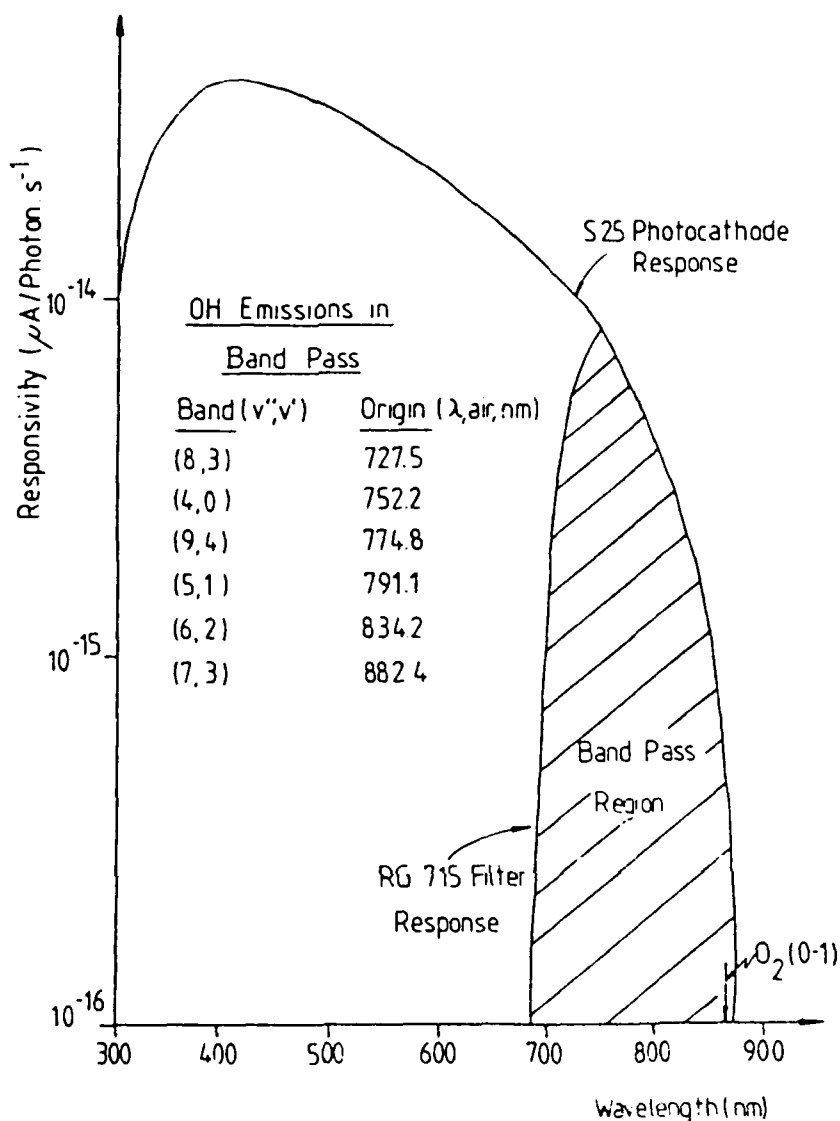


Figure 1-3. Isocon camera system spectral range including the OH emissions within that range [Taylor 1983-84].

Meinel bands [Taylor 1984]. The camera was fitted with a Nikon 85-mm, f/1.4 lens and was adjusted to give an almost square field of view of 15° horizontal by 13° vertical. The isocon camera used in this study is shown in Figure 2-9, mounted on the interferometer telescope.

The Southampton TV cameras have been used for many years to "photograph" the near-infrared OH airglow structure. An example of the quality of the video data gathered is shown in Figure 1-4. This video frame was taken in August of 1980 while observing over the Swiss Alps. The bright and dark bands each subtend about 1° of arc. These data were the basis upon which the interferometer's field of view was designed in order to resolve the spatial nature of the OH airglow structure.

Scope and Objectives

The specific goals and objectives are outlined as follows:

1. Design and develop an optical instrumentation system capable of quantifying the spatial, spectral, and temporal characteristics of OH near-infrared night airglow structure. The instrumental field of view must be one degree or less to resolve the structural characteristics of the airglow. The system must have spectral resolution of better than 3 cm^{-1} in order to provide spectra from which OH rotational temperatures can be calculated using appropriate algorithms and digital computer programs. The NESR must be sufficient to resolve the OH near-infrared airglow with scan times of less than 1 minute to resolve the temporal fluctuations of the airglow structure.



Figure 1-4. Image isocon photo of OH airglow structure taken by Taylor et al. [1980] in Switzerland in August of 1980.

2. Use the instrumentation system to measure the spectral, spatial, and temporal characteristics of OH near-infrared airglow structure from a mid-latitude observing site.
3. Develop and apply signal processing procedures extending the sampling and FFT work of Ware [1980] to extract both radiance and rotational temperature variations of OH airglow structure.
4. Derive error bounds on the measurement data, based upon system specifications such as field of view, scan speed, and spectral resolution, as well as instrument calibration, and signal processing techniques.
5. Present the observational results, correlate intensity variations, temperature fluctuations, and structure with simultaneous near-infrared video images, and compare the findings with expected OH airglow dynamics studies from other investigators.

CHAPTER II
OPTICAL INSTRUMENTATION SYSTEM DESIGN

Design Philosophy

The goal of this study was to develop a technique for simultaneously measuring the spatial, spectral, and temporal characteristics of OH near-infrared airglow structures. The basic instrumental approach chosen to provide the spectral resolving capability is a Michelson interferometer-spectrometer which is optically-compensated to achieve a very high throughput. The compensation technique used makes it possible for obliquely incident optical energy up to 5 degrees off axis to contribute to the detected signal without sacrificing spectral resolution. This resulting high throughput, within the interferometer, is matched at the input to a large diameter collecting telescope yielding a sub-degree field of view needed for spatial resolving power. The entire optical system is diagrammatically shown in Figure 2-1.

An optically-compensated interferometer has the high throughput needed to achieve a relatively high temporal resolving power, in other words, a scan time of less than a minute. Temporal variations are therefore identified while maintaining a spectral resolution of 2 cm^{-1} in the near-infrared. A spectral resolution nearly this high is

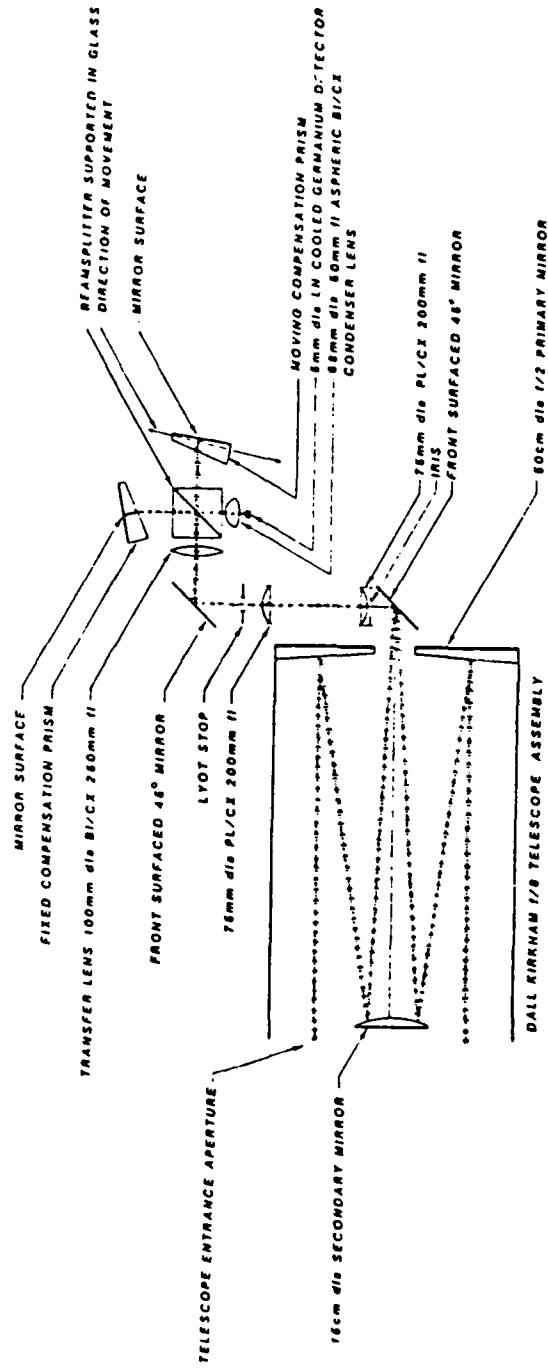


Figure 2-1. Optical layout of interferometer telescope system.

desirable in order to unambiguously compute OH rotational temperatures from the measured spectra. A free spectral range of 0.8 to 1.6 μm has been obtained using a cryogenically-cooled intrinsic germanium detector. The optical system was designed to maintain the high throughput capability ($0.285 \text{ cm}^2 \text{ sr}$) of the interferometer while operating at a narrow field of view ($\ll 1^\circ$) in order to be able to resolve the spatial nature of the airglow structure.

The design criteria and the resulting design for an optically-compensated interferometer are given in this chapter. Then an analysis is made of the resulting interferometer-spectrometer system.

High-Throughput Interferometer Design

The optical layout of a conventional Michelson interferometer was discussed in Chapter I. Referring to Figure 1-2, the retardation or path difference is a function of the entry angle of the incoming energy. The relationship is, $\Delta = 2d \cos \theta$, where d is the on-axis ($\theta = 0^\circ$) drive distance and θ is the angle of the off-axis ray. The maximum field of view for a standard Michelson interferometer is, $\Omega_{\text{max}} = 2\pi/R$ (Eq 1.1), where Ω_{max} is the maximum field of view of the instrument and R is the resolving power. When viewing faint airglow events this limitation on throughput is a severe one. The optical system is compensated to increase system throughput for temporal resolution. This high-throughput has been matched to a collector system to

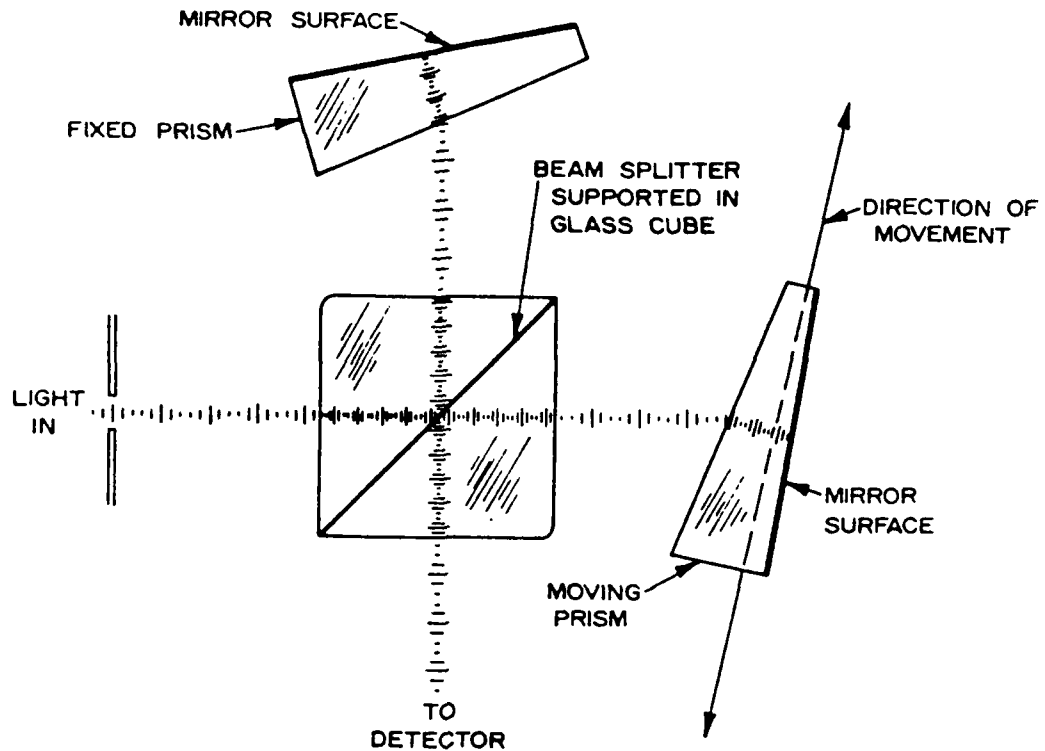


Figure 2-2. Optical compensation method conceived by Connes [1956].

maintain the throughput while narrowing the field of view (for spatial resolution).

The method used in this study to improve the throughput of the interferometer system is the one analyzed by Bouchareine and Connes [1963] and is depicted in Figure 2-2. The compensated-optics design used follows that developed by Despain et al. [1971], and the design limitations previously derived will be summarized here for completeness. Figure 2-3 shows the compensation analysis approach of Steed [1978]. With the optical compensation prisms inserted, the retardation is

$$\Delta_c = 2d \cos \theta + 2tn \cos \phi - 2t \cos \theta \quad , \quad (2.1)$$

where

Δ_c = retardation with compensation prisms inserted,

t = thickness of optical material,

n = index of refraction of optical material,

d = mirror drive distance, AC - AB,

θ = angle of off-axis ray,

ϕ = refraction angle of off-axis ray through optical material.

The retardation equation shown above can be expanded in a Taylor series and like terms collected to show the field of view dependency more directly; namely,

$$\begin{aligned} \Delta_c = & 2 \left[t(n - 1) + d \right] + \left[t \frac{n - 1}{n} - d \right] \theta^2 \\ & + \left[\frac{d}{12} + \frac{t(n^2 - 1)}{3n^3} + \frac{t}{12n^3} - \frac{t}{12} \right] \theta^4 \quad . \quad (2.2) \end{aligned}$$

which is a quartic equation in θ .

Ideally, the retardation Δ_c should be independent of the entry angle θ . Equation 2.2 shows that this is not possible by varying only the drive distance d and the index of refraction n . However, a significant improvement can be realized by designing such that,

$$d = t \left[\frac{n - 1}{n} \right] \quad , \quad (2.3)$$

which eliminates the θ^2 term in the retardation Equation 2.2 by forcing the θ^2 coefficient to zero. This leaves only

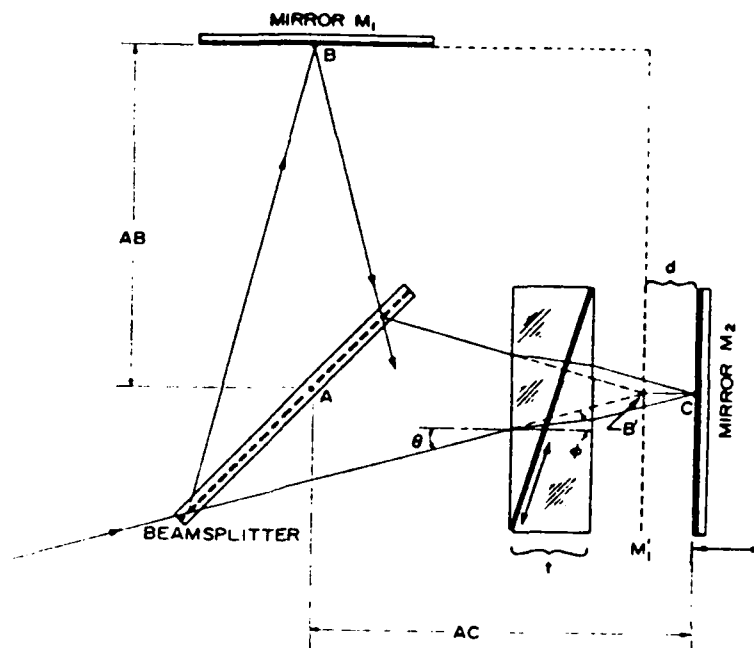


Figure 2-3. Optical compensation with an optical section inserted into one leg of a Michelson interferometer [Steed 1978].

the θ^4 term and since θ is small this term is relatively insignificant.

Designing the compensation wedges to satisfy Eq 2.3 and then solving Equation 2.2 for an on-axis ray ($\theta=0^\circ$), the resulting retardation Δ_{co} is

$$\Delta_{co} = \frac{2t}{n} [n^2 - 1] \quad . \quad (2.4)$$

Assuming a monochromatic wave front and using the results of Eq 2.4, the general retardation for the compensated case is

$$\Delta_c = \Delta_{co} + \Delta_{co} \left[\frac{\theta^4}{8n^2} \right] \quad , \quad (2.5)$$

where

- Δ_c = compensated retardation,
- Δ_{co} = retardation for an on-axis ray.
- θ = entry angle for incoming ray in radians
- n = index of refraction of compensation prisms.

The analysis for the Connes [1956] method shown in Figure 2-2, in which only one optical component is driven, is the same as for the system shown in Figure 2.3. The thickness of the optical material must, however, increase with the drive distance d in order to maintain optical compensation (see Equation 2.3). The increase in optical-material thickness needed to maintain compensation is obtained by driving one of the optical wedge/mirror assemblies in synchronism with the drive motor. Referring to Figure 2-2, it can be seen that the reflective elements or mirrors in this method are created by depositing the mirrored surface to the back side of each wedge.

Steed [1978] derived the limits on field of view as a function of resolving power based upon aberration limits. The results are categorized into several groups. The first is chromatic aberration, that is, differences in the compensation because the index of refraction of the optical material is a function of wavelength. The chromatic limit is

$$\Omega_c = \left[\frac{\Omega_M n(n^2 - 1) \lambda}{\delta n \Delta_{co}} \right] R, \quad (2.6)$$

where

Ω_C = field of view at wavelength λ in steradians,

Ω_M = field of view for conventional Michelson interferometer,

n = index of refraction at wavelength λ ,

$\delta n = n - n_C$ where n_C = index of refraction at compensated wavelength,

R = desired resolving power,

Δ_{CO} = retardation for on-axis ray,

λ = wavelength expressed in same units as Δ_{CO} .

The second limiting factor on field of view is that of spherical aberration. This limit is also derived by Steed [1978]. The maximum field of view assuming only spherical aberrations is

$$\Omega_S = \Omega_M n \sqrt{(2R)} \quad . \quad (2.7)$$

The third type of aberration is astigmatism. In the Connes method a wedge is placed in each leg of the interferometer; however, only one of the wedges is driven. This simplifies the mechanical design but because a wedge is in each optical path, astigmatism aberrations occur. The severity of the aberration increases as the angle (α) of the compensation wedges increases. Bouchareine and Connes [1963] quantify this aberration as

$$\Omega_A = 2\Omega_M / \tan^2 \alpha \quad , \quad (2.8)$$

where

α = prism angle of the compensation wedge.

The aberrations considered were each derived assuming the net effect of the distortion was a shift of one fringe in the interference pattern. These degradations prove to be the limiting factors upon the maximum usable field of view. Figure 2-4 is a plot of Equations 2.6, 2.7, and 2.8 and shows the relationship between these various limits. At least an order of magnitude improvement in throughput is obtainable using the wedge prism compensation technique.

The next step in the system design is to ascertain the optical retardation for the Connes [1956] method. Referring to Figure 2-5, Steed [1978] showed the drive plane is parallel with the apparent image plane of the optical wedges. The difference in optical path length or retardation between image points A1 and A2 separated by a drive distance X is

$$\Delta = 2X \sin(\beta - \gamma) \quad , \quad (2.9)$$

where

$$\beta = \sin^{-1}(n \sin \alpha),$$

$$\gamma = \alpha - \tan^{-1}\left[\left(\frac{n-1}{n}\right) \tan \alpha\right],$$

α = wedge angle,

X = drive distance.

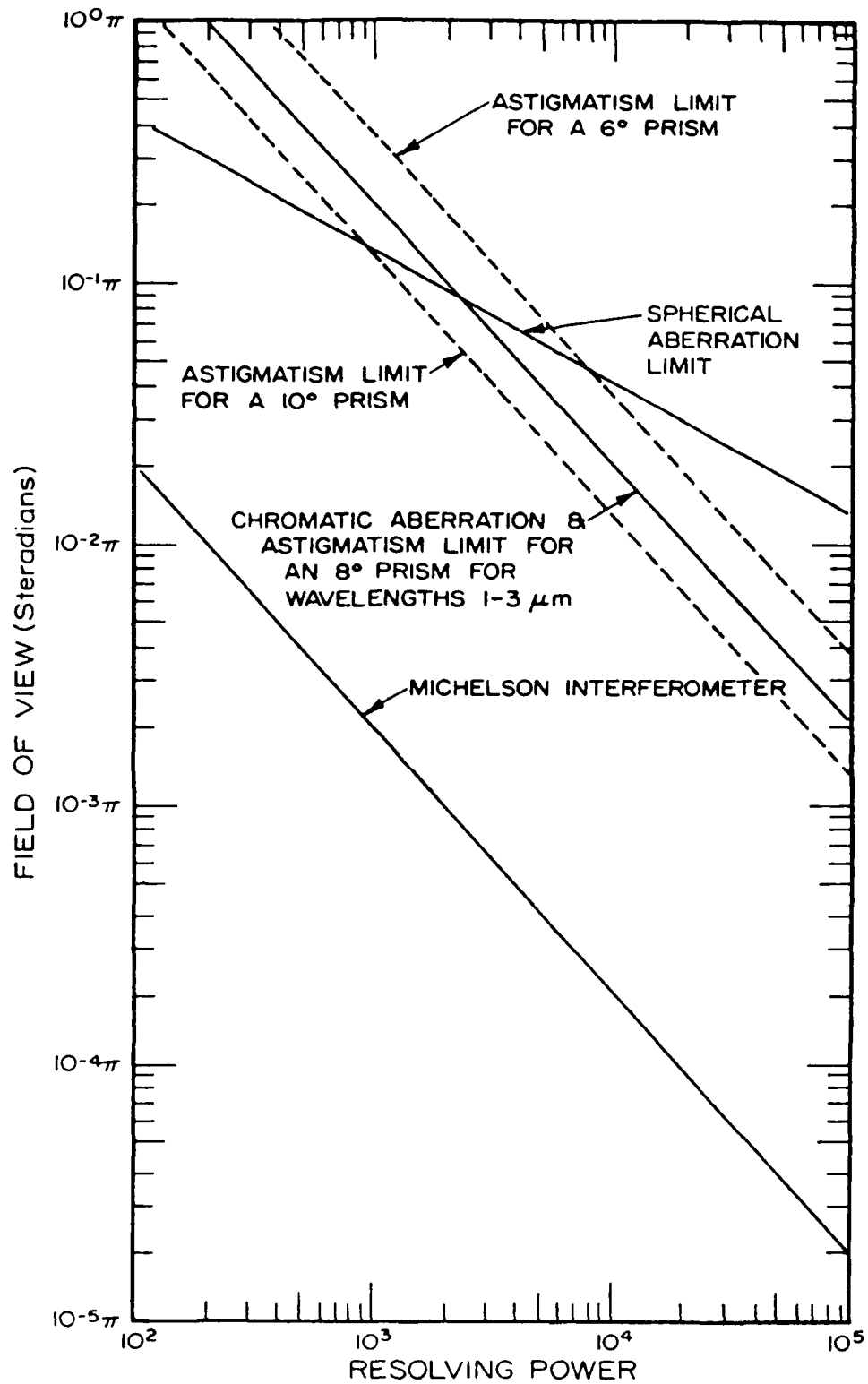


Figure 2-4. Plot of aberration limits for Connes [1956] method of optical compensation compared with conventional Michelson interferometer [Steed 1978].

Drive System

Examination of Equation 2.9 shows that the choice of a large wedge angle reduces the actual drive distance, thereby easing the mechanical drive requirements. However, the choice must be made in conjunction with the limits on distortion presented in Figure 2-4. The wedges and cube beamsplitter used in this instrument are made of a high quality quartz, namely, Infrasil I, manufactured by Amersil Corporation. The measured index of refraction for this material is 1.45. A compensation prism wedge angle of 8° was chosen. Solving Equation 2.9 for this wedge angle, then $\beta = 11.64^\circ$, $\gamma = 5.50^\circ$, and $\Delta = 0.21\lambda$. The optical retardation for this compensation technique is only about 20% of the drive distance, where as in a conventional Michelson interferometer the retardation is equal to $2d$ where d is the drive distance. Thus, for a given spectral resolution the compensated interferometer requires a drive distance of $2/.21=9.5$ times longer than the conventional Michelson approach.

An optically-compensated interferometer with a spectral resolution of 2 cm^{-1} requires a slide movement of 3.1 cm. This comparatively large drive distance is accomplished using a gas-lubricated platform, providing near-zero friction, developed by Haycock [1975]. The platform translates the optical wedge/mirror assembly and as such must maintain mechanical tolerances as close as possible to the wavelength dimensions of the infrared light being

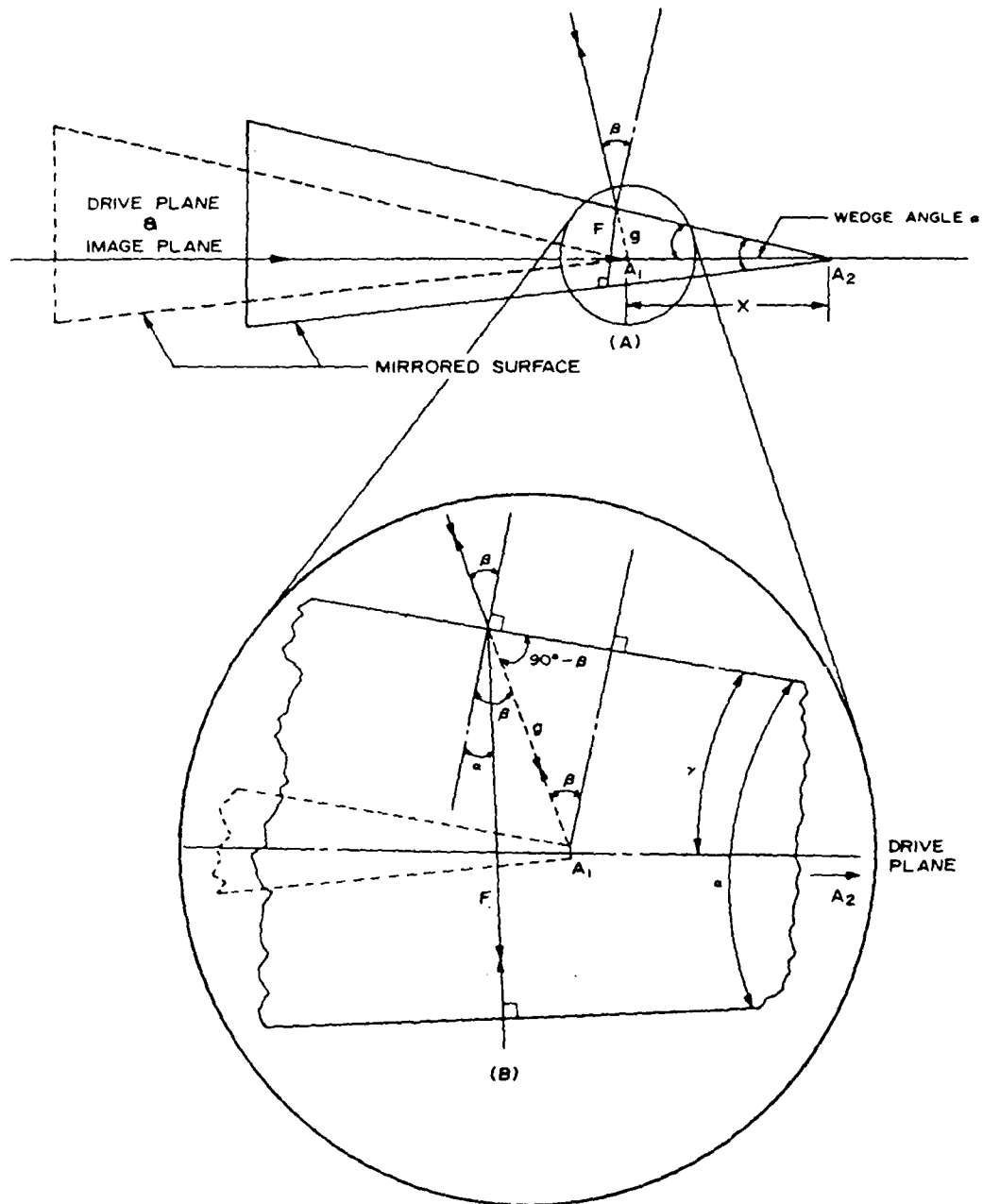


Figure 2-5. Cross section of optical wedge in two drive positions a distance X apart [Steed 1978].

measured. The gas bearing surfaces are lapped to a tolerance of about 1 wavelength of 5461 Å light and operate with a clearance of 2.5×10^{-4} cm. At an operating pressure of 6-12 psi the bearing will maintain an optical alignment of 1 arc second while translating 5 cm [Haycock 1975]. The optical components are then mounted on the bearing-supported optical platform. Adjustment for parallelism is accomplished on an optical bench using a laboratory He-Ne laser as a light source. The material used in the platform and bearing assembly is a specially formulated Invar alloy, chosen for its excellent temperature and stability characteristics and to match the thermal expansion characteristics of the optical material. This sophisticated platform provides the relatively long drive distances required (up to 5 cm) as well as the mechanical accuracy needed to translate the optical components properly.

The platform is driven by a "voice coil" motor and therefore makes no physical contact with the rest of the instrument. The motor is driven by a standard servo-amplifier with feedback from positional and velocity sensors located within the platform slide. The main signal driving the slide is generated by a digitally-controlled ramp which can be adjusted for slide velocity and drive distance. The slide controller can produce variable scan times of 5 seconds up to several minutes, and a drive distance of up to 5 cm. The completed interferometer uses a 10-cm cube beamsplitter and 11.4-cm diameter end wedges with a prism

angle of 8°. The interferometer with bearing system is shown in Figure 2-6.

For simplicity, a secondary HeNe laser-excited interferometer is used, with its independent moving mirror on the same optical platform as the primary optical signal channel, to monitor the slide position. The laser signal is counted down by 6 and used to digitize the main channel interferogram. This method provides sufficient sample points for a 16k fast Fourier transform.

The other specifications for accuracy of the optical and mechanical components are described in detail by Steed [1978]. The entire system was originally designed to be operated at liquid nitrogen temperature (77 °K) to reduce background radiation at longer wavelengths (>2 μm). The spectral range used in this study (0.8 to 1.6 μm) is not background limited and therefore does not require the added complexity of optical train cooling.

Detector System

The optically-compensated interferometer has a very large throughput ($A\Omega = 1 \text{ cm}^2 \text{ sr}$). The desired goal of optical compensation was to improve the sensitivity of the interferometer system; however, to take advantage of the large throughput a large diameter detector is required. For example, assuming a throughput of $1 \text{ cm}^2 \text{ sr}$ and collector optics with a very fast f-number of 0.5, the detector diameter would have to be 0.650 cm. Large infrared

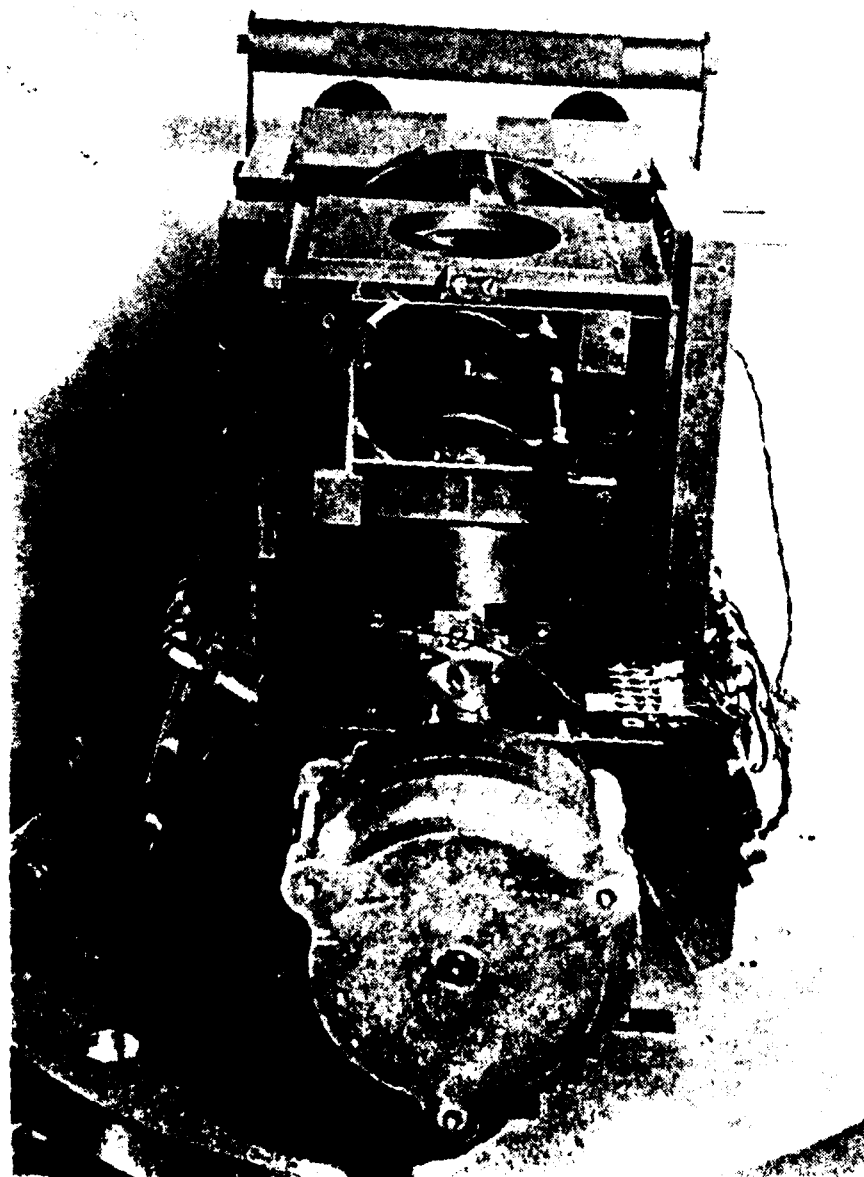


Figure 2-6. Optically-compensated interferometer showing beamsplitter, wedges, and bearing assemblies.

detectors with the necessary detectivity are very difficult to manufacture; therefore, some compromise was necessitated. The required detector diameter and the speed of the collecting optics shown in the example are both somewhat impractical.

A detector system was chosen which was readily available and had proven effective in the past. The detector selected was an RCA Ltd., solid state germanium device with a self-contained preamplifier and load resistor in a liquid-nitrogen dewar. Figure 2-7 is a picture of the detector dewar. The detector is 5 mm in diameter and has a noise equivalent power (NEP) of 1.12×10^{-14} W/Hz at $1.27 \mu\text{m}$ and covers a spectral range of 0.8 to $1.6 \mu\text{m}$.

It was decided that a scan rate of 30 seconds would be sufficient to resolve the temporal variations of first interest in the OH airglow structure. This decision was based upon video data gathered by Taylor et al. [1980]. A 30-second scan, a minimum wavelength of $0.8 \mu\text{m}$, and a drive distance of 3.1 cm (spectral resolution of 2 cm^{-1}) set the detector electrical bandwidth at 150 Hz. The RCA detector has a bandwidth of 600 Hz. Appendix A contains the detailed specifications of the detector system.

Telescope Design

The spatial characteristics of the airglow structure, shown by Taylor [1983-84], dictated that the instrument field of view be less than 1° full angle. The goal of the

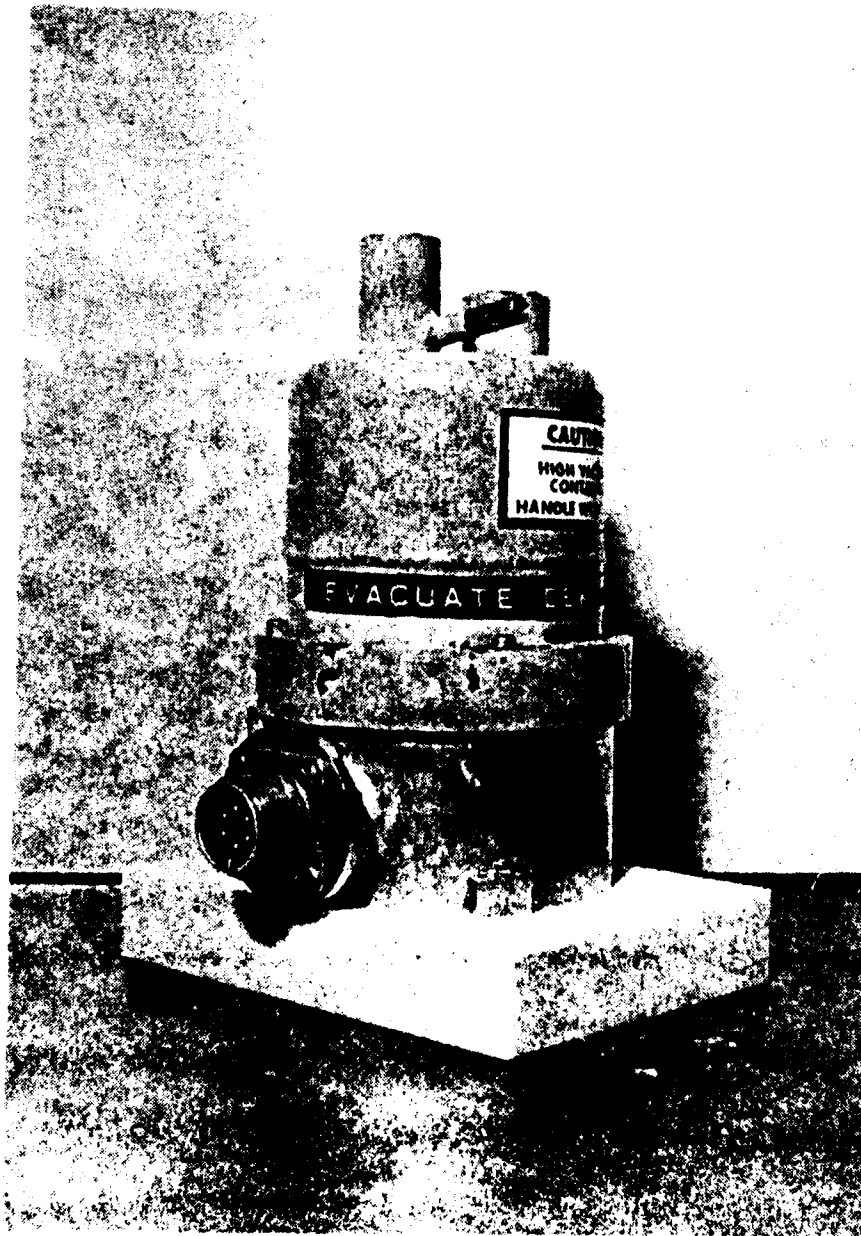


Figure 2-7. Picture of RCA Limited liquid-nitrogen cooled germanium detector system.

optical design was to maintain the inherent high throughput of the compensated interferometer throughout the entire system. All portions of the optical path were examined in order to ascertain where the system was throughput-limited. The choice of a detector, and practical limitations on the f-number of available condenser lenses proved to be the limiting factors. An optical system was designed, incorporating the interferometer, using a large diameter collector, which maintained the system throughput while narrowing the field of view to under 1°. The instrument system was now capable of measuring the temporal, spectral, and spatial variations of the airglow layer.

The design of the optical system began with the detector and choice of its condenser lens and proceeded back towards the telescope collector. The entire optical system is described diagrammatically in Figure 2-1. The diameter of the condenser lens must, however, allow the converging beam to pass through the beamsplitter and wedges without vignetting. A commercially available condenser lens with a diameter of 68 mm and an effective focal length of 50 mm was chosen. The condenser lens and detector diameter of 5 mm set the system throughput or $A\Omega$ at $0.28 \text{ cm}^2 \text{ sr}$. Referring to Figure 2-1, a throughput of $0.28 \text{ cm}^2 \text{ sr}$ translates to a beam diameter entering the interferometer of 92 mm and converging in a 6° full field of view. The physical dimensions of the detector optics outlined here fit well within the size constraints of the basic interferometer. The field of view

is also within the aberration limits, shown in Figure 2-4, for an optically-compensated interferometer.

The calculated throughput can now be used to design the telescope needed to narrow the field of view to 1° or less. A throughput, dictated by the detector system, of $0.28 \text{ cm}^2 \text{ sr}$ and a 1° field of view design goal, set the collector diameter at $D = \lambda \Omega / 2\pi (1 - \cos\theta) = 44 \text{ cm}$. A 50.8-cm (20-inch) diameter system was chosen because of availability and to allow for some error in aligning the telescope optics. Taking advantage of the larger collector, the field of view was narrowed to 0.8° requiring a 48-cm diameter collector, within the 50.8-cm mirror size and still allowing for some error in optical system alignment. For portability, an $f/2$ primary was specified to minimize the telescope length. An overall system f number of 8 was selected to transfer the telescope image to the proper position.

In this application, the purpose of the telescope is to gather energy and transfer it to the detector, rather than to transfer a spatial image. Therefore, the quality of the optical image within the field of view is not of as great a concern as it would be in an imaging system. Many types of folded telescope systems were considered. In order to simplify the optics Driscoll and Vaughan [1973] suggests a Dall-Kirkham type because of the spherical secondary, if the resulting image distortion is acceptable. The distortion for a Dall-Kirkham system of this size was calculated using the formula in Driscoll and Vaughan [1973], and found to be

less than 0.4% of the area (coma and astigmatism distortion were calculated in terms of primary mirror area that will be degraded) of the primary mirror. Therefore, a Dall-Kirkham type of telescope, being more than adequate, was chosen for its simplicity and relatively low cost. This type of telescope has a spherical secondary mirror and an elliptical primary mirror. The telescope-equipped interferometer system with the isocon camera mounted on the telescope is pictured in Figure 2-9.

The last step in the optical design was to provide an optical interface between the telescope and the detector sub-systems. Two primary considerations were given emphasis in this interface design: (1) imaging the detector on the primary mirror, and (2) imaging the condenser lens on the telescope focal plane. The detector may have an uneven response across its area, therefore imaging the detector on the primary mirror minimizes the effects of off-axis rays by illuminating the entire detector by light entering within the field of view of the instrument. An image of the detector condenser lens at the telescope focal plane allows for independent control of the system field of view.

An adjustable iris was then placed at the focal plane for adjusting the field of view while still allowing the entire detector to be illuminated by energy within the field of view. Careful choice of physical dimensions and optics allow the transfer of each image independent of the other.

The goal of placing a detector image on the primary mirror was accomplished by the use of two lenses. Referring to Figure 2-1, a transfer lens, which has a diameter of 100 mm and a focal length of 250 mm, is placed near the interferometer beamsplitter. This lens produces an image of the detector at a focal point near the physical entrance to the interferometer housing. The magnification ratio of this transfer lens focal length to the focal length (50 mm) of the condenser lens determines the detector image size at this point; therefore, the detector image is 25 mm in diameter. A field stop is placed at this point to limit the detector image size throughout the rest of the system. Another transfer lens, which has a 75-mm diameter and a focal length of 200 mm, is placed at the focal plane of the telescope. This lens transfers the detector image at the field stop onto the primary mirror. As can be seen from Figure 2-1, two angled mirrors were required to meet the physical constraints of the design.

The second design objective of the optical transfer system was to place an image of the detector condenser lens on the telescope focal plane. A collimated image of the condenser lens is generated by the 100-mm diameter transfer lens that is placed near the interferometer beamsplitter. The addition of a 75-mm diameter, 200-mm focal length lens placed at the field stop focuses this image at the telescope focal plane. The placement of this lens at a detector image point does not affect that image. An adjustable iris was

then placed at the telescope focal plane for control of the field of view. The field stop and the iris provide the limiting apertures for the entire system. The optical system described here was verified by Harris [1984] using a computer-aided optical ray-tracing program.

The optical lenses used in the design are made of commercial-grade optical glass and have no coatings. The beamsplitter and wedges are constructed of quartz and are not coated. The primary and secondary telescope mirrors are aluminized reflection surfaces with a SiO_2 coating.

Instrument Housing

The interferometer-spectrometer with its associated optical and telescope systems was placed in a 30-inch diameter, 45-inch tall, round container. The interferometer placed in the instrument housing is shown in Figure 2-8. The telescope attached to the container is shown in Figure 2-9. The large container size was chosen to support the telescope in a stable manner. The base of the package was mounted upon a rotating stand which provides the ability to move the telescope in azimuth. The rotating base has attached three large pneumatic tires for system mobility and three leveling screws to stabilize the interferometer for operation. The telescope is mounted to the side of the container with a 10-inch diameter ball-bearing allowing the telescope to be rotated in elevation. The two rotating joints provide the telescope with complete pointing freedom.

The specifications of the instrument with the telescope are given in Table 2-1.

TABLE 2-1. Summary of interferometer-spectrometer specifications.

Throughput	0.28 cm ² sr
Scan period (minimum)	1 scan/ 30 seconds
Collector diameter	50.8 cm
Field of view (full angle)	0.8 degrees
Spectral range	0.8 to 1.6 μm
Spectral resolution	2 cm ⁻¹
Detector type	Intrinsic germanium
Detector NEP	1.1 x 10 ⁻¹⁴ watts/√hz at 1.5 μm
Dynamic range	80 dB
System sensitivity	16 R/cm ⁻¹ at 1.5 μm

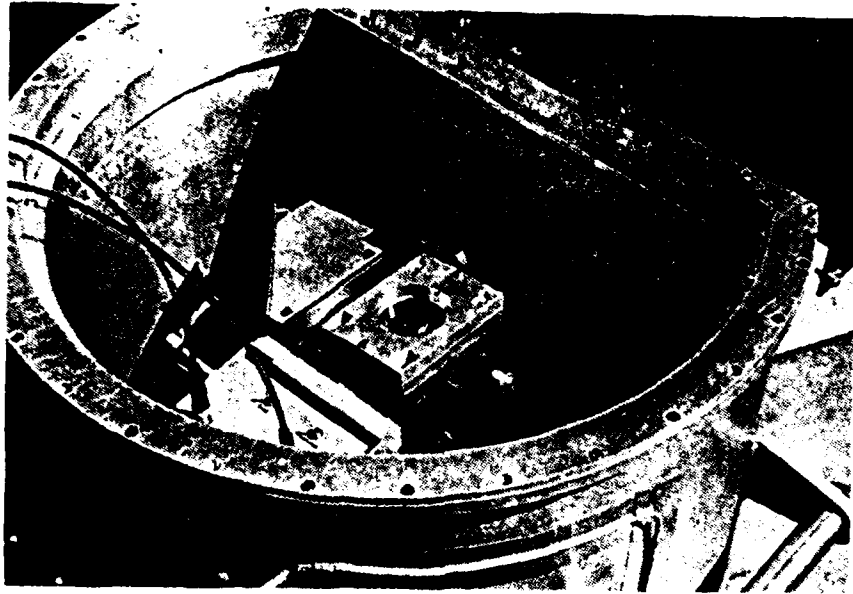


Figure 2-8. Interferometer placed inside housing.

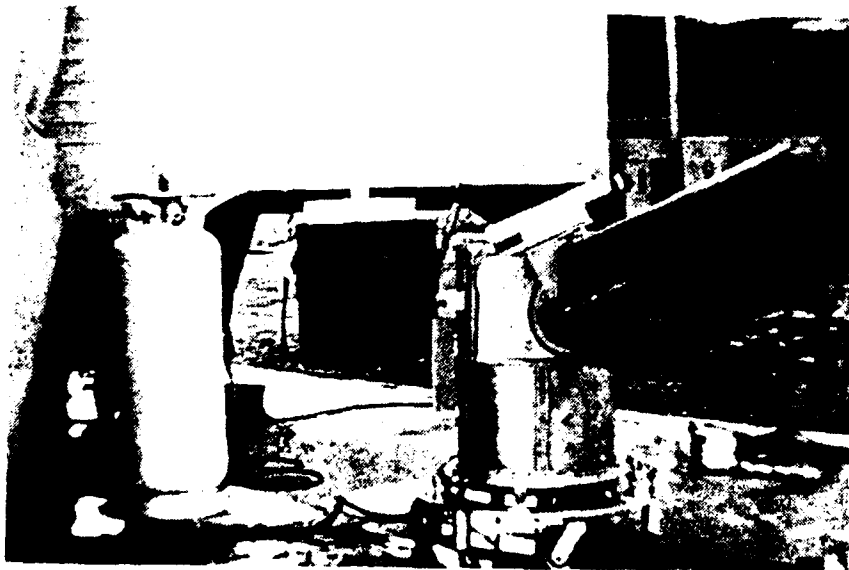


Figure 2-9. Interferometer system equipped with 20-inch diameter telescope. The isocon camera is also mounted on the telescope.

CHAPTER III
MEASUREMENT THEORY

The Interferogram

The electronic signal from the interferometer detector is a low-frequency time-continuous signal called an interferogram. The interferogram is a scaled analog of the incoming light frequency. Using the approach of Loewenstein [1971], and referring to the layout of a Michelson interferometer in Figure 1-1, the interferogram signal is of the form

$$f_s = v\sigma \quad , \quad (3.1)$$

where

σ = input light wavenumber in cm^{-1} ,

v = rate of change of effective path difference in
cm/second,

f_s = scaled frequency output of interferometer (the
interferogram) in Hz.

The detector used in this study is sensitive in the region from 12500 to 6250 cm^{-1} ($\lambda = 0.8$ to $1.6 \mu\text{m}$). The scan rate for the interferometer was set at 30 seconds; therefore, the input light frequency was scaled to audio frequencies of less than 200 Hz.

The light power reaching the detector in an ideal interferometer is [Loewenstein 1971]

$$P_{\text{det}} = 2A^2(1 + \cos 2\pi\sigma x) \quad , \quad (3.2)$$

where

A = amplitude of on-axis monochromatic point source,

x = effective path difference in cm.

In the Loewenstein model, the single line of Equation 3.2 is replaced by an input power density spectrum of the form $A^2 = B(\sigma)$. Making this substitution in Equation 3.2, neglecting the constant (dc) part, and integrating over σ produces

$$I(x) = 2 \int_0^* B(\sigma) \cos(2\pi\sigma x) d\sigma \quad , \quad (3.3)$$

where $I(x)$ is defined as the interferogram. The desired information $B(\sigma)$ (the input spectrum) is obtained by taking the inverse Fourier transform of $I(x)$. The signal produced by the interferometer is referred to as a "double-sided" or "symmetric" interferogram. An example of a double-sided interferogram is shown in Figure 3-1; note that the same information is available on both sides of the large center which occurs at zero path difference. The interferometer slide is moved an equal distance on each side of the optical zero path difference to create a symmetrical signal.

Since the interferogram $I(x)$ in Equation 3.3 is symmetric, the spectrum $B(\sigma)$ may be obtained using a simple

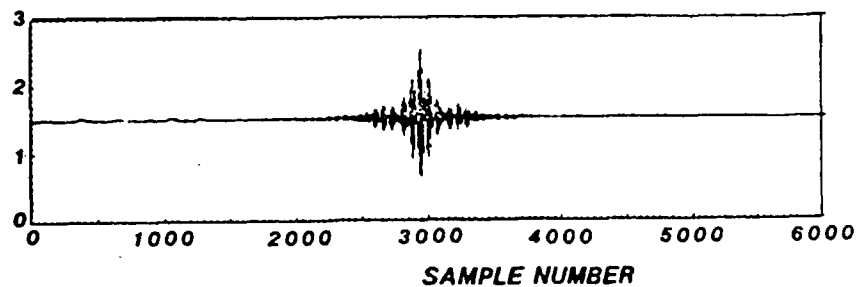


Figure 3-1 Typical "double sided" interferogram.

cosine transform of the form

$$B(\sigma) = \int_0^{\infty} I(x) \cos(2\pi\sigma x) dx \quad (3.4)$$

The power spectral density is computed with a digital computer using a Fast Fourier Transform (FFT). The FFT used to process the data for this study was developed by Ware [1980]. The digitized interferogram was produced using a 12 bit analog to digital converter on the detector amplifier output and enough samples were taken to perform a 16,384-point transform. The implementation of the FFT is beyond the scope of this paper but that used in Fourier transform spectroscopy was adapted by Forman [1966] from the radar signal processing work of Thomas Stockham, then at MIT Lincoln Laboratory. The FFT is explained extensively by Brigham [1974].

The computation of the FFT requires that the interferogram be sampled at uniform increments of path difference. Ideally, the laser reference channel should be a short wavelength laser beam which passes through the

interferometer optical train as does the signal. Otherwise, the reference beam may experience different motion stability than the signal beam, due to nonidentical geometry. However, for simplicity, a separate laser ($\lambda = 6328 \text{ \AA}$) interferometer channel was used and provides the uniform sampling function signal. The laser channel signal is divided to obtain a sample rate of 650 Hz. The interferogram is digitized at a free running rate of 50 kHz. The values taken between laser channel zero crossings are then averaged and stored as the data point for the slide position corresponding halfway between adjacent laser crossings. This over-sampling method will, according to Ware [1980], minimize the system noise gain as well as minimize the effects of slide velocity variations in the sampled data.

Calibration Source

The determination of relative OH spectral line strengths is sufficient to compute rotational temperatures. Since this is a major interest in this study, a calibration technique to produce a relative instrument response was developed. The absolute calibration of an interferometer-spectrometer is an intricate process; details of the approach are outlined by Wyatt [1978]. Ware [1980] performed an interferometer wavenumber response calibration as a function of optical alignment. He found that the relative response must be reestablished each time the

instrument is realigned at the time of data collection because the instrument would only remain in acceptable alignment for about 2 hours..

A relative instrument response was obtained by causing the interferometer to view a calibration source composed of a tungsten bulb illuminating a pair of ground glass diffusion screens (see Figure 3-2). The intensity of the illumination was controlled by placing a plate with a small 3-mm aperture between the bulb and the diffusion screens. The second screen was then imaged by a projector lens onto a 24-inch diameter ground glass viewing screen placed ten feet away. The net brightness of the source was adjusted so the calibration source intensity as viewed by the interferometer was approximately that of the night sky. The calibration source assembly was mounted inside of a 24-inch diameter, 10-foot long tube. The viewing screen was sufficiently large to completely fill the interferometer field of view, thus providing a diffuse source.

The long length (3.0 meters) of the calibration source was chosen to ensure that the illumination on the viewing screen was uniform across the entire surface viewed by the interferometer. The quality of the calibration source was calculated using the geometry described above and assuming the tungsten bulb was a blackbody source with correction for the emissivity of tungsten.

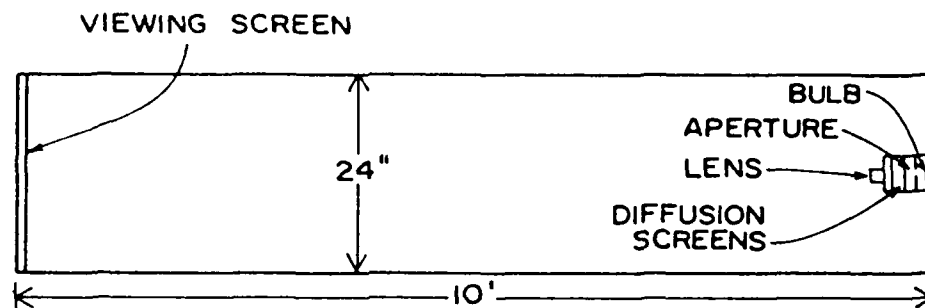


Figure 3-2. Interferometer Calibration Source.

Instrument Response

A relative instrument response was obtained each time the instrument was realigned during the data taking process. The calibration alignment process was repeated about every 2 hours. The interferograms obtained from the instrument when observing the calibration source were transformed using the same FFT and apodization (discussed later in this chapter) routines as were used for the airglow data signal processing described above. The calibration source spectral or "blackbody" curves were then averaged together (from 5 to 10 frames) to minimize noise and irregularities.

The tungsten bulb in the calibration source has a blackbody equivalent temperature of 2370 °K when operated at the specified current (750 mA), according to Gilway Technical Lamp [1982], its manufacturer. The Plank equation can be used to calculate the spectral sterance $L_B(\lambda)$ in watts/meter, for the assumed blackbody radiation source as, shown by Wyatt [1978]

$$L_B(\lambda) = \left[\frac{2hc^2}{\lambda^5 \left[\exp \frac{hc}{\lambda kT} - 1 \right]} \right] , \quad (3.5)$$

where

$h = 6.6262 \times 10^{-34}$ (Js) (Plank's constant) [Wyatt 1978],

$c = 2.9979 \times 10^8$ (m/s) (speed of light) [Wyatt 1978],

λ = wavelength (m),

$k = 1.3806 \times 10^{-23}$ (J/°K) (Boltzmann's constant) [Wyatt 1978],

T = absolute temperature (°K).

The interferometer detector measures energy coming from the interference of two light rays of the same optical frequency; and the germanium detector operates in a photon sensitive mode. As a consequence, in the analysis it is desirable to manipulate Plank's equation into terms of wavenumber and quanta (photons). The relationship between sterance and photon sterance is

$$L_p = L_B \lambda / (hc) . \quad (3.6)$$

Noting the relationship between wavenumber and wavelength and that Equation 3.5 is a density function

$$\sigma = 1/\lambda , \quad (3.7)$$

$$d\sigma = - 1/\lambda^2 d\lambda . \quad (3.8)$$

Using Equations 3.7 and 3.8 and converting from meters to centimeters, Plank's equation can now be shown in terms of photons $\text{cm}^{-2} \text{sr}^{-1} \text{sec}^{-1} \text{cm}^{-1}$ or

$$L_p(\sigma) = \left[\frac{2c\sigma^2}{\left(\exp \frac{hc\sigma}{kT} - 1\right)} \right] \quad (3.9)$$

The photon sterance for the 2370°K tungsten bulb calibration source was calculated using Equation 3.9 and corrected for the emissivity of tungsten using data from Weast [1977]. The averaged blackbody spectrum taken by viewing the calibration source, was then divided by the photon sterance. The resulting curve was normalized to its peak value and constitutes the relative instrument response used in the rotational temperature calculation model developed in Chapter IV. The values for the instrument response curve are shown as part of Tables 4-1, 4-2, 4-3, and 4-4.

Phase Correction

The spectrum computed from an interferogram using the selected FFT is algebraically complex (contains both real and imaginary parts) [Ware 1980]. The incoming signal contains no inherent phase information; therefore, any phase angle computed during the FFT process is an artifact of the system. A nonzero phase relationship is caused by two main factors. First, phase shifts occur in optically-compensated interferometers because the optical beamsplitter, wedges, and lenses are not strictly uniform as a function of wavenumber. Second, a linear phase shift occurs during the sampling of the interferogram for FFT processing, when the

zero path difference point is not centered in the signal time window.

The amplitude of the measured spectrum could be obtained by the magnitude operation (square root of the sum of the squares of the real and imaginary parts). However, this operation always yields positive noise components, increasing the noise by $\sqrt{2}$. This increase in noise is especially harmful when several frames of data are signal averaged (coadded) to help identify low weak features in the airglow emission spectrum. The sampling phase shift error may also vary from frame to frame. Consequently, a method of phase correction based upon the data within each frame must be used.

The phase characteristics of each data frame could be obtained by Fourier transforming a small data set around the "center" of the interferogram. This process would yield a very low resolution spectrum from which the slowly varying phase information could be easily extracted. However, this truncation and transform process is the same as convolving the original spectrum with the Fourier transform of the truncating function. As described by Ware [1980], this convolution is merely a digital filter operating in the frequency/phase domain. Hamming [1977] showed that for a given filter width the minimum noise gain is obtained when the convolving function is rectangular in shape. The phase characteristics are not related to the incoming signal in any way so the rectangular filtering process may be

repeated as many times as necessary to identify and remove the phase anomalies from the computed spectrum. When the filtering process is complete, the remaining "real" part of the transform is used as the measured spectrum (power spectral density function).

The spectral frames were phase corrected with convolving filter windows of 3, 5, 9, 17, and 65 sample point widths in a repetitive manner. Figure 3-3 shows an instrument uncorrected blackbody curve both before and after phase correction, and Figure 3-4 shows the same information for a spectral frame. Examination of Figures 3-3 and 3-4 show that the imaginary portion of the power spectral density (caused by chromatic variations within the instrument optics) has been eliminated by the phase correction algorithm.

Apodization and Interpolation

The calculation of OH airglow rotational temperatures was a major goal of this study. The calculation of temperature requires the extraction of relative spectral line intensities from the transform of the interferogram. The relative instrument response and phase correction steps described above are modifiers in signal processing the line intensities.

The shape of an individual spectral line is of interest because the shape will affect how the a best estimate of the line emission intensity is extracted from the data. Due to

the discrete nature of the transitions of the excited OH molecule, the spectral lines entering the interferometer are discrete in shape except for a small finite width due to Doppler and collisional broadening plus "time windowing" of each photon source. The numerical computation of an FFT requires that the sampling be limited in length. The truncation or multiplication of the interferogram by a rectangular "window" in the time domain is the same as frequency domain convolution of the discrete spectral frequencies with the Fourier transform of the rectangular window function. The Fourier transform of the rectangular window is a $(\sin x)/x$ or "sinc" function. This characteristic spectral line shape is referred to as an "instrument function." The high side lobe behavior of the sinc function (largest side lobe -13 dB down in amplitude) causes the various lines in the spectrum to interact or mesh together. Therefore, it is desirable to establish a technique to suppress the sinc function behavior and force the signal component into as much of a discrete line shape as possible.

The process of suppressing the sinc function side lobes is called apodization. The apodization of the spectral information can be accomplished either in the interferogram domain by multiplying the interferogram with another window then performing the FFT, or by convolving the transform of the window with the transformed interferogram. The

convolution of the spectral data with the transform of the chosen window is the method used for this study.

Numerous apodization functions have been tried for use with Fourier transform spectroscopy. In choosing an apodizing function the trade-off is among instrument function width (resolution), side lobe attenuation, and computational efficiency. Norton and Beer [1976] computed over 1100 different apodization windows and plotted each as a function of central peak width versus height of maximum side lobe. Their study indicated an optimal boundary existed between the two plotted parameters. Figure 3-5 shows the Norton and Beers limit with some specific functions also shown. Vagin [1980] independently computed over 3000 functions and also showed that this boundary exists. However, he went on to analytically show that for a chosen characteristic (either side lobe suppression or resolution) an optimal apodization function can be computed. Harris [1978] presents an excellent analysis of many of these apodization functions and shows the trade-offs associated with each. Nuttall [1981] shows some corrections to Harris's work and presents additional functions for consideration.

The present interferometer's full-width half-maximum (FWHM) instrument function is 1.8 cm^{-1} . The OH spectrum in the $1\text{-}\mu\text{m}$ wavelength region has line separations on the order of 10 cm^{-1} . This occurrence renders the prime consideration in the choice of an apodization function as one of side lobe

attenuation and ease of computation, rather than maximum resolution.

As can be seen from Figure 3-5 the Hamming window (sometimes referred to as the "minimum 2-point" window) is located on the optimal boundary. This function is comparatively simple to compute because it contains only two terms and provides side lobe attenuation of -43 dB (a 20 dB improvement over that provided by the sinc function). The additional side lobe attenuation is sufficient because the data collected for this study have signal-to-noise ratios of about 100, thus placing the side lobe behavior below the noise level. The Hamming window yields good spectral resolution by providing a FWHM central lobe of 2.7 cm^{-1} which is sufficient to identify the OH spectral characteristics. This window also has an asymptotic side lobe roll-off of 6 dB per octave [Harris 1978].

The Hamming convolution function takes the form

$$I_{\sigma_0} = \sum_{k=-6}^{k=+6} I_{\sigma} \left[0.53836 \text{ sinc}[\pi c(k\Delta\sigma_0)] + 0.46164 \left[\frac{\text{sinc}(\pi[c(k\Delta\sigma_0)+1]) + \text{sinc}(\pi[c(k\Delta\sigma_0)-1])}{2} \right] \right]$$

, (3.10)

where

$$\Delta\sigma = \sigma - \sigma_0,$$

k = counter for integer sample numbers centered at transform point nearest σ_0 ,

- σ = wavenumber at integer sample in cm^{-1} ,
 σ_0 = wavenumber at point where intensity is being computed in cm^{-1} ,
 I_σ = intensity of transformed data at integer transform wavenumber σ ,
 I_{σ_0} = intensity of apodized data at wavenumber σ_0 ,
 c = number of sample points per wavenumber.

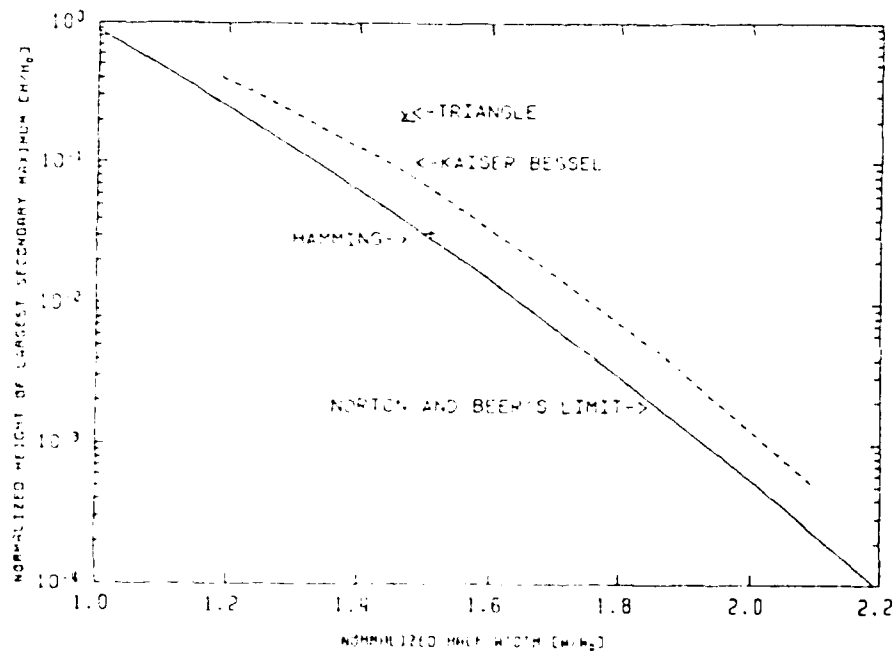


Figure 3-5. Optimal apodization functions, showing resolution vs. side lobe attenuation [Espy 1984].

The discrete spectral data points computed by the FFT occurred at 1.5-cm^{-1} intervals; therefore, as can be seen from Equation 3.10, the convolution computation was summed over ± 4 sample numbers. Examination of Equation 3.10 shows that this equation, in addition to suppressing side lobes, can be used to interpolate spectral values between the

discrete computed points of the FFT. Figure 3-6 shows the Hamming instrument function compared with the "square window" sinc function and also the common "triangle window" sinc^2 function. All three functions have been normalized to their respective peak values at 1000 for comparison.

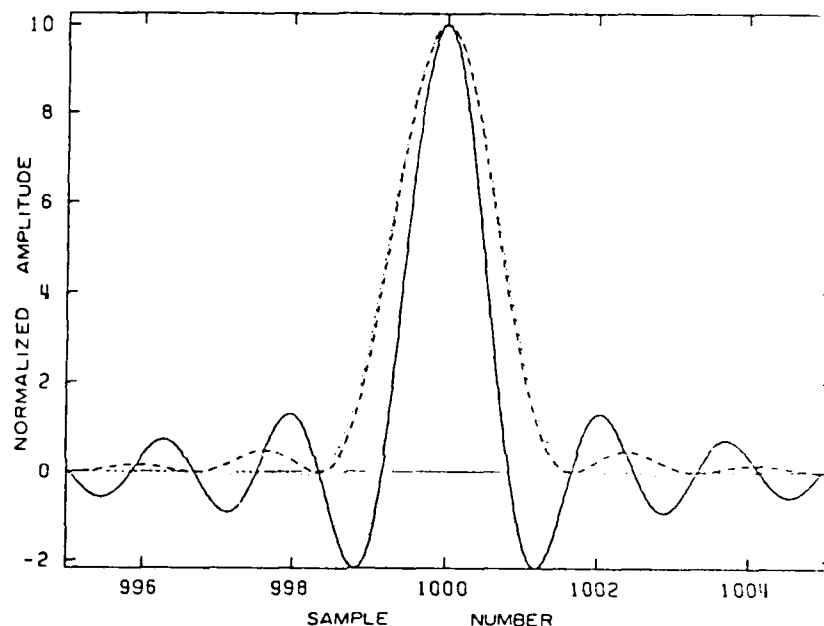


Figure 3-6. Comparison of normalized instrument functions; sinc (—), sinc^2 (- -), and Hamming (···) [Espy 1984].

Line Amplitude Extraction

The interferograms were recorded in "raw" form on analog tape during the measurement campaigns. The analog tapes were later played back, digitized, formatted by computer and stored on digital tape. The digitized interferograms were then submitted to the FFT signal processing routine. The power spectral density information generated by the FFT for

each interferogram was also stored on digital tape for later processing.

The information of interest within each spectral frame, needed for rotational temperature calculations, was the intensity of a few specific OH spectral lines (the temperature model is explained in Chapter IV). In order to identify the spectral features of interest, each of the transformed frames of data was plotted on paper using an x-y recorder and a simple computer routine which performed a straight line connect between each of the discrete points computed by the FFT. Each of the plotted frames was examined manually, and the lines of interest were identified by FFT sample number. The lines selected were bright lines within each OH band which were far enough apart as to not be contaminated by other features and situated at wavelengths of minimal atmospheric absorption by H_2O and CO_2 . Examination of the plots showed that the position of each line never varied from frame to frame more than ± 1 FFT sample number. The selected FFT sample point was then recorded as the initial position of each of the spectral lines of interest.

The extraction of spectral line intensities was accomplished using the Hamming apodization function to interpolate between the discrete FFT data points. Allowing for additional error in the chosen position of each line, the interpolation routine was operated in a sample number window ± 3 data points around that manually chosen line

position. The line intensity was then computed at 0.01 sample number increments (0.015 cm^{-1} increments) over the data point window using the Hamming function. The routine saved the maximum value found within the sample window as the line amplitude for that spectral feature.

The instrument calibration function and the correct spectral line amplitudes could now be used in the temperature model for extraction of OH rotational temperatures as a function of each interferometer scan.

CHAPTER IV
OH ROTATIONAL TEMPERATURE MODELING

Introduction

Hydroxyl is a minor atmospheric constituent, residing in a thin layer (about 7 km thick) at an altitude near 87 km [Baker et al. 1985]. Although minor in concentration (between 10^4 and 10^6 molecules/cm³ at night, Baker [1978]) it is the major atmospheric near-infrared airglow radiator at night. The radiation generated by OH occurs in spectral bands known as the Meinel bands, since their discovery and identification by Meinel [1950]. After their discovery, the measurement of these bands has been of great interest to the atmospheric science community. OH airglow emission band measurements contain information about mesospheric populations and temperatures, and as such provide insight into the dynamics of the entire middle atmospheric region. A rotational-temperature model is developed in this chapter similar to the technique used by Hill et al. [1979]. The field measurements are then fit to the model in a least-squares sense. The quality of the fit will also determine error bounds on both relative band intensity and absolute rotational temperature.

The Excited OH Radical

The hydroxyl radical is a diatomic heteronuclear molecule and has a nonzero electric dipole moment. The molecule, therefore, has the ability to be easily excited and radiate electromagnetic radiation. The OH Meinel radiation bands in the infrared are caused by vibration-rotation transitions within the ground electronic state of the OH molecule. (The electronic absorption and emission spectra of OH occur in the ultraviolet.)

Hydration of ozone and perhydroxyl reduction are the primary processes for the creation of vibrationally-excited OH in the earth's upper atmosphere [Baker 1978]. The vibrationally-excited states of OH are quantized and are populated according to certain dipole selection rules described by Hertzberg [1971]. The quantum numbers associated with the vibrationally-excited states take on values $v = 0, 1, 2, 3, \dots, 9$ and the allowed transitional changes during emission are

$$v' - v'' = \Delta v = 1, 2, 3, \dots, 9 \quad , \quad (4.1)$$

where v' is the upper-state energy level and v'' is the lower-state energy level. The Meinel radiation bands are known by the value of Δv associated with the transition. The band sequences measured in this study are $\Delta v=2$ (4,2 and 3,1) and $\Delta v=3$ (8,5 and 7,4) transitions since they have energy differences in the near-infrared region. A typical measured spectrum is shown in Figure 4-1.

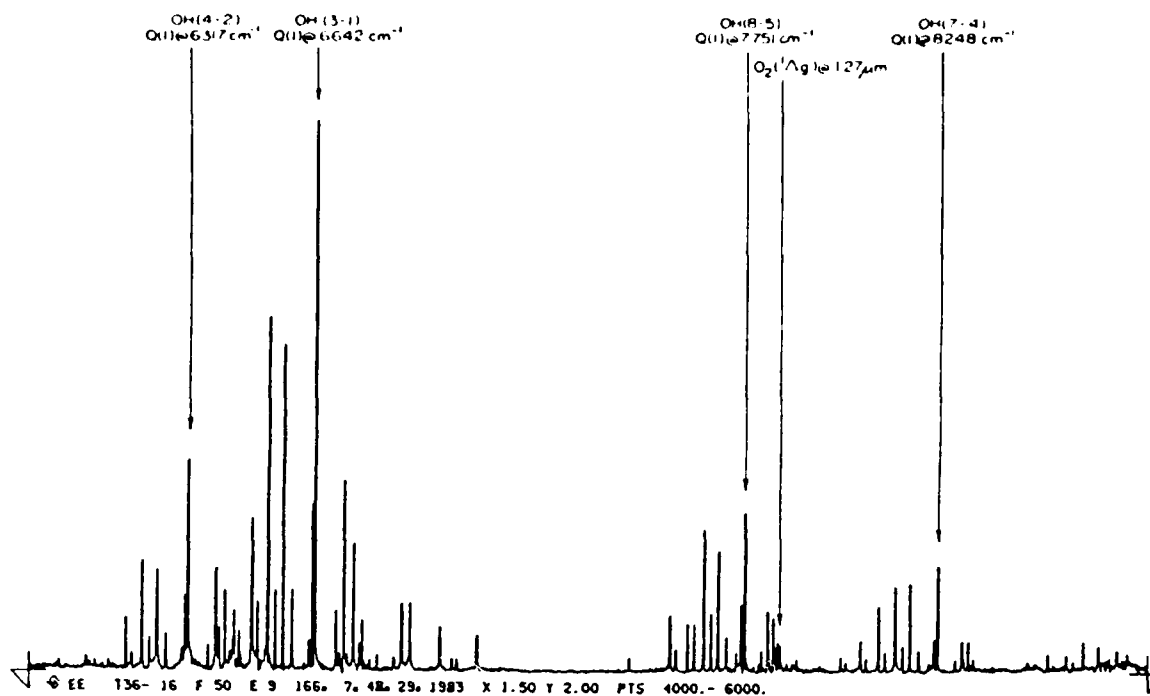


Figure 4-1. Measured OH spectra showing (4,2), (3,1), (8,5), and (7,4) Meinel bands.

Each band sequence shown in Figure 4-1 is a complex group of spectral lines. The complexity is due to transitions in molecular rotational energy in addition to the changes in vibrational levels. These angular momentum changes modulate the vibrational transitions causing the intricate spectral structure. Appendix A includes additional information on OH radical transition theory.

Rotational Temperature Model

In extracting temperatures from OH spectral data it is assumed that the OH molecular population is in rotational-state thermal equilibrium. The population distribution over the different quantum numbers can then be described by the

Maxwell-Boltzmann distribution law [Baker 1978],

$$N_{v',J'} = C_{v'} w_{J'} \exp(-E_{v',J'}/kT) \quad , \quad (4.2)$$

where

$N_{v',J'}$ = number of molecules in vibrational level v' and rotational level J' at temperature T ,

$w_{J'}$ = $2J'+1$ or the statistical weight of state J' with its $(2J'+1)$ -fold degeneracy, .

$C_{v'}$ = a constant, equal to $N_{v'}/Q_r$ where Q_r is the partition function for rotational level v ,

$E_{v',J'}$ = energy of the rotational state, and equal to $F_{v'}(J')/hc$, where $F_{v'}(J')$ is the term value for the upper-rotational state,

k = Boltzmann's constant.

The volume emission rate in photons $\text{sec}^{-1} \text{cm}^{-3}$ of a central line is given by Mies [1974] as

$$I_{v',J',v'',J''} = N_{v',J'} A_{v',J',v'',J''} \quad , \quad (4.3)$$

where

$I_{v',J',v'',J''}$ = intensity of emission from upper-state $v'J'$ to lower-state $v''J''$,

$A_{v',J',v'',J''}$ = Einstein transition probability of spontaneous emission from state $v'J'$ to state $v''J''$.

Inserting Equation 4.2 into Equation 4.3 gives the volume emission rate of each rotational line arising from a transition from an upper-state $v'J'$ to a lower-state $v''J''$.

$$I_{\nu_i, J_i, \nu_j, J_j} = C_{\nu_i} w_{\nu_i} A_{\nu_i, J_i, \nu_j, J_j} \exp(-E_{\nu_i, J_i} / kT) . \quad (4.4)$$

The computation of a rotational temperature from Equation 4.4 requires a value for the absolute line intensity $I_{\nu_i, J_i, \nu_j, J_j}$; however, the ratio of two relative line intensities can be taken and a temperature computed [Ware 1980] without the need for precise absolute spectral radiance values. However, the ratio technique proves to be a nonlinear (logarithmic) process and when several line pair temperatures within a band are calculated, the averaging of the pair temperatures to obtain a true band temperature is difficult. The line intensities are extracted from data whose noise characteristics are spectrally flat (white noise) and gaussian distributed [Ware 1980]. The difficulty comes about in the nonlinear temperature computation because the uncertainty of the calculation is not simply a linear extension of the input data uncertainty. The combining of the line pair temperatures, therefore, cannot be computed using traditional averaging techniques.

A model of the Boltzmann distributed data was developed to eliminate the problems described above. The model would describe all the lines that could occur within a band and then be fitted to the measured data using a least-squares technique. The mathematical model is

$$M_i(A_i, B_i) = \frac{A_i R_i \exp(-F_i B_i)}{\sum_j [R_j \exp(-F_j B_i)]} , \quad (4.5)$$

where

M_i = the value of the model at wavenumber i ,

A_0 = relative total integrated band intensity,

$f_i \propto A(2J'+1) = \sigma^3 S$, which is the Einstein coefficient times the J' state degeneracy or the wavenumber cubed times the line strength,

$B_0 = hc/kT$, where T is rotational temperature in $^{\circ}K$,

F_i = term value for upper-state transition,

R_i = relative instrument response at wavenumber i ,

Σ = summation over all lines within the band, is a scaling factor to ensure the entire band intensity is contained within the A_0 term.

The model shown above is similar to the intensity calculation shown in Equation 4.5. The difference is that the model pertains to an entire band of transitions and is modified by R_i to appear like the measured data. All quantities within the model are now known except the band intensity A_0 , and the temperature term B_0 . Within each OH band, the measured data points can be subtracted from the model at the same wavenumber and any differences will be contained within small changes of A_0 and B_0 times the derivative of the model at points A_0 and B_0 .

$$D_i - M_i = \Delta A_0 \left[\frac{\partial M_i(A_0, B_0)}{\partial A_0} \right] + \Delta B_0 \left[\frac{\partial M_i(A_0, B_0)}{\partial B_0} \right], \quad (4.6)$$

where D_i is the measured data point. Equation 4.6 can be shown for (j) data points within a band in matrix form as

$$\begin{bmatrix} (D_1 - M_1) \\ \vdots \\ (D_j - M_j) \end{bmatrix} = \begin{bmatrix} \left(\frac{\partial M_1}{\partial A_0}\right) & \left(\frac{\partial M_1}{\partial B_0}\right) \\ \vdots & \vdots \\ \left(\frac{\partial M_j}{\partial A_0}\right) & \left(\frac{\partial M_j}{\partial B_0}\right) \end{bmatrix} \begin{bmatrix} \Delta A_0 \\ \Delta B_0 \end{bmatrix}, \quad (4.7)$$

where the left matrix is the difference between each measured line intensity within a band and the line intensity as predicted by the model. The right hand side of Equation 4.7 must be equal to the preceding difference.

The computation of Equation 4.7 requires the solution for each of the derivatives

$$\frac{\partial M_i}{\partial A_0} = \frac{R_i I_i \exp(-F_i B_0)}{N}, \quad (4.8)$$

and,

$$\frac{\partial M_i}{\partial B_0} = \frac{A_i R_i I_i \exp(-F_i B_0)}{N^2} \left[\left[\sum_j (I_j F_j \exp(-F_j B_0)) \right] - N F_i \right], \quad (4.9)$$

where $N = \sum_j I_j \exp(-F_j B_0)$ or the normalization factor. All the terms in Equation 4.7 are computed and submitted to a least-squares fitting routine, developed by Lawson and Hanson [1974] which returns the values of ΔA_0 and ΔB_0 . The least-squares routine is used to solve problems of the form

$$Ax = B, \quad (4.10)$$

where

A = the derivative matrix of Equation 4.7,

x = the unknown or Δ matrix,

B = the difference matrix.

To begin the process a starting temperature was chosen and all terms computed. The result of this first fit is to determine an appropriate initial value for A_0 (A_0 is merely a relative intensity term). Once the initial values for B_0 and A_0 were ascertained, the least-square fitting routine was operated in a loop, the derivative matrix vectors were each scaled to unity value before submission to insure convergence of the fit, and each time the routine would return values for ΔA_0 and ΔB_0 . The Δ values were added to the previous values for A_0 and B_0 , the model values recomputed and resubmitted to the routine. The value of ΔB_0 was tested after each iteration until the temperature change (temperature is part of B_0) from the previous fit was less than 0.5° K. When the least-squares routine converged to the 0.5 °K limit the values for A_0 (relative band intensity) and T (the temperature part of B_0) were stored along with the time and date of the frame.

The constant terms used in the model were computed by Espy [1984] using the molecular constants measured by Coxon and Foster [1982] and OH dipole moments derived by Werner et al. [1983]. The values of these terms are given in Tables 4-1 through 4-4. The tables show the wavenumber, a typical relative instrument response, the term value for the upper-

TABLE 4-1. Molecular data for OH $\Delta v=2$, (4,2) band.

Line	Wavenumber (cm^{-1})	Relative Response	Term Value (cm^{-1})	Line Strength
P ₁ (4)*	6159.634	0.147	13421.921	0.23415100E+13
P ₂ (4)*	6174.994	0.166	13514.125	0.19663726E+13
P ₁ (3)*	6200.353	0.199	13320.758	0.16226162E+13
P ₂ (3)*	6219.070	0.224	13428.966	0.13226441E+13
P ₁ (2)*	6238.114	0.247	13248.923	0.88080260E+12
P ₂ (2)*	6260.766	0.275	13377.615	0.70291000E+12
Q ₁ (3)	6301.517	0.326	13421.922	0.25067365E+12
Q ₁ (2)	6309.948	0.336	13320.758	0.71495030E+12
Q ₁ (1)	6315.828	0.344	13248.923	0.11681950E+13
R ₂ (1)	6368.381	0.411	13428.966	0.60586570E+12
R ₁ (1)	6387.661	0.440	13320.758	0.74062960E+12
R ₁ (2)	6411.112	0.473	13421.921	0.12600000E+13

(* lines used in fit).

TABLE 4-2. Molecular data for OH $\Delta v=2$, (3,1) band.

Line	Wavenumber (cm^{-1})	Relative Response	Term Value (cm^{-1})	Line Strength
P ₁ (4)*	6480.230	0.572	10352.446	0.27218330E+13
P ₂ (4)*	6495.579	0.593	10443.293	0.22819520E+13
P ₁ (3)*	6522.332	0.626	10247.071	0.18861154E+13
P ₂ (3)*	6541.239	0.650	10354.206	0.15350037E+13
P ₁ (2)*	6561.409	0.679	10172.300	0.10240617E+13
P ₂ (2)*	6584.562	0.712	10300.410	0.81566820E+12
Q ₁ (3)	6627.706	0.770	10352.446	0.57940270E+12
Q ₁ (2)	6636.171	0.782	10247.071	0.82784900E+12
Q ₁ (1)	6642.081	0.789	10172.300	0.13556844E+13
R ₂ (1)	6697.063	0.867	10354.206	0.35196955E+12
R ₁ (1)	6716.853	0.892	10247.071	0.86348040E+12
R ₁ (2)	6741.555	0.931	10352.446	0.14703511E+13

(* lines used in fit)

TABLE 4-3. Molecular data for OH $\Delta v=3$, (8,5) band.

Line	Wavenumber (cm^{-1})	Relative Response	Term Value (cm^{-1})	Line Strength
P ₁ (5)	7555.155	1.000	24163.096	0.54607000E+13
P ₂ (5)	7569.641	0.997	24248.912	0.47194710E+13
P ₁ (4)	7600.862	0.992	24055.028	0.41913920E+13
P ₂ (4)	7617.468	0.990	24152.797	0.35340550E+13
P ₁ (3)*	7642.345	0.984	23971.237	0.29201550E+13
P ₂ (3)*	7661.252	0.985	24083.736	0.23944700E+13
P ₁ (2)*	7679.631	0.978	23911.582	0.15952644E+13
P ₂ (2)*	7700.808	0.972	24042.113	0.12846050E+13
Q ₁ (3)	7726.136	0.960	24055.028	0.95265240E+12
Q ₁ (2)	7739.286	0.952	23971.237	0.13444194E+13
Q ₁ (1)	7748.511	0.945	23911.582	0.21738030E+13
R ₂ (1)	7791.408	0.900	24803.736	0.11463823E+13
R ₁ (1)	7808.166	0.874	23971.237	0.13900488E+13
R ₁ (2)	7823.076	0.857	24055.028	0.23899920E+13

(* lines used in fit)

TABLE 4-4. Molecular data for $\Delta v=3$, (7,4) band.

Line	Wavenumber (cm^{-1})	Relative Response	Term Value (cm^{-1})	Line Strength
P ₁ (5)*	8049.708	0.786	21763.099	0.66072740E+13
P ₂ (5)*	8064.112	0.779	21847.340	0.56979800E+13
P ₁ (4)*	8096.397	0.765	21649.131	0.40669700E+13
P ₂ (4)*	8113.112	0.754	21745.519	0.42663300E+13
P ₁ (3)*	8138.903	0.740	21560.824	0.35302450E+13
P ₂ (3)*	8158.204	0.725	21672.328	0.28898620E+13
P ₁ (2)*	8177.237	0.711	21497.994	0.19277462E+13
P ₂ (2)*	8199.208	0.696	21628.204	0.15491604E+13
Q ₁ (3)	8227.210	0.680	21649.131	0.11407934E+13
Q ₁ (2)*	8240.067	0.672	21560.824	0.16141494E+13
Q ₁ (1)*	8249.071	0.668	21497.994	0.26171900E+13
R ₂ (1)*	8294.714	0.646	21672.328	0.13787860E+13
R ₁ (1)*	8311.901	0.642	21560.824	0.16761780E+13
R ₁ (2)*	8328.374	0.635	21649.131	0.28788900E+13

(* lines used in fit)

state transition, and the theoretical line strength for each line. The wavenumber shown is the average of the two A-doubled lines; the term value is also the average of the two lines, and the line strength given is the sum of the two line strengths. The sum of the line strengths was used because the measured line is actually the sum of the A-doubled pair. Data for all the strong lines are listed for use in the normalization factor of the model but only those with "*" were used in the fit. The reason all were not used in the fit was that many were determined to have been contaminated by water vapor absorption or by other emission lines [Roychoudhury 1983].

Error Analysis and Testing of Model

The model used here is over-determined with only two unknowns and at least four equations (in (8,5) band fit, more in other bands) and as such, the additional information can be used to estimate the accuracy of the least-squares fit. Examination of Equations 4.7 and 4.10 show that when the fitting routine is complete, the derivative matrix A is left as a 2×2 upper-triangulated matrix. The rest of the terms in the A matrix are of little significance because the least-squares routine has manipulated the data into the upper-triangulated portion in order to solve the equations. The upper-triangulated matrix now takes on the form

AD-A181 247

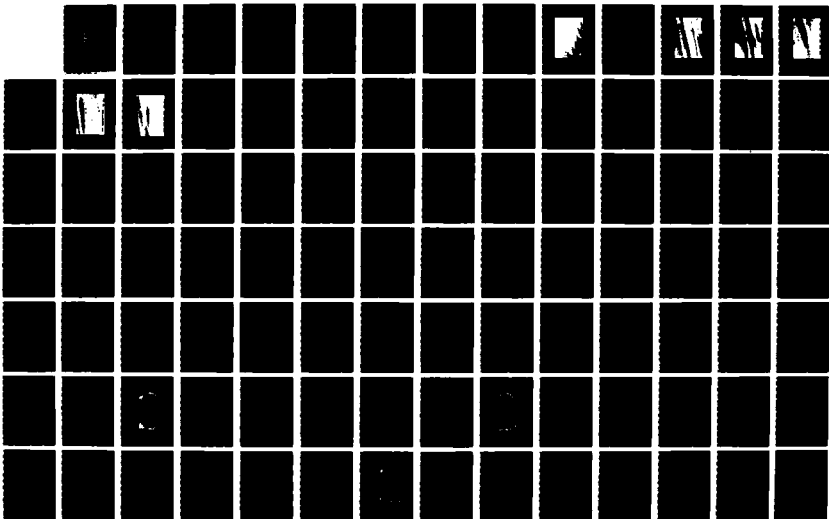
HIGH-RESOLUTION MEASUREMENT OF OH INFRARED AIRGLOW
STRUCTURE(U) UTAH STATE UNIV LOGAN SPACE DYNAMICS LABS
P C NEAL 18 OCT 85 SDL/85-075 AFGL-TR-85-0261
F19618-83-C-0056

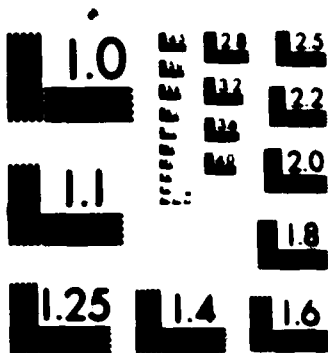
2/3

UNCLASSIFIED

F/G 4/1

NL





$$R = \begin{bmatrix} r_{1,1} & r_{1,2} \\ 0 & r_{2,2} \end{bmatrix} , \quad (4.11)$$

where

R = upper-triangulated coefficients returned in the derivative matrix A .

Upon completion of the fitting routine, the values left in the matrix x must be equal to zero, except for noise in the fit, and the upper two values in the vector B must also be equal to zero, also except for noise, because the system of equations has been solved. But because noise does exist in the fit then some residual remains. Therefore, the equation system is left in the form

$$R x = n , \quad (4.12)$$

where n is the noise vector.

In order to calculate the accuracy of the models' fit to the two system unknowns (temperature and band intensity) it is necessary to obtain the covariance matrix which contains the variance of each parameter in the least-squares fit. It can now be shown by manipulation of Equation 4.12 that the covariance matrix is [Lawson and Hanson 1974]

$$\langle x x^T \rangle = \bar{R} \langle n n^T \rangle \bar{R}^T , \quad (4.13)$$

where

$\langle x x^T \rangle$ = covariance matrix,

\bar{R} = inverse of R,

T indicates the transpose operation,

$\langle n n^T \rangle$ = the variance of white uncorrelated noise.

The noise in the system fit is assumed to be white and uncorrelated because all the mathematical manipulations performed were linear in nature.

A measure of the noise in the system is returned by the least-squares fitting routine. The returned parameter is the Euclidean norm of the residual vector and is called R_{norm} . The variance of the system fit can be computed from R_{norm} as

$$\sigma^2 = (R_{\text{norm}}^2) / (M-K) \quad , \quad (4.14)$$

where

σ^2 = variance of fit,

M = number of equations in the fit,

K = number of unknowns in the fit.

The covariance matrix can be solved in terms of the variance of the model's fit

$$\langle x x^T \rangle = \sigma^2 I \overline{(R^T R)} \quad , \quad (4.15)$$

where I is the identity matrix.

The standard deviation for each of the fit variables can be computed from Equation 4.15 in terms of the original variables of the residual matrix R and the variance σ^2 .

$$\sigma_A = \left[\frac{(r_{2,2}^2 + r_{1,2}^2)}{(r_{1,1} r_{2,2})^2} (\sigma^2) \right]^{\frac{1}{2}}, \quad (4.16)$$

where σ_A is the standard deviation of the intensity function.

The standard deviation on the variable B (temperature is part of B) is

$$\sigma_B = \left[\frac{\sigma^2}{r_{2,2}^2} \right]^{\frac{1}{2}}. \quad (4.17)$$

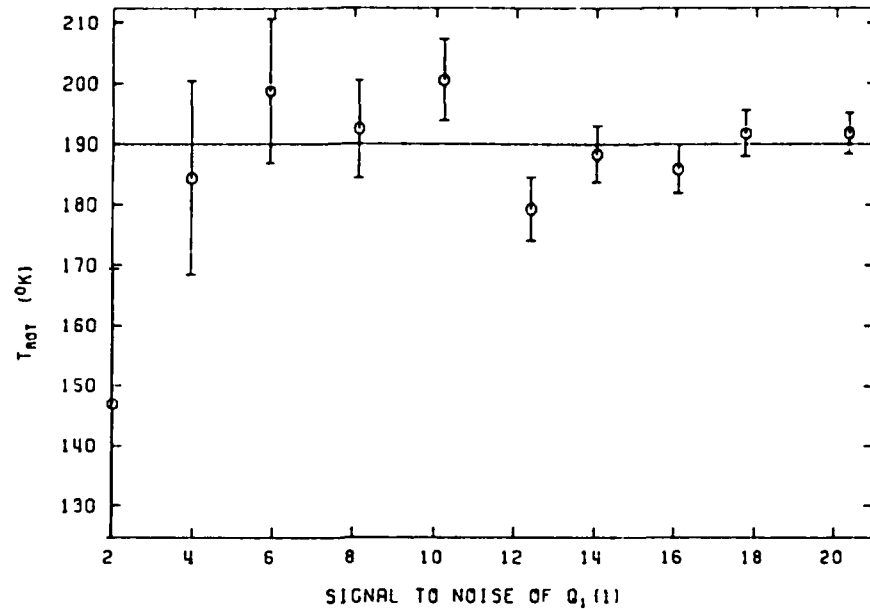
Referring to Equation 4.5 for the relationship between temperature T and the variable B, the standard deviation of the temperature can be calculated

$$\sigma_T = (\sigma_B hck) / (B^2), \quad (4.18)$$

where σ_T is the standard deviation of the temperature as calculated by the model.

The model presented herein provides a method for calculating relative band intensity, rotational temperature, and the standard deviation on both parameters. Appendix D presents the computer programs which implement the data processing algorithms developed.

As verification of the quality of the model, the process outlined was used to compute the intensity and temperature of synthetic spectra generated by Espy [1984]. The signal-to-noise ratio of the synthetic spectra was varied from a low of 2 to a high of 20 and then each was submitted to the



T_{ROT} VS. S/N OF $Q_1 (1)$ LINE FOR $T_{ROT}=190°K$ (1 RUN)

Figure 4-2. Model temperature test results on synthetic spectra vs. signal-to-noise ratio with standard deviation shown as bars [Espy 1984].

model for processing. Figures 4-2 and 4-3 show the results of the test. As can be seen, the mean intensity and temperature of the model closely track the actual parameters even in very high-noise environments. The error bars shown on both figures indicate a 1 sigma uncertainty associated with the calculation, and as the noise increased, the uncertainty of the calculation increased as expected. The tests were conducted on a single frame of data; therefore, an improvement could be made by averaging frames at the cost of temporal resolution degradation. The signal-to-noise ratio of the measured data was usually about 100, which is

much higher than the signal-to-noise ratio of the test frames; therefore, the uncertainty should continue to decrease so the confidence in the model is very high.

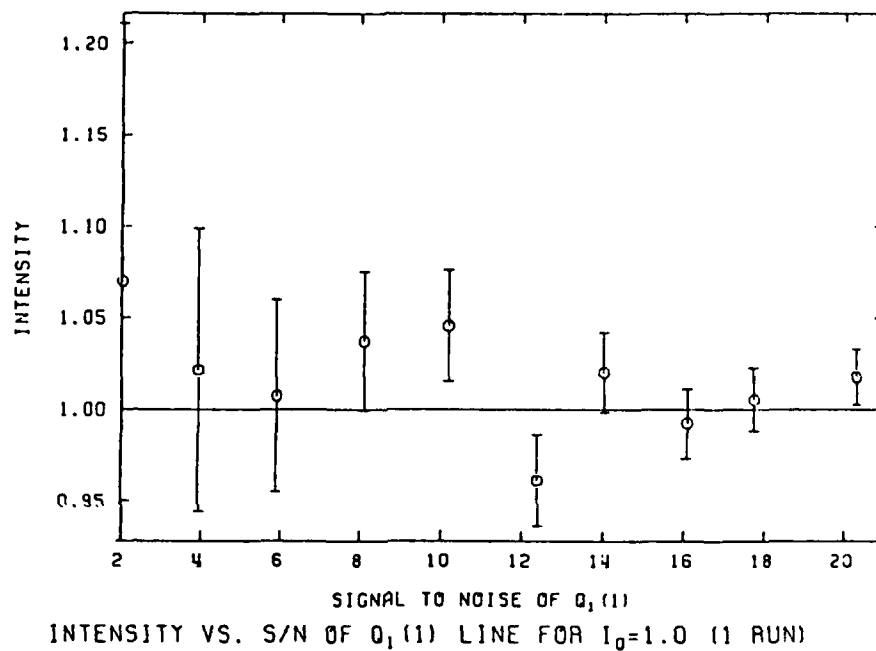


Figure 4-3. Model intensity test results on synthetic spectra vs. signal-to-noise ratio with standard deviation shown as bars [Espy 1984].

CHAPTER V

RESULTS

Introduction

The high-throughput, narrow field of view interferometer-spectrometer was taken to several airglow observation sites in the western United States in the spring of 1983. Over several months of observation, one of the brightest airglow structure events was seen and recorded on June 15, 1983, thus fulfilling the primary goal of this study. The observation was made from Sacramento Peak, New Mexico. The site is located at $105^{\circ}48'16''$ west longitude, $32^{\circ}47'57''$ north latitude at an elevation of 9570 feet. The results presented in this chapter were taken from this site between June 13 and June 15, 1983. A complete catalog of the results computed from the interferometer data is presented in Appendix C.

Background

The interferometer with an image-intensified infrared isocon camera mounted on and coaligned with the interferometer telescope (see Figure 2-9) was used to collect data at the observation sites. A second Isocon camera was mounted on its own tripod and was used to search the skies for indication of structure prior to moving the

more bulky interferometer. The infrared cameras were supplied by the University of Southampton, England. Taylor [1983-84] operated the camera equipment and provided experience and expertise in the search for airglow structure events. The cameras were the "eyes" for the interferometer in determining if any OH airglow structure was present. Once an area of OH airglow structure was located in the sky the camera-interferometer system was positioned to view that area. The data from the two coaligned systems were used to correlate the viewed and calculated intensities and temperatures.

An infrared radiometer [Huppi 1976] was also used to gather trend and absolute intensity data of the OH activity. The radiometer looked in the zenith and has a field of view of 9°. The radiometer spectral bandpass was centered at 1.53 μm wavelength.

Infrared Isocon Camera Results

The Isocon camera systems' response is in the near-infrared from about 700 to 850 nm. The response curve and the OH transitions which occur within this bandpass are shown in Figure 1-3.

Figure 5-1 shows a video frame taken with the large, independently-mounted isocon camera at 8:15 hrs. UT on June 15, 1983. The field of view for the photo is 28° vertical and 37° horizontal at an azimuth of about 320° and the bottom of the picture beginning at 10° elevation.



Figure 5-1. Large Isocon IR camera photo, day 166, 8:15 hrs. UT, camera field of view 28° vertical, 37° horizontal, at an elevation of about 10°.

Examination of this frame shows 7 distinct bright OH emission bands. The bands are moving northward in a direction normal to the bands (moving towards lower right hand corner of frame). These structural bands extended across the entire northern half of the sky. The structure depicted in Figure 5-1 was observed and recorded beginning at 7:30 hrs. UT continuing until 10:15 hrs. UT on this date.

Using the video record, Taylor [1983-84] calculated the apparent wavelength and velocity of the band structure, with techniques described by Hapgood and Taylor [1982]. Using the location and altitude of the observation site, radius of the earth, viewing angles of the camera, and assuming that the band structure resided on a spherical shell at a constant altitude of 87 km, the apparent temporal wavelength derived was 24 ± 1 km, and the apparent period was 14 ± 1 minutes. Based on these two values the apparent velocity is 28 ± 2 meters/second which agrees closely with other similar observations [Taylor et al. 1980].

The small isocon camera which was mounted on and coaligned with the interferometer, was operated during the same time frame as the large camera. The field of view of the small camera is nearly square being 13° vertical by 15° horizontal.

Figures 5-2 through 5-4 show a sequence of video frames beginning at 7:32 hrs. UT and taken at 8 minute intervals with the small camera. Each frame again shows, in more detail, the OH emission structure. The "X" in each frame



Figure 5-2. Isocon IR camera photo, day 166, 7:32 hrs. UT, field of view = 13° vertical 15° horizontal, interferometer looking at "X" on a bright band.



Figure 5-3. Isocon IR camera photo, day 166, 7:40 hrs. UT, field of view = 13° vertical 13° horizontal, interferometer looking at "X" on a dark band.



Figure 5-4. Isocon IR camera photo, day 166, 7:48 hrs. UT, field of view = 13° vertical 15° horizontal, interferometer looking at "X" on a bright band.

marks the center of the interferometer's field of view within the video frame. The interferometer's field of view is 0.8° full field and, therefore, is about 0.4 inches in diameter on each frame. This small field of view permits the interferometer to resolve the bright and dark portions of the structure. The interferometer is viewing at an elevation angle of 17° and an azimuth angle of 328° in the sequence. The three photos show one of the periods where the interferometer was able to view a bright, a dark, and a bright band in sequence as the structure moved through the field of view.

Figures 5-5 and 5-6 show another similar sequence of video frames observed later in the night beginning at 8:31 hrs. UT at an interval of 11 minutes. This later series of frames again shows the interferometer viewing a dark then a bright emission band as the structure moves. The interferometer was viewing at an elevation angle of 15.5° and an azimuth angle of 340° in these last two figures.

Taylor [1983-84] compared the bright and dark bands recorded by the small isocon camera with the OH (3,1) band intensity plots computed using the interferometer data (shown later in Chapter V and in Appendix C). In the time period from 7:30 to 10:15 hrs. UT the two independent records show that for each bright or dark band depicted in the video data a corresponding increase or decrease in intensity is also shown in the interferometer data. This



Figure 5-5. Isocon IR camera photo, day 166, 8:31 hrs. UT, field of view = 13° vertical 15° horizontal, interferometer looking at "X" on a dark band.



Figure 5-6. Isocon IR camera photo, day 166, 8:42 hrs. UT, field of view = 13° vertical 15° horizontal, interferometer looking at "X" on a bright band.

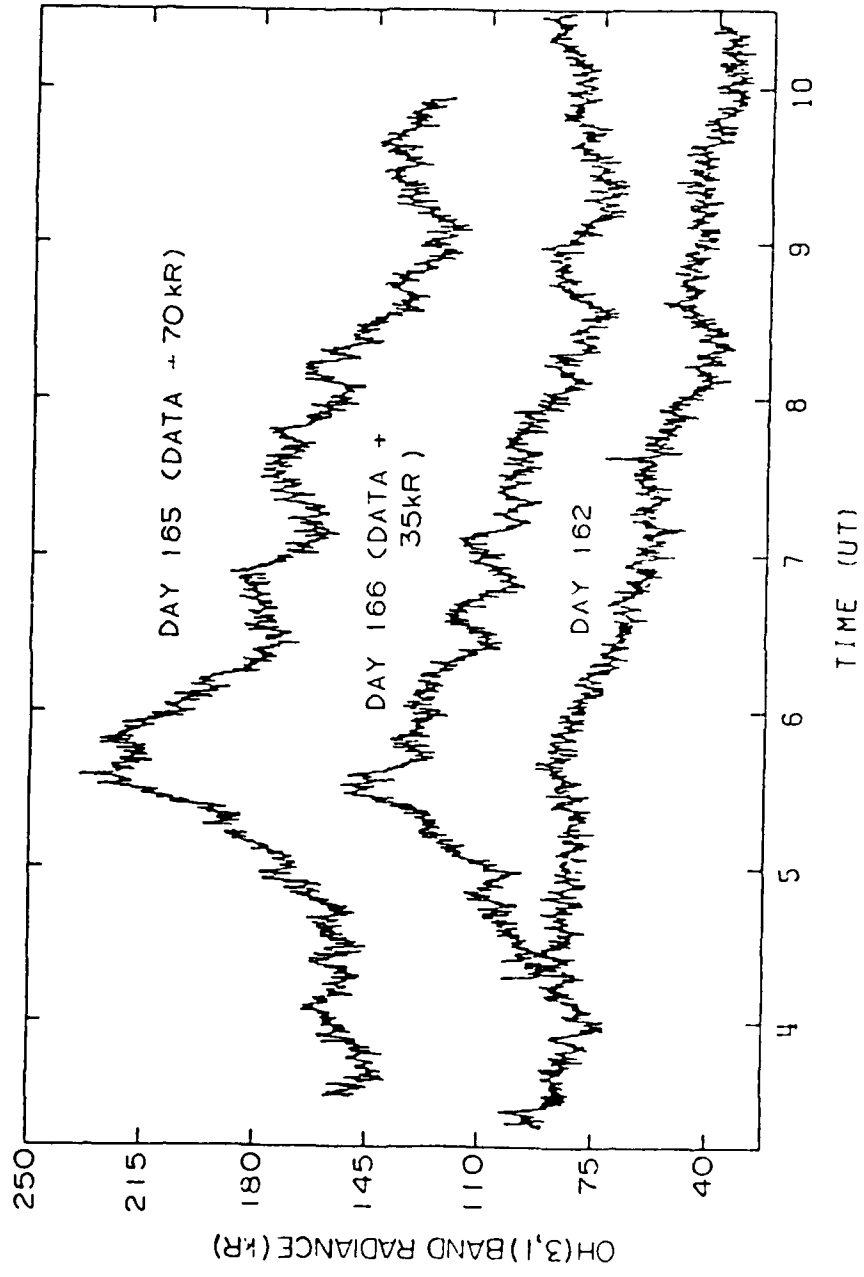
comparison showed 16 distinct points of correlation between the video frames and the interferometer intensity plots.

Infrared Radiometer Data

The radiometer was used to show trend and absolute radiance values for the OH infrared activity as viewed within a 9° field of view in the zenith. Radiometer data are included to show for the night before (June 14, 1983) and the night of (June 15, 1983) the recorded structure, OH airglow emission intensity exhibited some unusual trends and modulations. Figure 5-7 shows the radiometer data for three specific days and is calibrated in kilo-Rayleighs (kR) of intensity of OH (3,1) band emission. The scale has been shifted to show the three days all on one chart.

Day 162 is a typical curve of near-infrared OH activity and was taken from White Sands Missile Range (4300 feet elevation) and located about 30 miles from the Sacramento Peak site. As can be seen from the Day 162 curve, the intensity of the 1.53 μm radiation steadily decreases after local sunset (sunset occurred about 3:30 hrs. UT) and throughout the night.

The Day 165 radiometer curve, however, shows a markedly different trend in the OH activity. The post-sunset decrease starts, but at about two hours before local midnight (or 5:00 hrs. UT) the OH activity dramatically increased. After the peak, the OH activity remains high but also shows some modulation that could be interpreted as



IR RADIOMETER 1.53μ CHANNEL

Figure 5-7. Radiometer readings for UT days 162, 165, and 166 during 1983. The data is for the 1.53 μm channel.

distinct large-scale wave structure passing overhead. The period of these intensity waves ranges from 30 to 60 minutes with a modulation (or contrast ratio) of from 5 to 10 percent. The waves were not distinguishable in the zenith with the infrared camera equipment because the zenith emission intensity is too faint and their large size exceeded the camera's field of view. A camera was lowered in elevation in an attempt to view the waves (lower elevations view the structure obliquely thus the waves appear compressed together and brighter due to the van Rhijn effect) but no structures were distinguishable by the camera throughout the entire night.

The radiometer curve in Figure 5-7 for day 166 also shows enhanced OH activity. Although not as intense as the previous night, a similar pre-midnight maximum is observed. After the pre-midnight maximum, the decrease is slower than normal and again some distinct wave structure is observed. The structure has periods of about 25 minutes and modulations in intensity of about 5 percent. Shortly after local midnight (7:00 hrs. UT), the moon had set far enough to lower the sensitive camera to the horizon to search for observable structure. The measurements gathered throughout the remainder of the night with the cameras and interferometer also exhibit high-contrast OH emission structure.

Direct Comparison of Interferometer
and Radiometer Intensities

Prior to moonset on UT days 165 and 166 the interferometer was pointed to the zenith and was viewing the sky coincident with the radiometer. Therefore a direct comparison is made between the two records. Figure 5-8 shows the OH (3,1) band intensity from 3:30 to 7:15 hrs. UT on day 165. The radiometer data were used to provide the absolute calibration for the interferometer, but as the figure shows the trends in the interferometer intensity curve track the radiometer curve closely. The intensity peak appears at about 5:40 hrs. UT on this day. The standard deviation of the interferometer intensity calculation is about 2% (the standard deviation curve is included in Appendix C). The interferometer was realigned at 6:30 hrs. UT. Just prior to realignment, the standard deviation of the intensity increased. After alignment the intensity appeared to have increased. These observations make the rapid intensity decline at 6:00 hrs. UT suspect, as an instrument alignment drift problem.

Figure 5-9 presents the interferometer OH (3,1) band intensity for UT day 166. Again it compares favorably with the radiometer curve for the same day in Figure 5-7. The intensity peak occurs on this day at 5:30 hrs. UT. The same reservations about alignment drift occurred on this day at 6:00 UT as happened on the previous day.

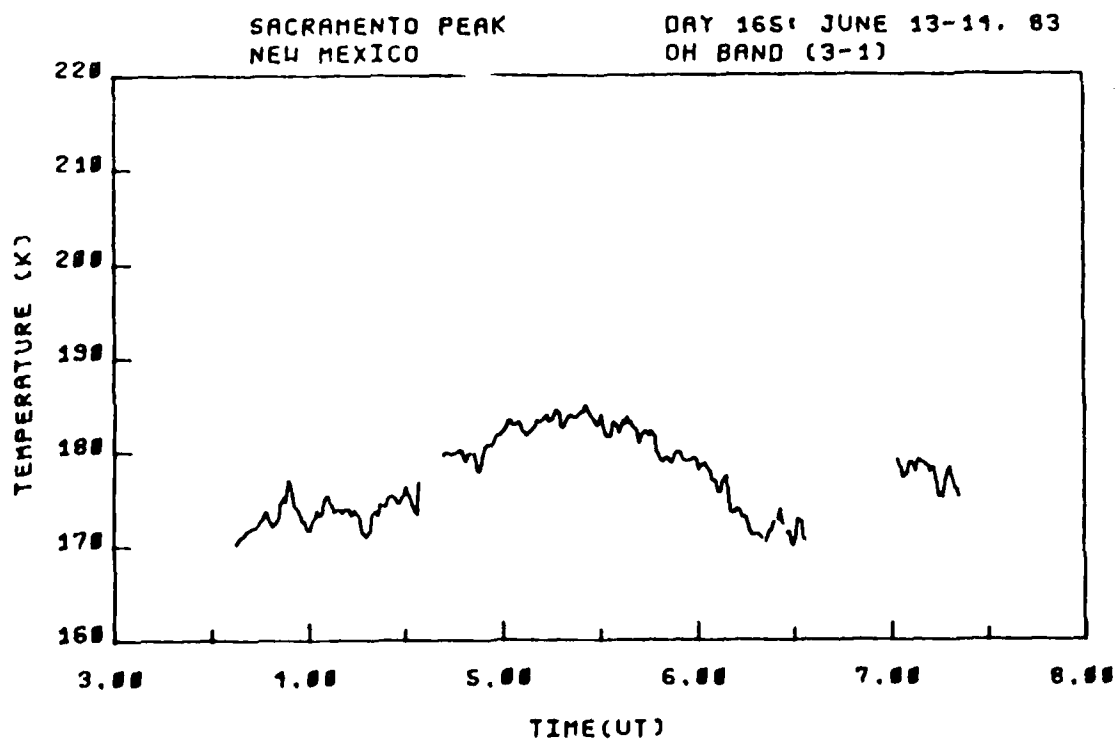
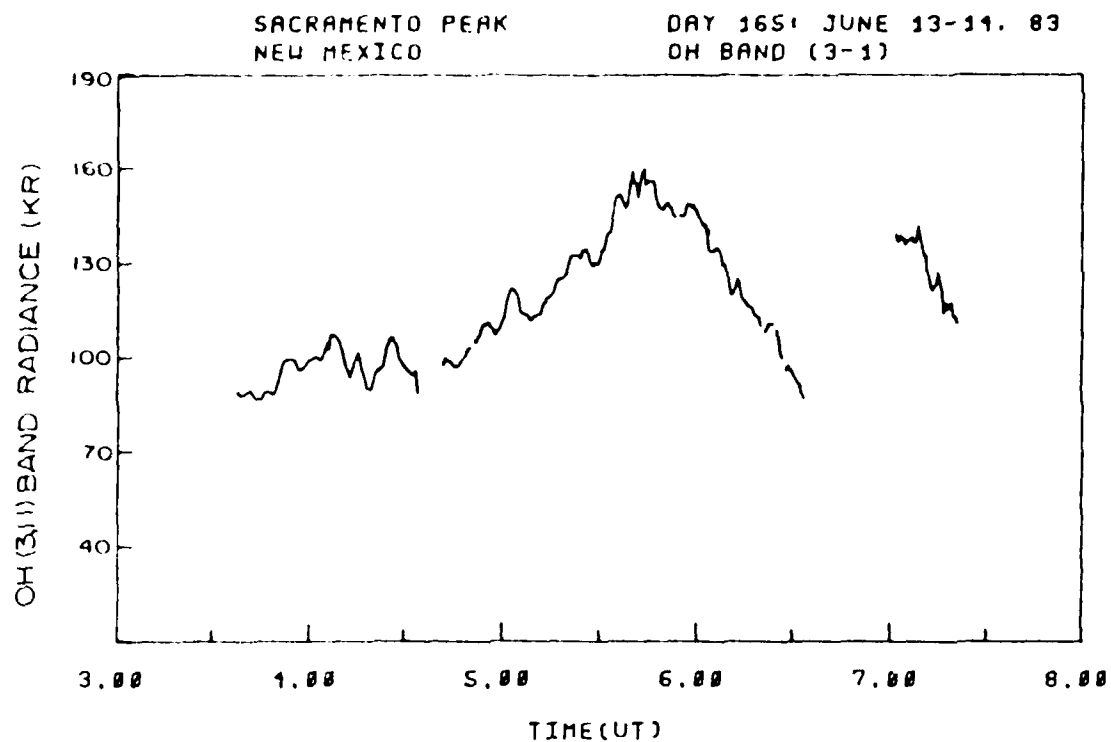


Figure 5-8. OH (3,1) band radiance and rotational temperature, viewing angle = zenith, day 165, 3:30-7:30 hrs. UT.

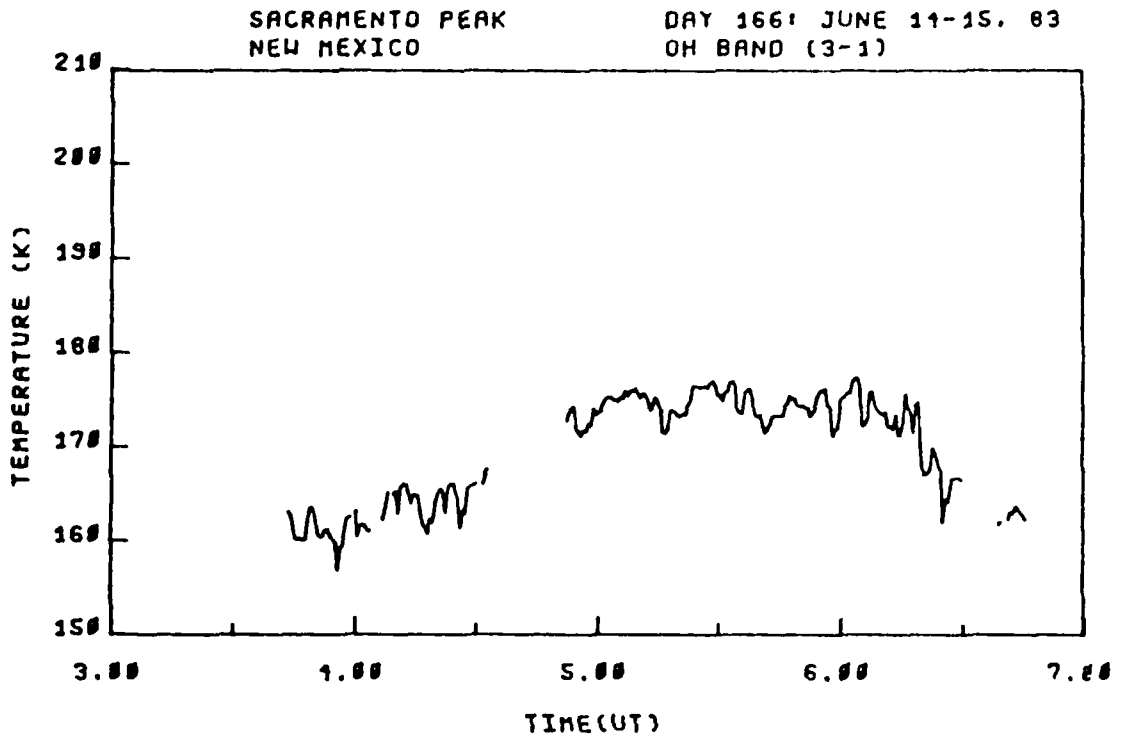
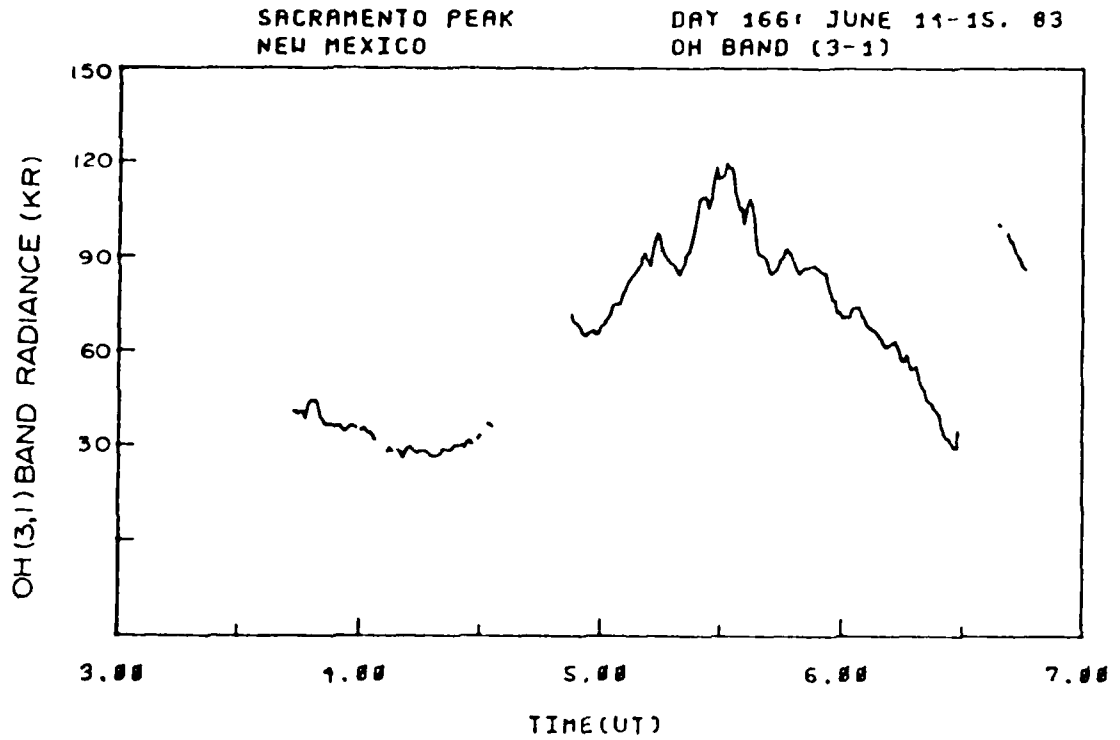


Figure 5-9. OH (3,1) band radiance and rotational temperature, viewing angle = zenith, day 166, 3:30-6:45 hrs. UT.

The calculated interferometer OH radiance and temperature curves for the other OH Meinel bands measured in this study are included in Appendix C. The absolute scales of radiance for the other OH bands were based on the (3,1) band (the radiometer was calibrated in terms of the (3,1) band) and using the band intensity ratios developed by Turnbull and Lowe [1983] ($I(4,2)=I(3,1)\times 1.03$, $I(8,5)=I(3,1)\times 0.14$, $I(7,4)=I(3,1)\times 0.09$). Only when the interferometer is viewing in the zenith are the intensity curves plotted in absolute terms. The geometry of looking at low elevation angles for the other data precluded inclusion of absolute scales. Also shown in the Appendix are the standard deviations for all the calculations.

Rotational Temperatures for Interferometer Zenith Data

Included in Figures 5-8 and 5-9 are the calculated rotational temperatures for days 165 and 166 when the interferometer is viewing in the zenith. The temperature for day 165 indicates a rise in temperature and intensity, beginning at about 4:00 hrs. UT, with a mean temperature of about 175 °K. The total rise in temperature is 15 °K with the peak occurring at 5:20 hrs. UT. The temperature curve for day 166 shows the same increasing trend as on the previous day. The mean is about 170 °K with a total rise in temperature of 15 °K. The temperature peaks on day 166 at 5:10 hrs. UT. On both days as the interferometer views the

zenith, the peak of the temperature curve precedes the peak of the intensity curve by about 20 minutes (discussed more in Chapter VI).

Rotational Temperature

Smoothing Algorithm

The curve of calculated rotational temperatures appeared quite noisy at times. Consequently, smoothing algorithms were employed. The smoothing technique used is a 3 frame wide sliding window where the averaging is a weighted one. Only 3 data points were used so as to not degrade the temporal resolution of the data (this is about a 2 minute time window) and still provide sufficient smoothing. The weighting is accomplished using the reciprocal of the standard deviation squared (or reciprocal of variance) for each data point as its weighting factor in the running sum; therefore, if a particular data point has a large uncertainty it is weighted less in the average. This algorithm was chosen because in data sets with large differences from data point to data point, with significant differences in the variance of each point, this weighting technique best identifies the mean curve through all data points [Bevington 1969].

The specific algorithm used for the rotational temperature smoothing is

$$\bar{T}_i = \left[\frac{\sum_{i=1}^3 (T_i / (\sigma_{T_i})^2)}{\sum_{i=1}^3 (1 / (\sigma_{T_i})^2)} \right] , \quad (5.1)$$

where

\bar{T}_i = weighted average temperature at time i ,

T_i = temperature at time i ,

σ_{T_i} = standard deviation of temperature T_i .

The standard deviation on the smoothed curve is also changed due to the weighting and is recalculated using

$$\bar{\sigma}_{T_i} = \left[\sum_{i=1}^3 (1 / (\sigma_{T_i})^2) \right]^{-\frac{1}{2}} , \quad (5.2)$$

where

$\bar{\sigma}_{T_i}$ = averaged standard deviation at time i .

Figure 5-10 shows temperature and standard deviation curves before smoothing and Figure 5-11 shows the same curves after smoothing. All the temperature curves in Appendix C show a set of temperature curves for both before and after smoothing.

Interferometer Recorded Structure

This research project was undertaken in an attempt to quantify the intensity modulations and anticipated OH rotational temperature modulations associated with airglow structure events typified in Figure 1-4. The presentation in this section is the result of the processed interferometer OH (3,1) band records, which were observed during the airglow structure event of June 15, 1983. The

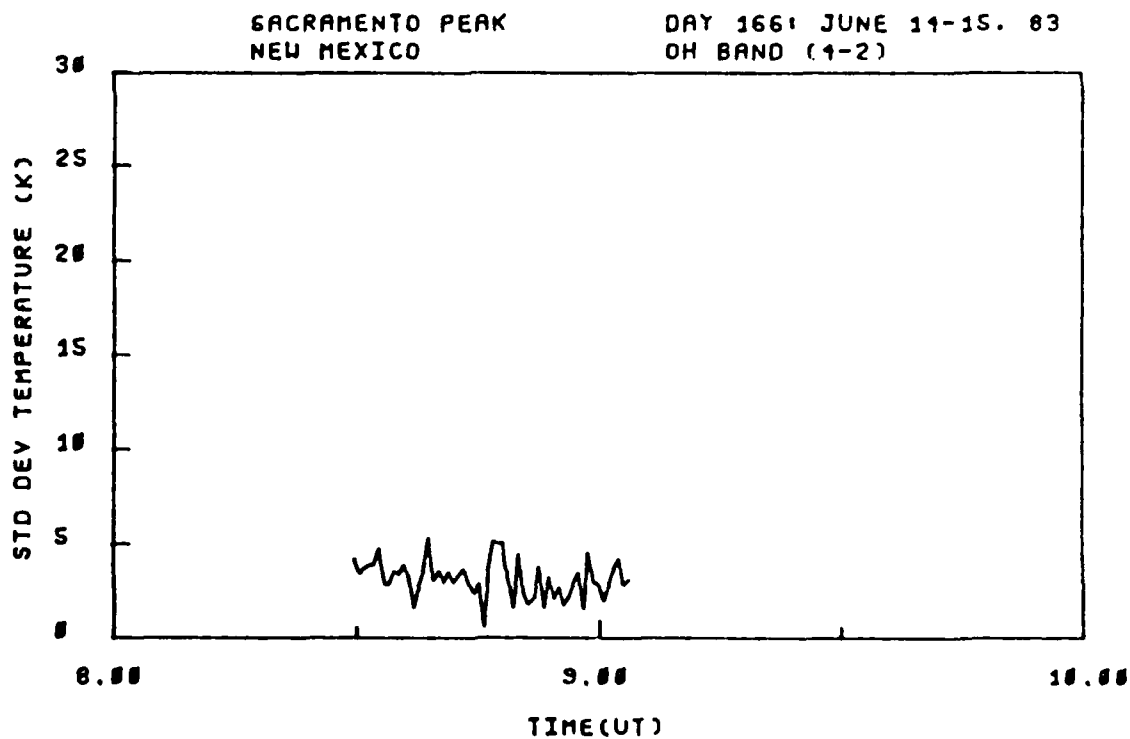
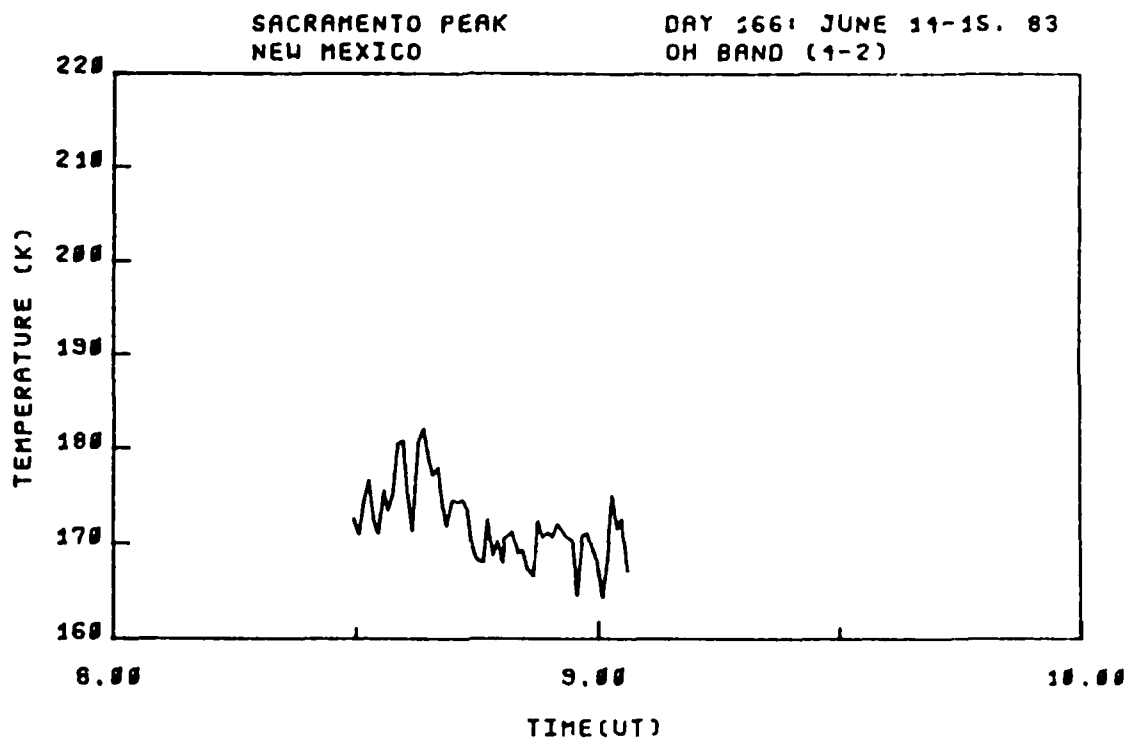


Figure 5-10. OH (4,2) band rotational temperature and standard deviation before smoothing.

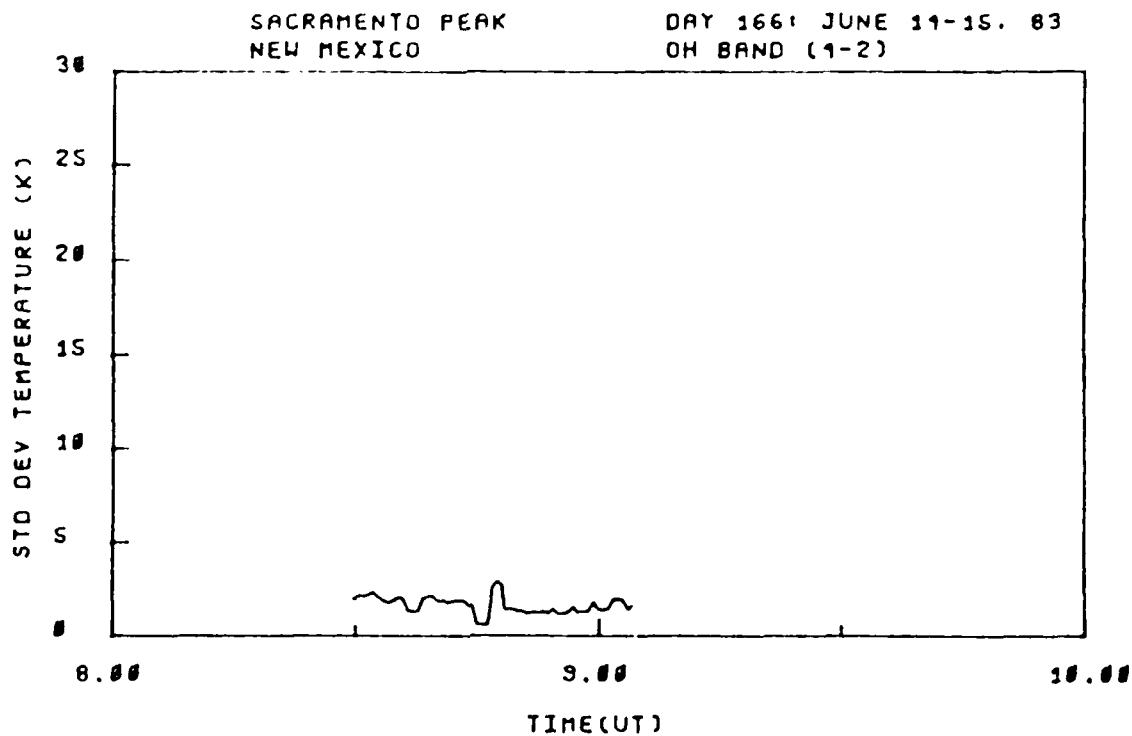
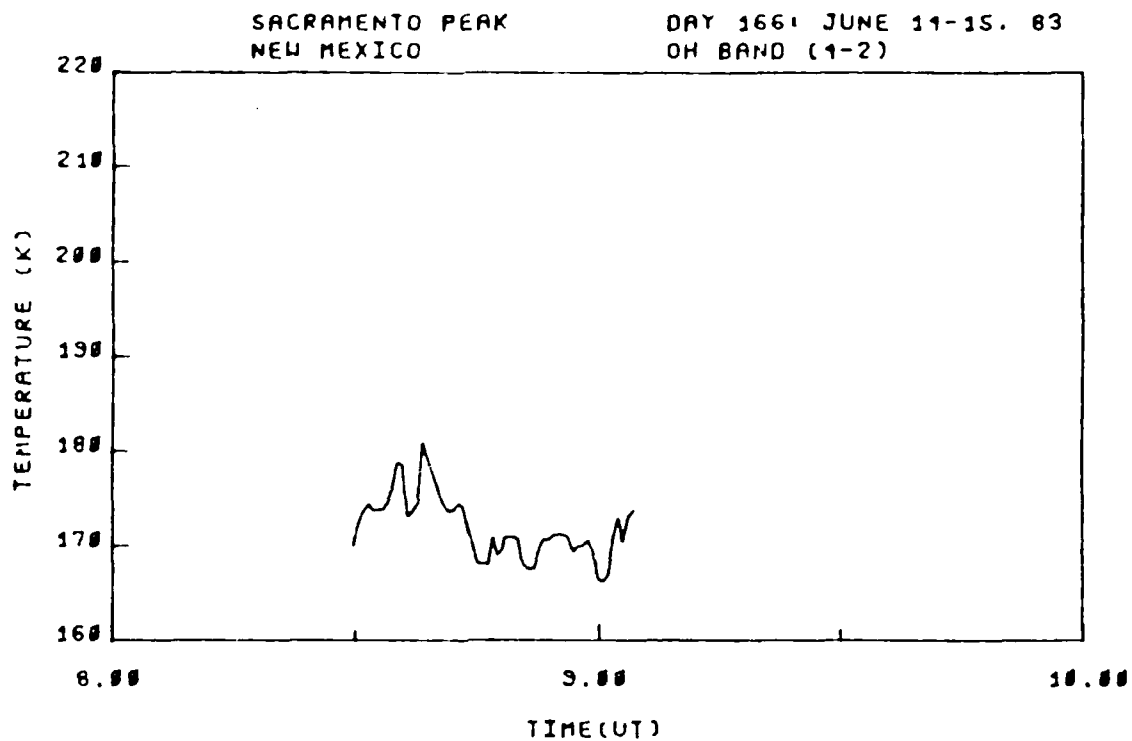


Figure 5-11. OH (4,2) band rotational temperature and standard deviation after smoothing.

OH (3,1) band data have the highest signal-to-noise ratio and, therefore, are felt to be the most reliable. The presentation is given in three segments corresponding to when the instrument was moved in viewing elevation or azimuth. A complete catalog of all the observed OH band intensities and rotational temperatures is contained in Appendix C.

The interferometer-isocon camera system was lowered to a viewing elevation angle of 17° and an azimuth angle of 328° at about 7:30 hrs. UT (after moonset) on this date. Figure 5-12 show the intensity modulations (and standard deviation) as seen by the interferometer until about 8:30 hrs. UT. The bright band, dark band, bright band sequence show a modulation in intensity of about 20%. This same sequence is also shown in the isocon video frames in Figures 5-2 through 5-4. Following the last bright band, the intensity falls off by 40%, indicating a relatively dark band. The simultaneous plot of the OH rotational temperature shown in Figure 5-13 has a mean temperature of about 165°K . The modulations seen are in phase and correspond to the increases and decreases in intensity in Figure 5-12. The magnitude of the temperature modulations are from 5 to 8°K . The standard deviation on the temperature calculation is about $\pm 3^\circ\text{K}$.

The interferometer was moved to a different viewing location at about 8:30 hrs. UT and remained there until about 9:15 hrs. UT. The new viewing angles were 15.5°

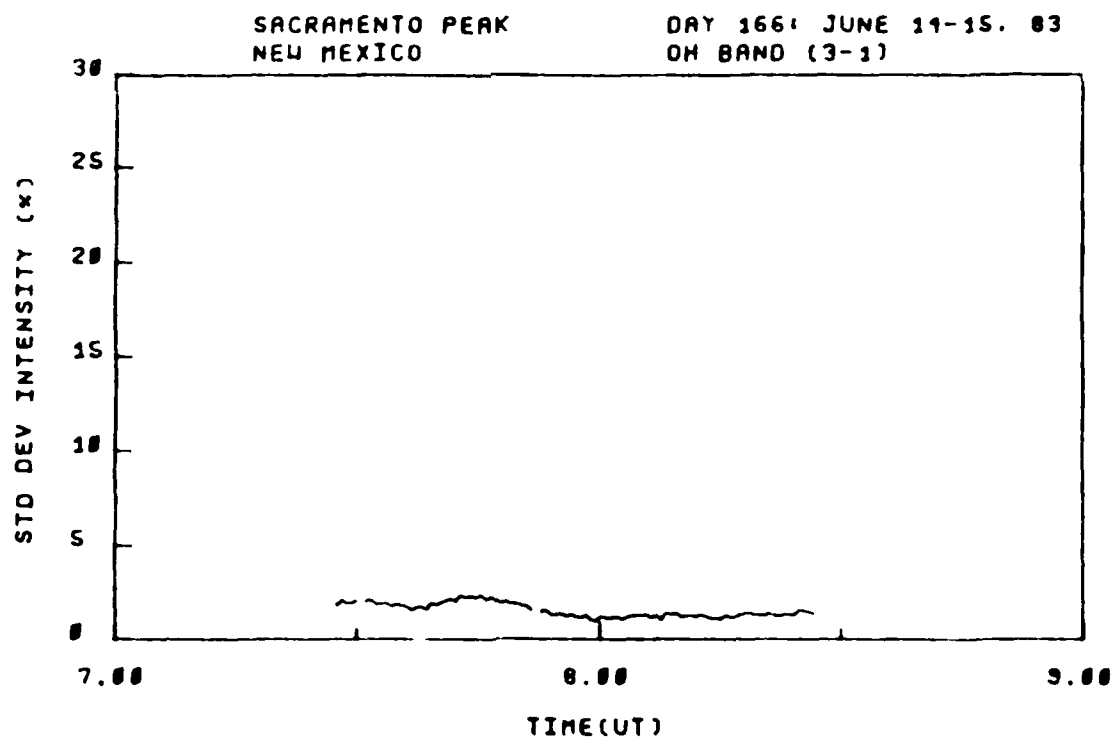
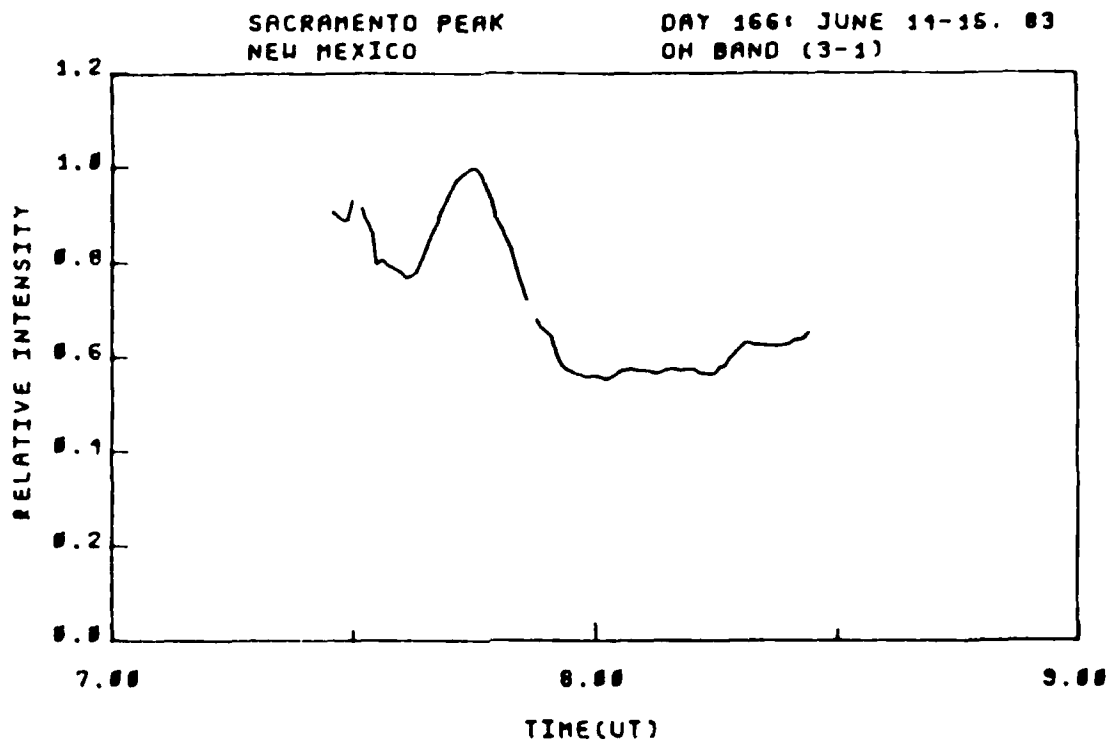


Figure 5-12. OH (3,1) band relative intensity and standard deviation, viewing angle = 17° El. 328° Az., day 166, 7:30-8:30 hrs. UT.

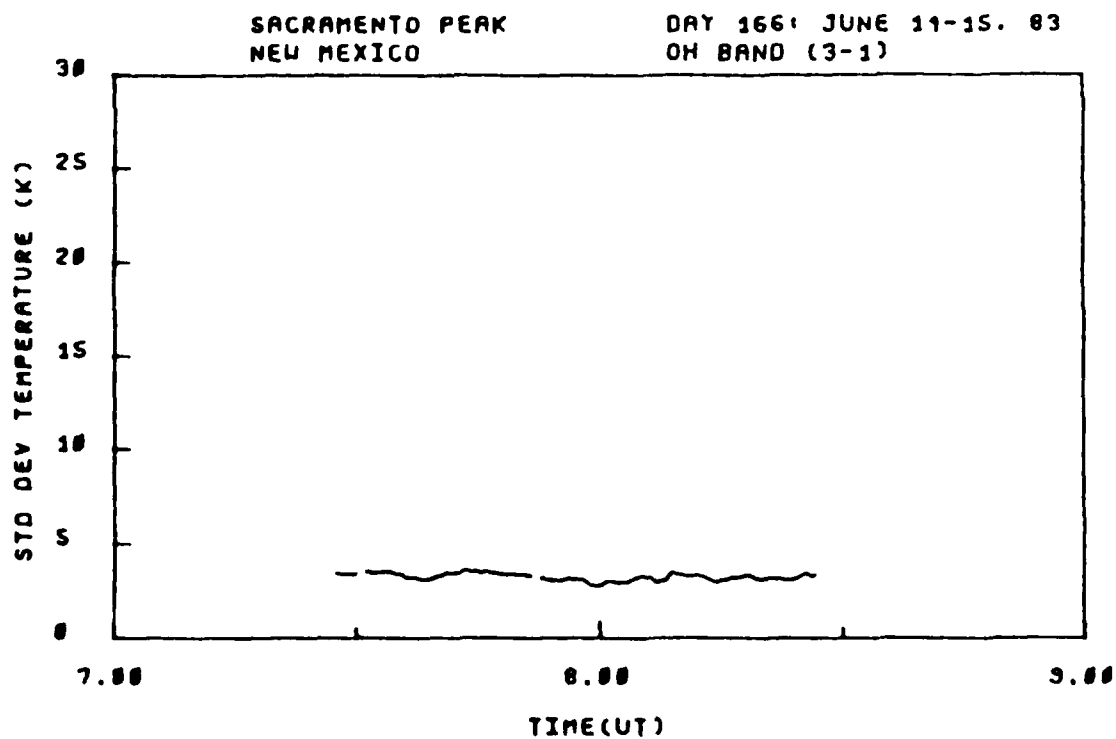
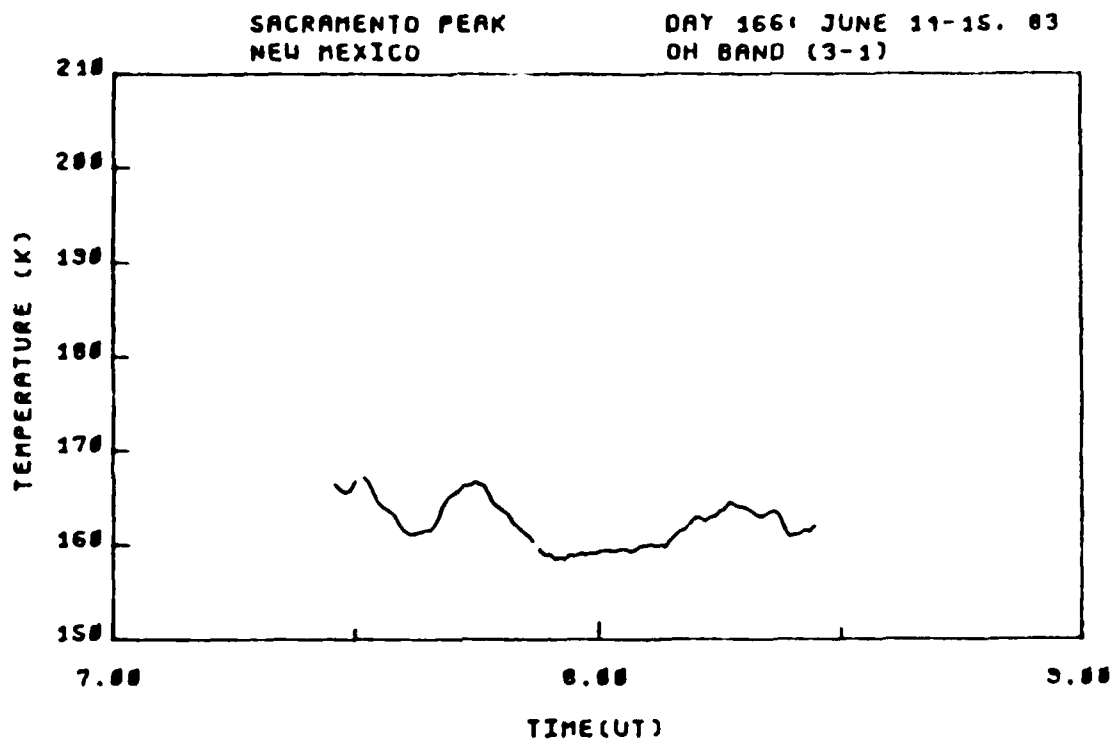


Figure 5-13. OH (3,1) band smoothed rotation temperature and standard deviation, viewing angle = 17° El. 328° Az., day 166, 7:30-8:30 hrs. UT.

elevation and 340° azimuth. The intensity modulations at this viewing position are shown in Figure 5-14. The first dark band, bright band, dark band sequence in this figure show a modulation of 40%. The intensity modulations shown after the first bright band are much smaller, being on the order of 10%. The video frames in Figures 5-5 and 5-6 correspond to the first dark band and occur just after the peak of the very bright band of Figure 5-14. The rotational temperature plot for this same time period is shown in Figure 5-15. The mean temperature is about 165°K . with a maximum modulation of 10°K . The uncertainty on the temperature calculations is about $\pm 4^\circ\text{K}$ during this time frame. The temperature and intensity modulations, at the beginning of this measurement period, are again in phase with each other. The 10% intensity modulations shown in Figure 5-14 occurring after 8:50 hrs. UT, however, do not show any discernible modulations in the temperature.

The last observations of the night began at about 9:15 and lasted until 10:15 hrs. UT. The viewing position of the interferometer was again changed to 15.5° elevation and 309° azimuth. Figure 5-16 presents the intensity modulation record for this period. The curve shows the first sequence of structure exhibiting a modulation of 40% and three more bright and associated dark bands with modulations of about 20%. The corresponding rotational temperature plot, Figure 5-17, once again has a mean temperature of 165°K . The temperature modulations are from 5 to 8°K with each rise

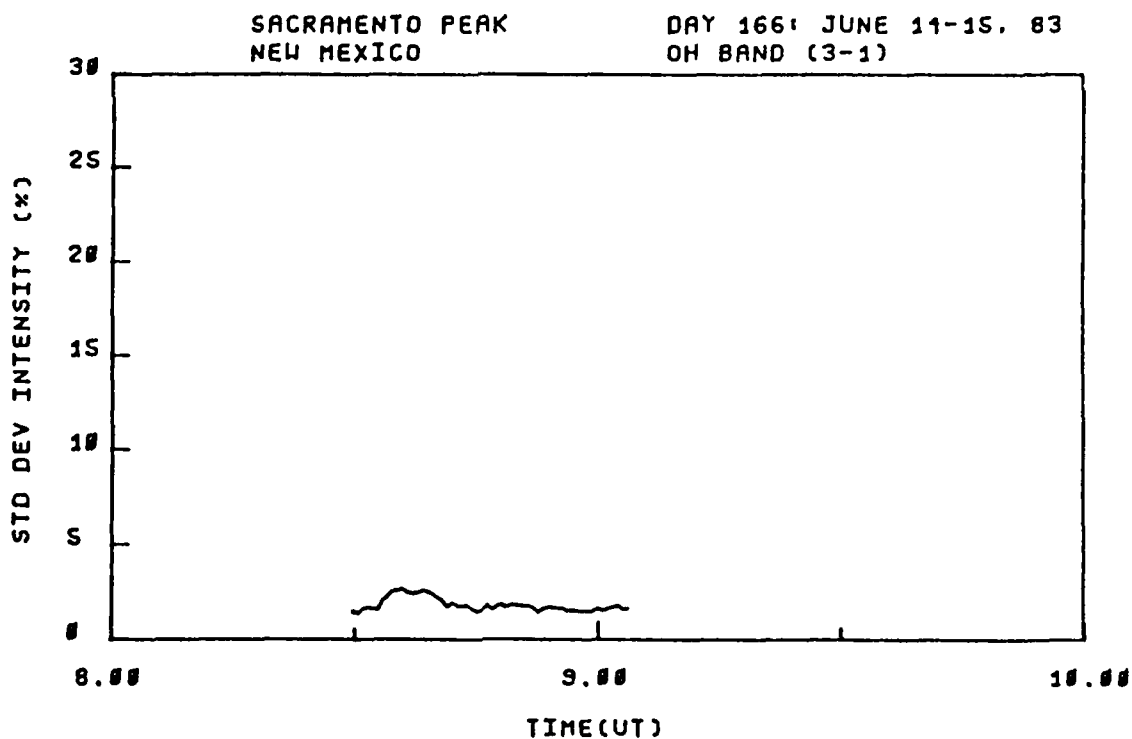
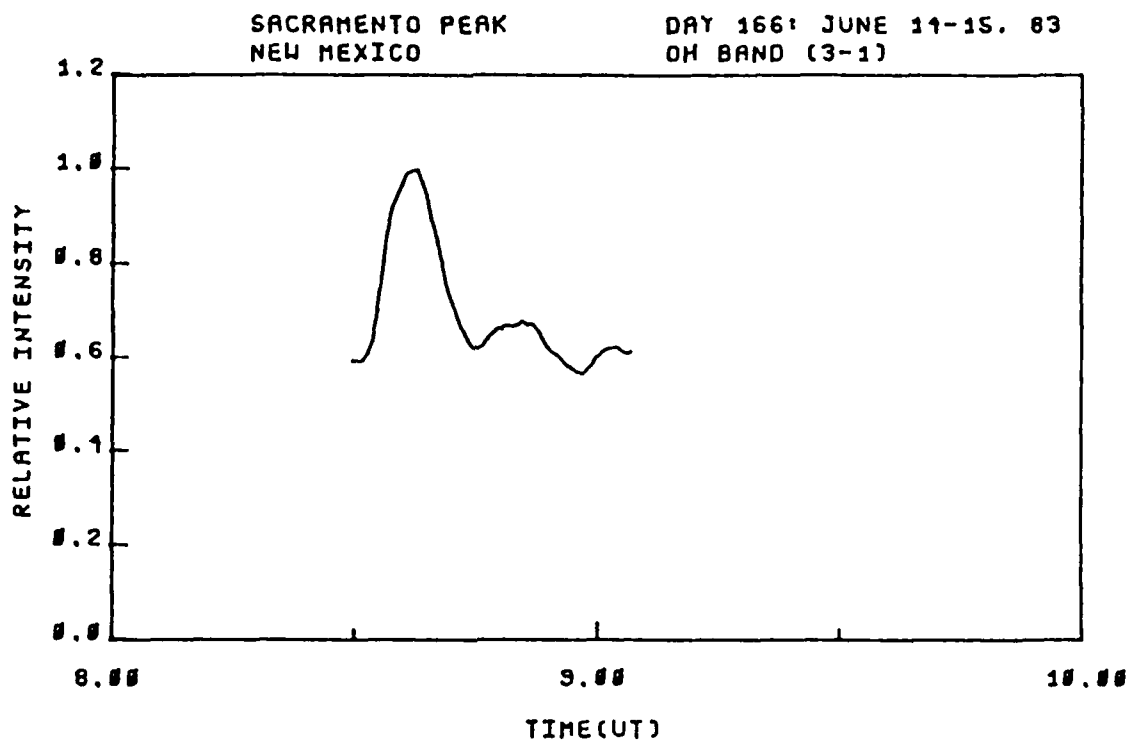


Figure 5-14. OH (3,1) band relative intensity and standard deviation, viewing angle = 15.5° El. 340° Az., day 166, 8:30-9:15 hrs. UT.

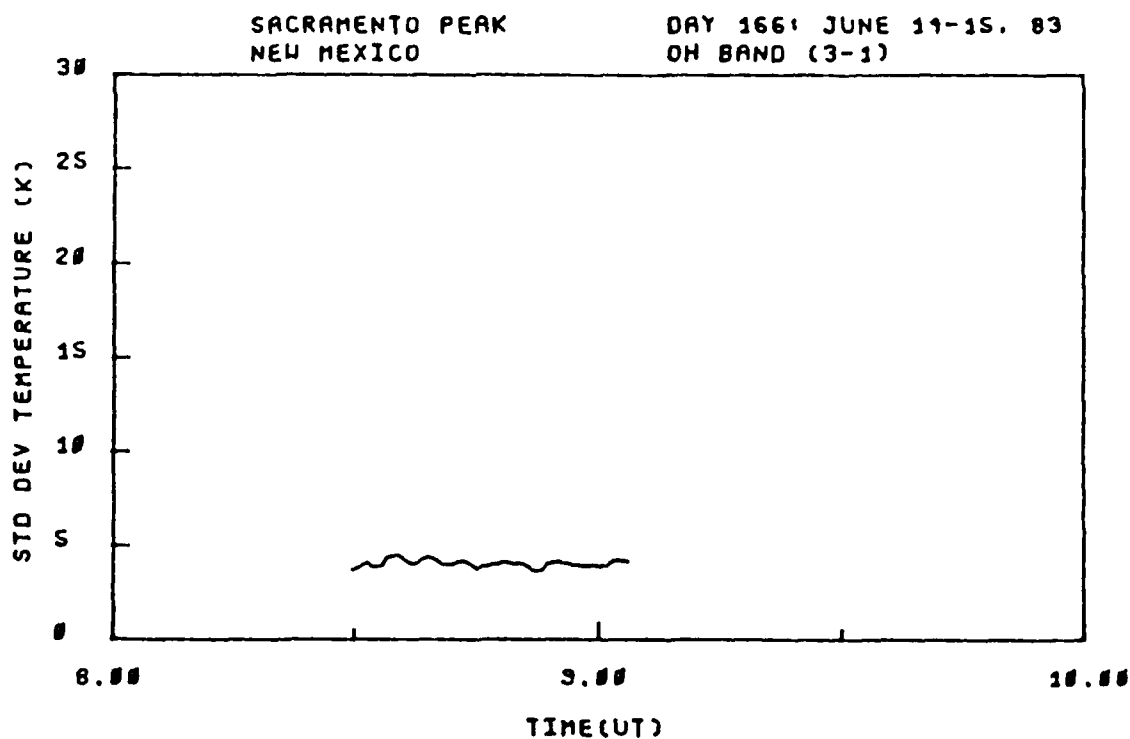
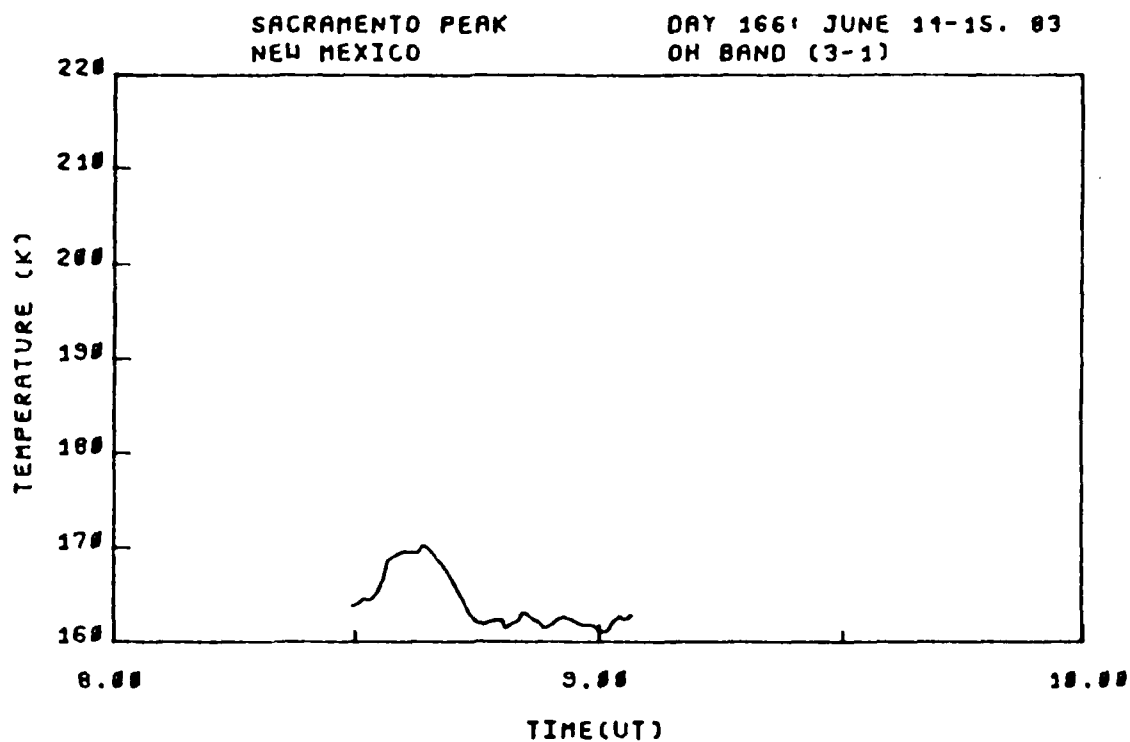


Figure 5-15. OH (3,1) band smoothed rotation temperature and standard deviation, viewing angle = 15.5° El. 340° Az., day 166, 8:30-9:15 hrs. UT.

in temperature having a corresponding rise in intensity of at least 20%. The uncertainty on the temperature calculations is again about ± 4 °K.

The presentation in this chapter of the interferometer-recorded structure for June 15, 1983 is focused on the information extracted from the OH (3,1) band. Examination of the Appendix C records for the other OH bands, presents an additional observation. The two $\Delta v=2$ band temperatures track each other within the standard deviation of the calculations. The two $\Delta v=3$ band temperatures track each other within the standard deviation of the calculations. The $\Delta v=3$ band temperatures, however, are consistently from 15 to 32 °K hotter than the $\Delta v=2$ band temperatures (discussed more in Chapter VI). Figure 5-18 is an example with additional data available in Appendix C. Table 5-1 outlines a summary of the results presented in this chapter.

TABLE 5-1. Summary of OH airglow structure measurement results for June 15, 1983.

1. Apparent structure period	14 \pm 1 minutes
2. Apparent structure temporal wavelength	24 \pm 1 km
3. Apparent structure phase velocity	28 \pm 2 meters/sec
4. Intensity modulations measured	10 to 40 %
5. Rotational temperature modulations measured	5 to 10 °K
6. Phase relationship of recorded rotational temperature and intensity measurements	In phase
7. Mean zenith OH (3,1) band intensity	75 kR

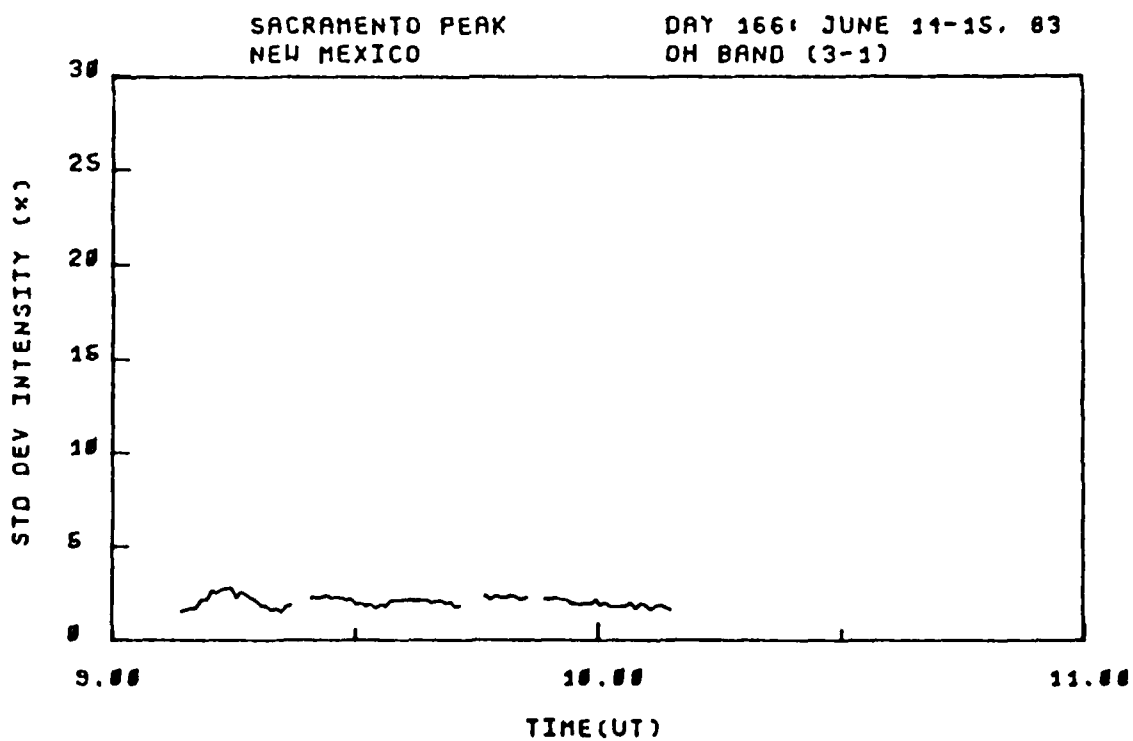
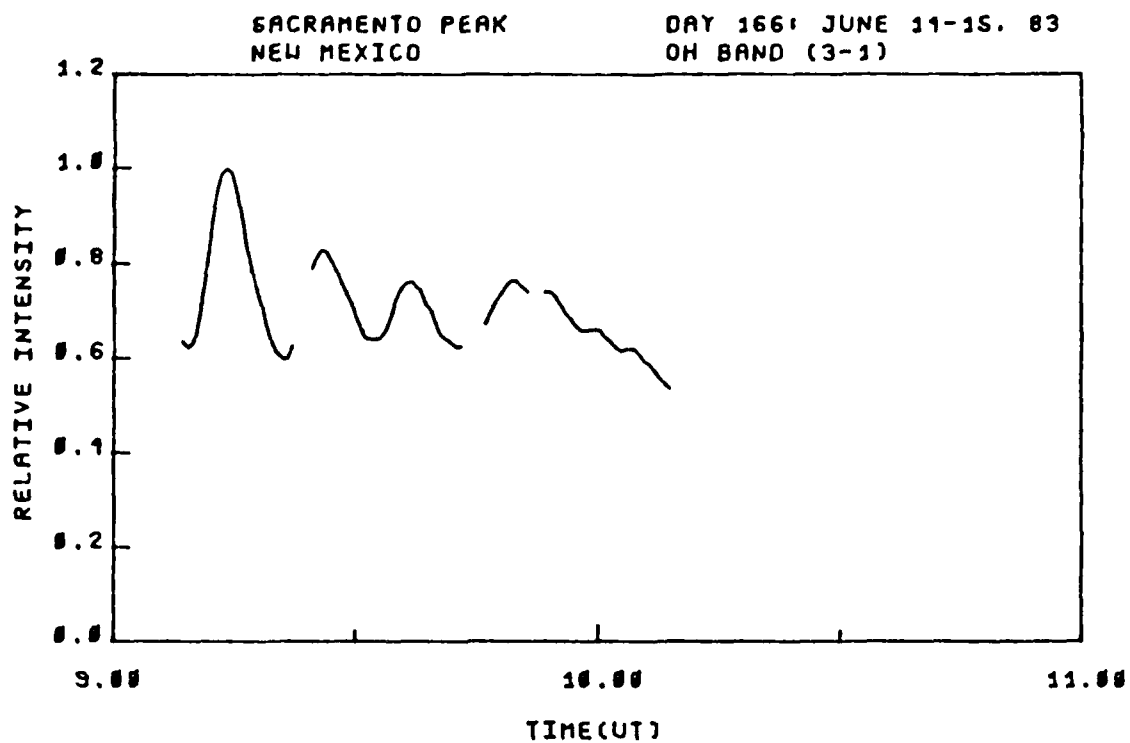


Figure 5-16. OH (3,1) band relative intensity and standard deviation, viewing angle = 15.5° El. 309° Az., day 166, 9:15-10:15 hrs. UT.

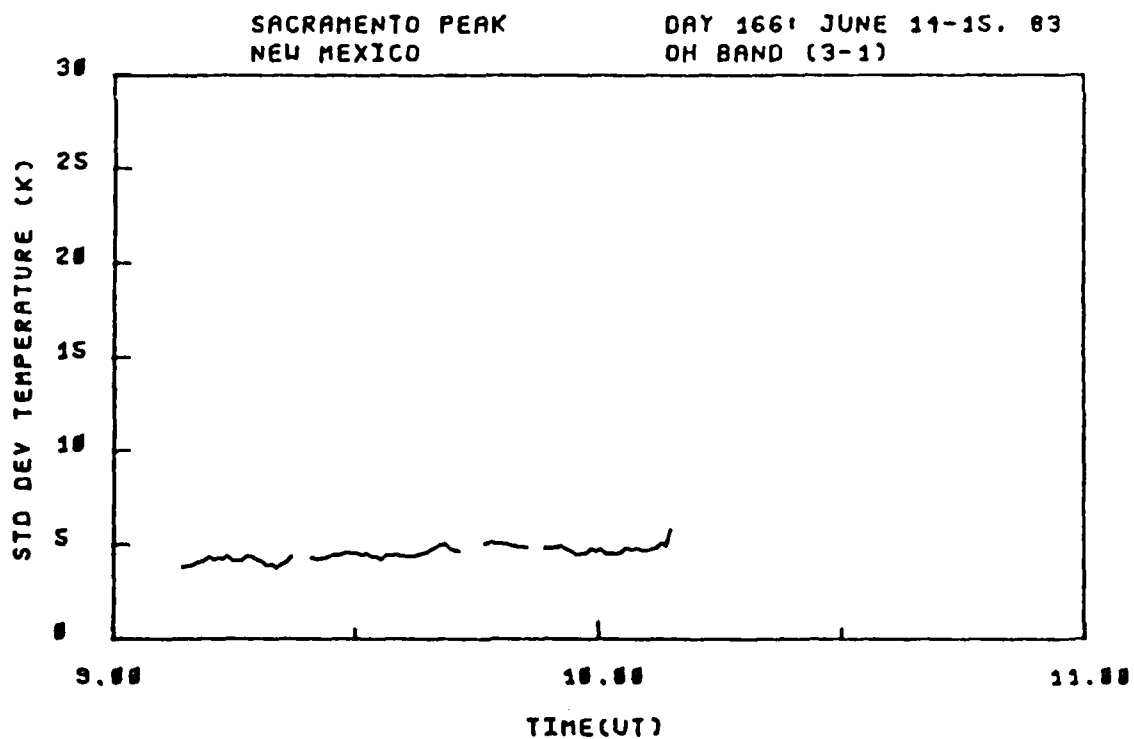
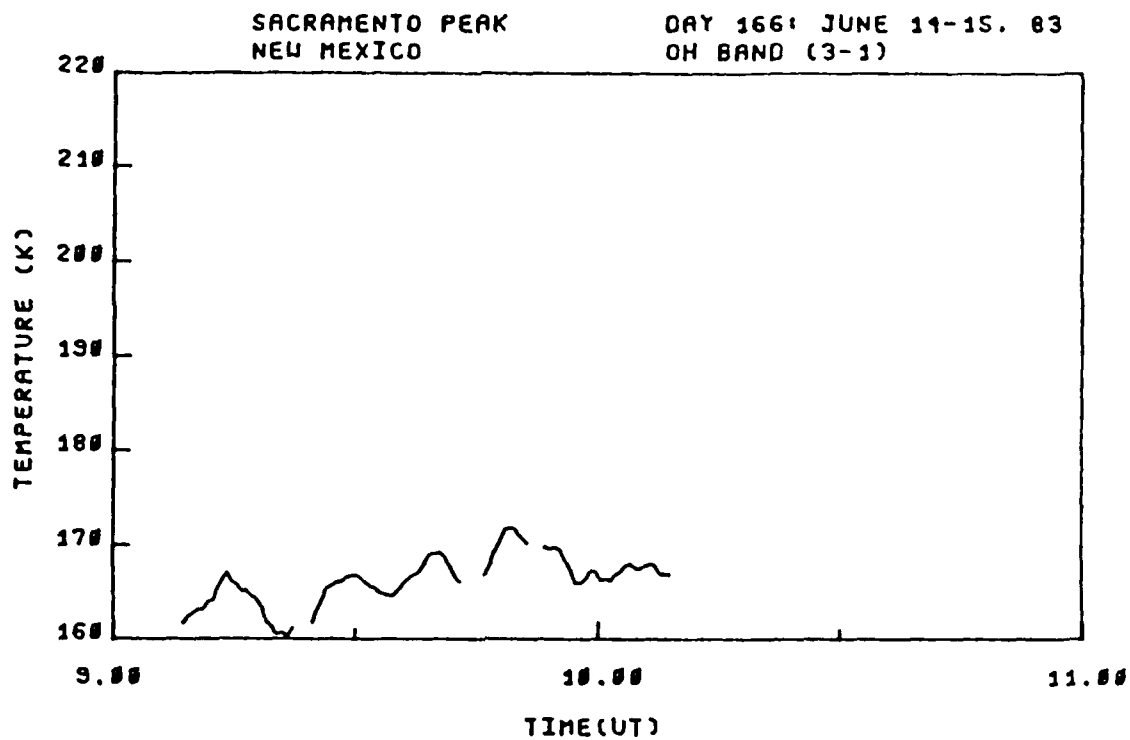


Figure 5-17. OH (3,1) band smoothed rotation temperature and standard deviation, viewing angle = 15.5° El. 309° Az., day 166, 9:15-10:15 hrs. UT.

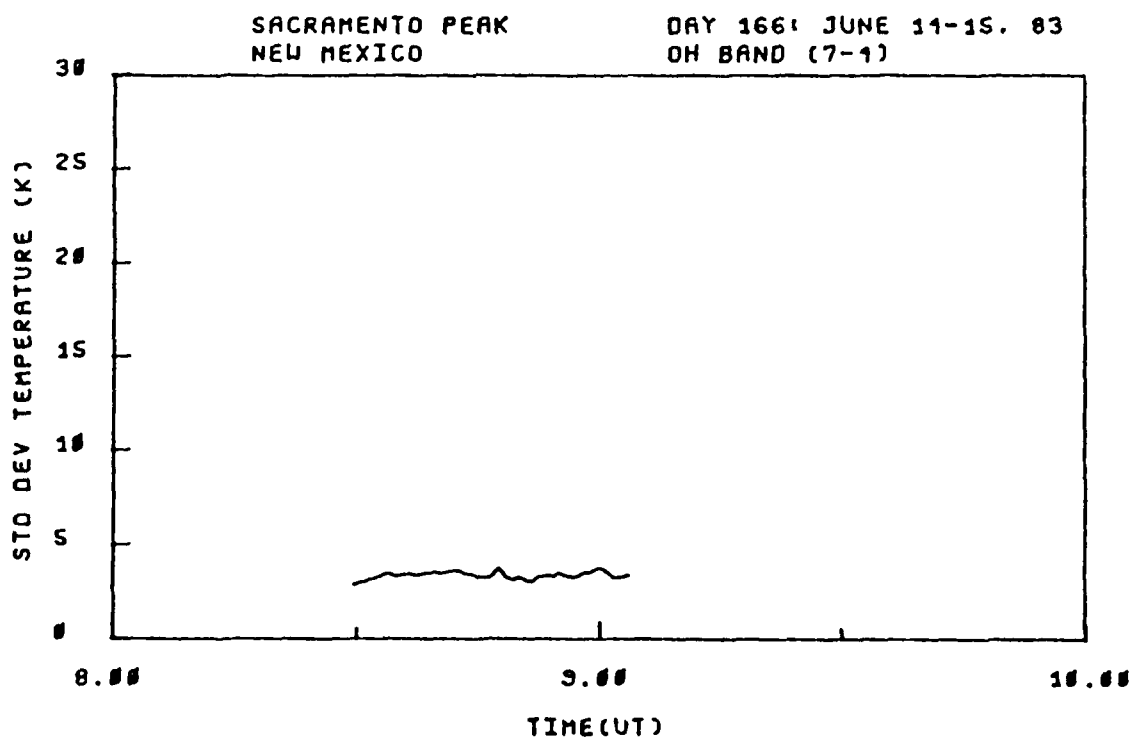
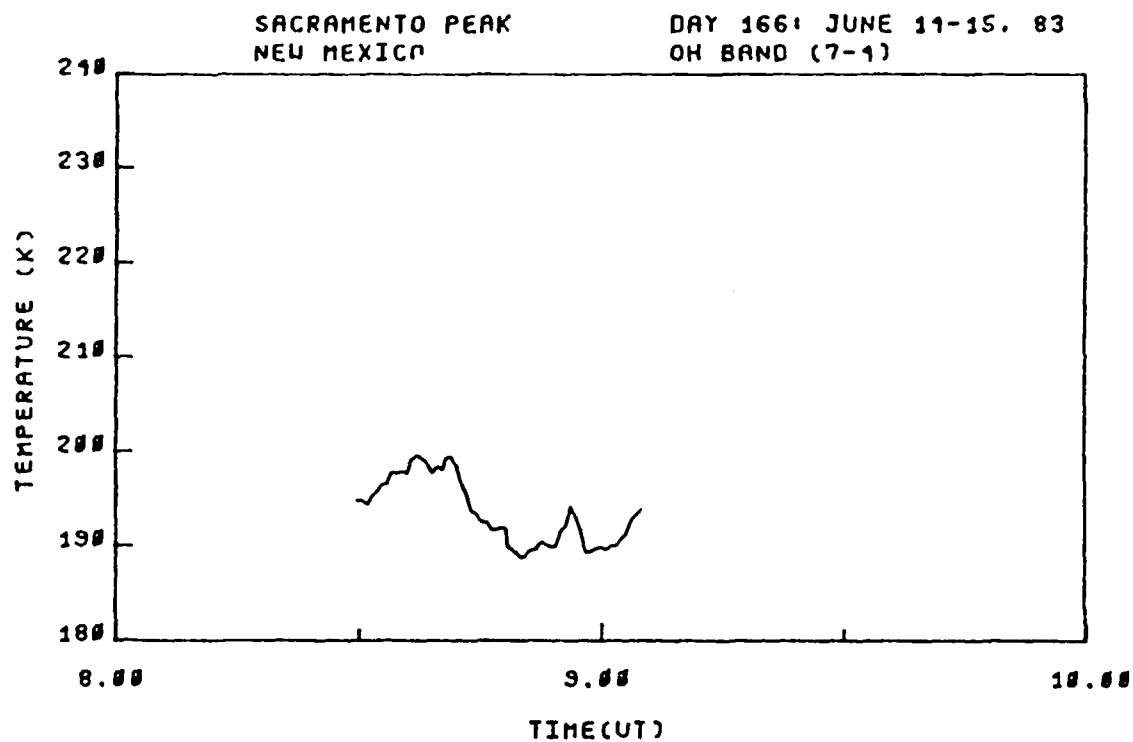


Figure 5-18. OH (7,4) band smoothed rotation temperature and standard deviation, viewing angle = 15.5° El. 340° Az., day 166, 8:30-9:15 hrs. UT.

CHAPTER VI

DISCUSSION OF RESULTS

Rotational Temperatures

The mean mesopause temperature for the month of June at a mid-latitude site is expected to be about 170 °K with variations of ± 20 °K possible during the month [NOAA 1976 and references therein]. Noxon [1978] also recorded OH Meinel rotational temperatures at Fritz Peak, Colorado ($\approx 40^\circ$ N) during May 1977. During the last few days of May, he recorded nightly mean temperatures of about 160 °K.

The mean OH rotation temperatures presented in Chapter V are for an observing site at $\approx 32^\circ$ N and are between 165 °K and 175 °K. The references cited above suggest that these rotational temperatures are typical of the mesopause temperatures expected at mid-latitudes during the summer season.

Examination of the standard deviation plots on temperature (Chapter V and Appendix C) reveals typical values in the range 3-7 °K. This uncertainty is nearly as large as many of the temperature changes obtained from the structure measurements. It is felt, however, that much of the computed standard deviation may be systematic rather than statistical. The model used for the determination of rotational temperature is based on the assumption that OH

rotational populations are in true thermal equilibrium and are thus strictly Boltzmann distributed. A slight deviation from this assumption would cause a systematic error. Another possible source of error results from the assumption that all OH airglow radiation is emitted from a thin uniform layer; whereas in reality, the layer is about 7 km in thickness. In addition, at low viewing elevation angles $\approx 10^\circ$ the layer geometry is much more complicated. At these low elevation angles atmospheric extinction, van Rhijn effect, and curved spherical geometry potentially have a significant impact on the interpretation of the measurements.

The interferometer spectral response calibration is very sensitive to alignment. The instrument typically remained in alignment for about 2 hours. As can be seen from the increase in the standard deviation as a function of time (7:30 to 10:15 hrs. UT, day 166), the alignment changed significantly and this change could account for a portion of the uncertainty. Therefore, the temperature modulations obtained from the spectral data are felt to be more accurately defined than is suggested by the standard deviation.

The assumption that the low observation elevation angles associated with the structure measurements did not unduly impact the computed temperature is supported by the fact that the temperature at 6:45 hrs. UT on day 166 was 163 °K (see Figure 5-9) and the temperature at 7:30 hrs. on the

same day was 166 °K (see Figure 5-13). These temperatures represent the values computed just before and just after the interferometer "look direction" was changed from the zenith to near the horizon.

Rotational Temperature and Intensity Modulations

The ranges of temperature and intensity modulations observed in the OH Meinel airglow structures are given in Chapter V. The "adiabatic oscillation" and "IGW" modeling of the OH Meinel airglow variations mentioned in Chapter I utilize a parameter which is readily calculated from the intensity and temperature modulations. This parameter is the ratio of the change in emission intensity normalized by the mean emission intensity, divided by the change in temperature normalized by the mean temperature and is deemed useful in studies of the OH airglow structure phenomena. The parameter is usually represented by the Greek letter eta (η) and is defined as follows:

$$\eta = [(\Delta I / \bar{I}) / (\Delta T / \bar{T})] \quad , \quad (6.1)$$

where

- ΔI = change or modulation in emission intensity,
- \bar{I} = mean value of the emission intensity,
- ΔT = change or modulation in rotational temperature,
- \bar{T} = mean value of the rotational temperature.

The value of η is potentially useful in distinguishing between chemical processes which give rise to the OH airglow emission and temperature structure. The physics of this parameter is discussed by Krassovsky [1972] and Weinstock [1978]. Pendleton [1985] has summarized the essential features of this parameter in Figure 6-1. In this figure, the η value is plotted versus the ratio (H/H_x) , where H is the appropriate atmospheric scale height, and H_x is the scale height (near 85 km) of minor species "x". Here the letter "x" represents either oxygen (O) or hydrogen (H). The simple adiabatic-oscillation model of Krassovsky [1972] yields η values which are independent of (H/H_x) , whereas the gravity-wave model of Weinstock [1978] yields (H/H_x) dependent values. The range of η values expected on the basis of values of (H/H_x) inferred from several measured atomic oxygen profiles is also shown in the figure. The information in Figure 6-1 indicates that values of η in the range from 3 to 6 might be expected based on current gravity-wave modeling and the ozone hydration process.

Using the numbers for the intensity and temperature modulations and means, presented in Chapter V, the range of calculated values for η are from 8 to 12. These values are about a factor of 2 greater than those shown in Figure 6-1. In view of the relatively large standard deviations on the temperature determinations, the nominal factor of two disparity between predicted and measured η values is not deemed significant.

The η values calculated for the time periods when the interferometer was viewing in the zenith were obtained by assuming the pre-midnight increase in both temperature and intensity reflected a wave-like disturbance. The zenith-viewing η values associated with the major pre-midnight (I,T) fluctuations on UT days 165 and 166 were found to be consistent with η values deduced from the low-elevation-angle data. The consistency of these two sets of calculations lends credence to the idea, once again, that viewing near the horizon had little impact on the η determinations although the modulation in both intensity and temperature may have been impacted by the geometry of the measurements.

The field of view (FOV) of the interferometer is 0.8° full field. Consideration of the OH structures in the nominally 13° by 15° video frames suggests that the 0.8° FOV of the interferometer results in a horizontal spatial integration over about one half cycle in the quasi-period structures. This integration will degrade the horizontal spatial resolution of the interferometer measurements. If the wave is assumed to be sinusoidal in nature and restricted to a very thin spherical shell, a simple integration over $1/2$ cycle indicates that the rotational temperature modulations could be degraded by a factor of about 1.5. The horizontal intensity structure is expected to be more complex than the temperature structure [Weinstock 1978]. However, if a similar "degradation factor" were

applicable to the intensity measurements, then the satisfactory agreement of the η values deduced from the zenith-viewing and near-horizon-viewing measurements could be explained.

Temperature Differences Observed Between Bands

Rotational temperature differences between the high- v' and low- v' levels characterized both the zenith-viewing and near-horizon-viewing measurements. The high- v' rotational temperatures were consistently higher than those obtained from low- v' bands. The bands used for detailed comparison are the high- v' (7,4) band and the low- v' (3,1) band. These bands were chosen because of favorable instrument response and alignment stability in the spectral regions of occurrence. The temperature differences observed ranged between 15 and 32 °K. The smaller difference applied when looking in the zenith, and the difference gradually increased throughout the night as the telescope was physically moved, affecting the alignment. The increase in the temperature difference is largely attributed to instrument alignment drift because the standard deviations on the temperature calculations (which also reflect misalignment) increase simultaneously with (and at about the same rate) the increase in temperature difference.

Explanations were sought for this difference. It was discovered that an error in the line strength constant for

the OH (7,4), P₁(4) line had been entered into the processing system. The constant was about 20% low in value. In order to assess the impact of this error, a synthetic OH spectrum was generated assuming a typical temperature with the associated error entered, and a Boltzmann plot was made. A line was fit to the points in a least-squares sense and an associated temperature extracted. The OH (7,4) band model used 12 lines in the fit; therefore, because the model fit is least-squares in nature the error from this incorrect constant was found to be less than 1%.

Another possible explanation of the high- v' , low- v' temperature difference is slightly different (\approx 1-3 km) emitting altitudes. The ratio of ΔT to the mean temperature \bar{T} , if different for the high- v' low- v' measurements, would support such a difference in mean emitting heights [Pendleton 1985]. The $\Delta T/\bar{T}$ ratio within each observational time frame was calculated and the difference in the ratio, between the high and low rotational levels, was found to be less than 10%, with less than 30% difference among all frames. These differences in the $\Delta T/\bar{T}$ ratio between high- v' and low- v' bands when viewed in terms of the calculated standard deviations does not provide evidence for differences in mean emitting altitude.

Within the standard deviation of the calculations, the rotational temperature differences between the high- v' and low- v' levels appears to be real. The magnitude for this

difference, as was mentioned in Chapter I, is within the range reported by Krassovsky and Shagaev [1977].

Temperature and Intensity

Phase Relationship

The modeling of IGW's mentioned earlier predicts that the changes in the OH Meinel rotational temperature should be in phase with the IGW [Hines 1960]. The change in intensity, however, should be related to the IGW temporal structure in a potentially more complicated manner. This situation arises partly because of the finite chemical time constant associated with mesospheric ozone. The appropriate time constant for the cool ($T \approx 160$ °K) summer-mesopause conditions is about 25 minutes [Pendleton 1985]. For IGW periods somewhat in excess of this value, chemical conversion of O_3 is expected to be a significant factor in the phenomenology, whereas for much smaller IGW periods chemical conversion should be unimportant. Examination of Figures 5-8 and 5-9 shows that the temperature maxima lead the intensity maxima by about 20 minutes. This apparent phase difference may relate to the aforementioned O_3 time constant, but it would be premature to draw this conclusion. It is suggested that additional attention be given to this interesting possibility.

The small-scale structures observed near the horizon on UT day 166 exhibit an in-phase relationship between intensity and temperature. The only exception to this is

when the measured intensity modulation was less than about 20%. Under these conditions, no direct correlation between intensity and temperature could be drawn. Since the measured period of the small-scale OH Meinel structures was significantly less than the nominal 85-km O_3 time constant, it does not appear that the in-phase behavior of the larger-amplitude fluctuations is necessarily inconsistent with the zenith measurements.

CHAPTER VII

CONCLUSIONS AND RECOMMENDATIONS

Overview

The goal of this study was to design, develop, and operate an instrument system capable of performing simultaneous spatial, spectral, and temporal high-resolution OH airglow measurements. The design herein, and the resulting data demonstrate the effectiveness of the technique. An airglow structure event which occurred on June 15, 1983 was measured with the interferometer-spectrometer system. OH Meinel intensities and rotational temperatures were obtained for the peaks and troughs of this wavelike structure.

Conclusions

The following are the specific accomplishments of this study. The areas addressed pertain both to the instrument designed for airglow structure measurements and to the data processing techniques used.

1. An optically-compensated interferometer for high throughput ($\Delta\Omega=0.285 \text{ cm}^2 \text{ sr}$), was matched to a large area collector (50-cm diameter) to narrow the field of view (0.8°). A noise equivalent spectral radiance (NESR) (sensitivity) of 16 R/cm^{-1} at $1.5 \text{ }\mu\text{m}$ was

achieved. In comparison, a conventional Michelson interferometer-spectrometer with the same detector, collector area, resolution, and scan time would have a NESR of 128 R/cm^{-1} , a factor of 8 less sensitive than the one developed for this study. When compared with a conventional Ebert spectrometer, using the same detector and operated at the same resolution, a sensitivity of 208 R/cm^{-1} could be achieved, a factor of 13 less sensitive.

2. A spectral resolution of 2 cm^{-1} was sufficient to resolve the OH emission line structure for the extraction of OH rotational temperatures. Based upon a rotational line separation of 10 cm^{-1} and the Hamming apodization function used, the spectral resolution of the instrument could be lowered to no more than 4 cm^{-1} .
3. Based upon the video records, the bright or dark bands of OH structure subtend about 1° of arc at these low elevation angles ($\approx 15^\circ$). The apparent temporal wavelength was $24 \pm 1 \text{ km}$, with a period of $14 \pm 1 \text{ minutes}$, and an apparent phase velocity of $28 \pm 2 \text{ meters/second}$.
4. The interferometer system field of view was measured at 0.8° . The interferometer FOV is sufficiently narrow to independently view a "bright" or a "dark" structure band. Based on this limited data set and simple wave geometry, the field of view could be as large as 7° if these structures were viewed in the zenith.

5. The measured intensity modulations (contrast ratios) for the OH airglow structures ranged between 20 and 40% with interferometer recorded periods of 14 minutes. The calculated standard deviation was typically 3%.
6. The mean calculated OH Meinel rotational temperature for the aforementioned event was 165 °K. The measured modulations in rotational temperatures associated with the changes in intensity ranged from 5-10 °K and are in phase with the intensity modulations. Typical standard deviations on the rotational temperature calculations ranged from 2-7 °K. The mean temperature and magnitude of the temperature fluctuations are consistent with both IGW theory and previous mesospheric temperature measurements.
7. The least-squares model used to extract band intensity and rotational temperature provides a computational efficient way (convergence to final values occurred within 4 iterations of the fitting routine) to simultaneously derive these values. The model also provides a measure (standard deviation) of how well the data fit a Boltzmann distribution.
8. The insight needed to identify what is being observed from the airglow layer can only be provided by the camera (or similar) video system. The measurement of OH airglow structure events with the interferometer system would not be possible without the simultaneous use of

the isocon camera, because with the interferometer alone, exactly what was being viewed would be unknown.

Recommendations for Future Research

The interferometer worked as designed and proved to be an excellent tool for this type of study. The model developed for the extraction of rotational temperatures and intensities is an accurate technique and provides computational flexibility. However, several suggestions are made for consideration for future work.

1. The optical path within the interferometer is very complex. There are 20 optical surfaces through which the incoming energy must pass before reaching the detector. Assuming a typical loss of 4% per surface, 80% of the incoming signal is lost before reaching the detector. This complex optical path should be redesigned to minimize the number of optical elements and optically coat the remaining elements to minimize reflection loss.
2. The physical size of the instrument should be reduced to facilitate portability to remote sites.
3. The instrument is very sensitive to optical alignment. The optical components need to be mounted in a more stable manner to hold their location better.
4. The alignment is very sensitive to temperature. It is necessary therefore to temperature control the

interferometer environment to preclude instrument changes as the outside temperature fluctuates.

5. The telescope pointing system needs to be automated. The sensitivity of alignment to physical motion as well as the need to point the instrument to an area of interest demand that the positioning of the system be automated.
6. An infrared camera system, like the one provided by the University of Southampton, needs to be permanently incorporated as part of the interferometer system. The interferometer cannot effectively gather data on airglow structure if the location of the structure is not known and the camera provides this input.
7. The instrument must be provided a better means of calibration. The blackbody sources used in this study give a reasonable indication of alignment and instrument response but as the system alignment drifts the calibration is less meaningful. Perhaps a technique utilizing OH spectral line pair ratios which are independent of rotational temperature but sensitive to alignment could be used as a dynamic measure of instrument alignment.
8. A recommendation is made to investigate other detectors, in order to extend the ability of the interferometer, with a wider spectral bandwidth and higher sensitivity. The RCA detector used in this study is an excellent detector where it is sensitive but is somewhat limited

in spectral bandwidth. A larger detector could also be used to increase the throughput, although the throughput is now almost limited by the size of the interferometer optics.

9. A new data system should be developed to record the interferometer data allowing for at least the digitization of the data during recording. The analog tapes are bulky and expensive but more importantly, playing back the tapes for data reduction is too time consuming.
10. The calibration curves provided to the model derived from occasional alignment processes with a tungsten blackbody could be improved. As was mentioned earlier, a dynamic calibration using information inherent in the spectrum could be used to better adjust the model to the instrument response.
11. Examination of Figures 3-3 and 3-4 shows that the phase correction used to eliminate the chromatic effects of the instrument on the data works well on the slowly varying blackbody curve but the negative information on the spectrum makes the technique suspect when applied to the rapidly changing data. A phase correction technique which operates in the interferogram "domain" where the shaping could be done with simple multiplication could prove to be more accurate.

12. The extraction of line amplitudes from the interferometer could be improved in two areas. First, the approximate locations of the spectral lines of interest are found in a manual manner. A template using a synthetic spectrum could be designed for each OH band and a correlation routine could be used to automatically search the raw data for the location of the lines. Secondly, the apodization routine used to extract the actual line amplitude from the data should be modified to calculate a line area rather than amplitude. The area routine would provide for the averaging out of noise whereas the amplitude routine always searches for the most positive peak.
13. The model should be modified to use the "Q" branches of the OH bands. To do this the molecular constants for both Q_1 and Q_2 would need to be averaged as one because the interferometer does not resolve the two groups. This addition should add more accuracy to the model because the Q branches are the largest lines within each band.
14. The model could be modified to include a third variable, water column content, based on the several lines within the OH bands which are severely affected by water absorption. The model then could provide additional information about the atmosphere.

REFERENCES

- Baker, D.J. 1978. Studies of Atmospheric Infrared Emissions. Final Report, AFGL-TR-78-0251. Air Force Geophysics Laboratory. Hanscom AFB, Mass. 79 p. ADA072831
- Baker, D.J., A.J. Steed, G.A. Ware, D. Offermann, G. Lange, and H. Lauche. 1985. Ground-Based Atmospheric Infrared and Visible Emission Measurements. *Journal of Atmospheric and Terrestrial Physics* 47(1-3):133-145.
- Banks, P.M., and G. Kockarts. 1973. *Aeronomy*, Part A. Academic Press, New York and London. 430 p.
- Bevington, P.R. 1969. *Data Reduction and Analysis for the Physical Sciences*. McGraw-Hill Book Company, New York. 336 p.
- Bouchareine, P., and P. Connes. 1963. Interferometer with a Compensated Field of Spectroscopy by the Fourier Transform. *Le Journal De Physique Et Le Radium* 24:134-138.
- Brigham, E.O. 1974. *The Fast Fourier Transform*. Prentice-Hall, Inc., Englewood Cliffs, New Jersey. 252 p.
- Chamberlain, J.W. 1961. *Physics of the Aurora and Airglow*. Academic Press, New York and London. 704 p.
- Connes, P. 1956. Augmentation du Produit Luminosite x Resolution des Interferometres Par l'emploi d'une Difference de Marche Independante de l'incidence. *Revue Opt. Theor. Instrum.* 35:37-42.
- Connes, J. 1963. *Spectroscopic Studies Using Fourier Transformations*. NAVWEPS Report 8099. U.S. Naval Ordnance Test Station, China Lake, California. AD 409 869. 127 p.
- Coxon, J.A., and S.C. Foster. 1982. Rotational Analysis of Hydroxyl Vibration-Rotation Emission Bands: Molecular Constants for OH X²Π, 65 v ≥ 10. *Canadian Journal of Physics* 60:41-48.
- Crawford, J., P. Rothwell, and N. Wells. 1975. Airborne Television Observations of Airglow Clouds in the Near Infrared. *Nature* 257:650-651.

- Despain, A.M., F.R. Brown Jr., A.J. Steed, and D.J. Baker. 1971. A Large Aperture Field-Widened Interferometer-Spectrometer for Airglow Studies, p. 293-300. In G.A. Vanasse, D.J. Baker and A.T. Stair, Jr. (Eds.). Aspen International Conference on Fourier Spectroscopy, 1970. Air Force Cambridge Research Laboratories, AFCRL-71-0019, Special Reports No. 114, Hanscom AFB, Mass. 477 p. AD724100
- Driscoll, W.G. (Ed.), and W. Vaughan (Associate Ed.). 1973. The Handbook of Optics. Sponsored by Optical Society of America. McGraw Hill, New York. Chapter 2:62-63.
- Espy, P. 1984. Private communication with Mr. Espy, Physics Department, Utah State University, Logan, Utah. March.
- Fellgett, P. 1949. Private communication to M.J.E. Golay. Multi-slit Spectrometry. Journal of the Optical Society of America 39:437-439.
- Forman, M.L. 1966. Fast Fourier-Transform Technique and Its Application to Fourier Spectroscopy. Journal of the Optical Society of America 56:978-985.
- Gebbie, H.A., and G.A. Vanasse. 1956. Interferometric Spectroscopy in the Far Infrared. Nature 178:432-436.
- Gilway Technical Lamp Catalog. 1982. Part No. 8010. 272 New Boston Park, Woburn, MA.
- Hamming, R.W. 1977. Digital Filters. Prentice Hall, Englewood Cliffs, New Jersey. 226 p.
- Hapgood, M.A., and M.J. Taylor. 1982. Analysis of Airglow Data. Annales de Geophysique t. 38 fasc. 6:805-813.
- Harris, C.R. 1984. Private communication with Mr. Harris, Data Reduction Specialist, Space Dynamics Laboratory, Utah State University, Logan, Utah. April.
- Harris, F.J. 1978. On the Use of Windows for Harmonic Analysis with the Discrete Fourier Transform. Proceedings of the IEEE 66(1):51-83.
- Haycock, R.H. 1975. A Gas Lubricated Precision Platform for Interferometric Measurements. PhD dissertation. Utah State University Library, Logan, Utah. 178 p.
- Haycock, R.H., and D.J. Baker. 1975. Infrared Prism Interferometer-Spectrometer using a Gas-Lubricated Drive Bearing. Infrared Physics 14:259-265.
- Hertzberg, G. 1971. The Spectra and the Structures of Simple Free Radicals. Cornell University Press Ithaca, New York. 195 p.

- Hill, R.A., A.J. Mulac, D.P. Afschliman, and W.L. Flower. 1979. Temperatures From Rotational-Vibrational Raman Q-branches. *Journal of Quantum Spectroscopy Radiation Transfer*. Pergamon Press Ltd., Great Britian, 21:213-230.
- Hines, C.O. 1960. Internal Atmospheric Gravity Waves at Ionospheric Heights. *Canadian Journal of Physics* 38:1441-1481.
- Hines, C.O. 1965. Dynamical Heating of the Upper Atmosphere. *Journal of Geophysical Research* 70(1):177-183.
- Hoffmeister, C. 1952. Investigations on Bright Night Sky and Luminous Bands. *Journal of the British Astronomical Association* 62(8):288-292.
- Huppi, R.J. 1976. Radiometric Instrumentation and Techniques of Measuring Infrared Emissions from the Atmosphere and Targets. AFGL-TR-76-0253, Air Force Geophysics Laboratory, Hanscom AFB, Mass. 65 p. ADA042757
- Huppi, R.J., and D.J. Baker. 1976. Intensity Variations of Atmospheric Hydroxyl Emissions. Scientific Report No. 1, AFCRL-TR-76-0032, Contract No. F19628-74-C-0190, Utah State University, Logan, Utah. Air Force Geophysics Laboratory, Hanscom AFB, Mass. 77 p. ADA023684
- Jacquinet, P. 1954. The Luninosity of Spectrometers with Prisms, Gratings, or Fabry-Perot Etalons. *Journal of the Optical Society of America*, 44:761-764.
- Kieffaber, L.M. 1973. Structure and Fluctuations of the OH Airglow at 1.65 and 2.15 μ . PhD Dissertation. University of New Mexico Library, Albuquerque, New Mexico. 127 p.
- Kochanski, A. 1964. Atmospheric Motions from Sodium Cloud Drifts. *Journal of Geophysical Research* 69:3651-3656.
- Krassovsky, V.I. 1972. Infrasonic Variations of OH Emission in the Upper Atmosphere. *Annales de Geophysique* 28:739-747.
- Krassovsky, V.I., and M.V. Shagaev. 1977. Research Note, On the Nature of Hydroxyl Airglow. *Planetary and Space Science* 25:509-510.
- Krassovsky, V.I., B.P. Potapov, A.I. Semenov, M.V. Shagaev, N.N. Shefov, V.G. Sobolev, and T.I. Toroshelidze. 1977. Internal Gravity Waves Near the Mesopause and the Hydroxyl Emission. *Annales de Geophysique t. 33 fasc. 3:347-356.*

- Lawson, C.L., and R.J. Hanson. 1974. Solving Least Squares Problems. Prentice-Hall, Inc., Englewood Cliffs, New Jersey. 340 p.
- Loewenstein, E.V. 1971. Fourier Spectroscopy; An Introduction, p. 3-18. In G.A. Vanasse, D.J. Baker and A.T. Stair, Jr. (Eds.). Aspen International Conference on Fourier Spectroscopy, 1970. Air Force Cambridge Research Laboratories, AFCRL-71 0019, Special Reports No. 114, Hanscom AFB, Mass. 477 p. AD724100.
- Meinel, A.B. 1950. OH Emission Bands in the Spectrum of the Night Sky. Astrophysics Journal 111:555-561.
- Mertz, L. 1959. Paper presented at Congress de Stockholm, Heterodyne Interference Spectroscopy.
- Mies, F.H. 1974. Calculated Vibrational Transitional Probabilities (X^2). Journal of Molecular Spectroscopy 53:150-188.
- Moreels, G., and M. Herse. 1977. Photographic Evidence of Waves Around the 85 km Level. Planetary and Space Science 25:265-273.
- National Oceanic and Atmospheric Administration (NOAA). 1976. U.S. Standard Atmosphere. Washington D.C. 227 p.
- Norton, R.H., and R. Beer. 1976. New Apodizing Functions for Fourier Spectrometry. Journal of the Optical Society of America 66:259-264.
- Noxon, J.F. 1978. Effect of Internal Gravity Waves Upon Night Airglow Temperatures. Geophysical Research Letters 5(1):25-27.
- Nuttall, A.H. 1981. Some Windows with Very Good Sidelobe Behavior. IEEE Transactions on Acoustics, Speech, and Signal Processing ASSP-29(1):84-91.
- Pendleton, W.I. Jr. 1985. Private communication with Dr. Pendleton, Dept. of Physics and Space Dynamics Laboratories, Utah State University, Logan, Utah. July.
- Peterson, A.W. 1979. Airglow Events Visible to the Naked Eye. Applied Optics 18(20):3390-3393.
- Peterson, A.W., and G.W. Adams. 1983. OH Airglow Phenomena During the 5-6 July 1982 Total Lunar Eclipse. Applied Optics 22(17):2682-2685.
- Peterson, A.W., and L.M. Kieffaber. 1973. Infrared Photography of OH Airglow Structures. Nature 242:321-322.

- Peterson, A.W., and L.M. Kieffaber. 1975. Photography and Photometry of the Near Infrared OH Airglow. *Nature* 257:649-650.
- Rai, D.B., and B.G. Fejer. 1971. Evidence of Internal Gravity Waves in the Lower Ionosphere. *Planetary and Space Science* 19:561-566.
- Rayleigh, Lord (Strutt, R.J.). 1931. On a Night Sky of Exceptional Brightness, and on the Distinction between the Polar Aurora and the Night Sky. *Proceeding of the Royal Society, London*, A131:376-381.
- Roychourdhury, D.K. 1983. Airglow Technique to Compute Mesospheric Temperature and Integrated Water Vapor Concentration of the Atmosphere. Masters Thesis. Utah State University Library, Logan, Utah. 135 p.
- Shankland, R.S. 1974. Michelson and His Interferometer. *Physics Today* 4:37-48.
- Soule, H.V. 1968. *Electro-Optical Photography at Low Illumination Levels*. John Wiley and Sons, Inc., New York. 392 p.
- Steed, A.J. 1978. The Design, Evaluation, Optimization and Calibration of a Field-Widened Interferometer-Spectrometer used for Near Infrared Atmospheric Measurements. PhD dissertation. Utah State University Library, Logan, Utah. 145 p.
- Strong, J.D., and G.A. Vanasse. 1959. Interferometric Spectroscopy in the Far Infrared. *Journal of the Optical Society of America* 49:844-851.
- Takeuchi, I., and K. Misawa. 1981. Short-Period Oscillations of Intensity and Rotational Temperature of the OH(6-2) Band. *Annales de Geophysique t. 37 fasc. 2*:315-319.
- Taylor, M.J. 1983-84. Private communication with Mr. Taylor, Department of Physics, University Southampton, England.
- Taylor, M.J. 1984. Paper presented at The International Workshop on Noctilucent Clouds. TV Observations of Mesospheric Wave Structures. Tallinn, Estonian SSR, USSR, August.

- Taylor, M.J., M. Hapgood, and P. Rothwell. 1980. Upper Atmosphere Wave Structure Imaged in Oxygen Green Line, Sodium and the Near Infrared Hydroxyl Airglow Emissions, p. 95-105. *In Proc. of the Eight Annual Meeting on Upper Atmosphere Studies by Optical Methods*, Dublin, Ireland, E. O'Mongain (Ed.), University College, Dublin, Sept.
- Turnbull, D.N., and R.P. Lowe. 1983. Vibrational Population Distribution in Hydroxyl Night Airglow. *Canadian Journal of Physics* 61:244-250.
- Vagin, V.A. 1980. Optimal Apodization in Fourier Spectrometry. *Optical Spectrometry (USSR)* 48(2):190-193.
- Vanasse, G.A. (Ed). 1977. *Spectrometric Techniques*, Vol. 1. Academic Press, New York. 355 p.
- Vanasse, G.A., D.J. Baker, and A.T. Stair Jr. (Eds.). 1971. *Aspen International Conference on Fourier Spectroscopy, 1970*. Air Force Cambridge Research Laboratories, AFCRL-71-0019, Special Reports No. 114, Hanscom AFB, Mass. 477 p. AD724100
- Ware, G.A. 1980. OH Rotational Temperatures Using Optimal Interferometric Techniques. PhD dissertation. Utah State University Library, Logan, Utah. 271 p.
- Weast, R.C., (Ed.). 1977. *CRC Handbook of Chemistry and Physics*. CRC Press, Cleveland, Ohio. p. E-204.
- Weinstock, J. 1978. Theory of Interaction of Gravity Waves with $O_2(^1\Sigma)$ Airglow. *Journal of Geophysical Research* 13(A11):5175-5185.
- Werner, H., P. Rosmus, and E. Reinsch. 1983. Molecular Properties from MCSCF-SCEP Wave Functions. I. Accurate Dipole Moment Functions of OH, OH-, and OH+. *Journal of Chemical Physics*, July 15, 79(2):905-916.
- Wyatt, C.L. 1978. *Radiometric Calibration: Theory and Methods*. Academic Press, New York. 200 p.

APPENDICES

Appendix A

OH Transitions

This appendix briefly describes why the radiation from the OH molecule is so complex. The many spectral lines generated by the excited radical are depicted in Figure 4.1. The molecule rotates and vibrates simultaneously, and each of the motions are quantized and interactive.

The total molecular angular momentum without electronic spin \vec{K} is also quantized and is identified by the quantum number K . The quantity \vec{K} is comprised of two parts

$$\vec{K} = \vec{N} + \vec{A} \quad (A.1)$$

The vector \vec{N} is the nuclear angular momentum and the vector \vec{A} is the angular momentum of the orbiting electron cloud projected onto the internuclear axis. The quantum number A associated with the electronic orbital momentum can take on a value of +1 or -1 depending upon which way the electron cloud is orbiting with respect to the nuclear rotation. The double degeneracy of A leads to the so-called A splitting of each state; however, the split is less than 1 cm^{-1} at low rotational speeds [Baker 1978], which is less than the instrument resolution used for this study, therefore the A -split lines will be considered as one.

The quantum number K can take on values $K = 1, 2, 3, \dots$. The selection rule; however, is

$$\Delta k = 0, \pm 1 \quad . \quad (A.2)$$

The collection of lines within each band, grouped according to their respective Δk , are called branches. The branch with $\Delta k = 0$ is called the Q branch, that for $\Delta k = +1$ is the R branch, and that for $\Delta k = -1$ is called the P branch.

The OH molecule has an odd number of electrons. This imbalance results in a net electronic spin angular momentum \vec{S} and is represented by quantum number S . The odd electron gives rise to an even multiplicity $2S+1$. Since the total number of electrons is odd, S is half integral ($S = \pm 1/2$), each transition state is a doublet. It is sometimes convenient to consider the total electron angular momentum $\vec{\Omega}$ as a separate entity. The total electron angular momentum is

$$\vec{\Omega} = \vec{\Lambda} + \vec{S} \quad . \quad (A.3)$$

Therefore, each vibration-rotation transition will split into two separate spectral lines according to whether $\Omega=3/2$ or $\Omega=1/2$.

The OH molecule is very light and as a consequence the odd electron spin \vec{S} is only weakly coupled to the internuclear axis. The molecule is therefore, modeled as Hund's case (b) [Hertzberg 1971]. The total molecular angular momentum \vec{J} can now be formed

$$\vec{J} = \vec{K} + \vec{S} \quad . \quad (A.4)$$

As can be seen from Equation A.4, for each value of K there are two values for J . Each branch of the OH spectra must also take on two values. If $\Omega=3/2$, then

$$J = K + 1/2 = 1.5, 2.5, 3.5, \dots \quad . \quad (A.5)$$

These values for J lead to a set of spectral lines known as P_1 , Q_1 , and R_1 branches. If $\Omega=1/2$, then

$$J = K - 1/2 = 0.5, 1.5, 2.5, \dots \quad . \quad (A.6)$$

These values for J give rise to a set of spectral lines known as P_2 , Q_2 , and R_2 branches. Additional information on the physics of OH molecule is readily available in the literature, among them are Baker [1978], Hertzberg [1971], and Mies [1974].

APPENDIX B.

RCA LIMITED GERMANIUM DETECTOR SPECIFICATIONS

RCA supplied the following specifications for their limited germanium detector:

TE-71 Series

$$\text{NEP}(1.42,10,1) = 10^{-14} \text{ WHz}^{-1/2}$$

TM-71 Series

$$\text{NEP}(1.42,500,1) = 10^{-14} \text{ WHz}^{-1/2}$$

$$\text{Area} = 0.20 \text{ cm}^2$$

Cooled to 77 K

$$\text{Responsivity} \approx 10^7 - 10^8 \text{ VW}^{-1}$$

In order to achieve good noise performance, it is necessary to cool both the detector and the preamplifier.

Special Optics: The standard window is quartz; different window material, special filter or condensing optics can be fitted provided no substantial mechanical redesign is necessary. The normal field of view for the detector is close to 90°.

If the user desires to operate the TM-71 system at very high frequencies, it is possible to trade NEP for frequency response. Other special features may be added to these developmental systems.

The responsivity varies according to the spectral curve. Some variation in this curve is possible according to the customer requirements.

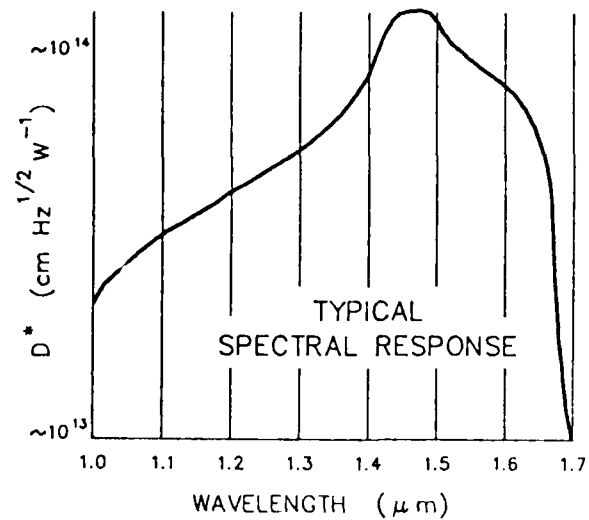


Figure B-1. Typical detector spectral response. The responsivity varies according to the spectral curve. Some variation in this curve is possible according to the customer requirements.

TABLE B-1. Germanium Detector Technical Data

	<u>TE Series 71</u>	<u>TM Series 71</u>
Operating Temperature	77 K	77 K
Noise Equivalent Power (guaranteed), $\text{WHz}^{-1/2}$	$\text{NEP}(1.42, 10, 1) = 1 \times 10^{-14}$	$\text{NEP}(1.42, 500, 1) = 1 \times 10^{-14}$
Best NEP (previously achieved), $\text{WHz}^{-1/2}$	$\text{NEP}(1.42, 23, 1) = 1 \times 10^{-15}$	$\text{NEP}(1.42, 4000, 1) = 1 \times 10^{-15}$
Noise level (at output)	$\sim 1 \mu\text{V}$	$\sim 10 \mu\text{V}$
Impedance level (at output)	$\sim 5000 \Omega$	$\sim 500 \Omega$
Responsivity, VW^{-1}	$\sim 5 \times 10^{-7}$	$\sim 5 \times 10^{-7}$
Linear range for power, W	$10^{-14} - 10^{-10}$	$10^{-14} - 10^{-10}$
Useable limit (power), W	$\sim 6 \times 10^{-9}$	$\sim 2 \times 10^{-9}$
Frequency characteristic	f^{-1}	flat, 3dB at 500 Hz
Detector area (circular), cm^2	0.2	0.2
Typical Operating Volts, V	-10	-10, +10

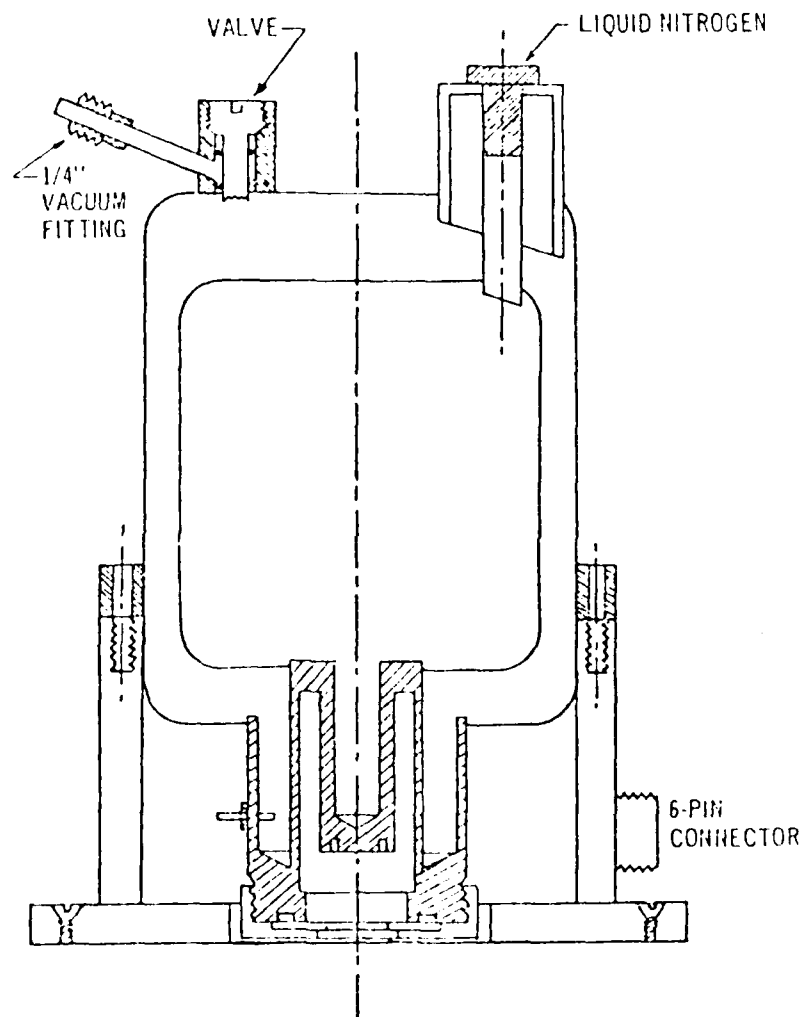


Figure B-2. RCA germanium detector liquid-nitrogen dewar outline.

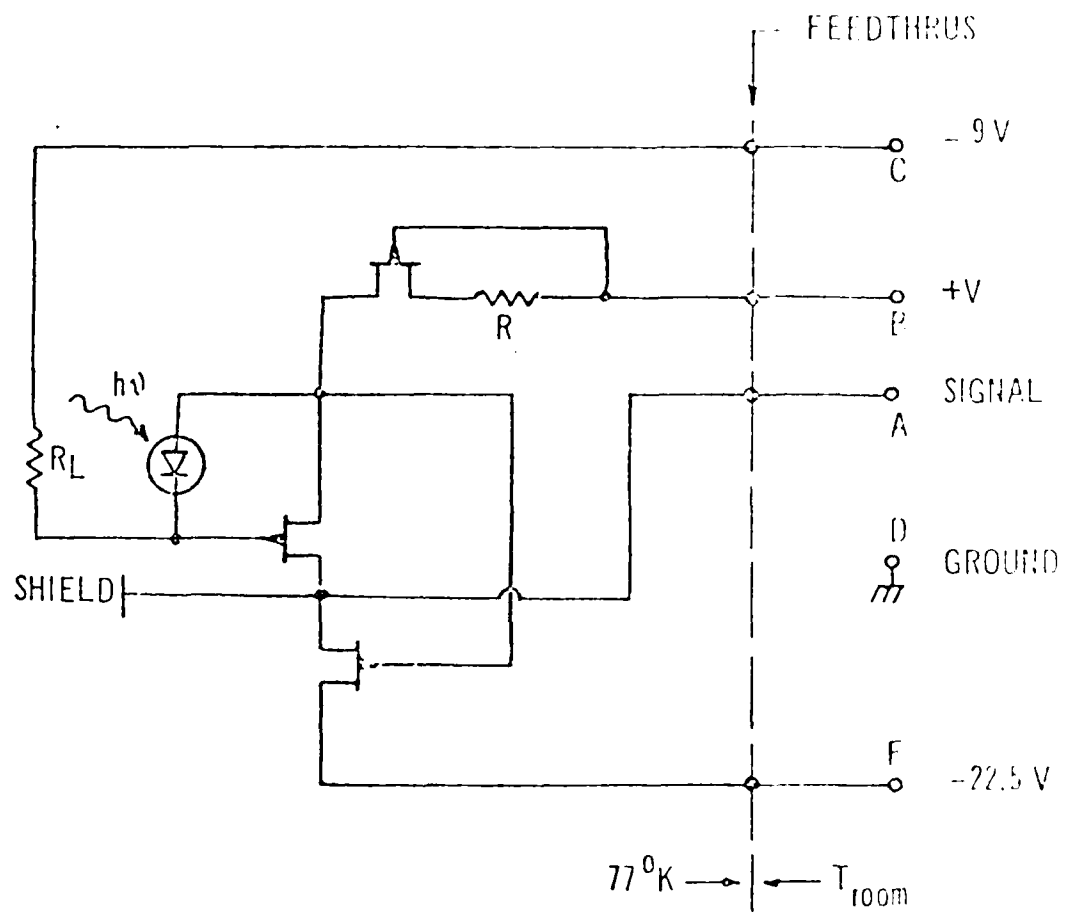


Figure B-3. Detector preamplifier circuit.

TABLE B-2. Detailed Specifications on RCA Detector.

AVAILABILITY MECHANISM	NEP WATT	MEASURED SIGNAL EFFICIENCY	CALCULATED QUANTUM EFFICIENCY	ABSORPTION COEFFICIENT	NEUTRAL DENSITY FILTER	DIODE SIGNAL (MVOLT)	THERMOPILE SIGNAL GAIN 1000X (MVOLT)	DRUM POSITION (3DEGS)	POWER ON DIODE (WATT)	RESPONSIVITY (VOLT/WATT)
1.1000	2.57E-14	2.37E-01	3.11E-01	12000.000	770.0	42.50	23.00	0.50	1.707E-09	2.490E 07
1.1500	2.37E-14	2.37E-01	3.47E-01	10000.000	735.0	54.00	25.70	2.00	1.999E-09	2.703E 07
1.1700	1.90E-14	3.54E-01	3.66E-01	9000.000	785.0	70.00	28.50	3.80	2.075E-09	3.374E 07
1.1500	1.56E-14	4.11E-01	3.81E-01	8300.000	795.0	89.90	30.50	5.50	2.192E-09	4.101E 07
1.2000	1.37E-14	4.51E-01	3.98E-01	7500.000	755.0	110.00	31.00	7.20	2.346E-09	4.688E 07
1.2500	1.19E-14	4.98E-01	4.15E-01	6700.000	765.0	125.00	31.00	9.00	2.316E-09	5.398E 07
1.3000	1.02E-14	5.55E-01	4.56E-01	5000.000	780.0	142.00	31.00	10.60	2.271E-09	6.253E 07
1.3500	1.04E-14	5.28E-01	4.82E-01	4000.000	750.0	130.00	27.60	12.30	2.103E-09	6.182E 07
1.4000	9.97E-15	5.29E-01	5.03E-01	3200.000	700.0	77.00	14.70	14.00	1.200E-09	6.417E 07
1.4500	8.49E-15	6.00E-01	5.54E-01	40.000	725.0	148.00	24.90	15.80	1.963E-09	7.541E 07
1.5000	1.10E-14	4.47E-01	4.82E-01	15.000	745.0	120.00	26.90	17.50	2.063E-09	5.816E 07
1.5500	1.65E-14	2.89E-01	4.03E-01	8.000	745.0	76.00	25.50	19.10	1.956E-09	3.886E 07
1.6000	2.79E-14	1.65E-01	2.56E-01	2.000	720.0	44.00	24.20	20.90	1.921E-09	2.291E 07
1.6500	5.47E-14	8.18E-02	9.18E-02	0.350	725.0	21.20	23.00	22.50	1.813E-09	1.169E 07
1.7000	1.66E-13	2.62E-02	1.92E-02	0.060	750.0	6.20	21.10	24.20	1.608E-09	3.857E 06

Appendix C
Interferometer Data Catalog

The interferometer data for observations taken on June 13-15, 1983 are contained within this appendix in their entirety. All data presented were recorded at Sacramento Peak, New Mexico. The figures are all organized chronologically beginning on day 165 at 3:30 hrs. UT and proceeding through day 166, 10:15 hrs. UT.

Both of the observation days' records begin with the interferometer viewing in the zenith. At moonset on day 166 the interferometer and camera systems were lowered to view near the horizon. The low elevation viewing period during day 166 is divided into three time frames, corresponding to when the interferometer was adjusted in viewing location. The time period and viewing position are identified in each figure caption.

Within each time segment of the data presentation, the figures are organized according to the OH Meinel band from which the data were calculated. First is the OH (4,2) band, second the OH (3,1), third the OH (8,5) band, and fourth the OH (7,4) band. Each of the band groups shows curves for first the intensity, second the rotational temperature, and third the smoothed rotational temperature calculation with the associated standard deviation for each.

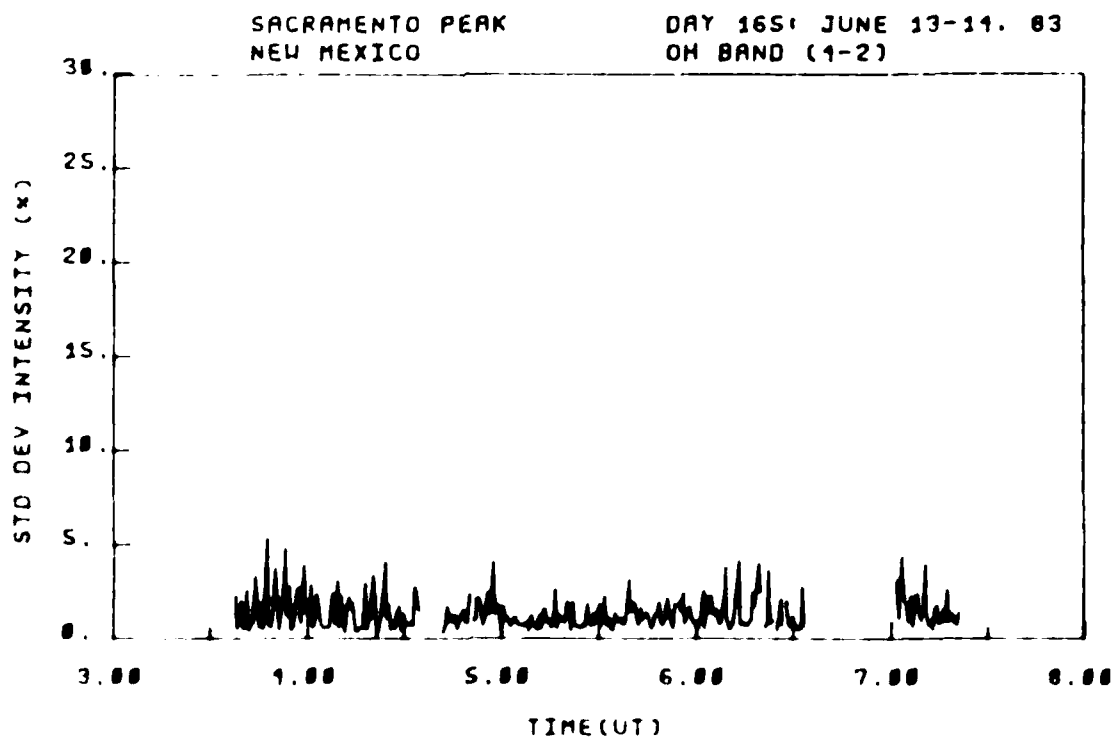
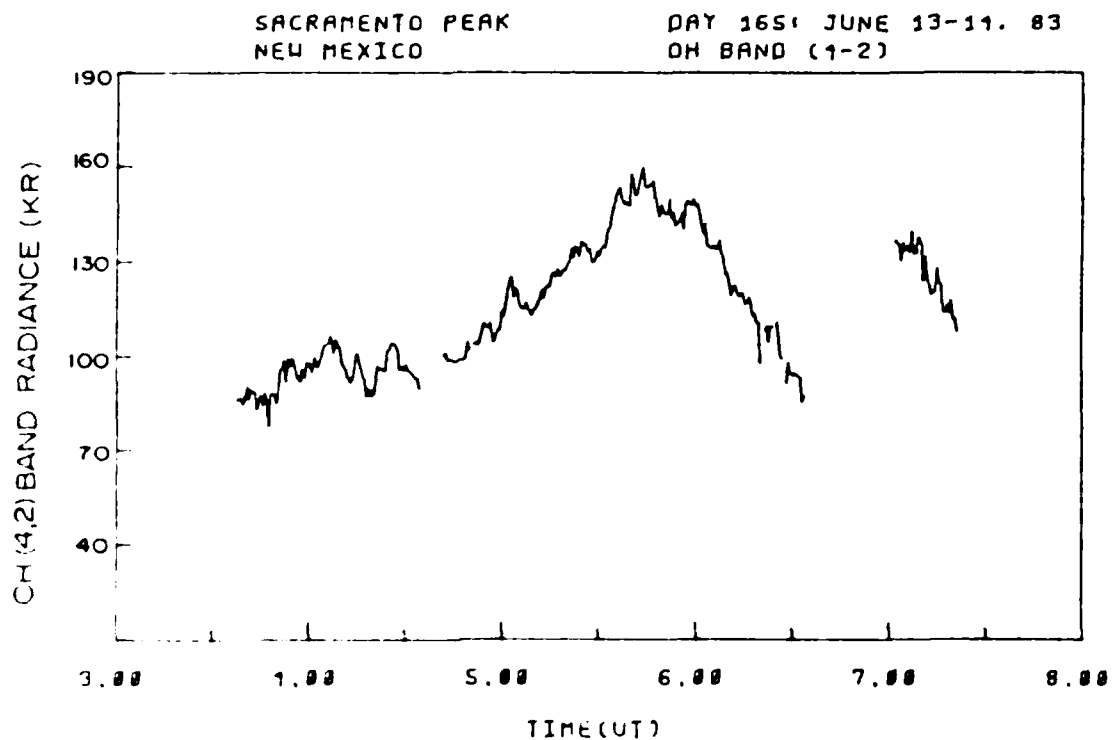


Figure C-1. OH (4,2) band radiance and standard deviation, viewing angle = zenith, day 165, 3:30-7:30 hrs. UT.

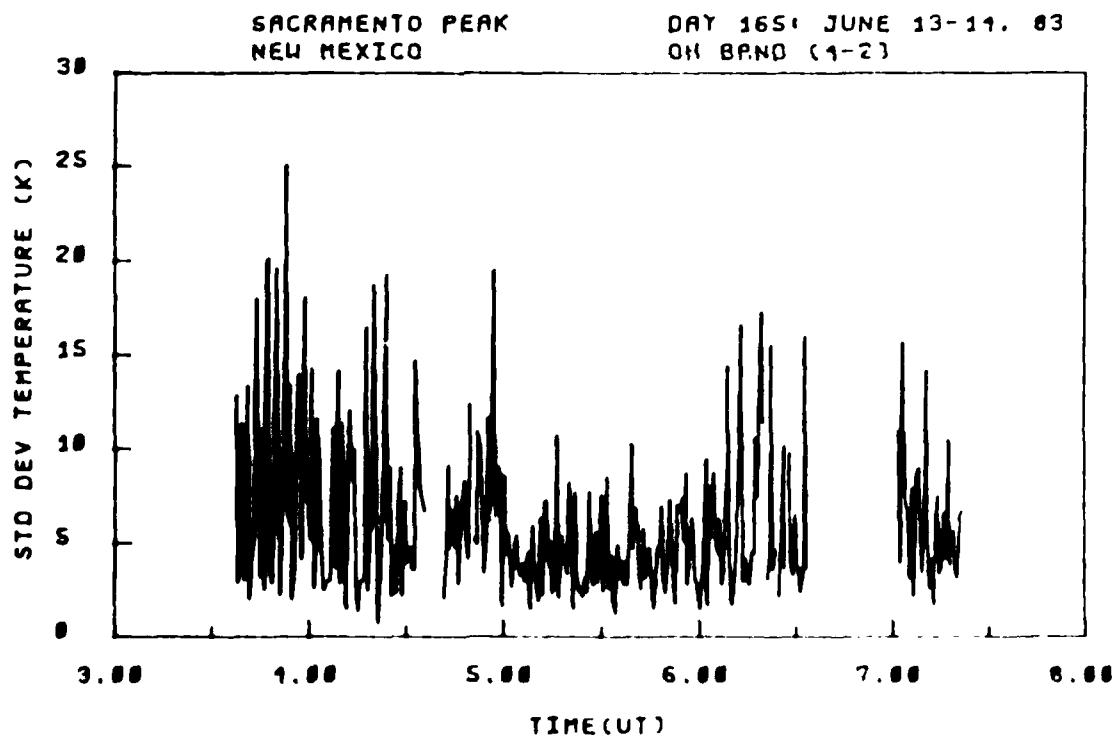
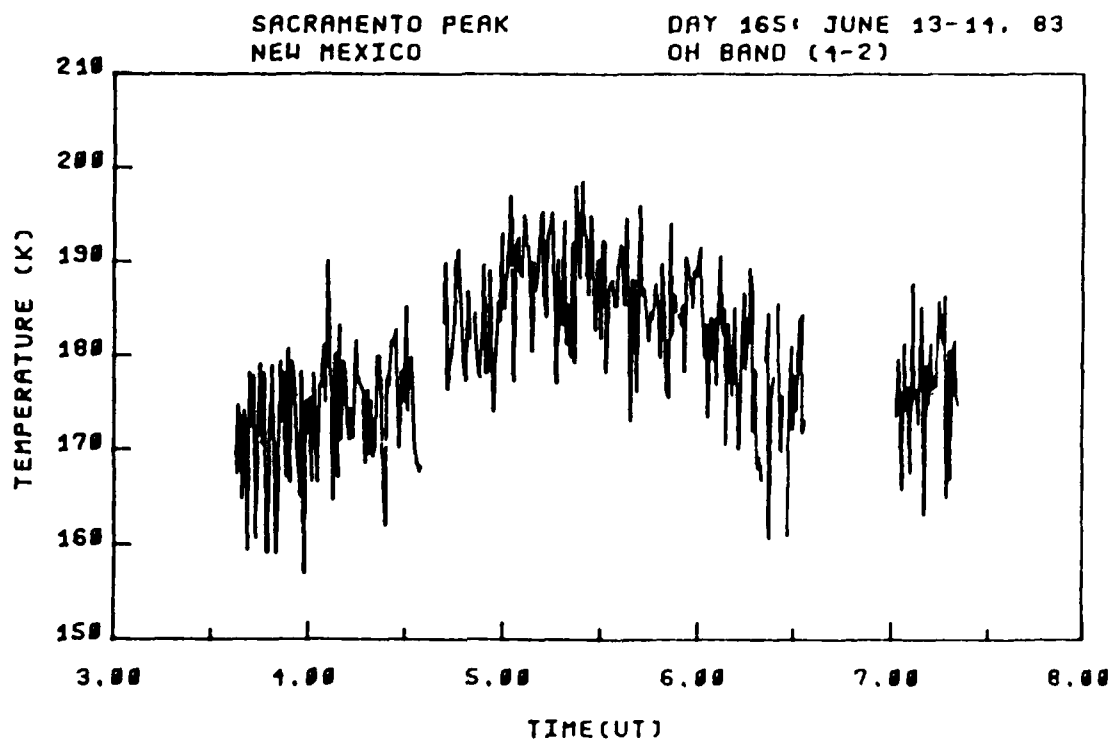


Figure C-2. OH (4,2) band rotational temperature and standard deviation, viewing angle = zenith, day 165, 3:30 7:30 hrs. UT.

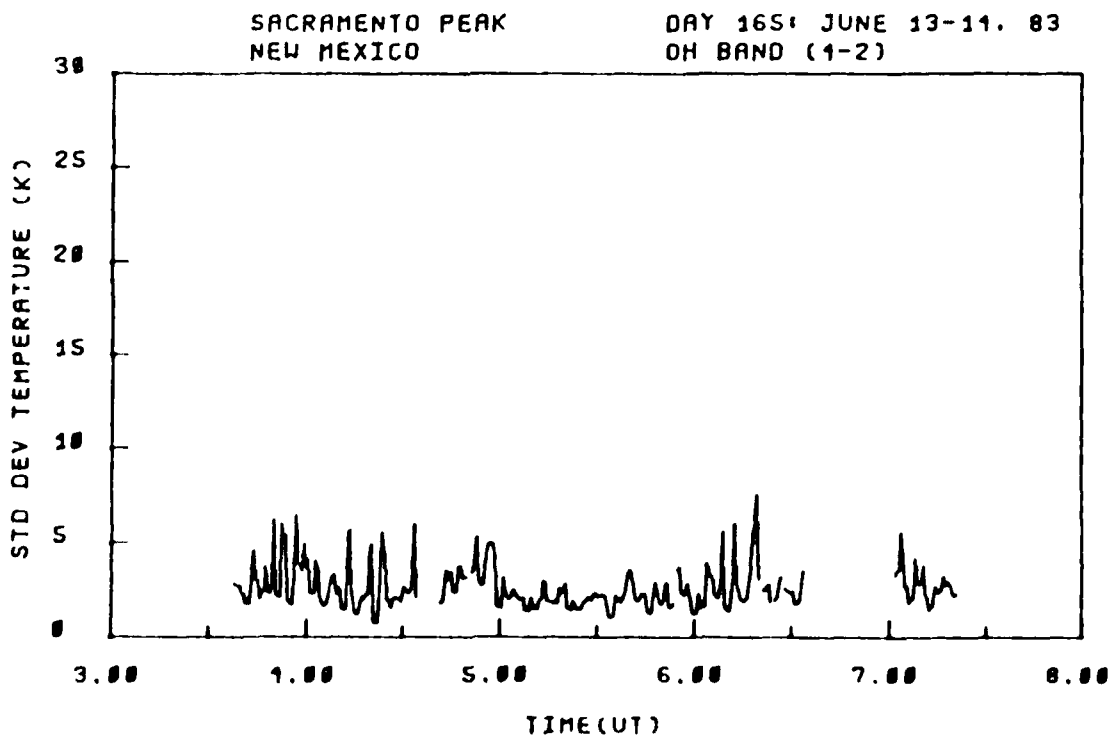
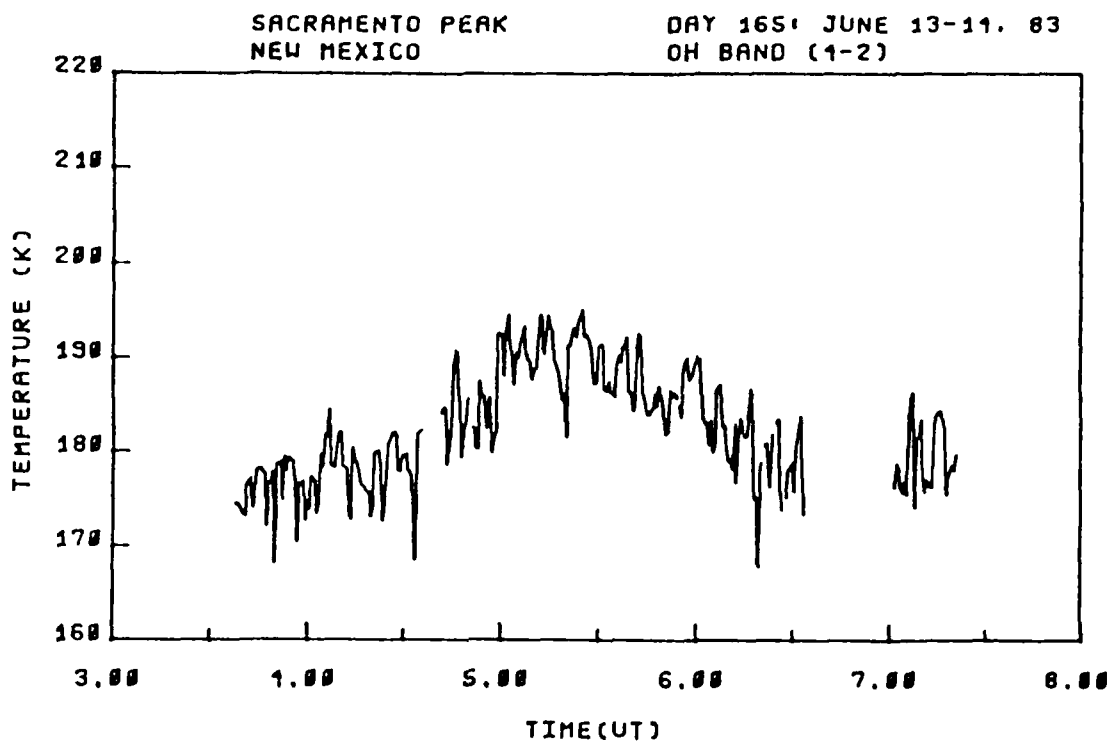


Figure C-3. OH (4,2) band smoothed rotational temperature and standard deviation, viewing angle = zenith, day 165, 3:30-7:30 hrs. UT.

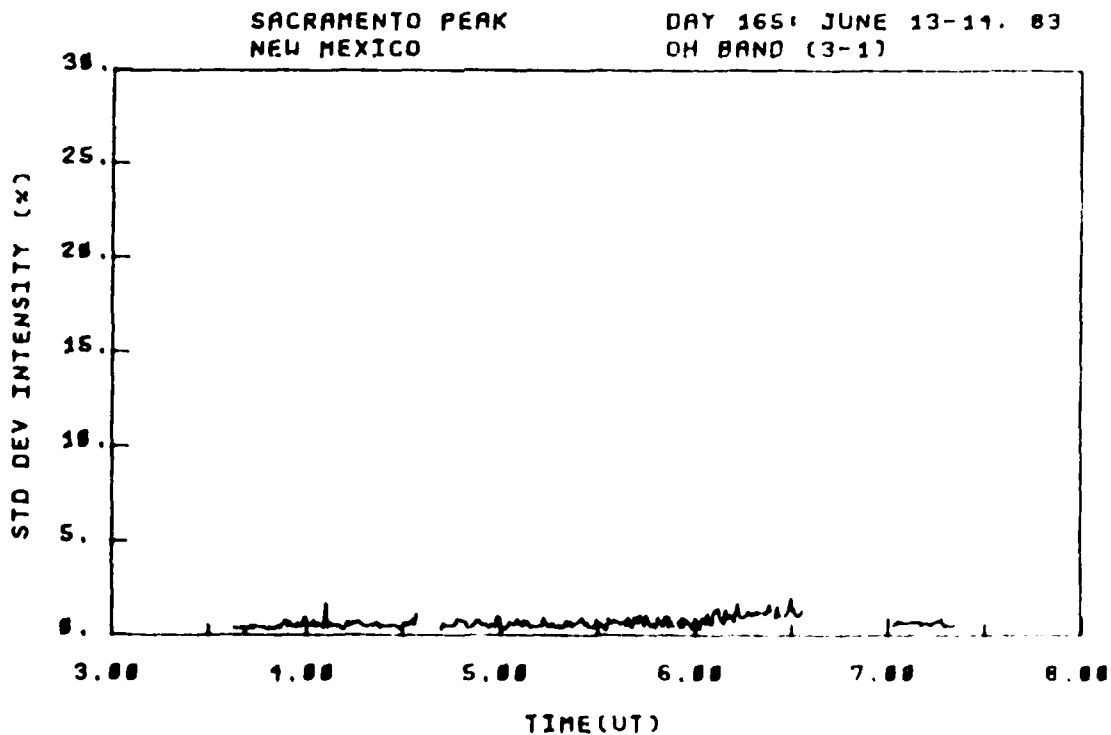
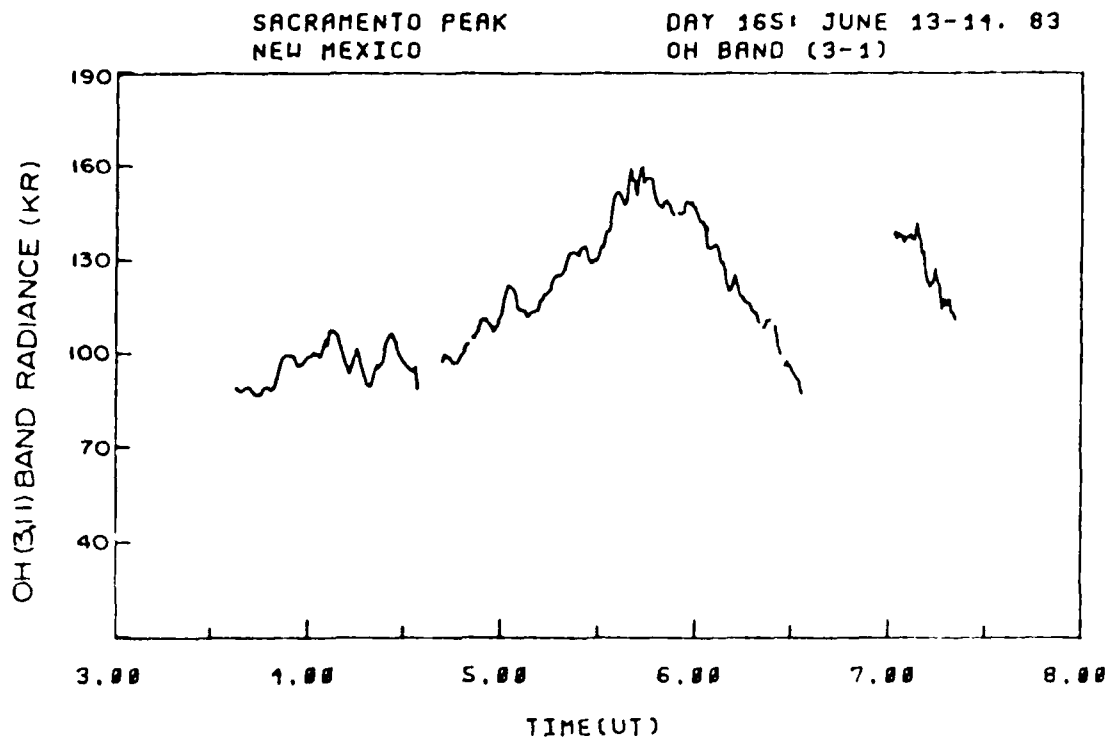


Figure C-4. OH (3,1) band radiance and standard deviation, viewing angle = zenith, day 165, 3:30-7:30 hrs. UT.

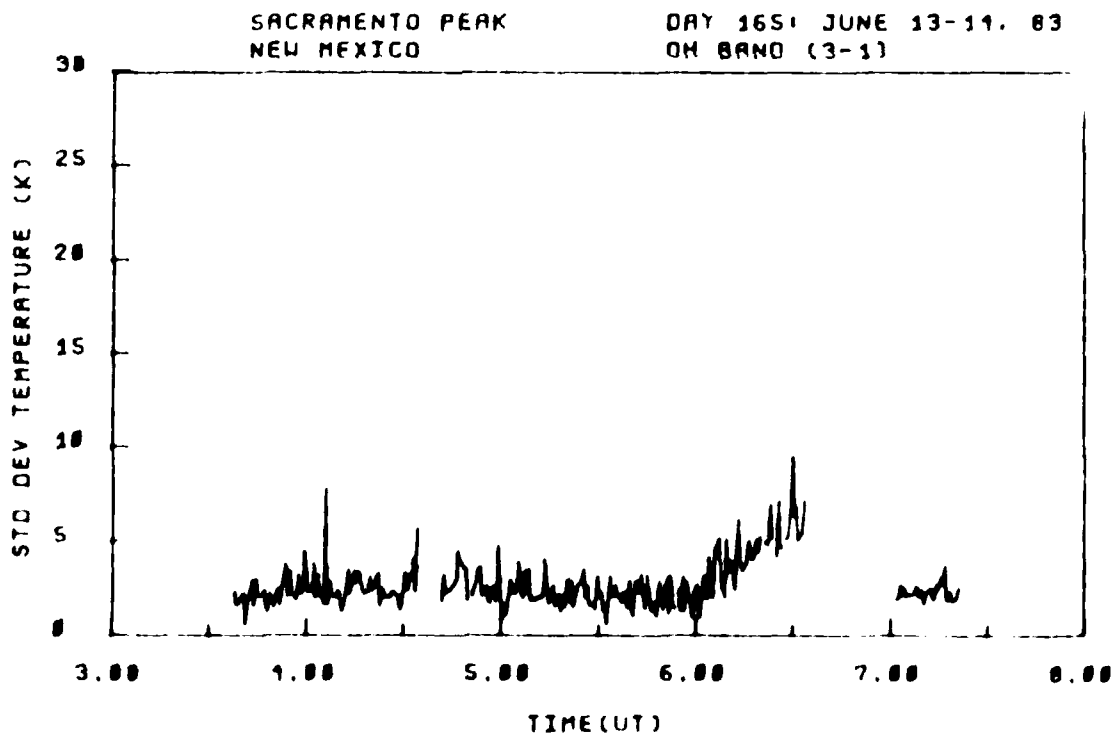
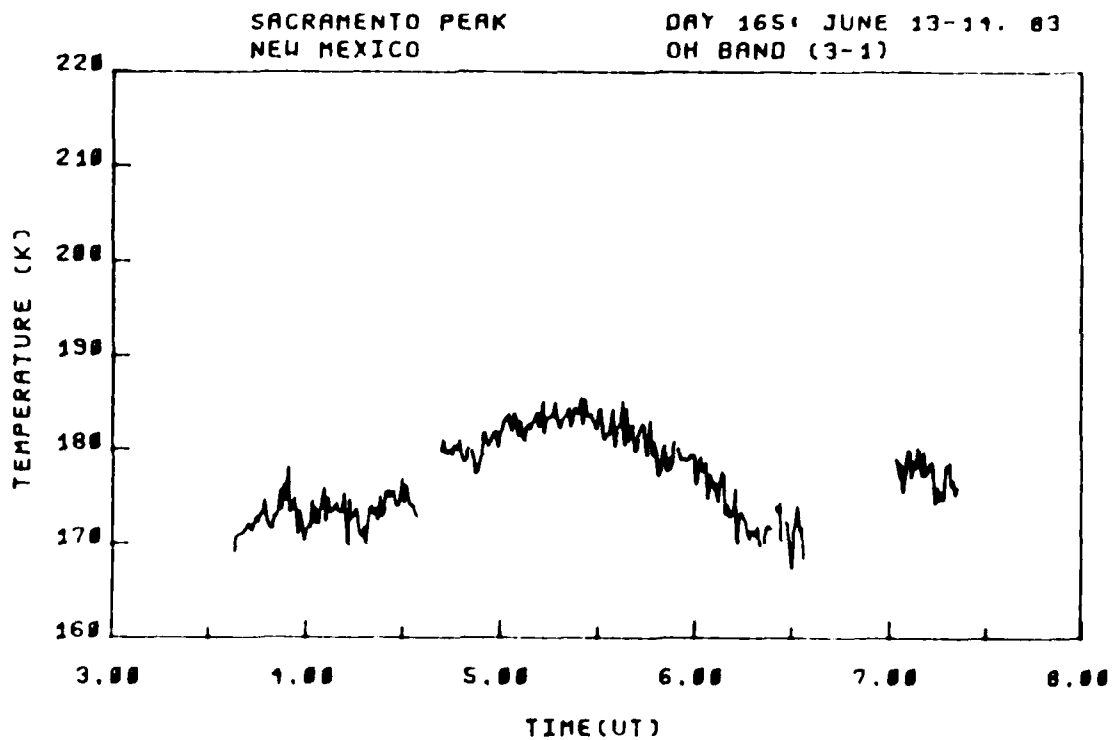


Figure C-5. OH (3,1) band rotational temperature and standard deviation, viewing angle = zenith, day 165, 3:30-7:30 hrs. UT.

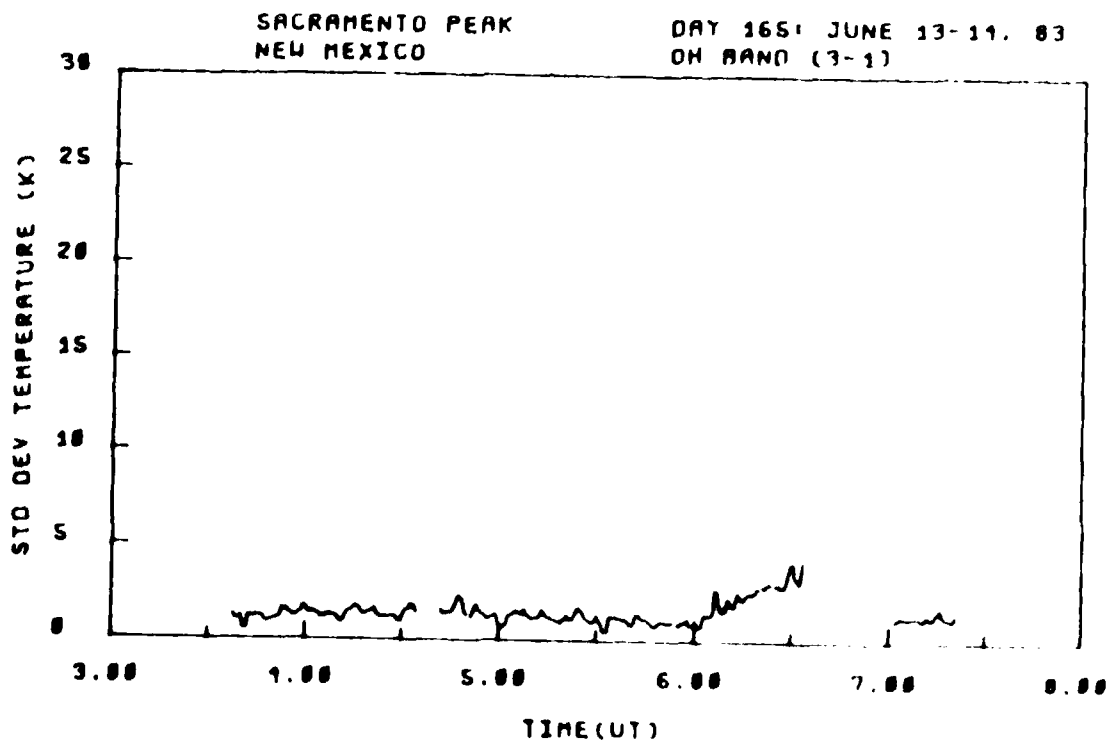
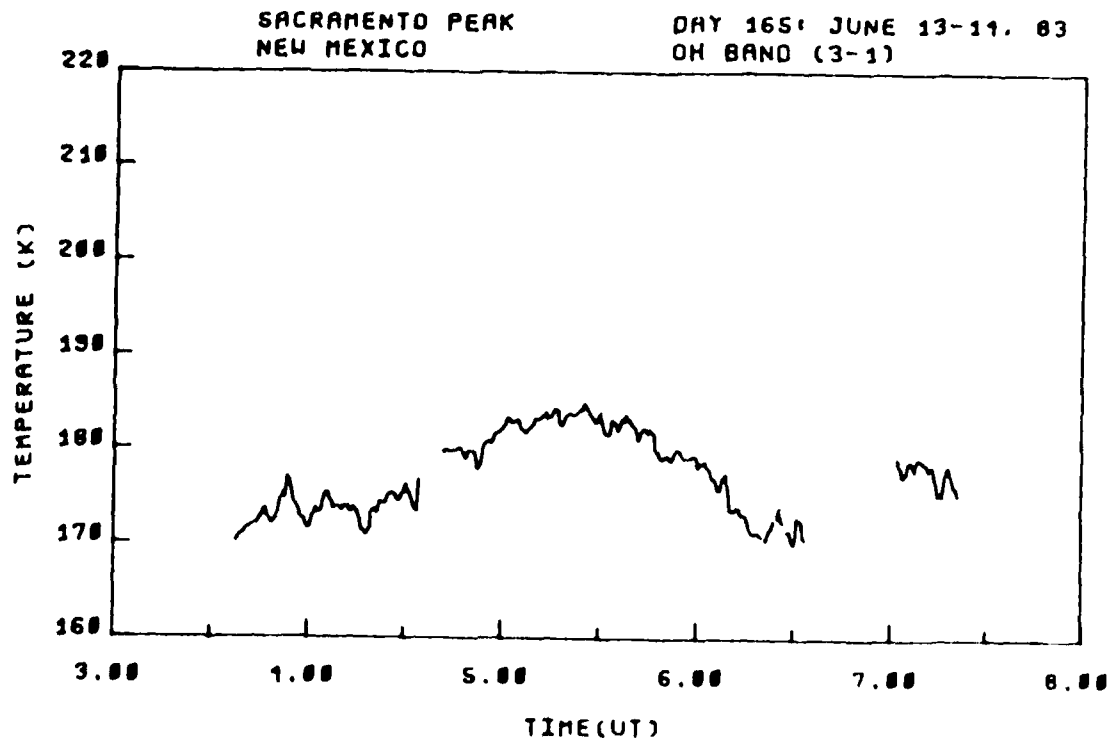


Figure C-6. OH (3,1) band smoothed rotational temperature and standard deviation, viewing angle = zenith, day 165, 3:30-7:30 hrs. UT.

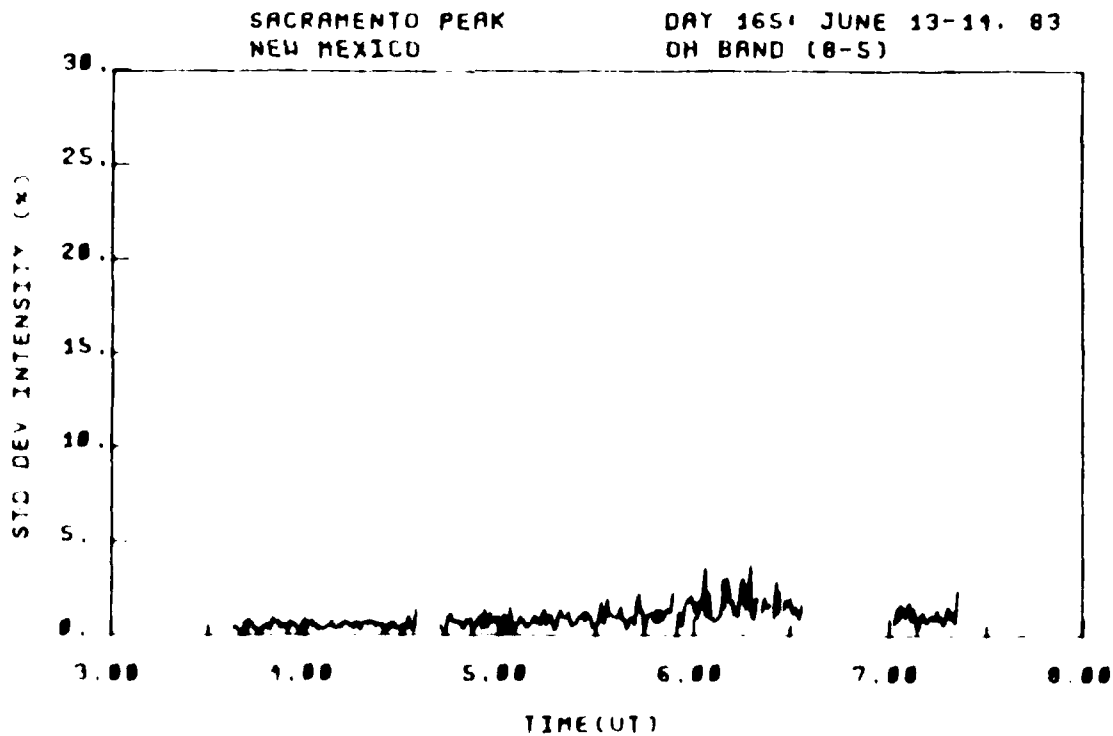
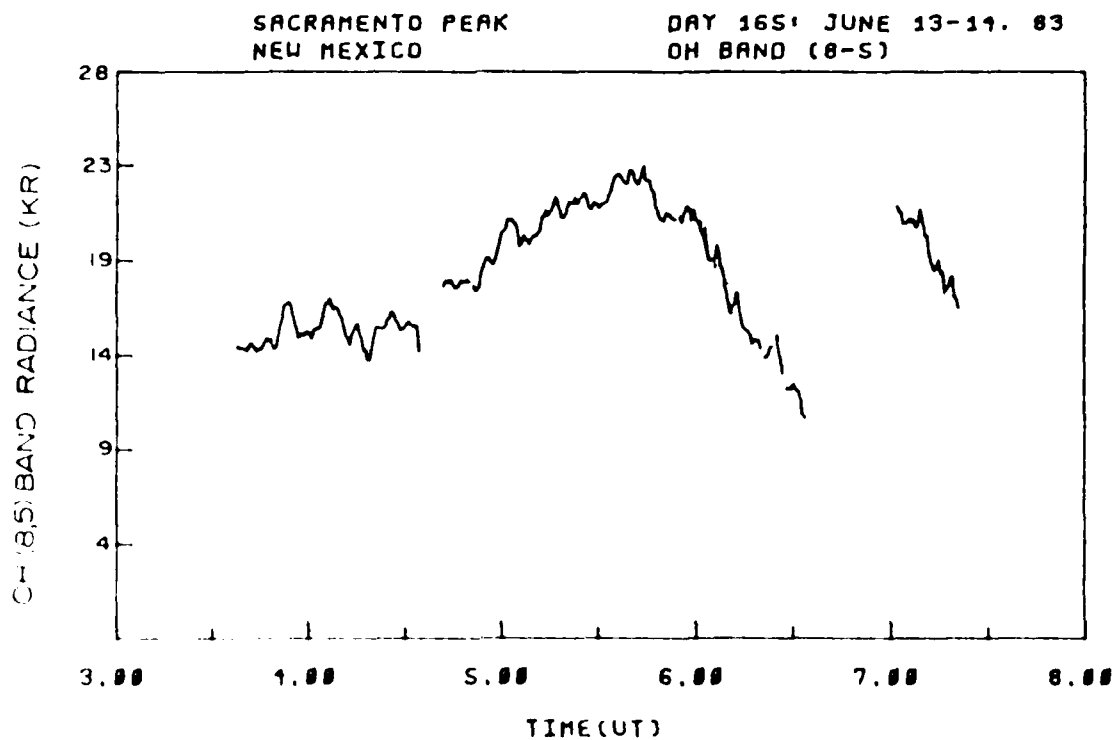


Figure C-7. OH (8,5) band radiance and standard deviation, viewing angle = zenith, day 165, 3:30-7:30 hrs. UT.

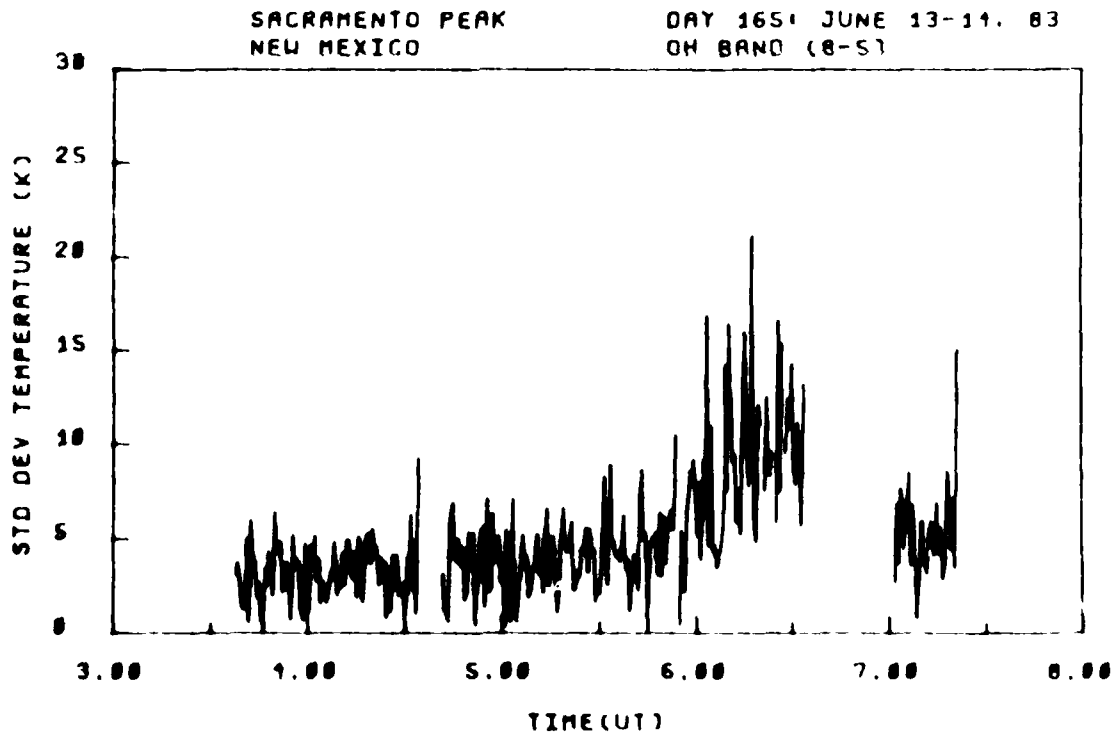
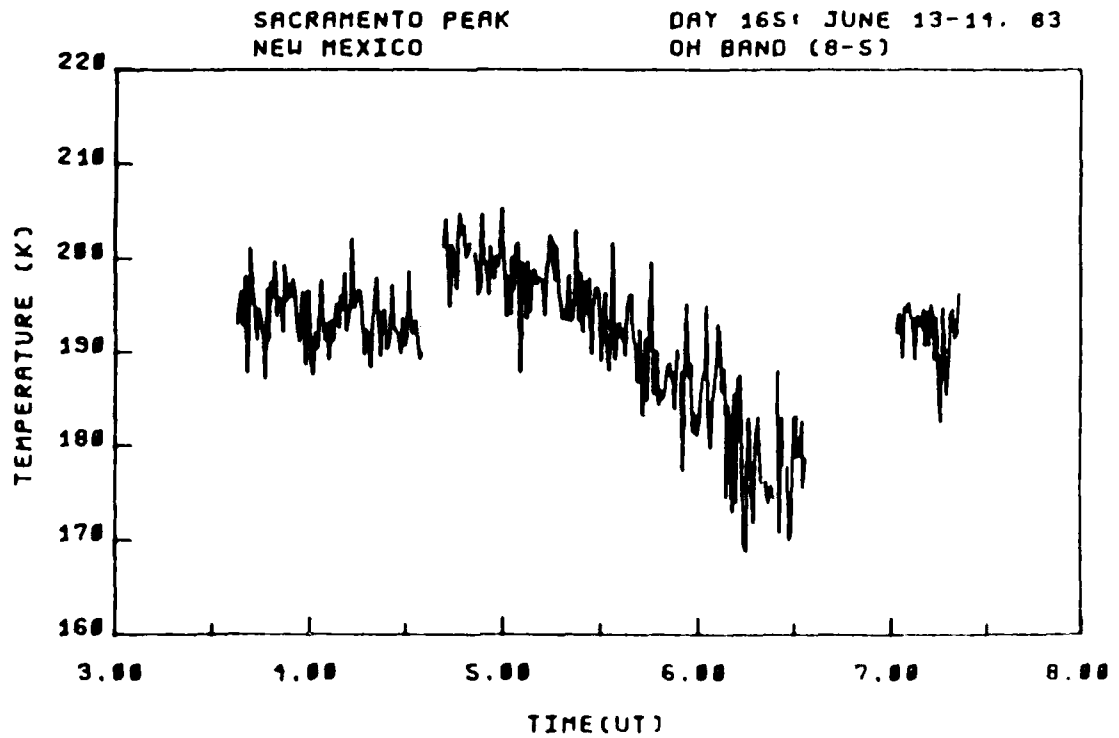


Figure C-8. OH (8,5) band rotational temperature and standard deviation, viewing angle = zenith, day 165, 3:30-7:30 hrs. UT.

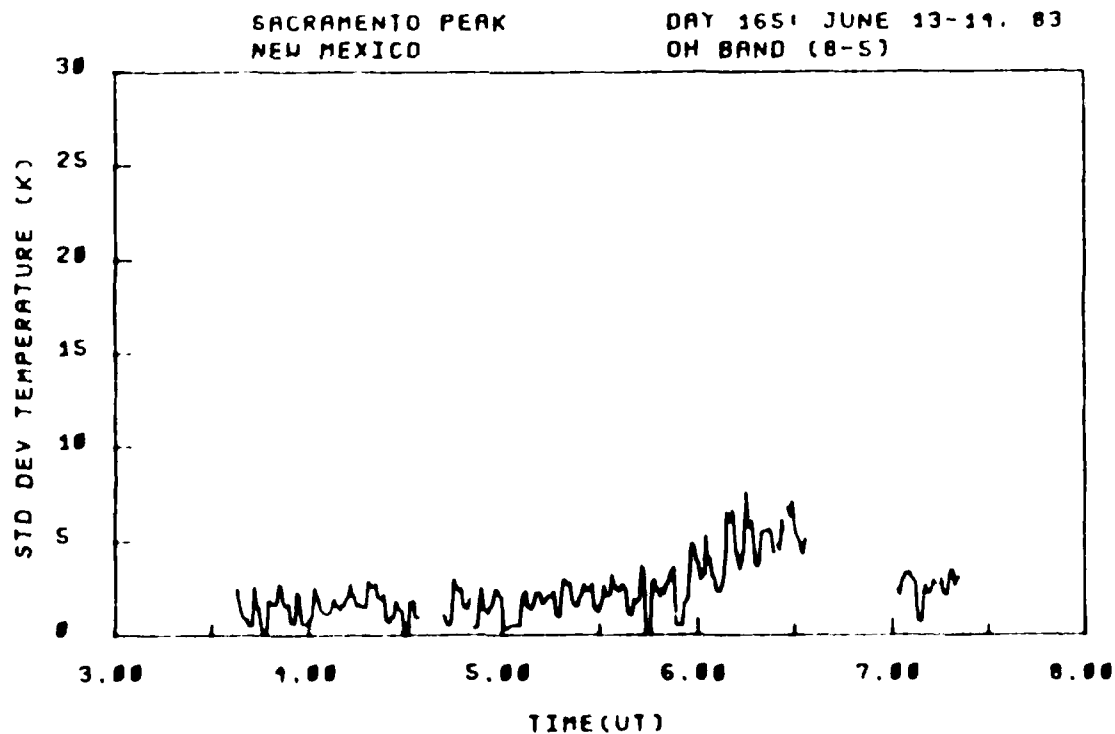
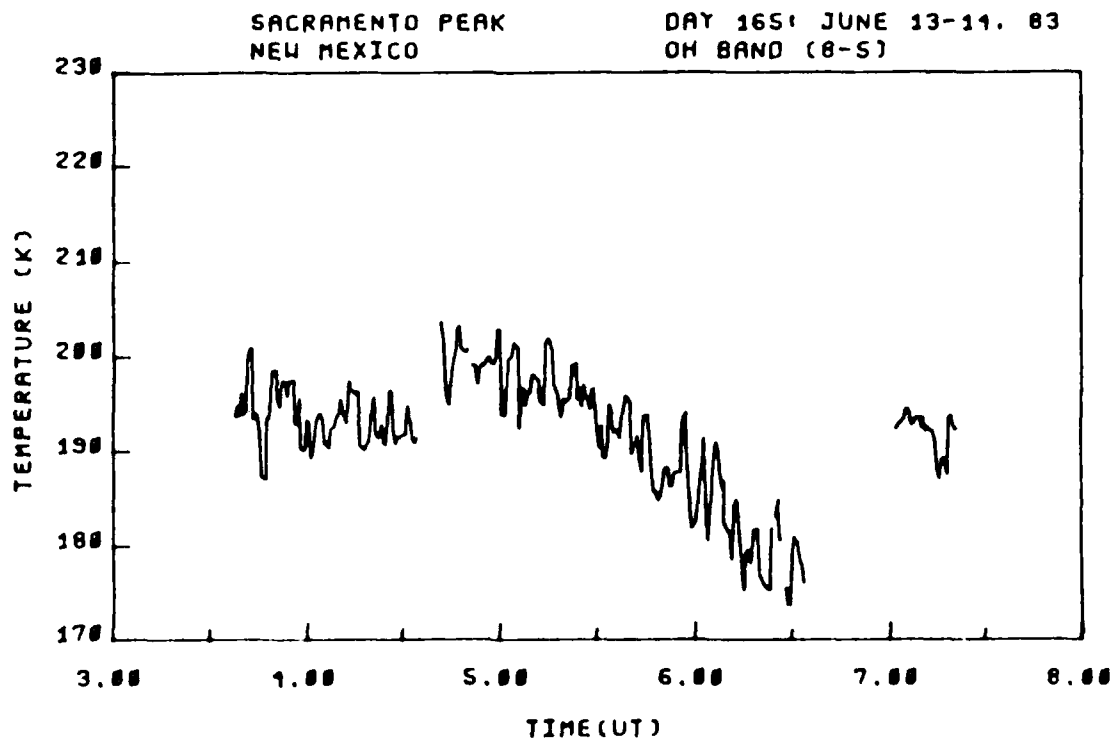


Figure C-9. OH (8,5) band smoothed rotational temperature and standard deviation, viewing angle = zenith, day 165, 3:30-7:30 hrs. UT.

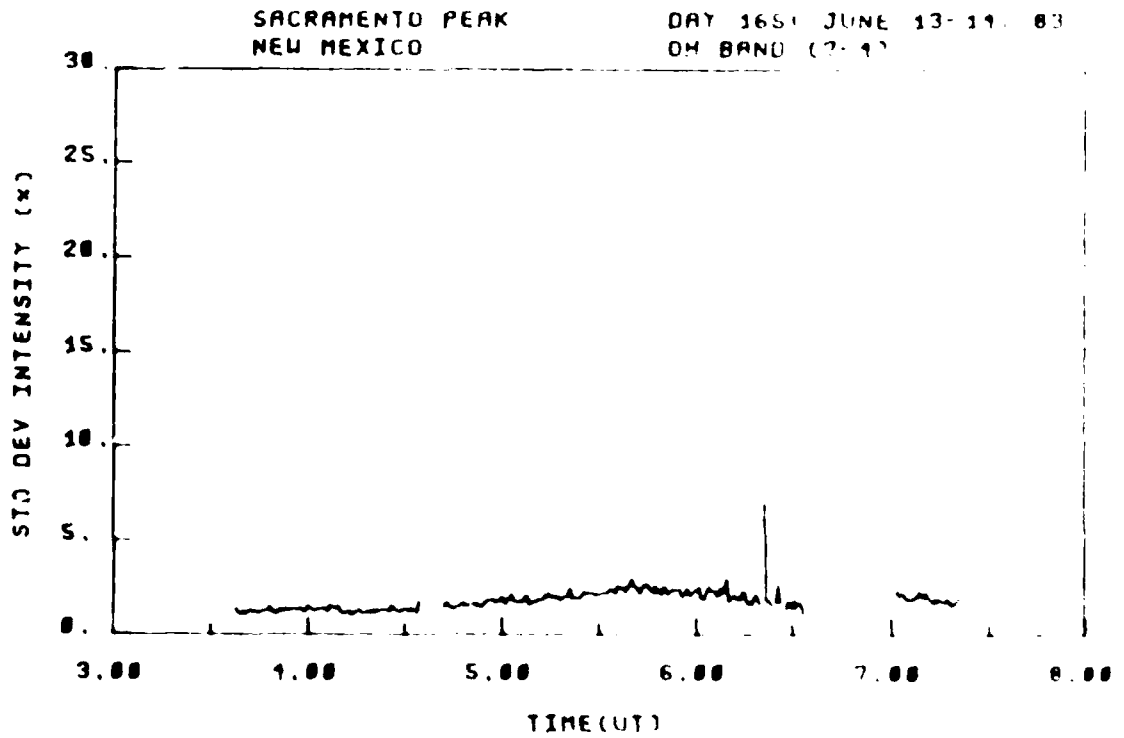
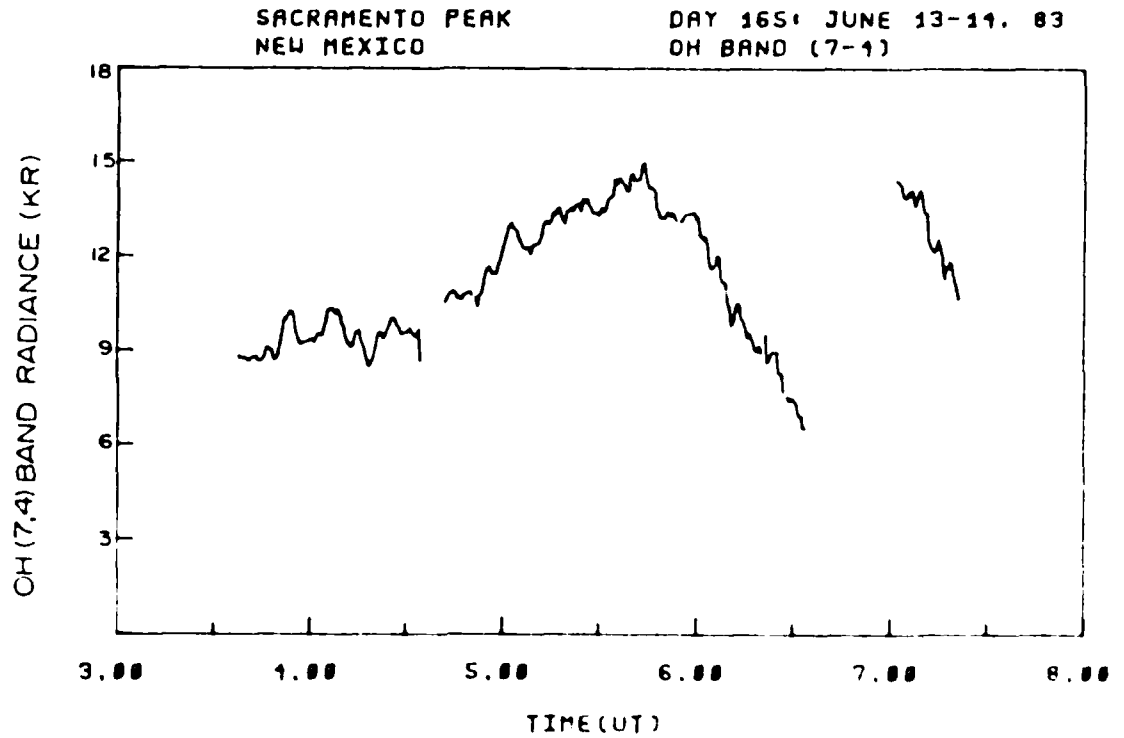


Figure C-10. OH (7,4) band radiance and standard deviation, viewing angle = zenith, day 165, 3:30-7:30 hrs. UT.

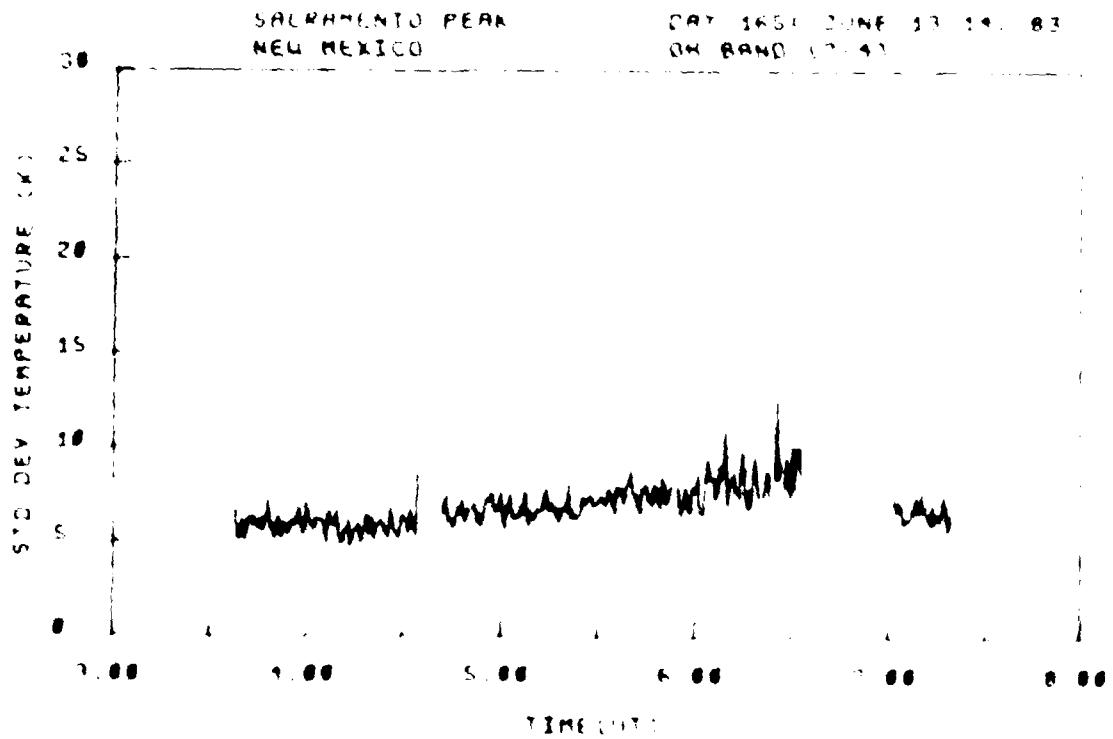
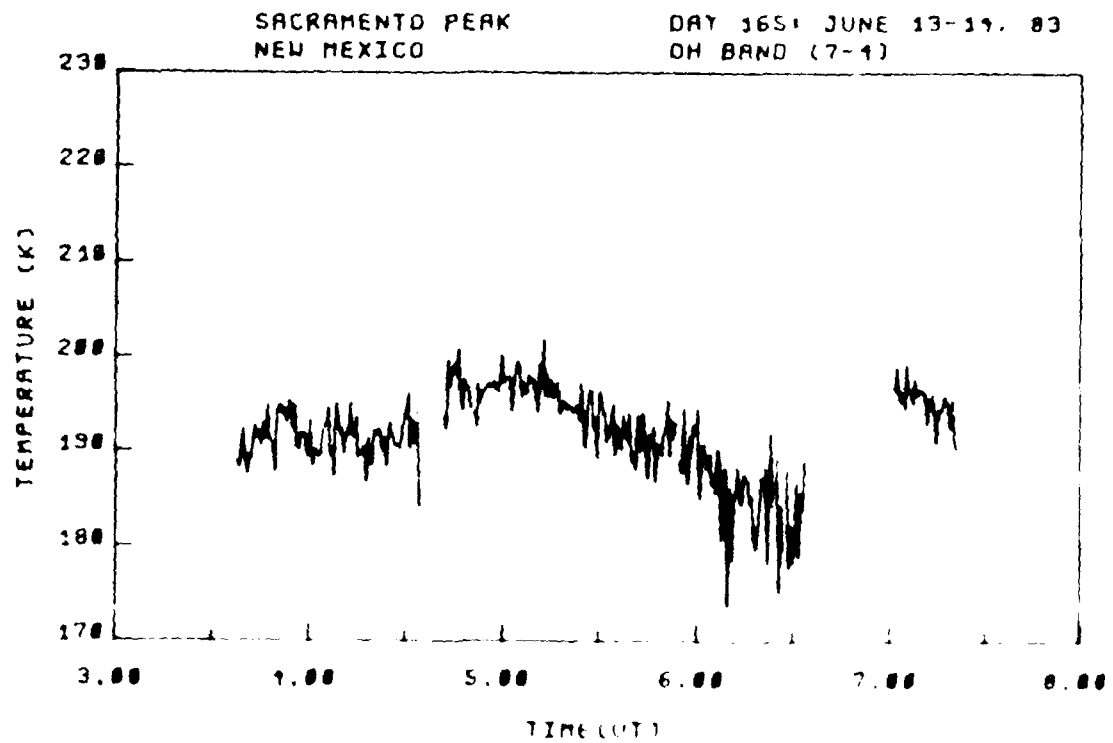


Figure C-11. 700-7.4 μ band rotational temperature and standard deviation. Centered on the zeroth day, 165, 1983. Note the UT.

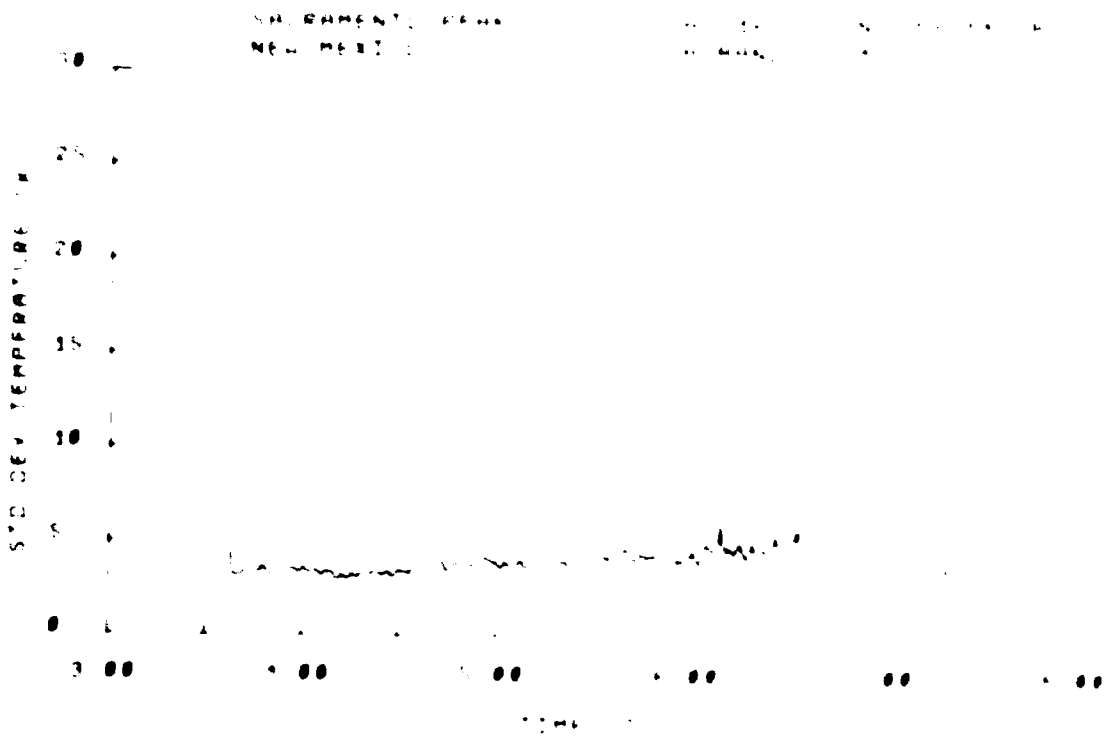
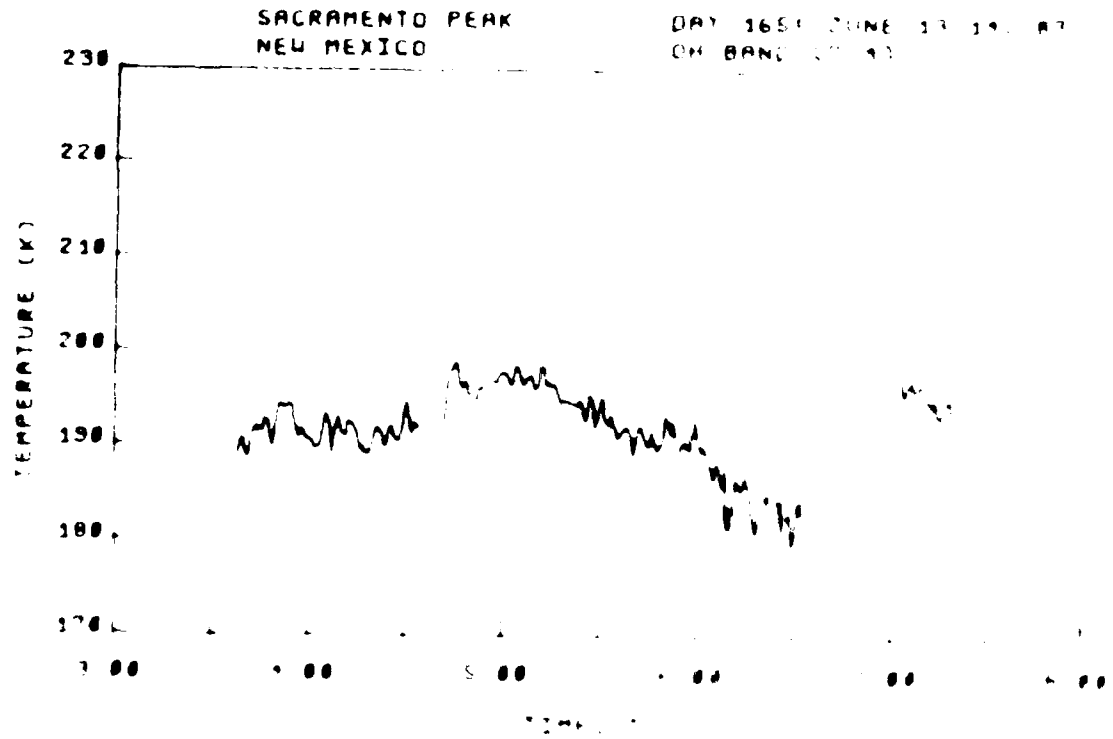
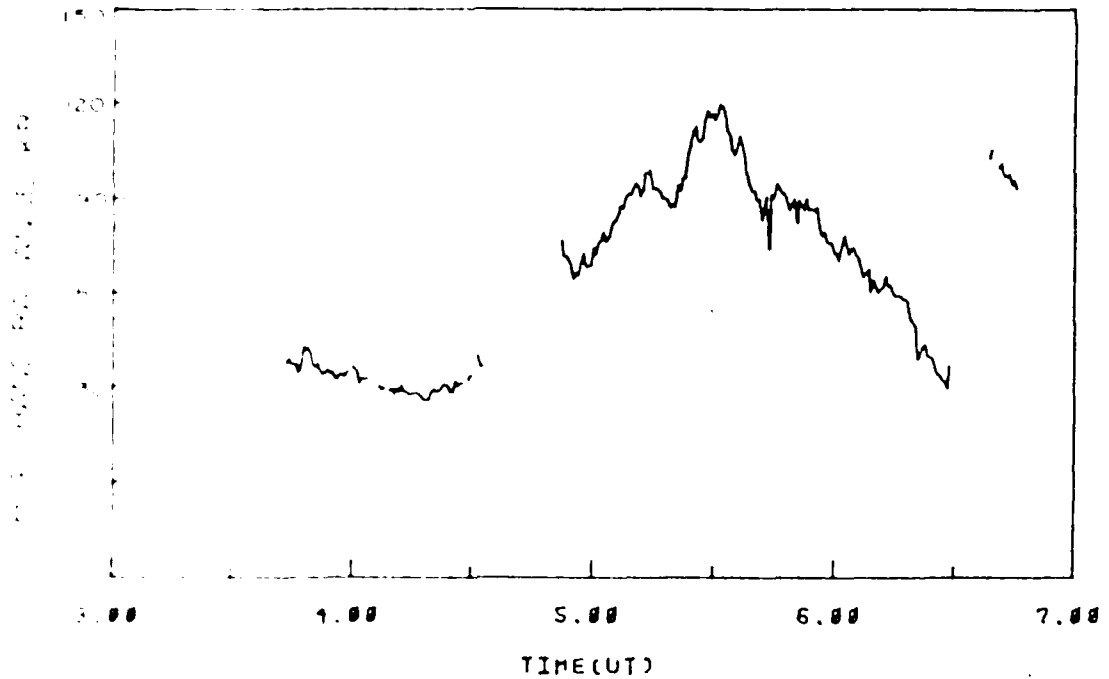


Figure C-12. On 27.93 band, smooth curve of temperature and standard deviation, measured on the Sacramento Peak 1967-1968.

SACRAMENTO PEAK
NEW MEXICO

DAY 166: JUNE 11-15, 83
OH BAND (4-2)



SACRAMENTO PEAK
NEW MEXICO

DAY 166: JUNE 11-15, 83
OH BAND (4-2)

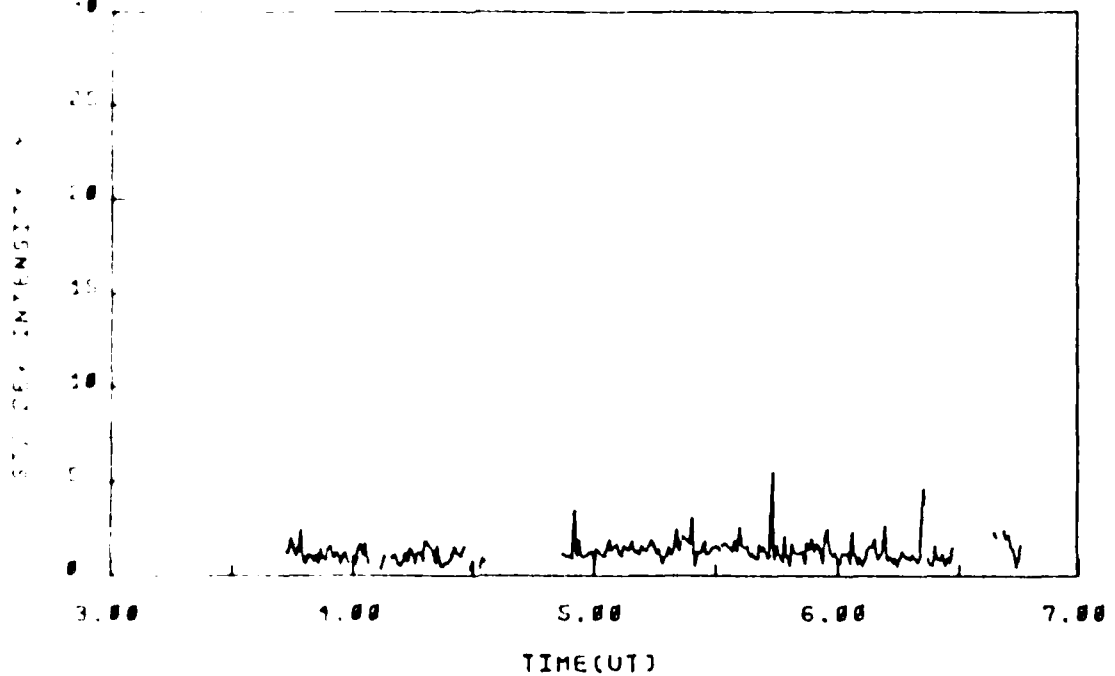


Figure C. 13. OH (4,2) band radiance and standard deviation, viewing angle = zenith, day 166, 3:30-6:45 hrs. UT.

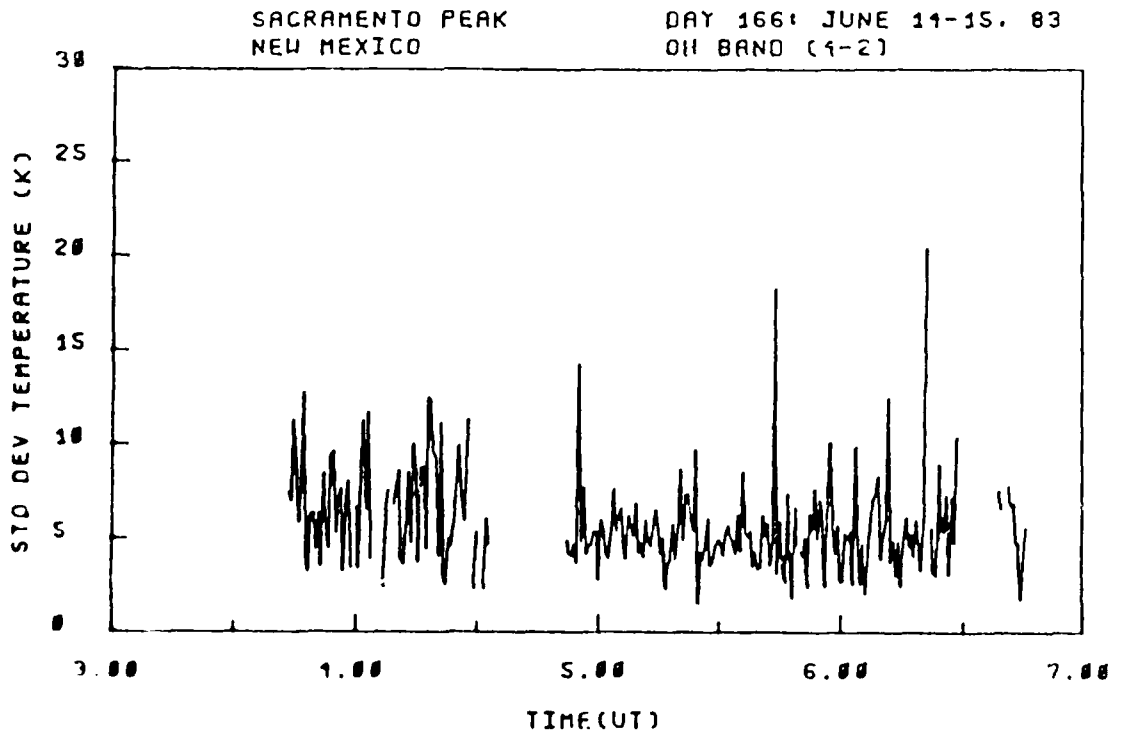
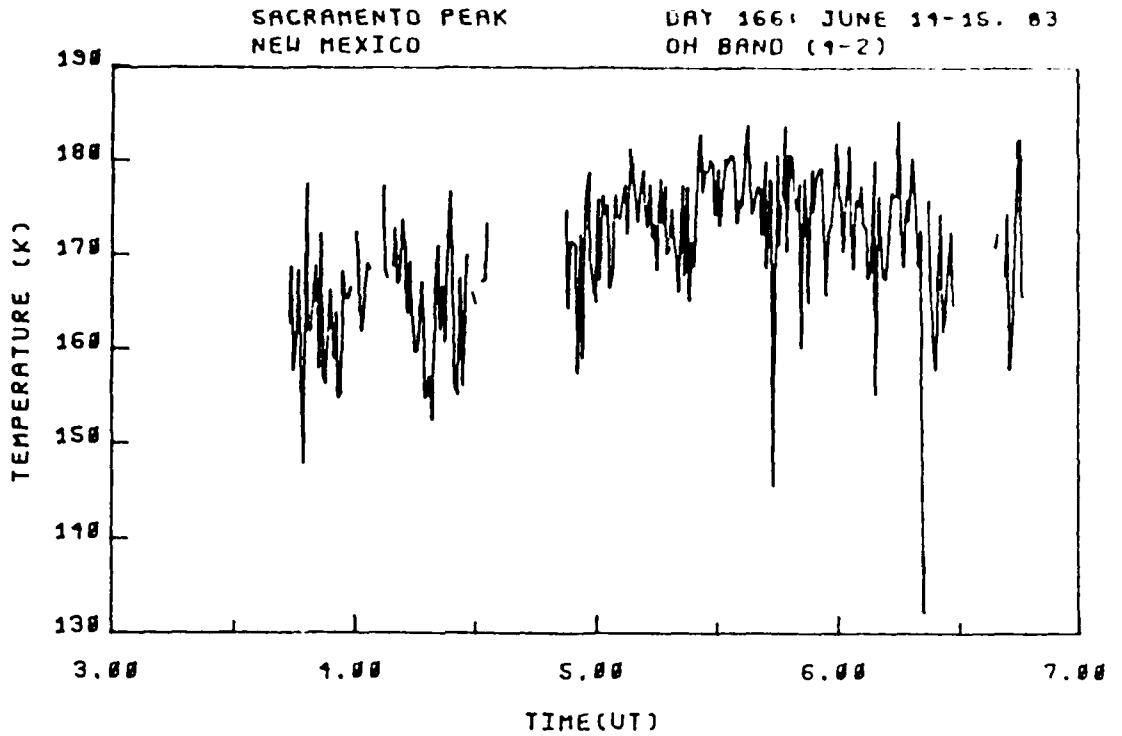


Figure 14. OH (4,2) band rotational temperature and standard deviation, viewing angle = zenith, day 166, 3:30-7:00 UT.

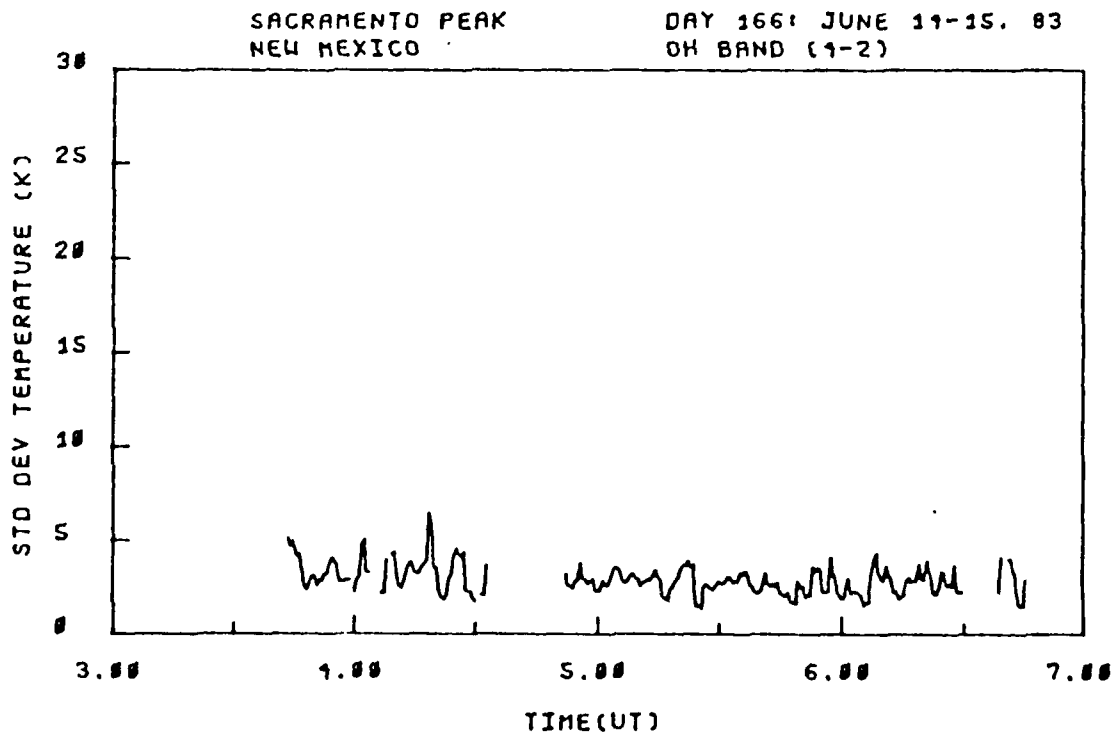
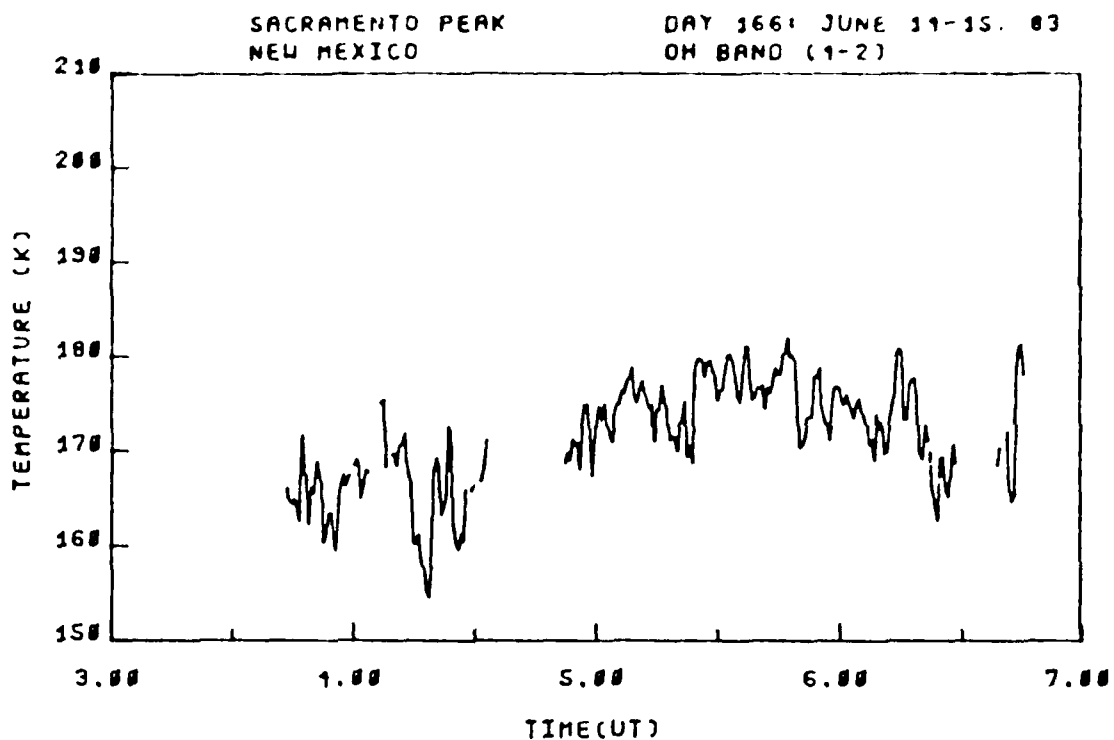


Figure C-15. OH (4,2) band smoothed rotational temperature and standard deviation, viewing angle = zenith, day 166, 3:30-6:45 hrs. UT.

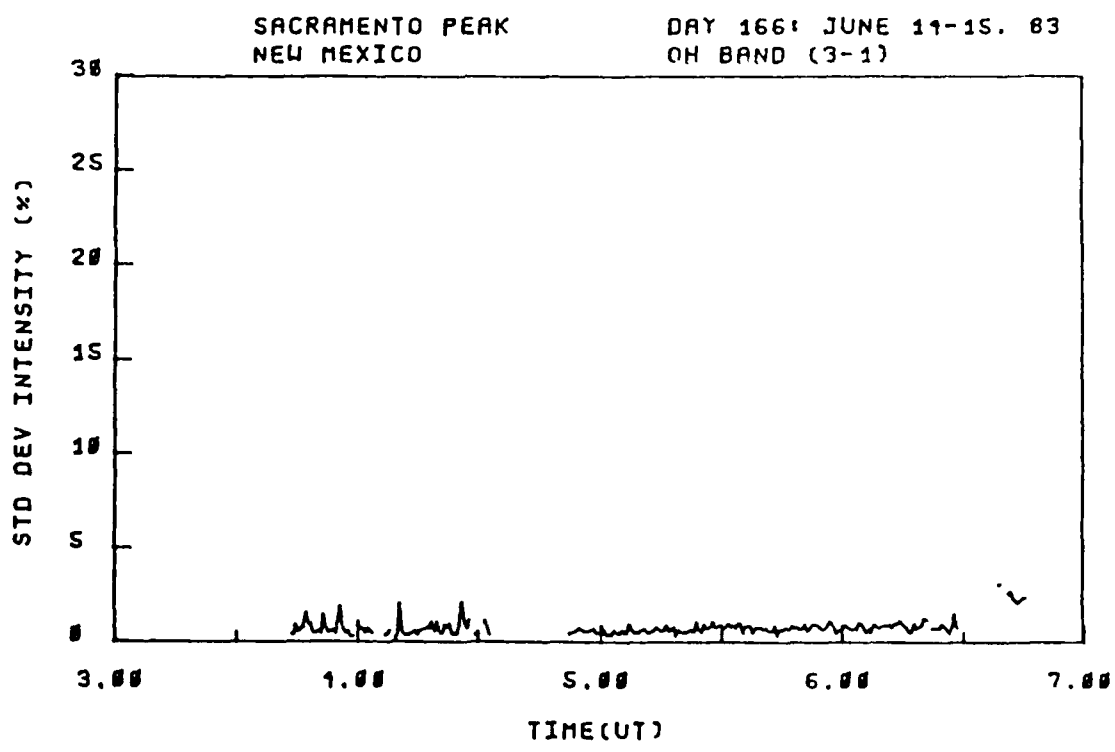
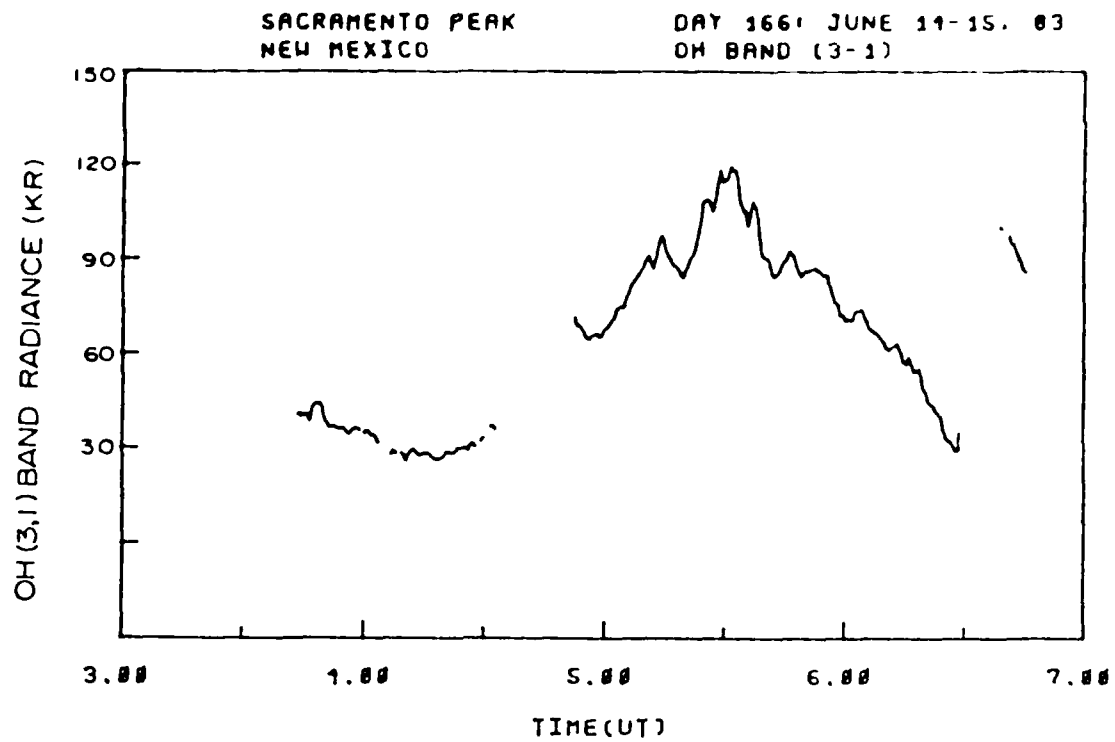


Figure C-16. OH (3,1) band radiance and standard deviation, viewing angle = zenith, day 166, 3:30-6:45 hrs. UT.

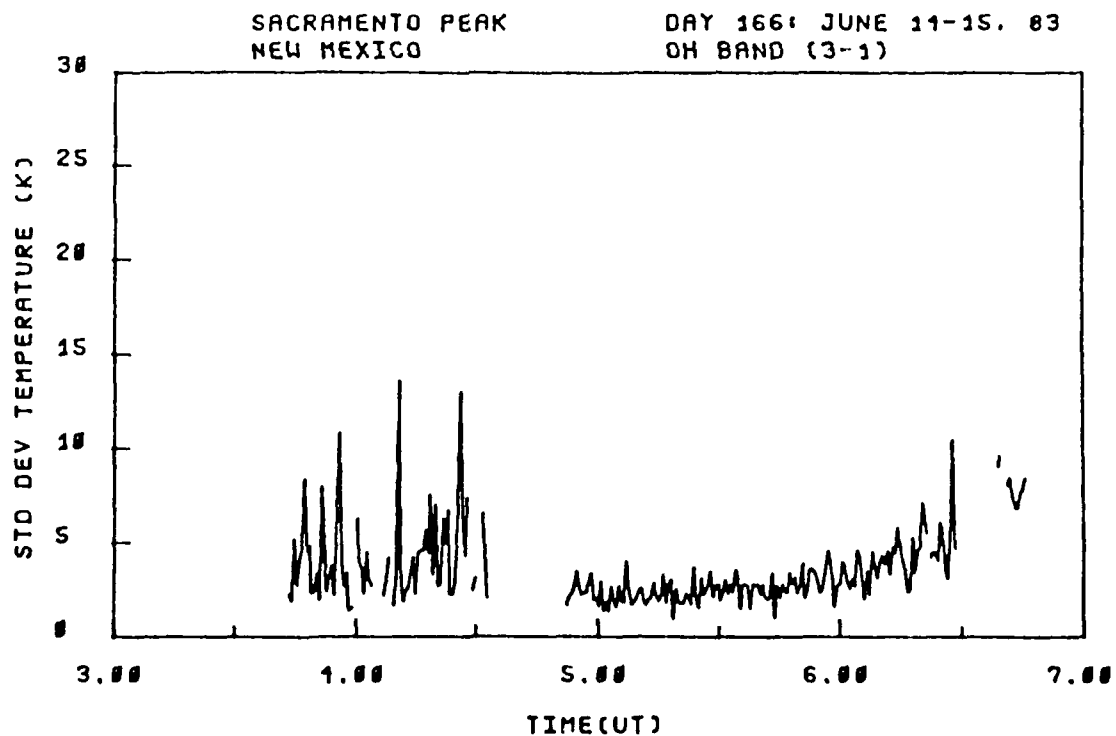
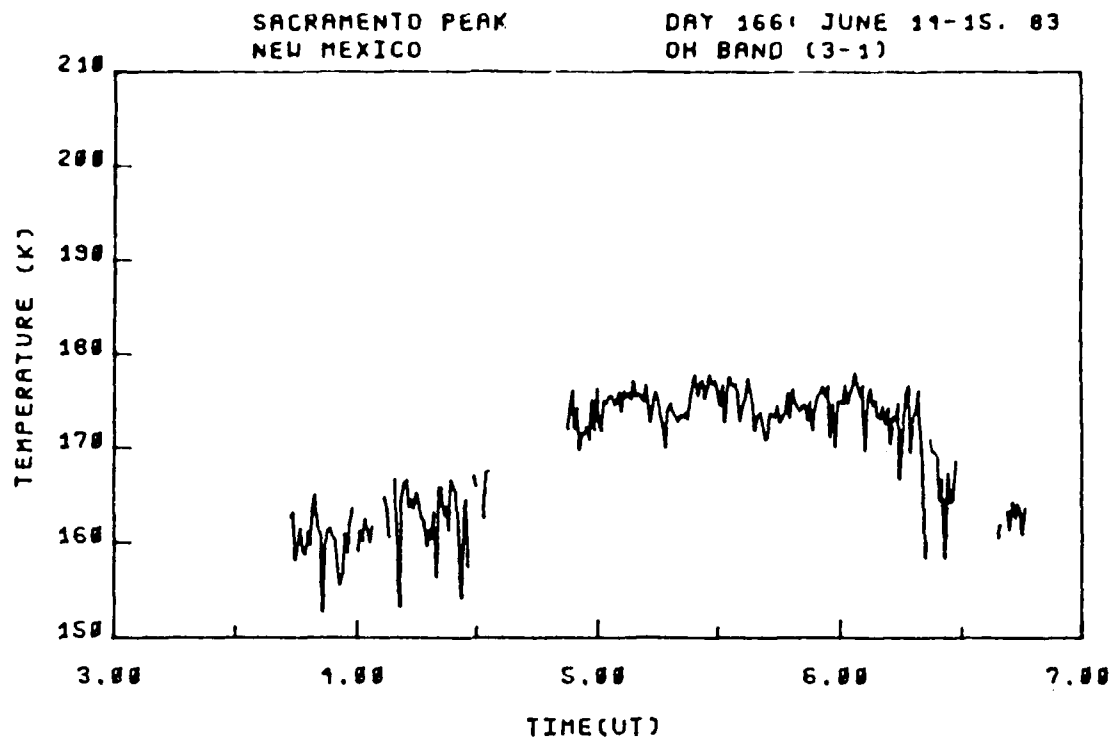


Figure C-17. OH (3,1) band rotational temperature and standard deviation, viewing angle = zenith, day 166, 3:30-6:45 hrs. UT.

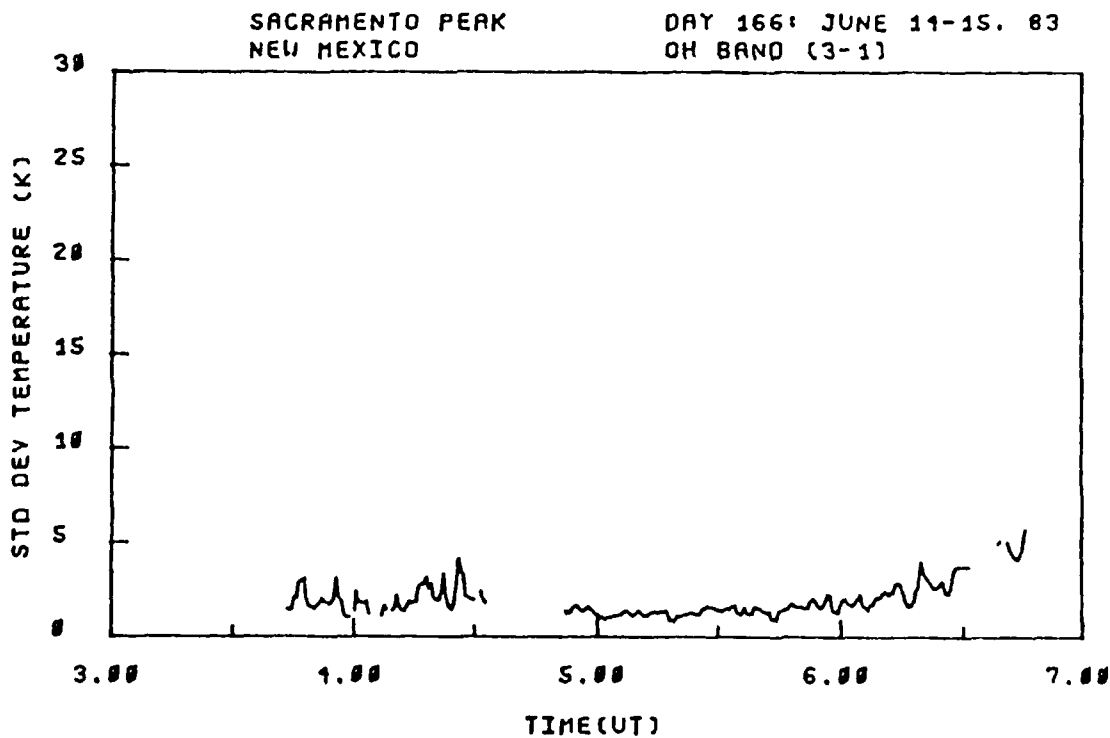
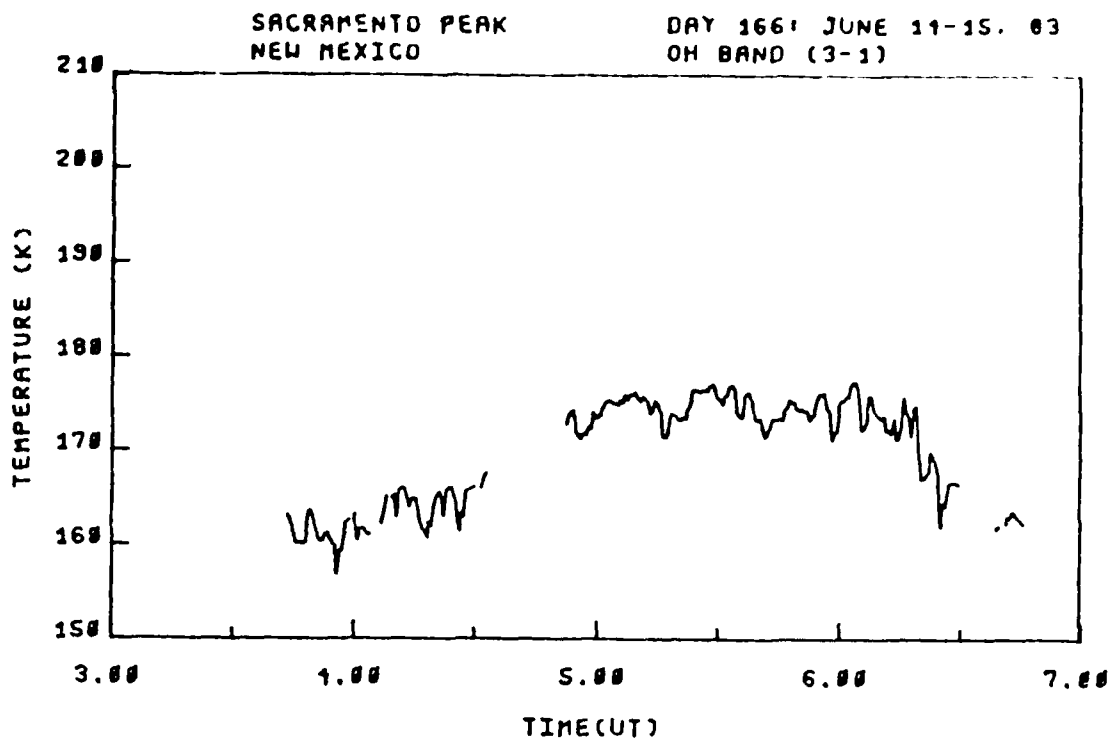


Figure C-18. OH (3,1) band smoothed rotational temperature and standard deviation, viewing angle = zenith, day 166, 3:30-6:45 hrs. UT.

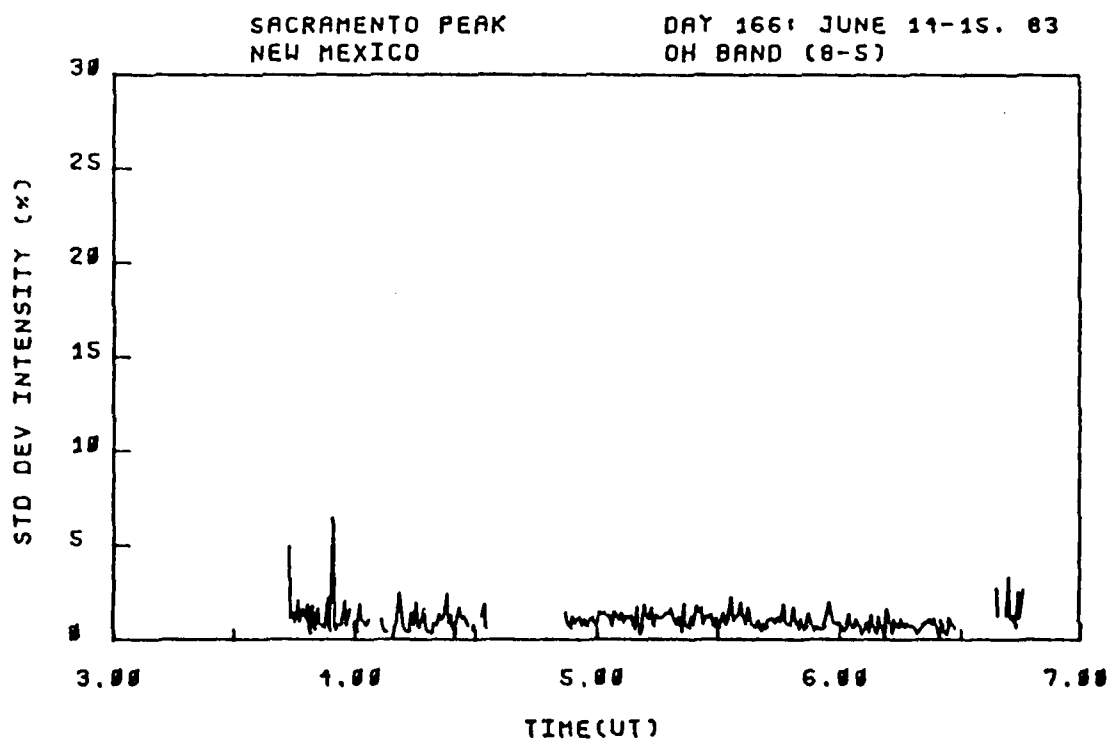
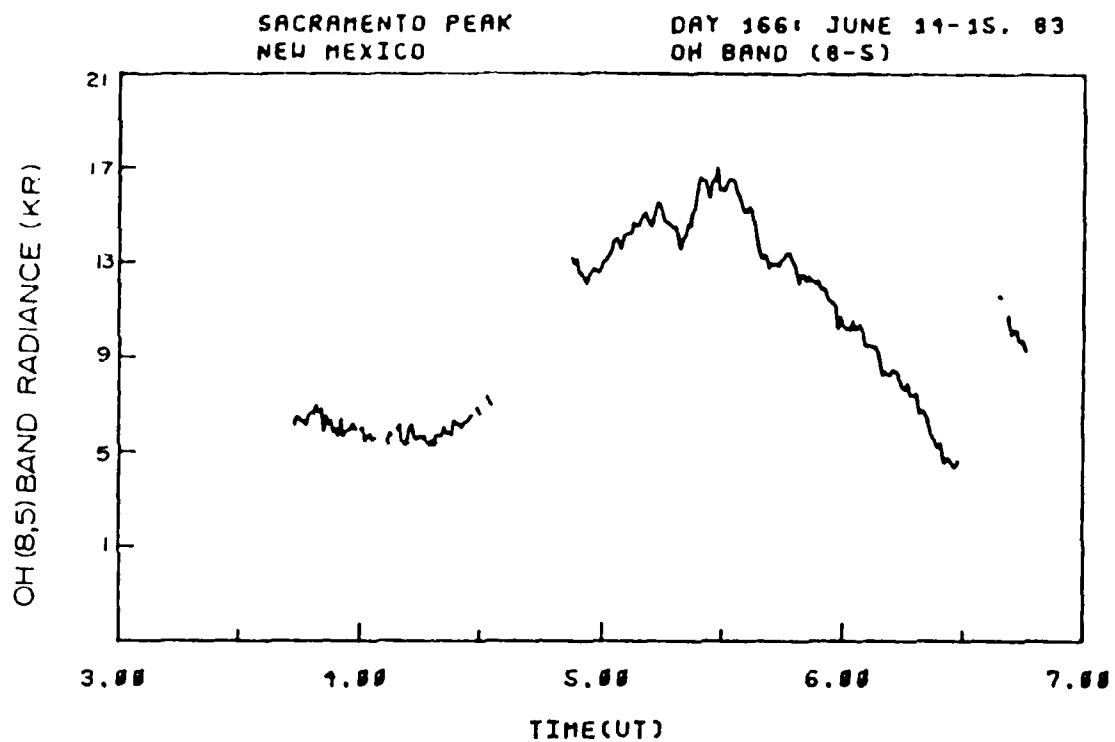


Figure C-19. OH (8,5) band radiance and standard deviation, viewing angle = zenith, day 166, 3:30-6:45 hrs. UT.

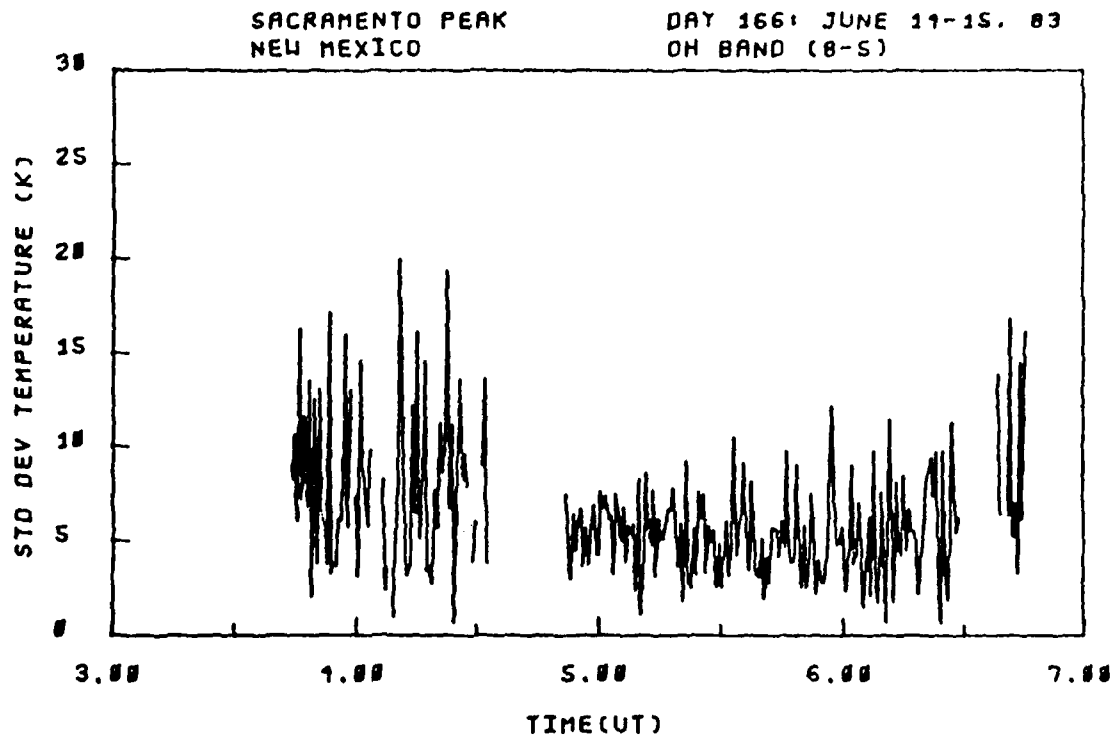
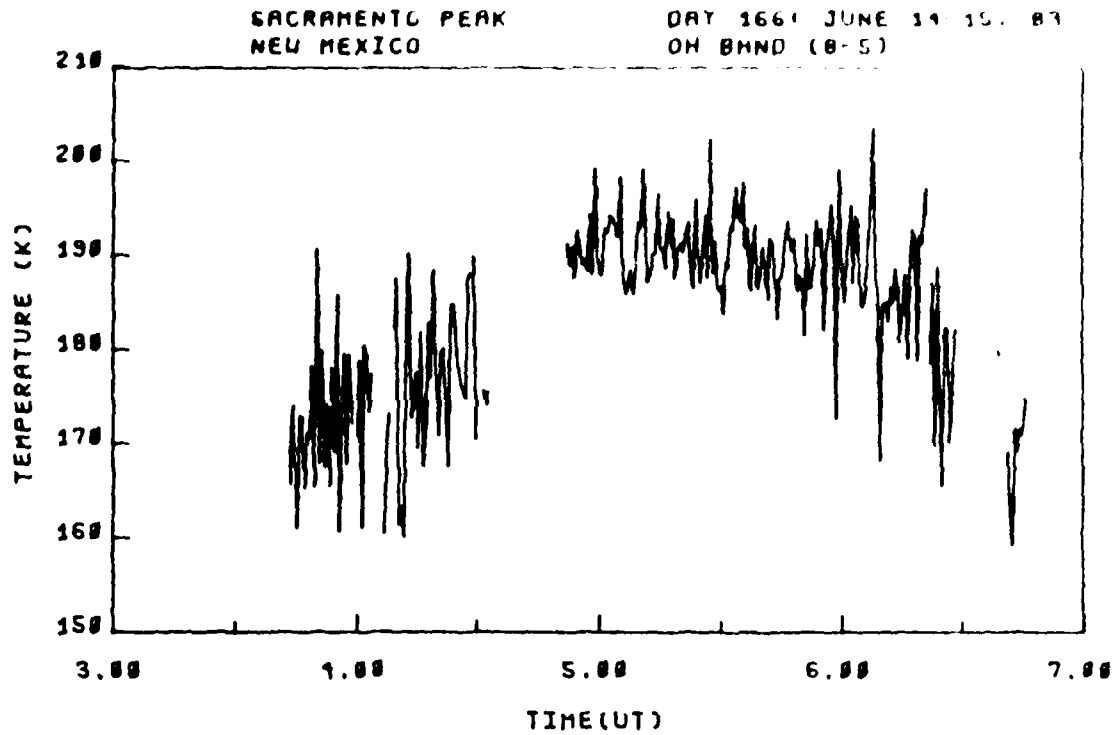


Figure C-20. OH (8,5) band rotational temperature and standard deviation, viewing angle = zenith, day 166, 3:30-6:45 hrs. UT.

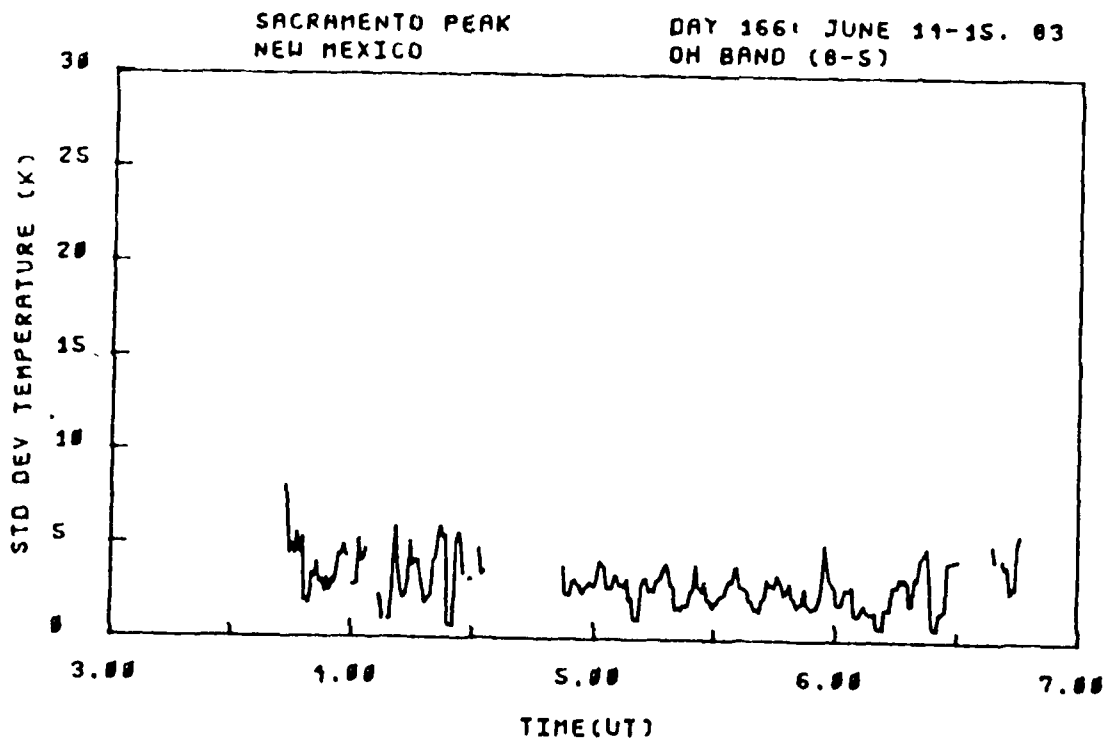
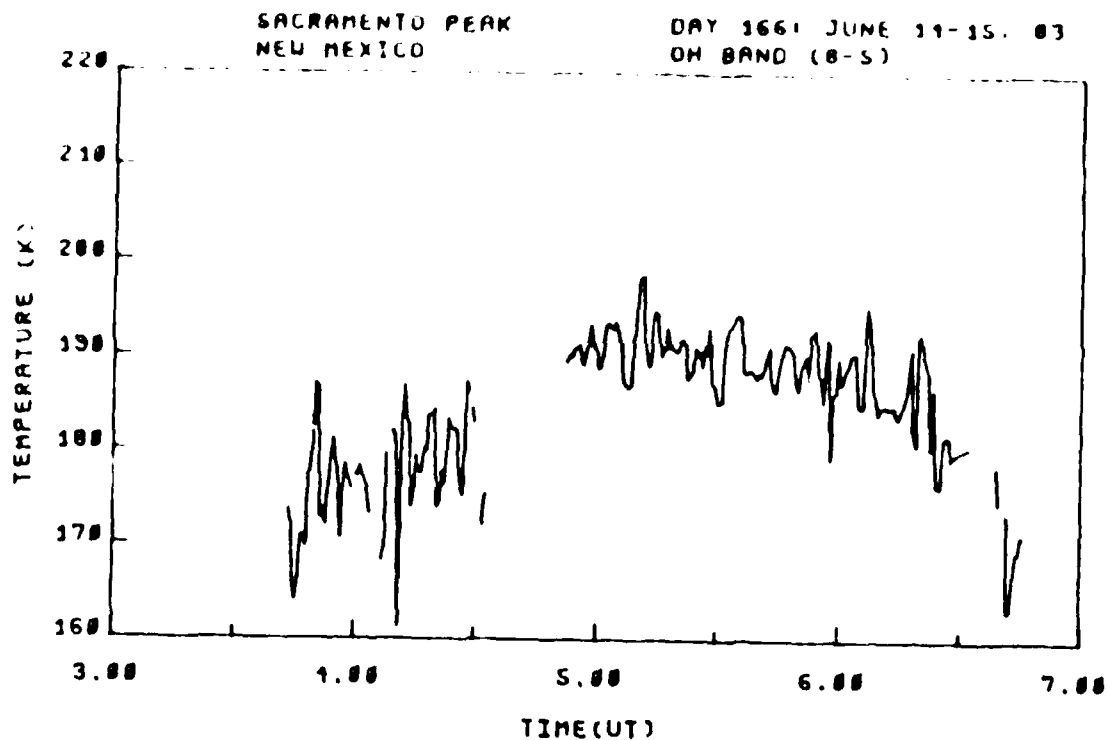


Figure C-21. OH (8,5) band smoothed rotational temperature and standard deviation, viewing angle = zenith, day 166, 3:30-6:45 hrs. UT.

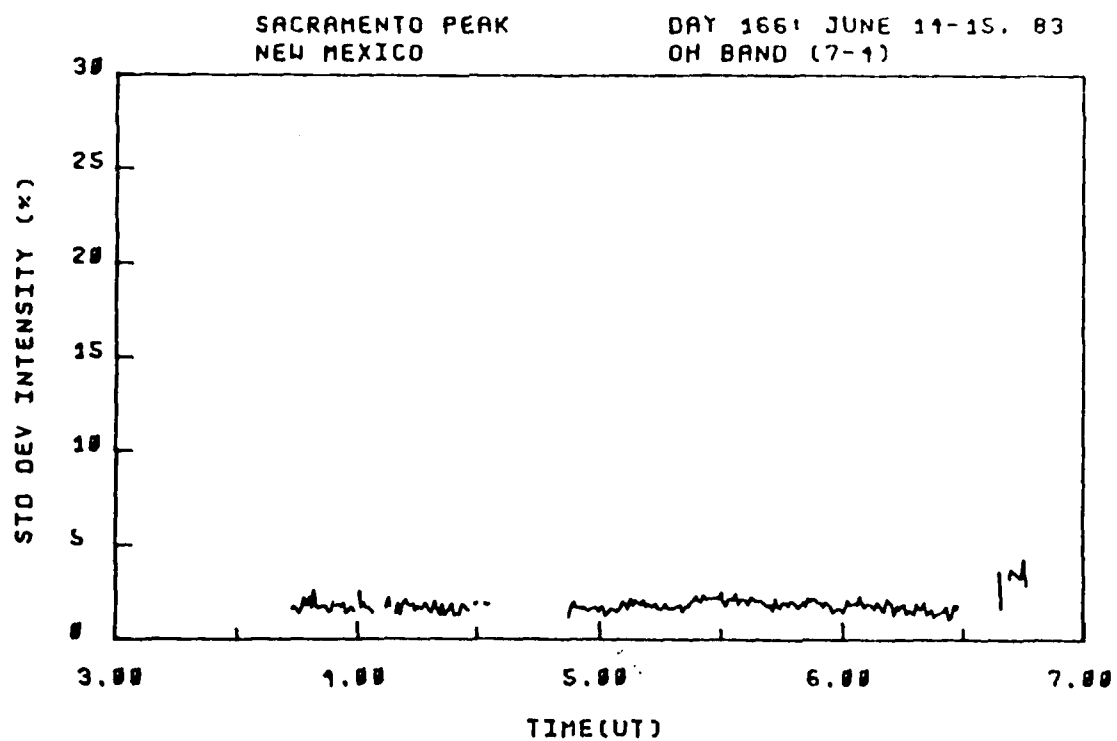
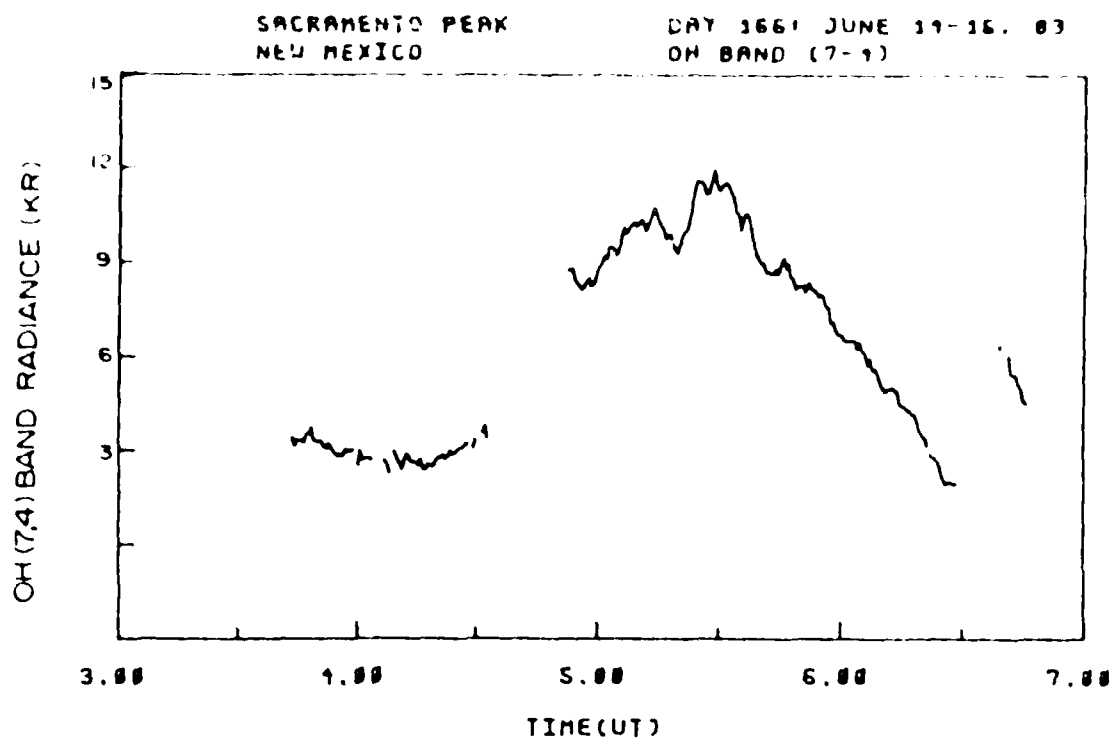


Figure C-22. OH (7,4) band radiance and standard deviation, viewing angle = zenith, day 166, 3:30-6:45 hrs. UT.

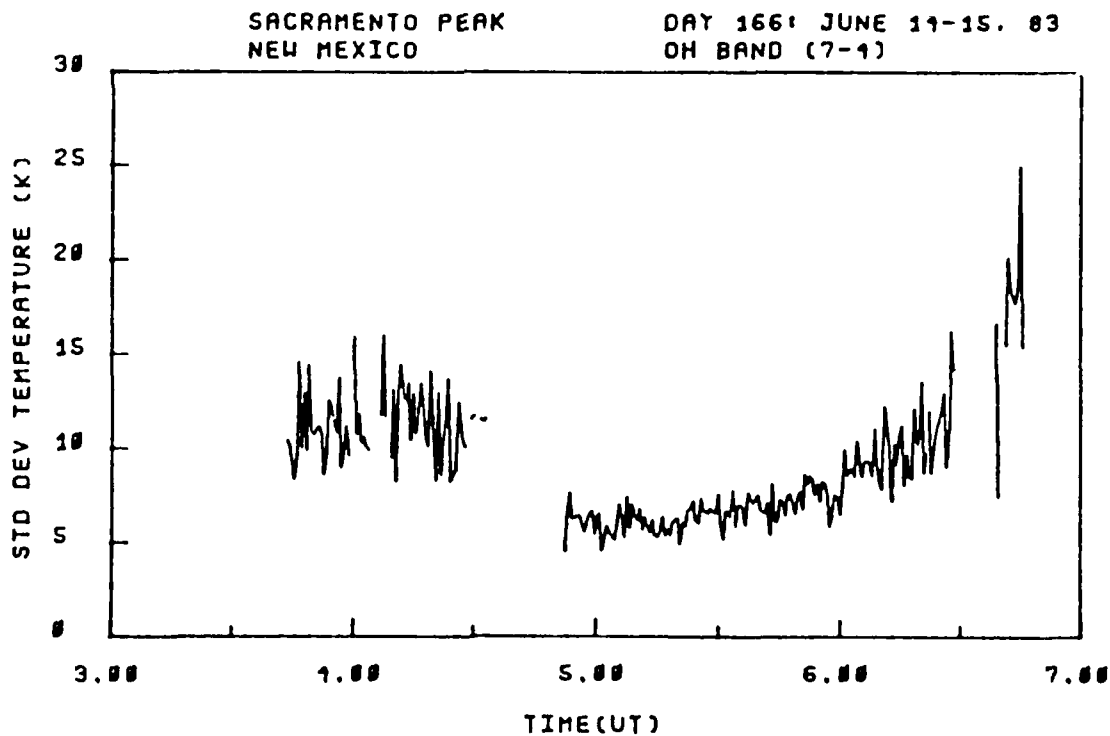
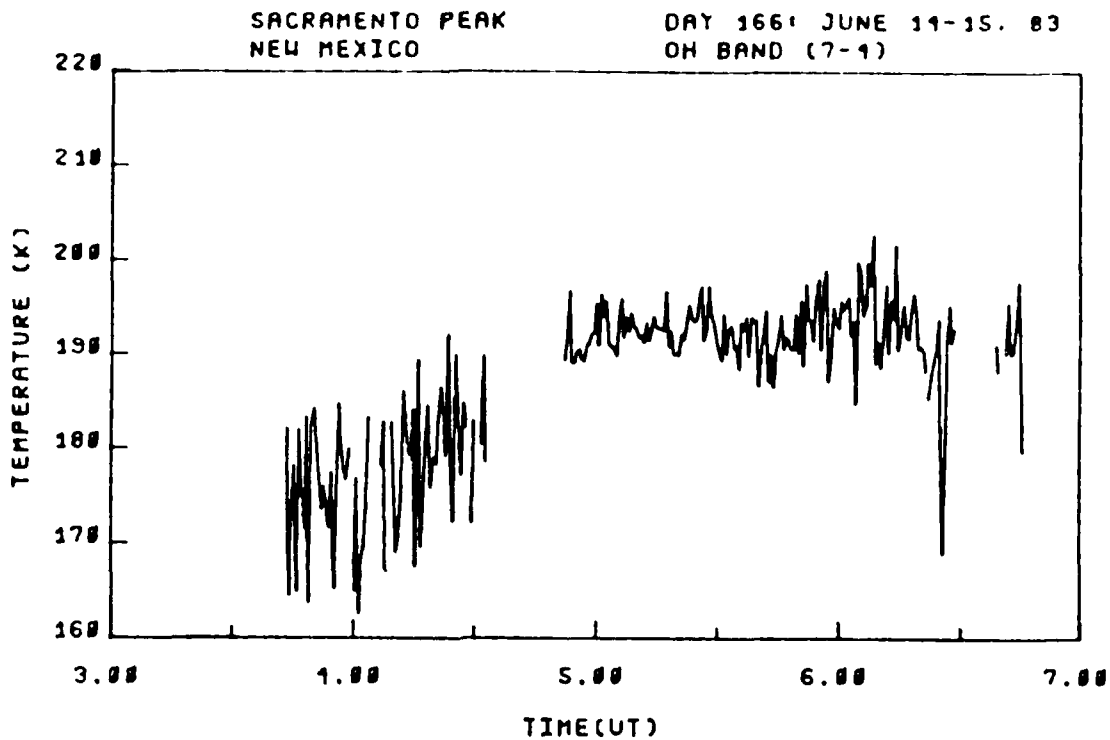


Figure C-23. OH (7,4) band rotational temperature and standard deviation, viewing angle = zenith, day 166, 3:30-6:45 hrs. UT.

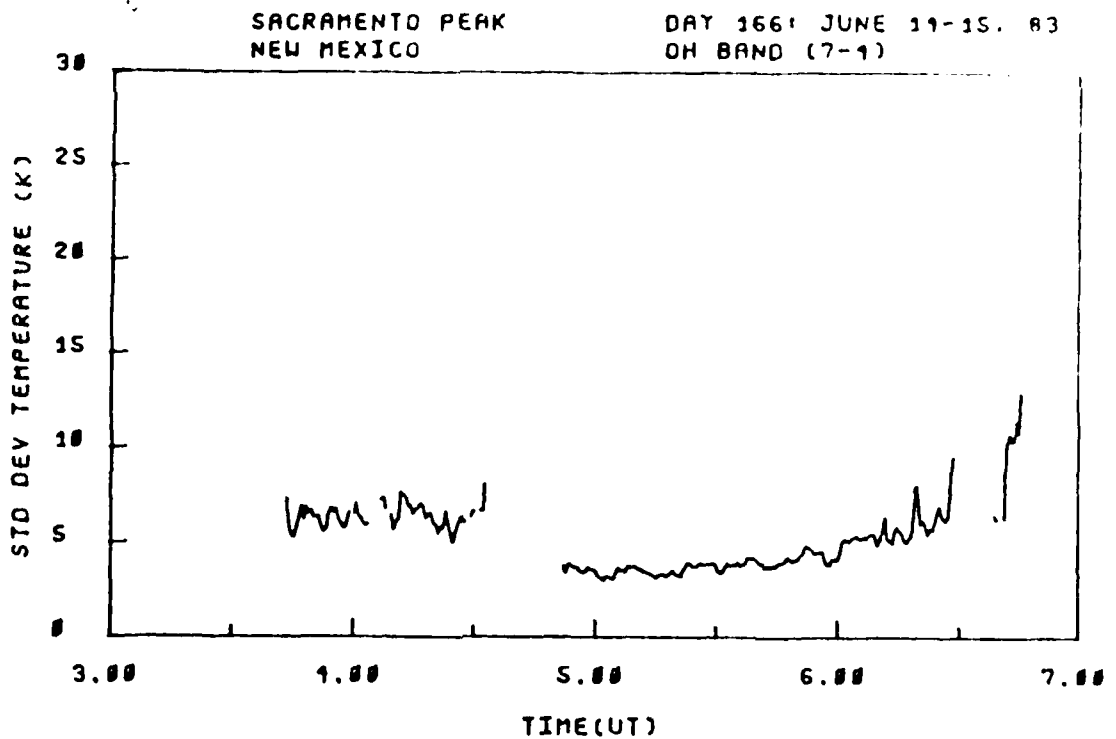
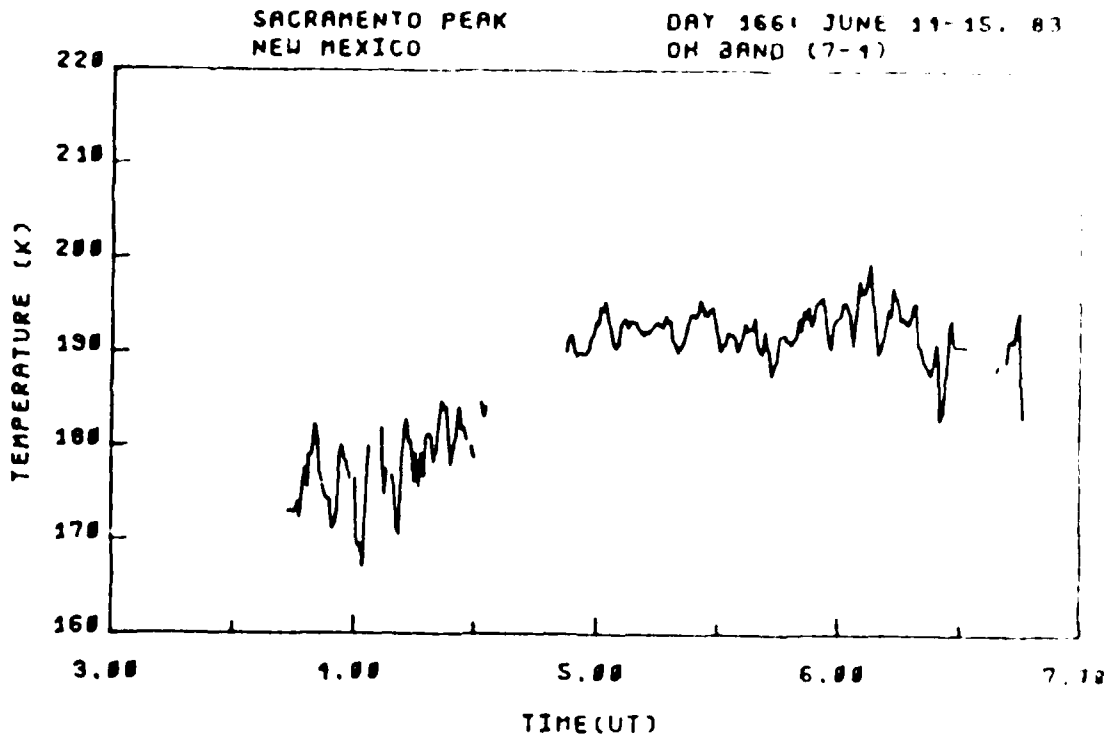


Figure C-24. OH (7,4) band smoothed rotational temperature and standard deviation, viewing angle = zenith, day 166, 3:30-6:45 hrs. UT.

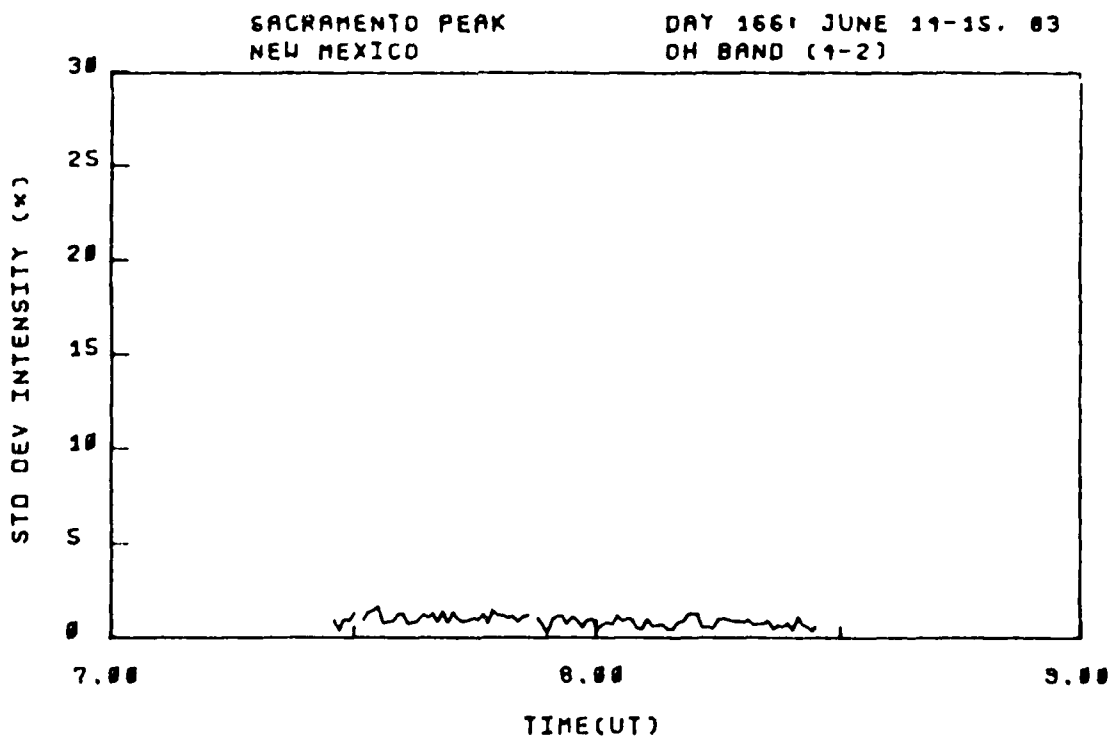
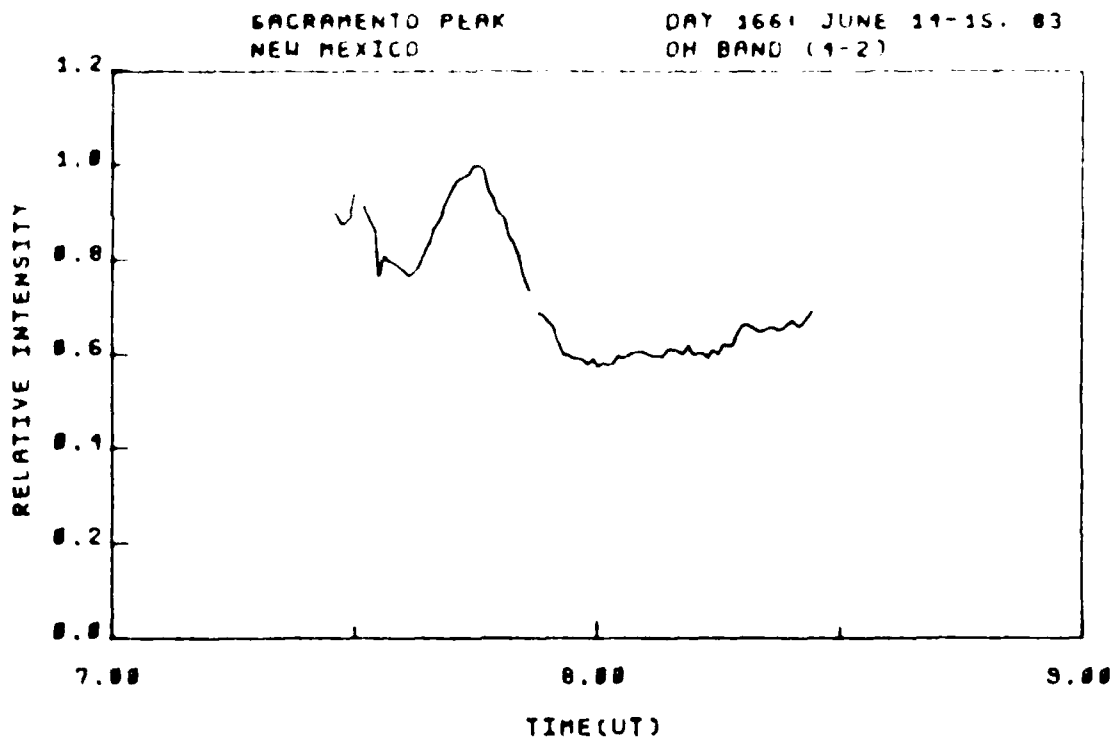


Figure C-25. OH (4,2) band relative intensity and standard deviation, viewing angle = 17° El. 328° Az., day 166, 7:30-8:30 hrs. UT.

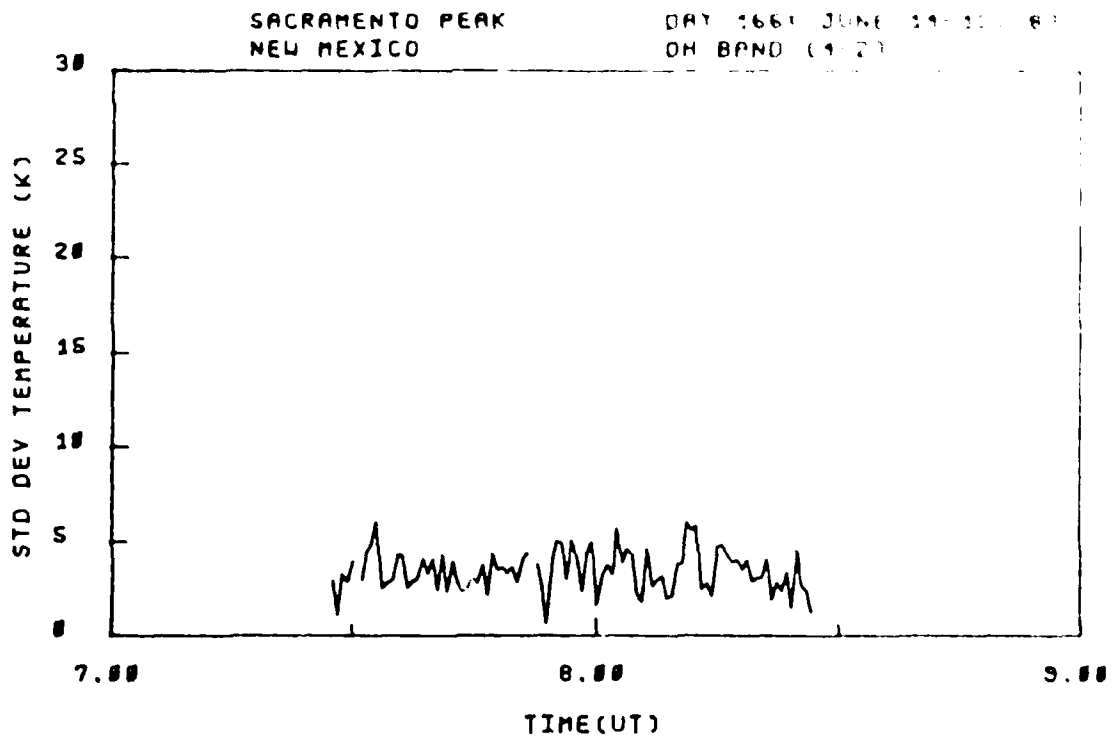
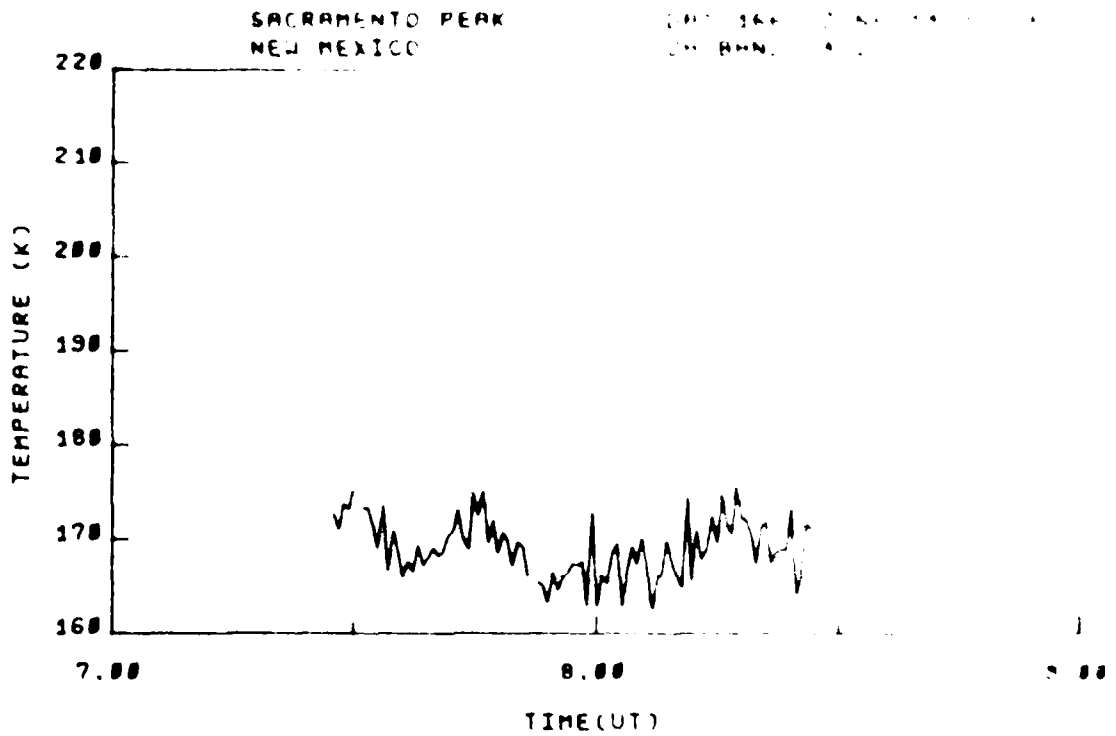


Figure C-26. OH (4,2) band rotational temperature and standard deviation, viewing angle = 17° El. 328° Az., day 166, 7:30-8:30 hrs. UT.

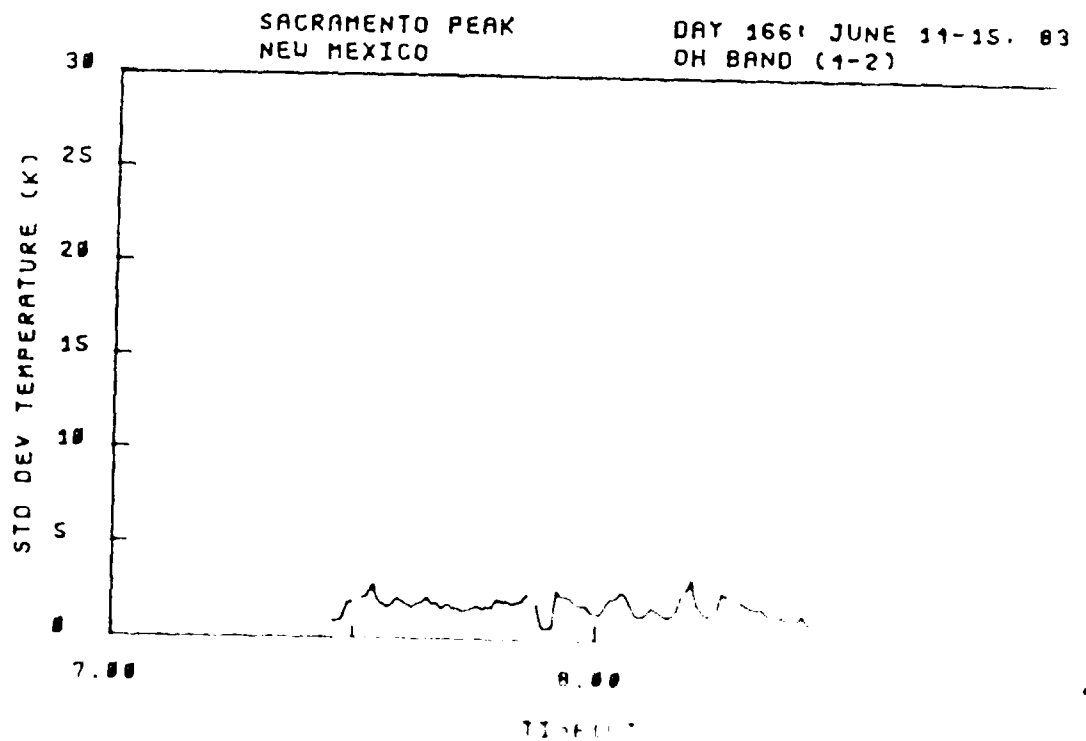
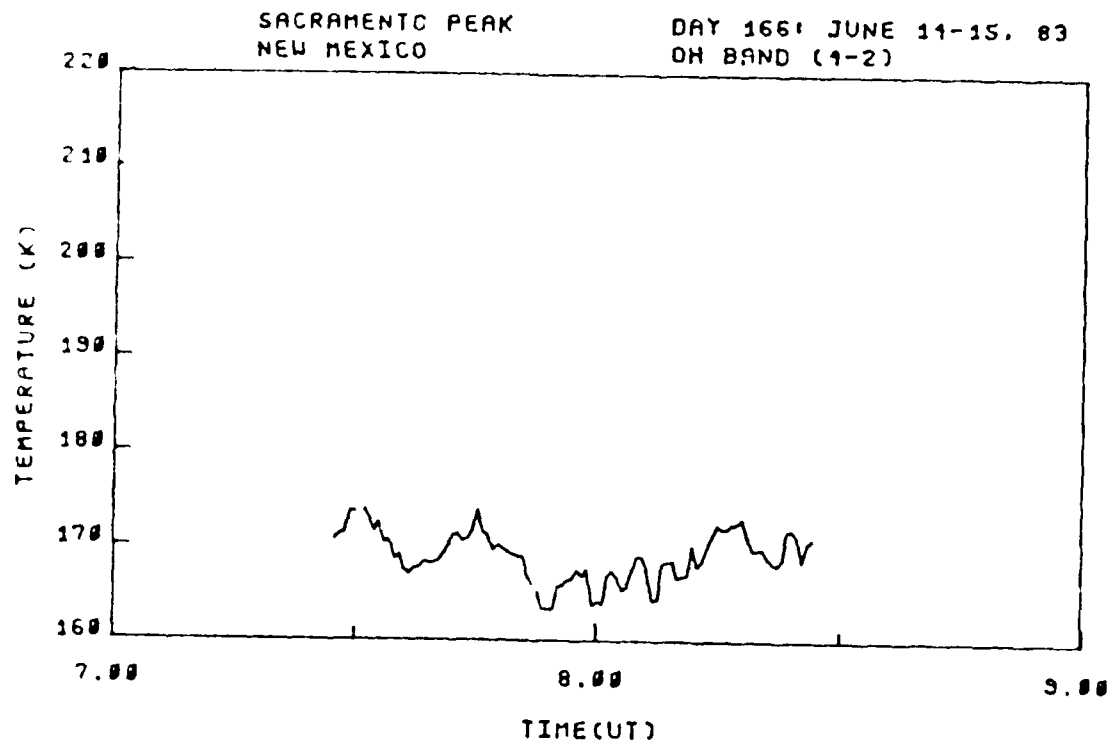


Figure C-27. OH (1,2) band emission line and standard deviation, viewed from day 166, 7:30-8:30 hrs. UT.

AD-A181 247

HIGH-RESOLUTION MEASUREMENT OF OH INFRARED AIRGLOW
STRUCTURE(U) UTAH STATE UNIV LOGAN SPACE DYNAMICS LABS
P C NEAL 18 OCT 85 SDL/85-075 AFGL-TR-85-0261
F19618-83-C-0056

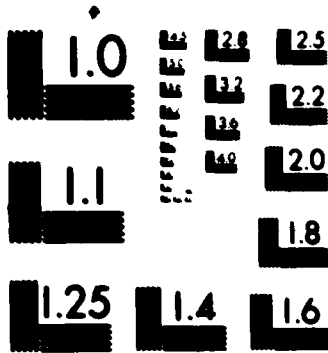
3/3

UNCLASSIFIED

F/G 4/1

NL

							END 7 BT DTC						



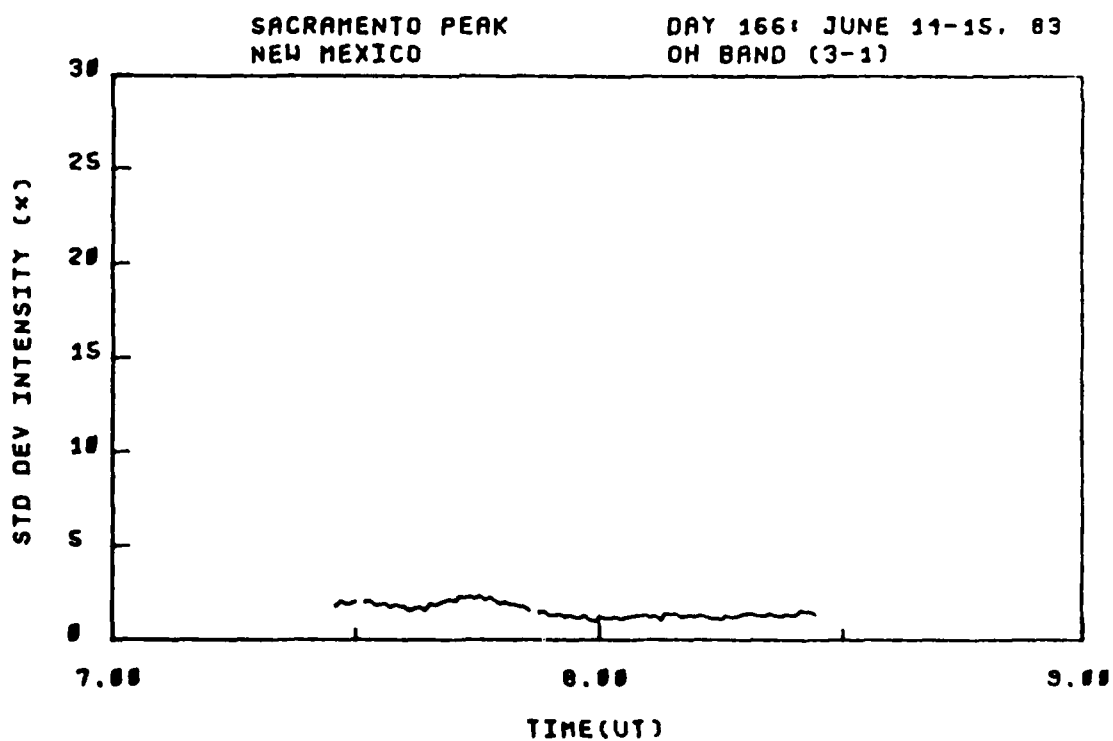
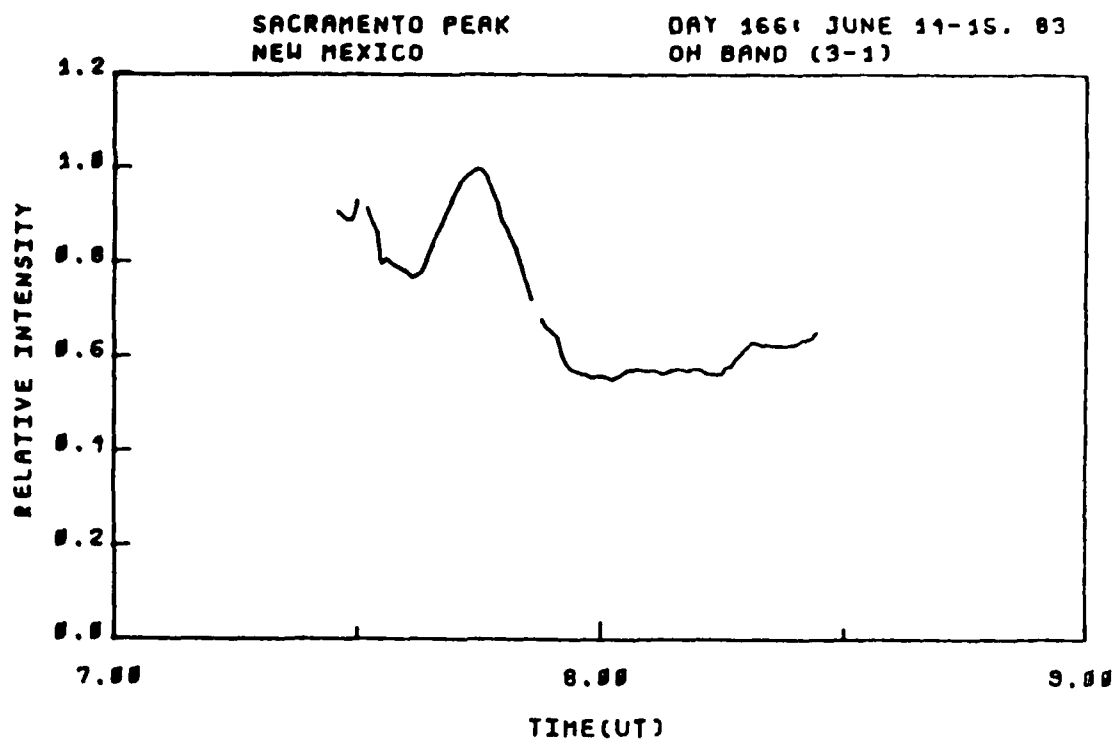


Figure C-28. OH (3,1) band relative intensity and standard deviation, viewing angle = 17° El. 328° Az., day 166, 7:30-8:30 hrs. UT.

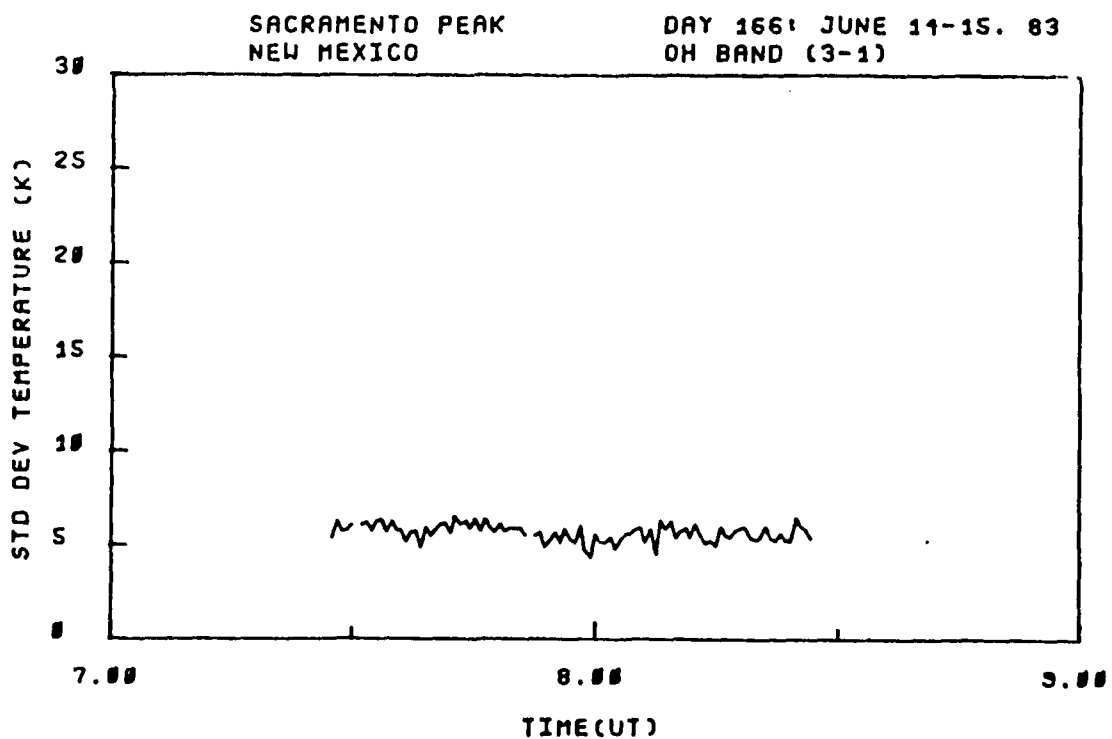
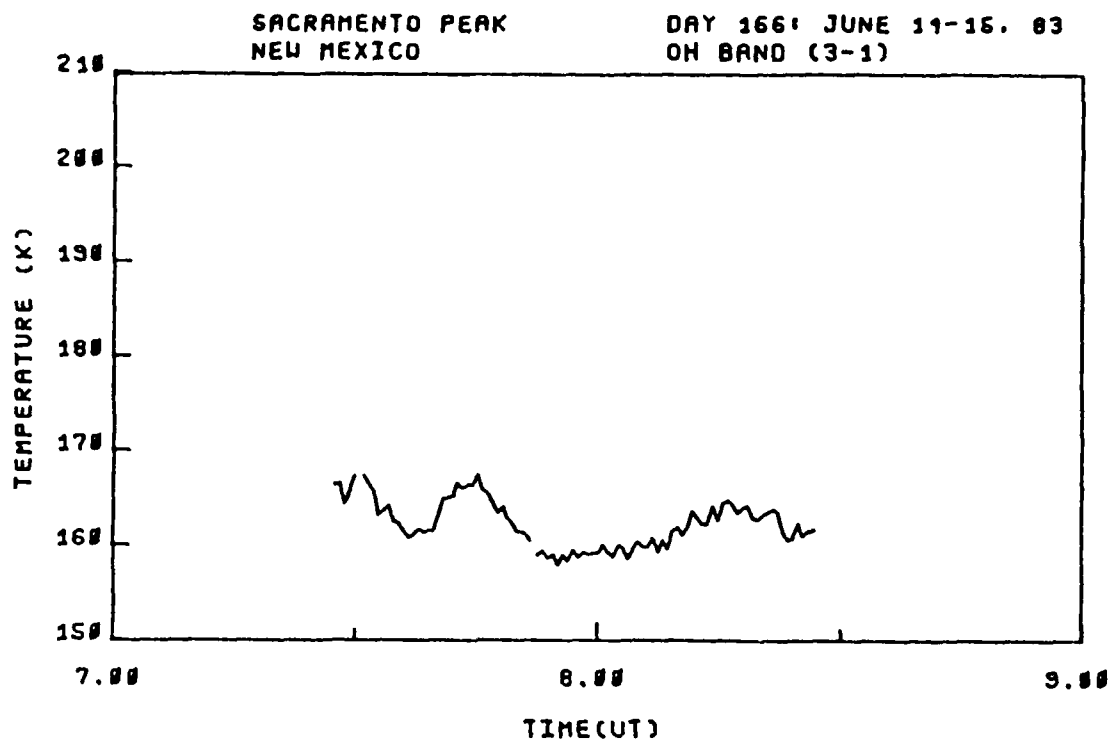


Figure C-29. OH (3,1) band rotational temperature and standard deviation, viewing angle = 17° El. 328° Az., day 166, 7:30-8:30 hrs. UT.

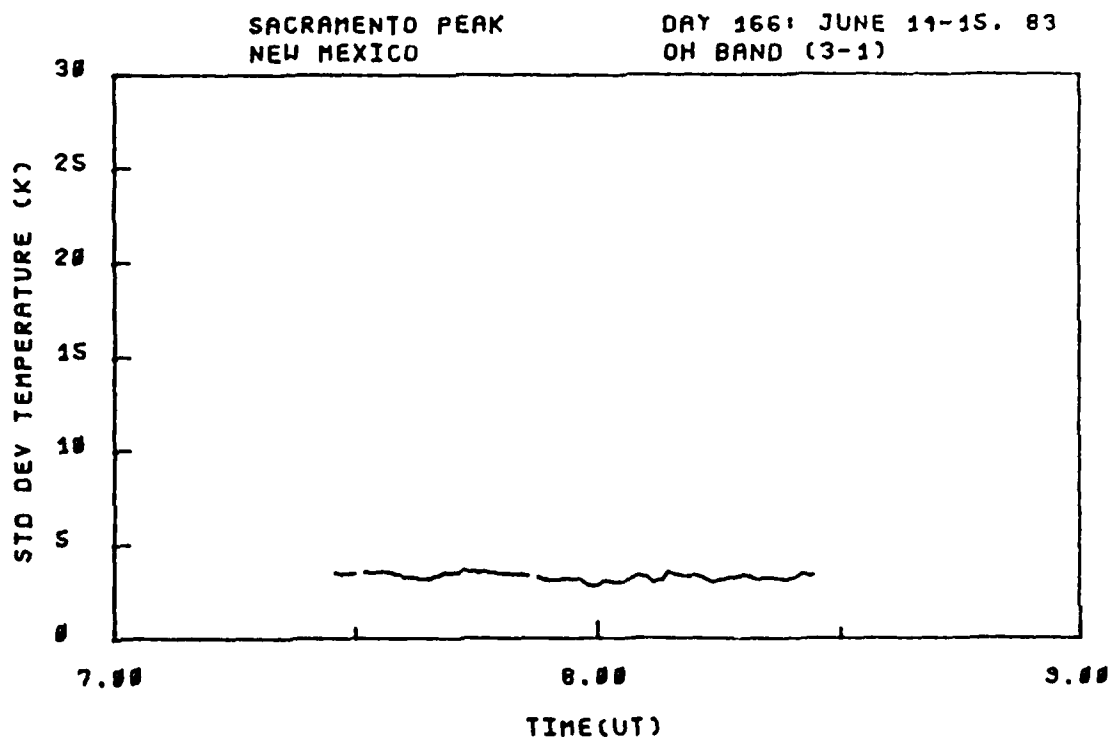
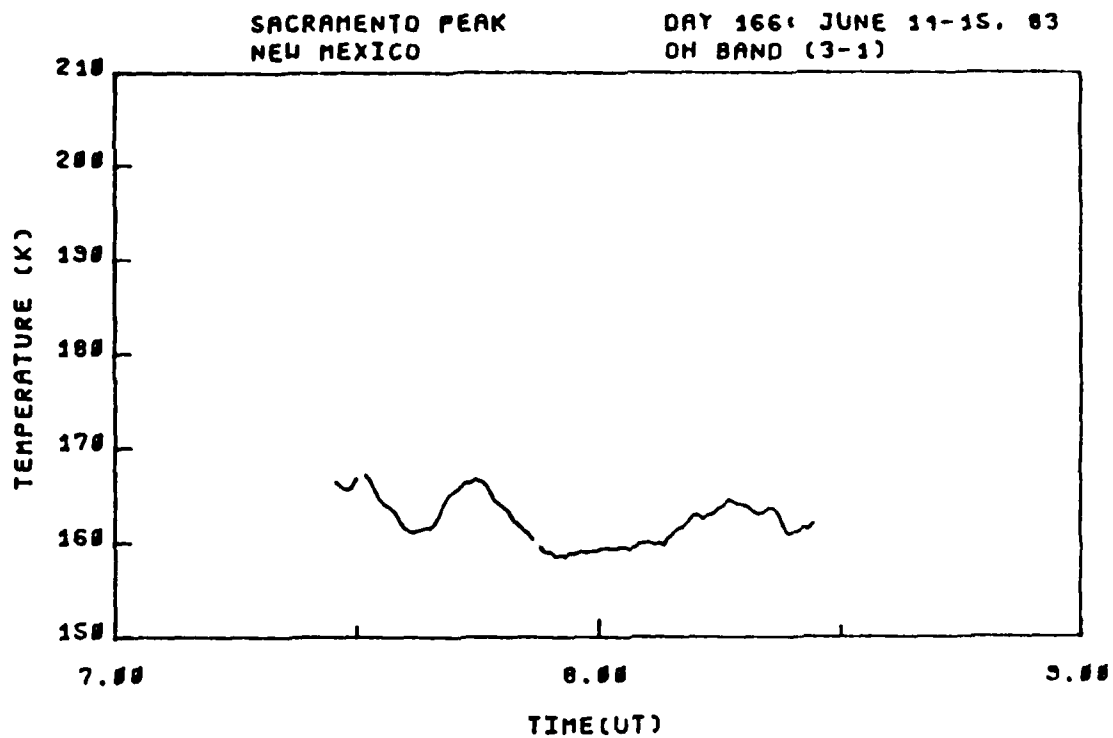


Figure C-30. OH (3,1) band smoothed rotational temperature and standard deviation, viewing angle = 17° El. 328° Az., day 166, 7:30-8:30 hrs. UT.

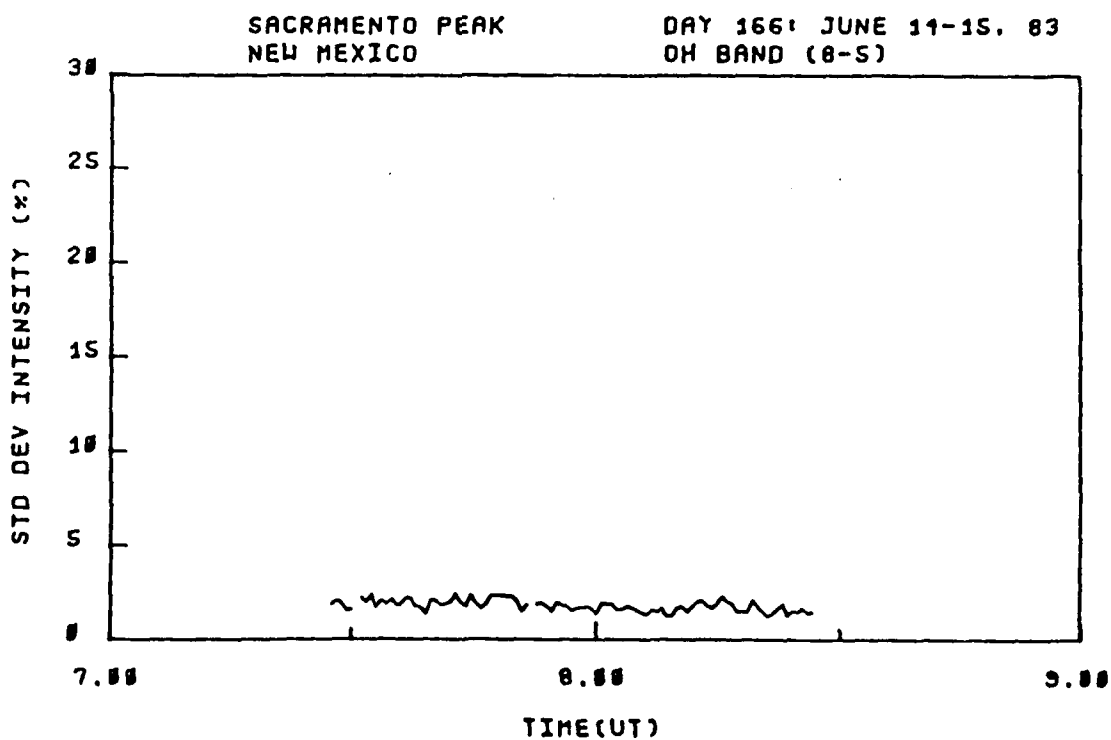
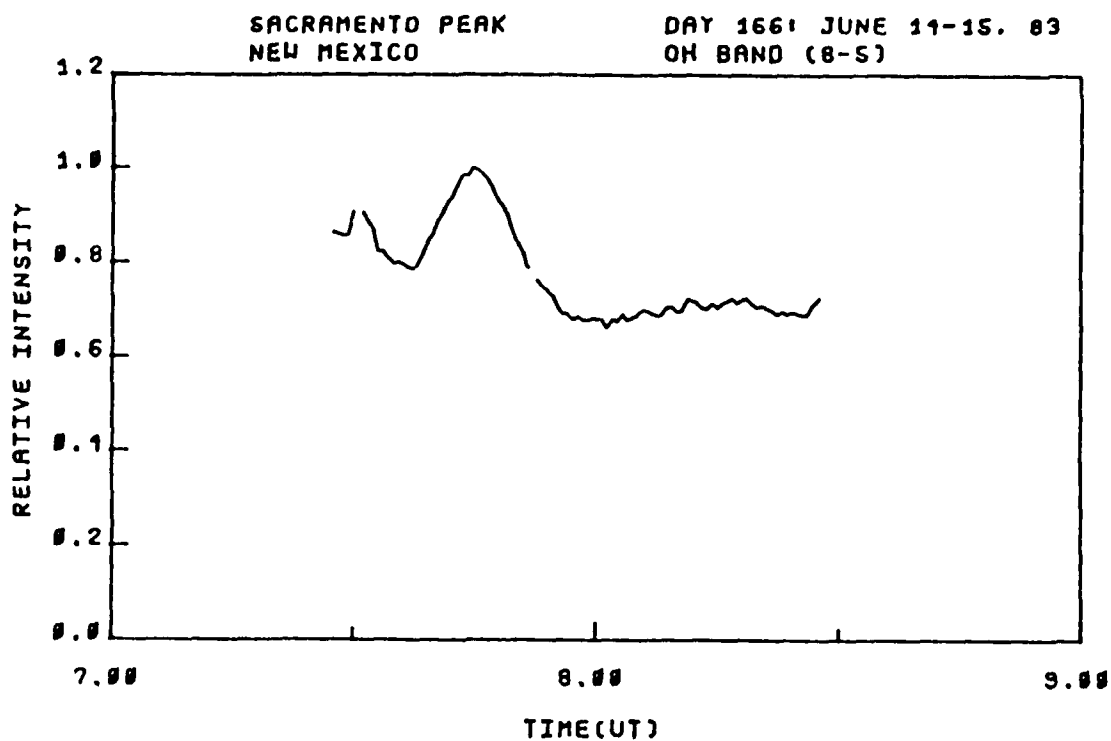


Figure C-31. OH (8,5) band relative intensity and standard deviation, viewing angle = 17° El. 328° Az., day 166, 7:30-8:30 hrs. UT.

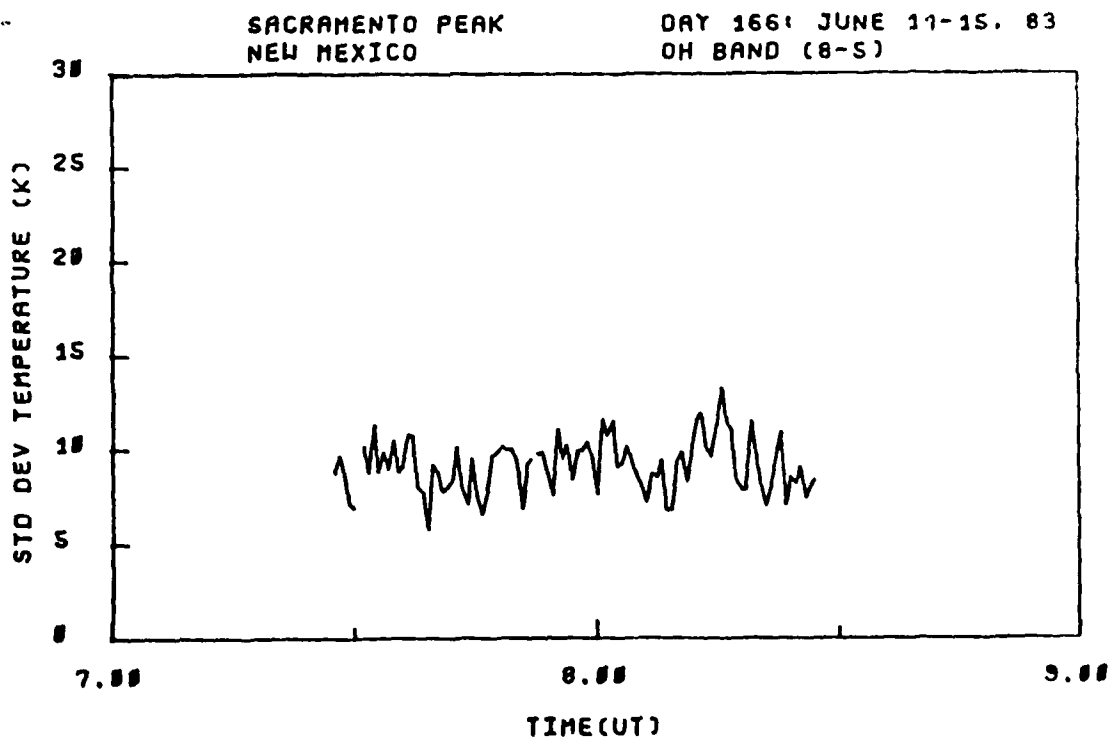
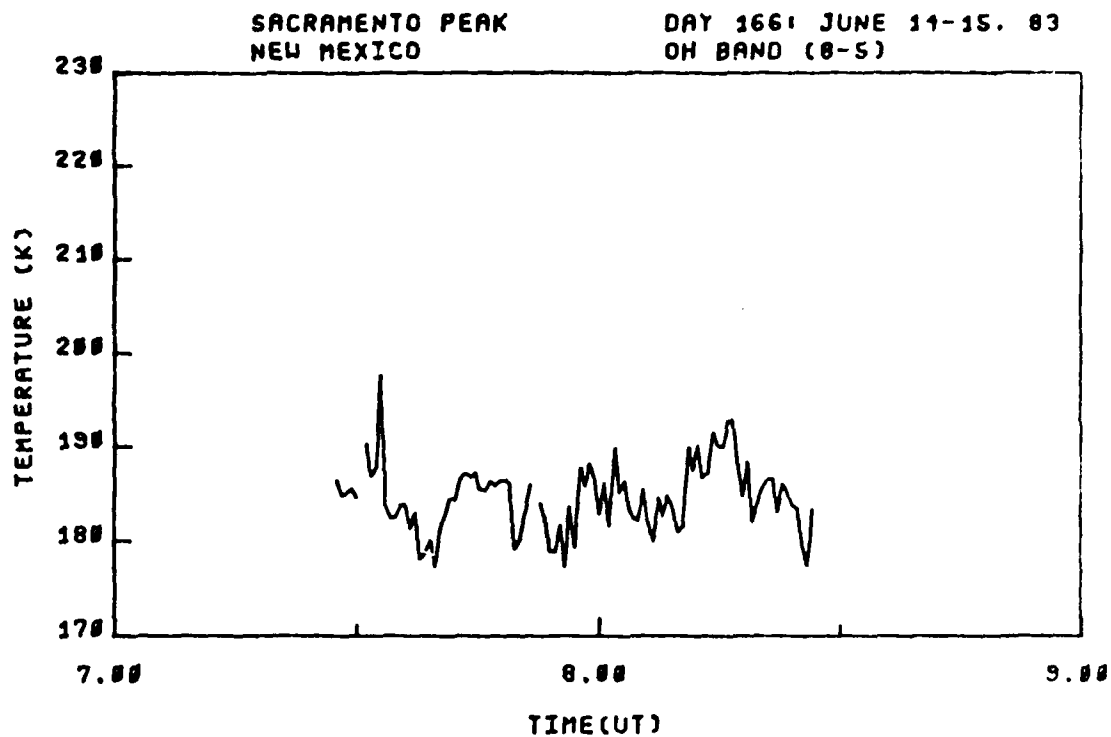


Figure C-32. OH (8,5) band rotational temperature and standard deviation, viewing angle = 17° El. 328° Az., day 166, 7:30-8:30 hrs. UT.

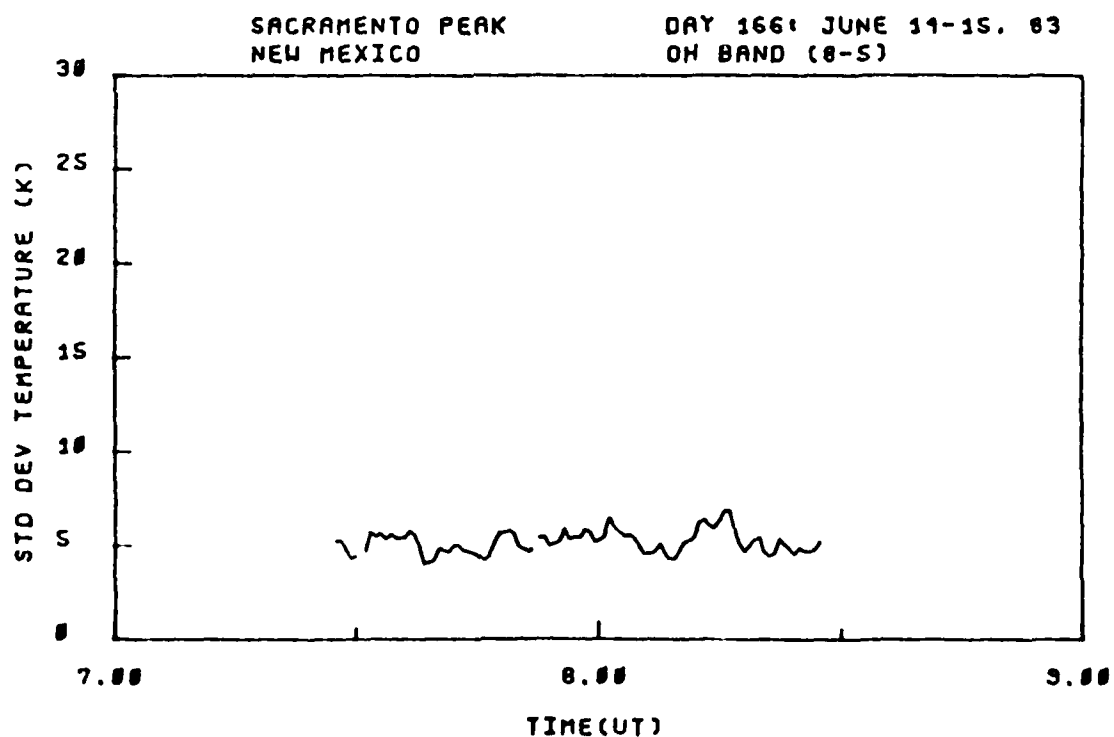
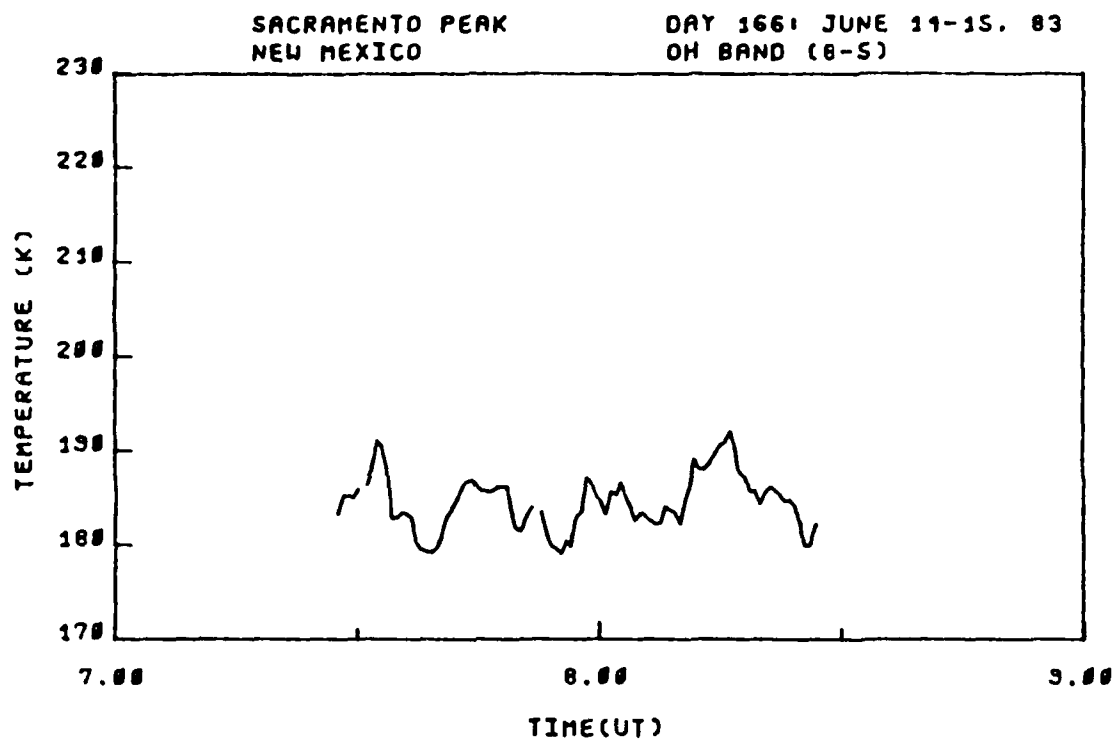


Figure C-33. OH (8,5) band smoothed rotational temperature and standard deviation, viewing angle = 17° El. 328° Az., day 166, 7:30-8:30 hrs. UT.

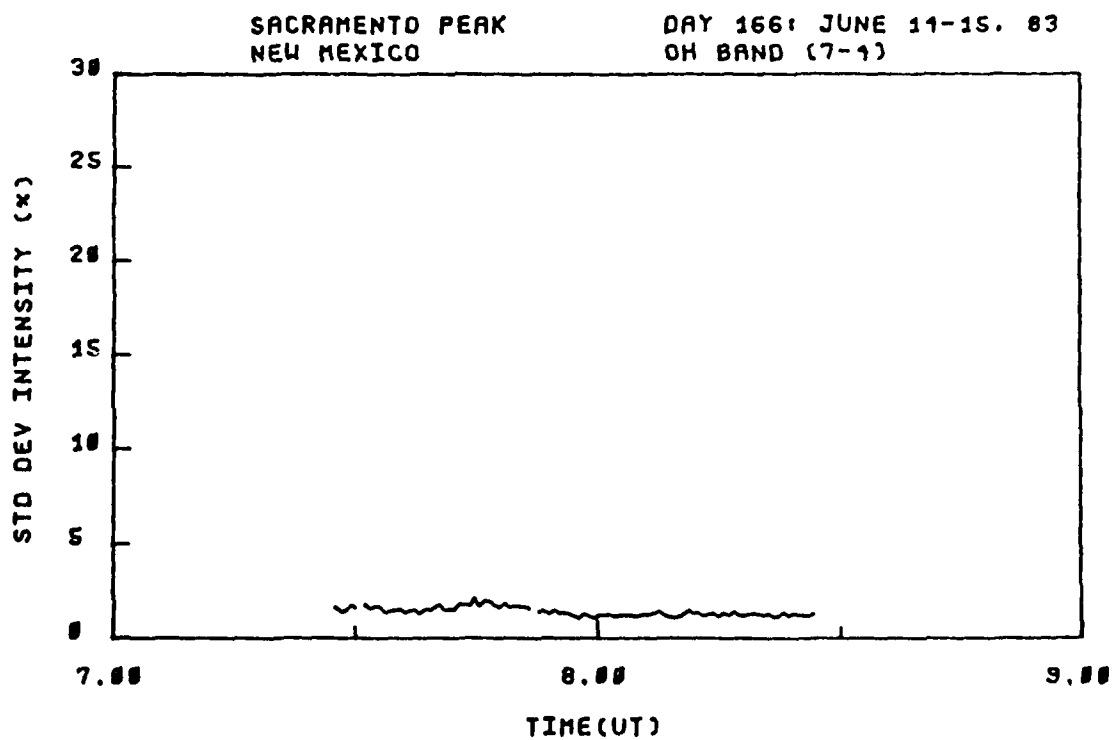
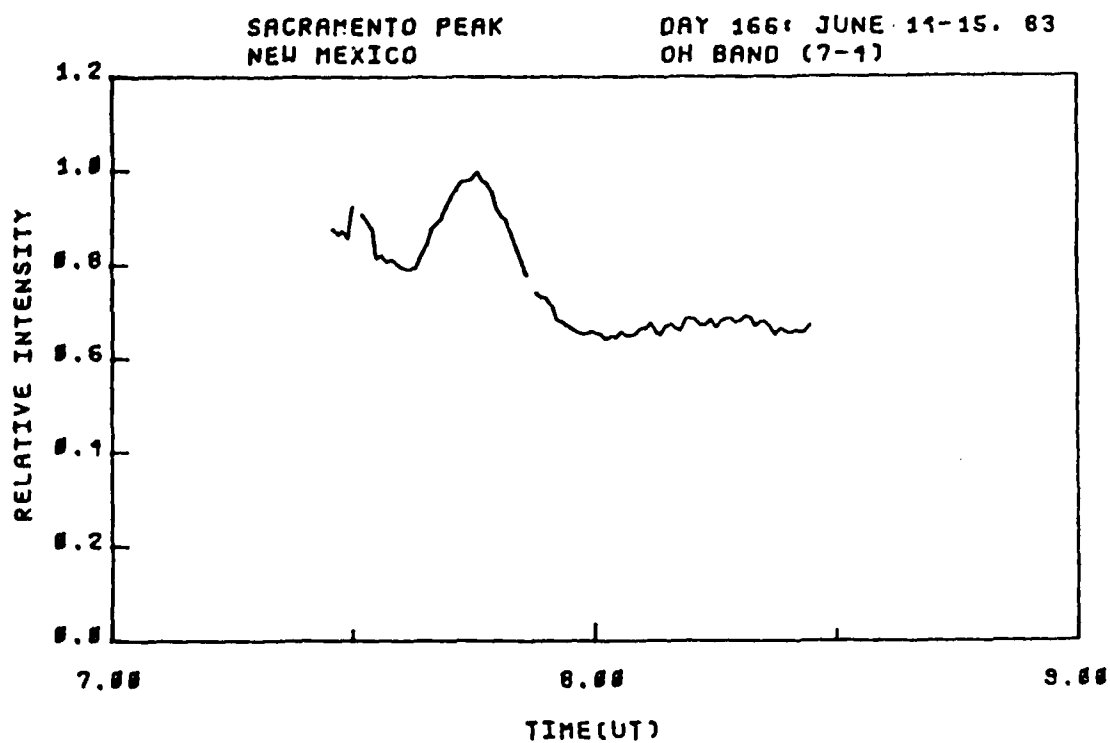


Figure C-34. OH (7,4) band relative intensity and standard deviation, viewing angle = 17° El. 328° Az., day 166, 7:30-8:30 hrs. UT.

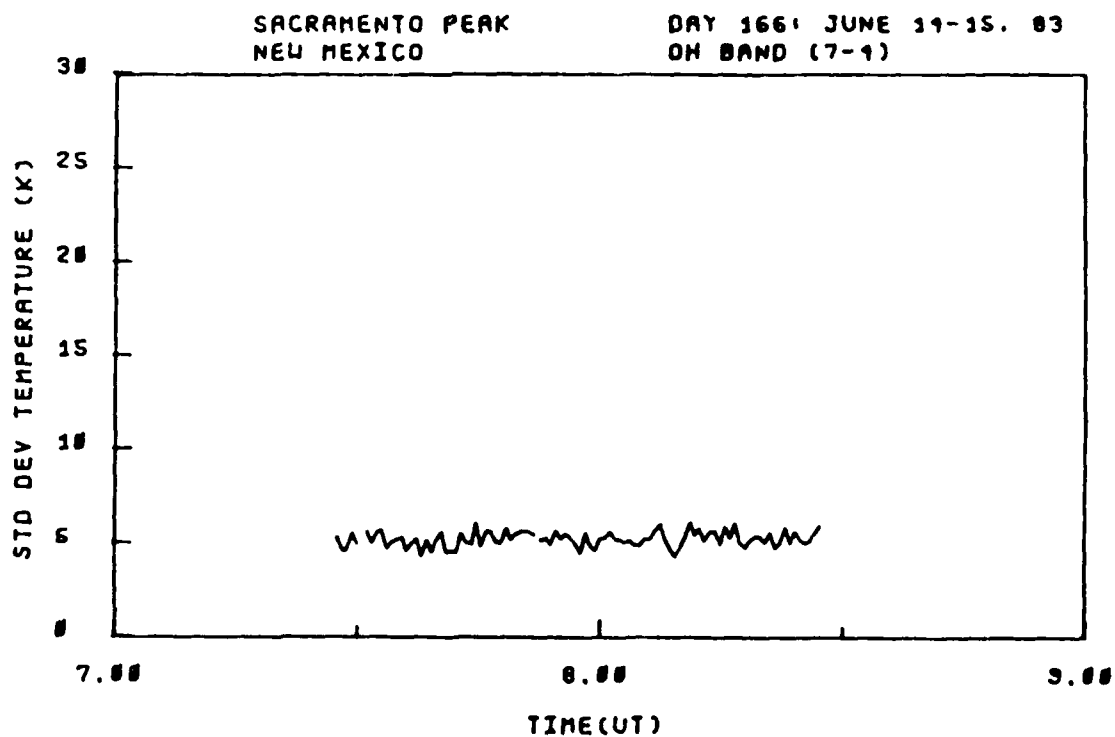
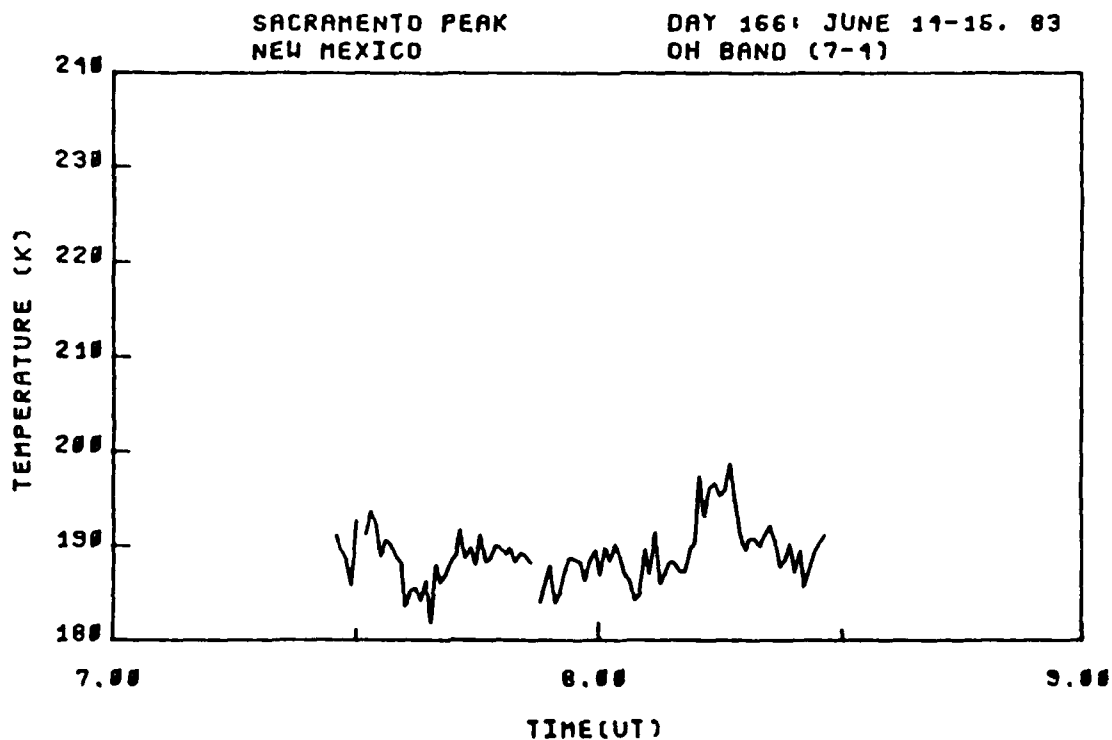


Figure C-35. OH (7,4) band rotational temperature and standard deviation, viewing angle = 17° El. 328° Az., day 166, 7:30-8:30 hrs. UT.

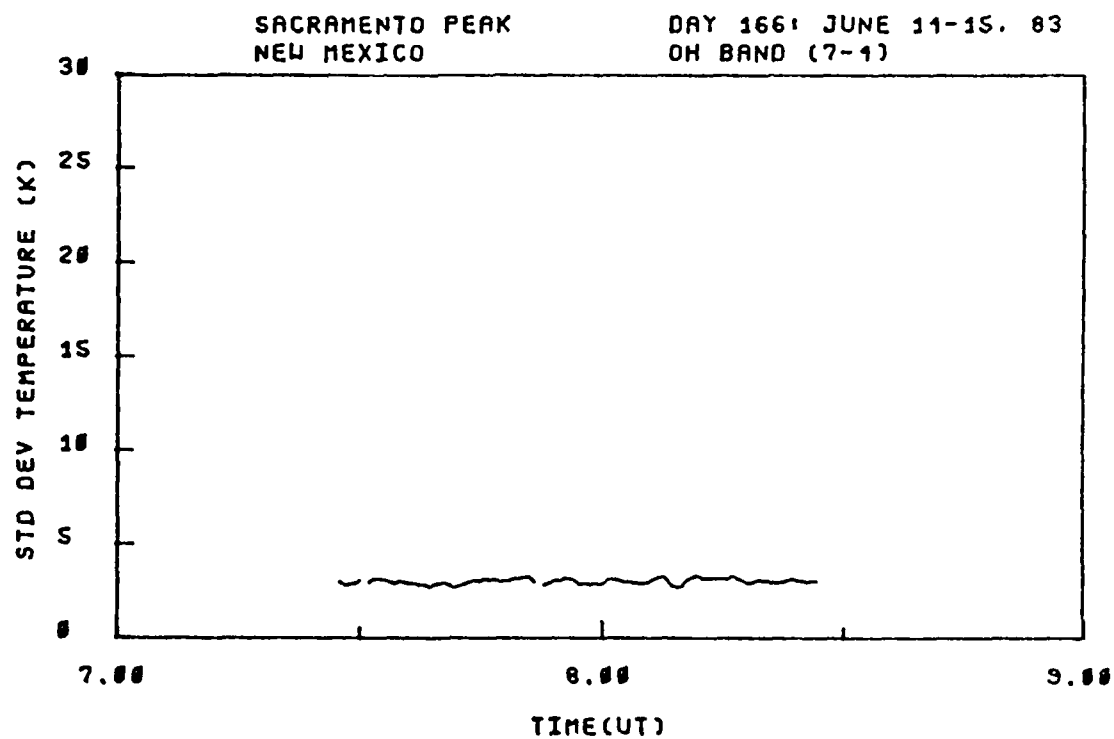
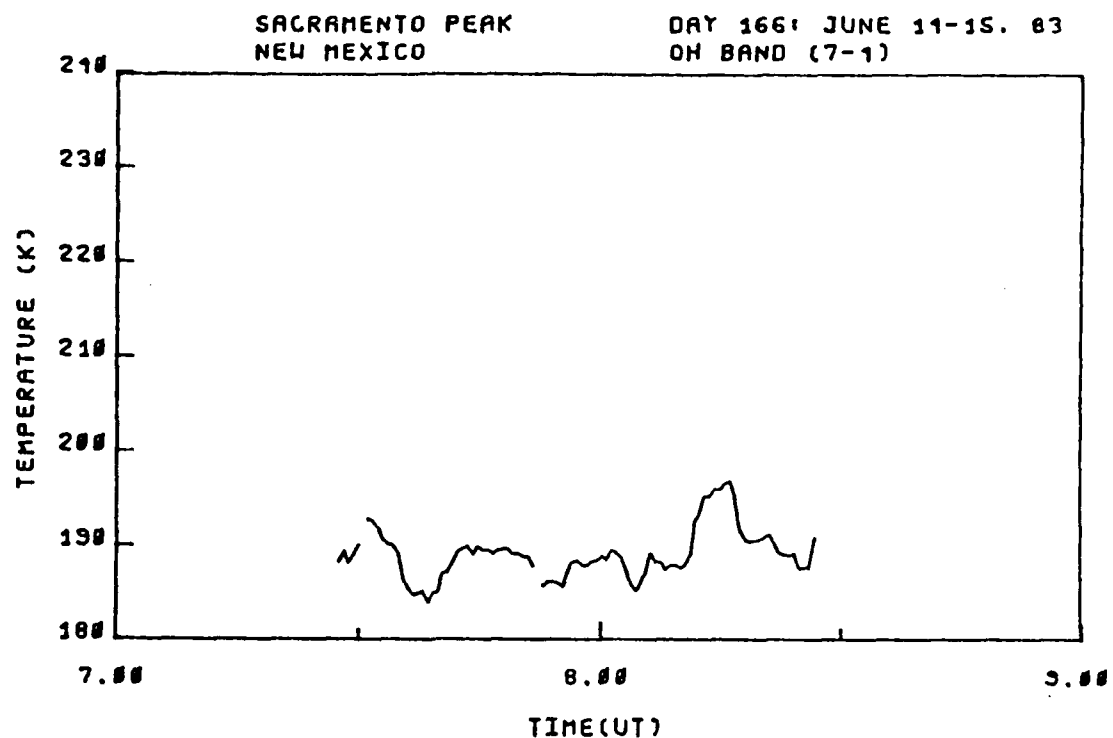


Figure C-36. OH (7,4) band smoothed rotational temperature and standard deviation, viewing angle = 17° El. 328° Az., day 166, 7:30-8:30 hrs. UT.

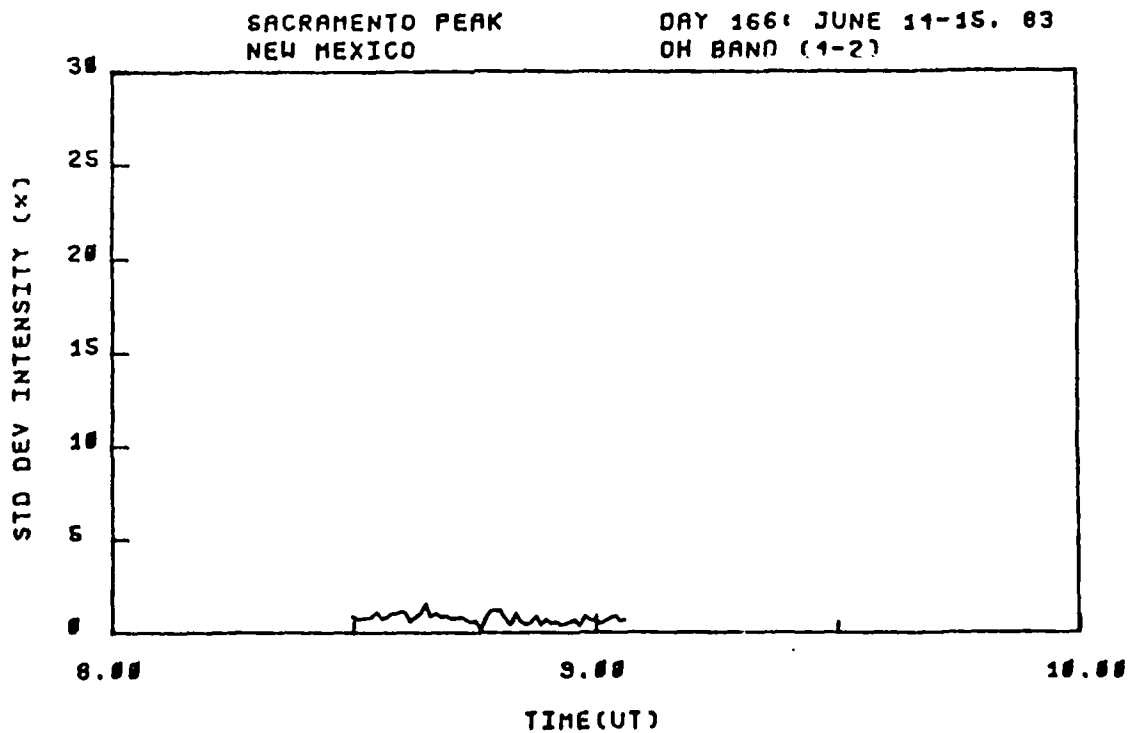
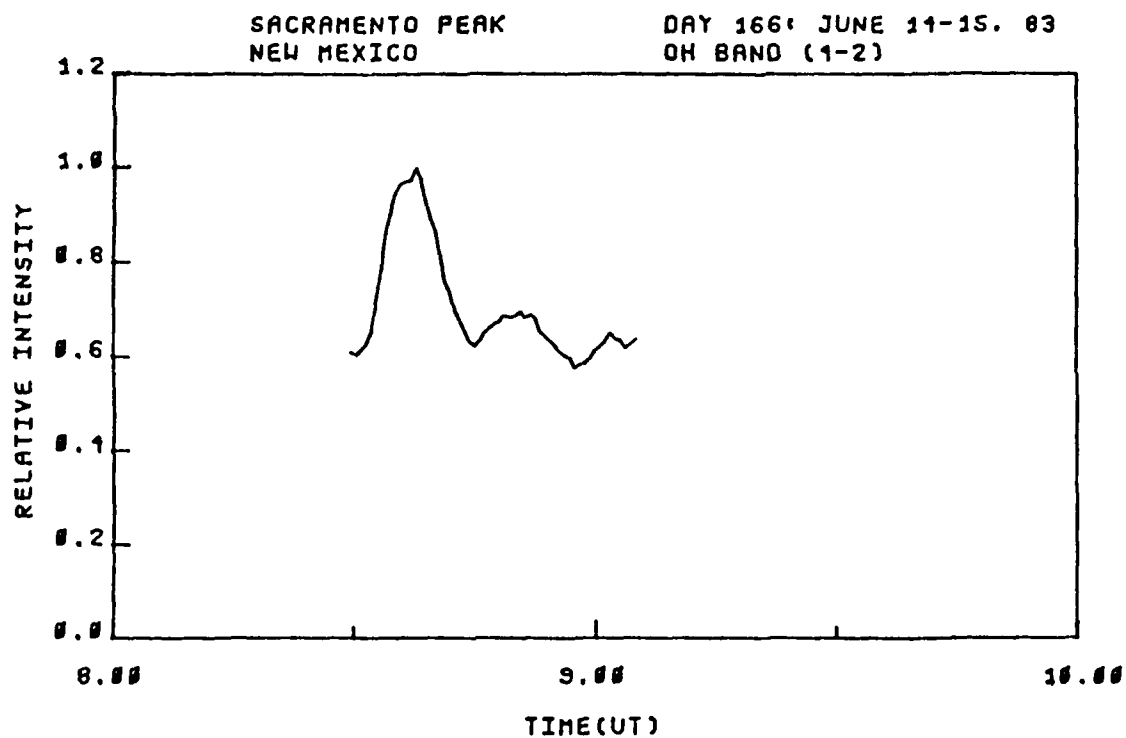


Figure C-37. OH (4,2) band relative intensity and standard deviation, viewing angle = 15.5° El. 340° Az., day 166, 8:30-9:15 hrs. UT.

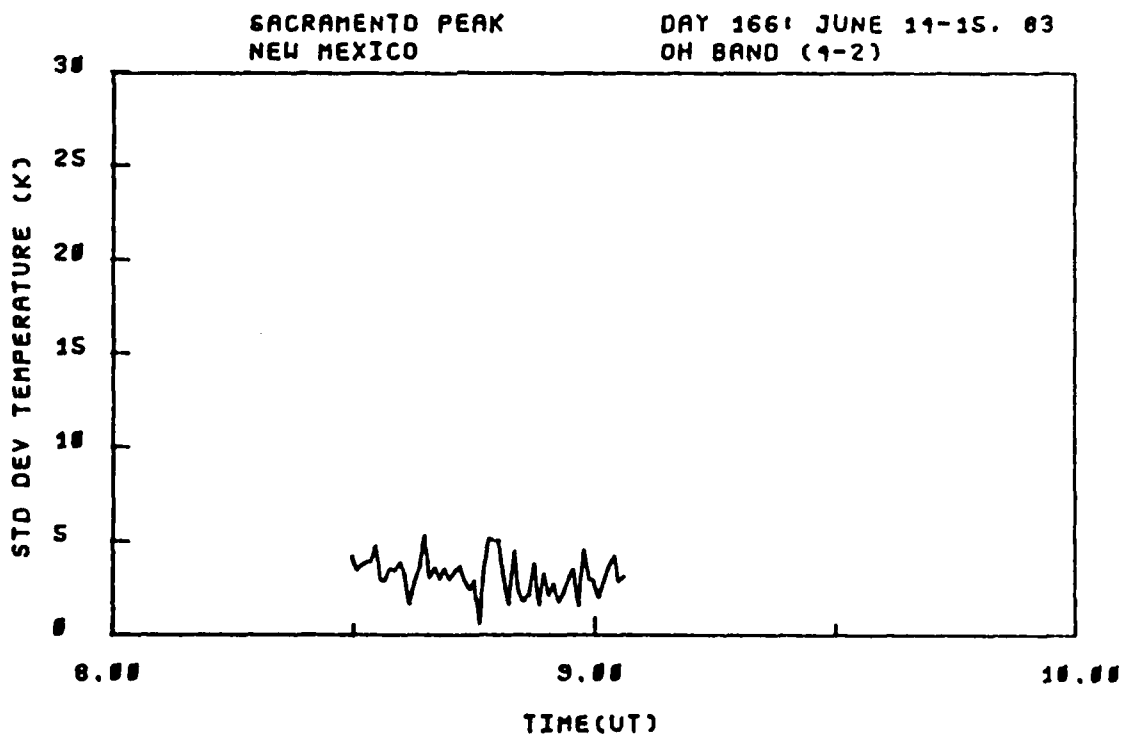
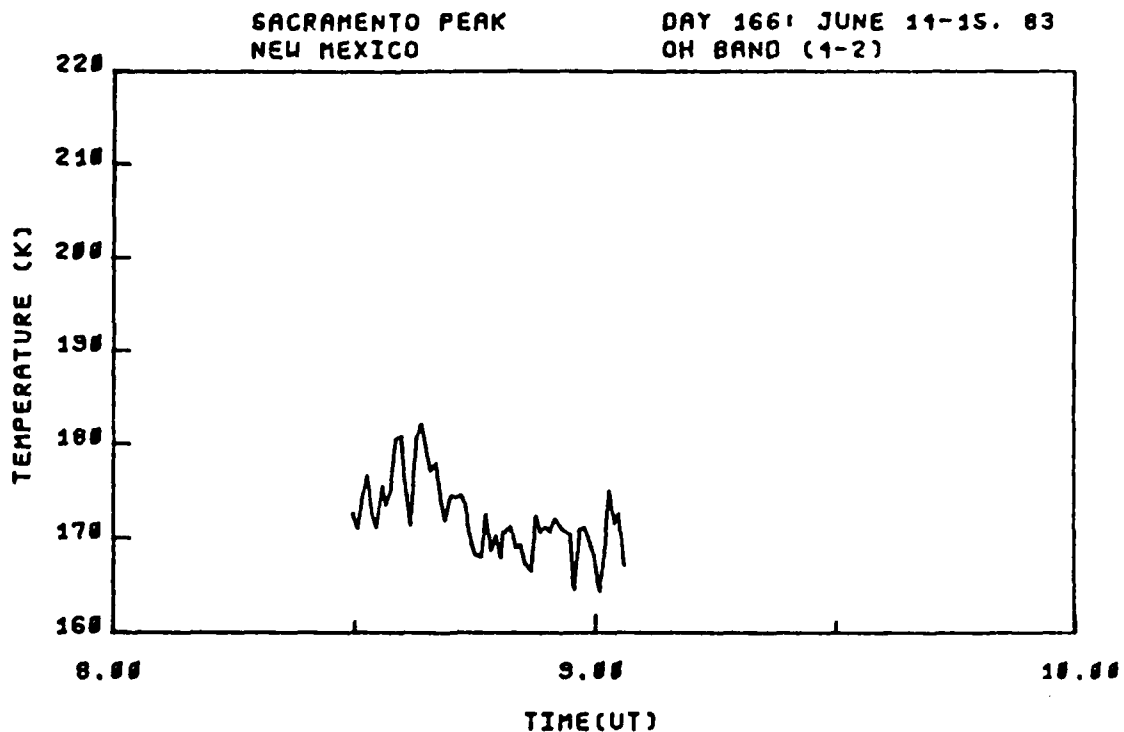


Figure C-38. OH (4,2) band rotational temperature and standard deviation, viewing angle = 15.5° El. 340° Az., day 166, 8:30-9:15 hrs. UT.

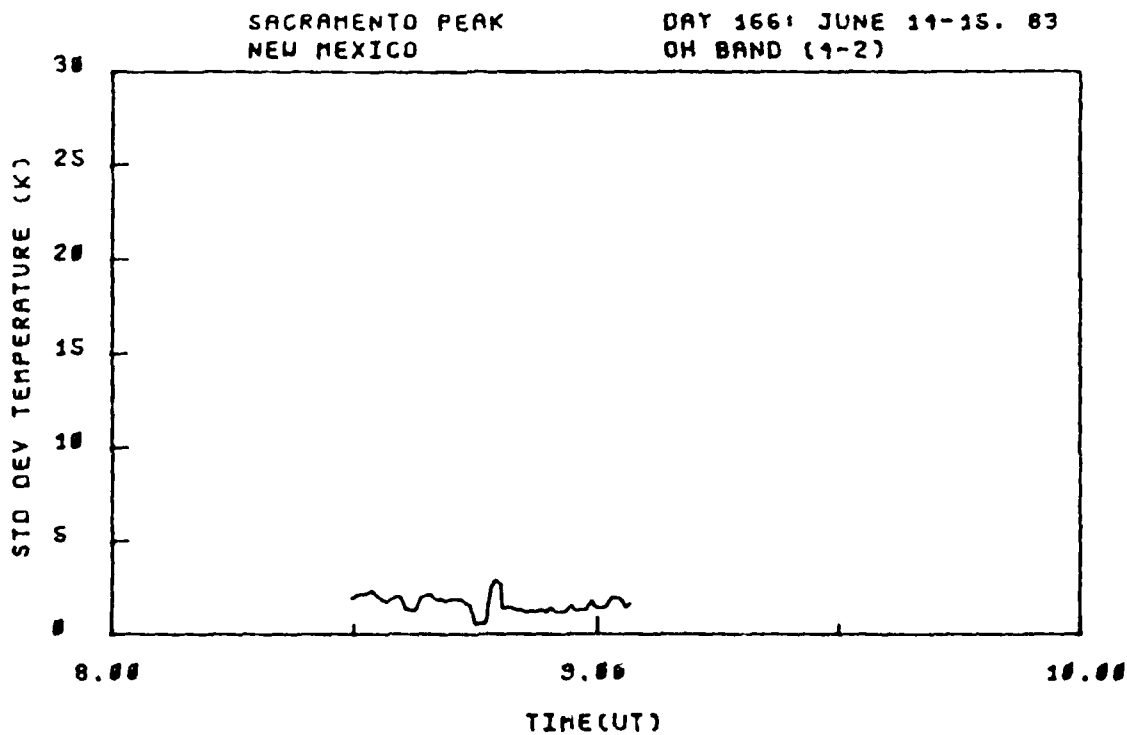
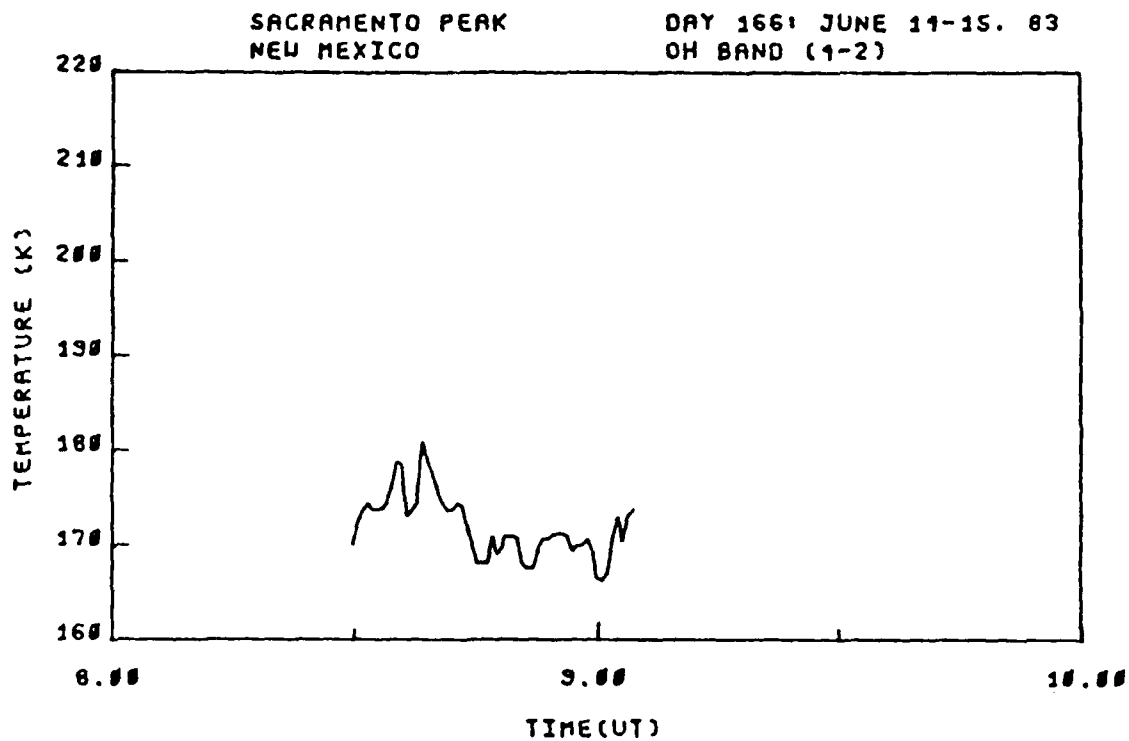


Figure C-39. OH (4,2) band smoothed rotational temperature and standard deviation, viewing angle = 15.5° El. 340° Az., day 166, 8:30-9:15 hrs. UT.

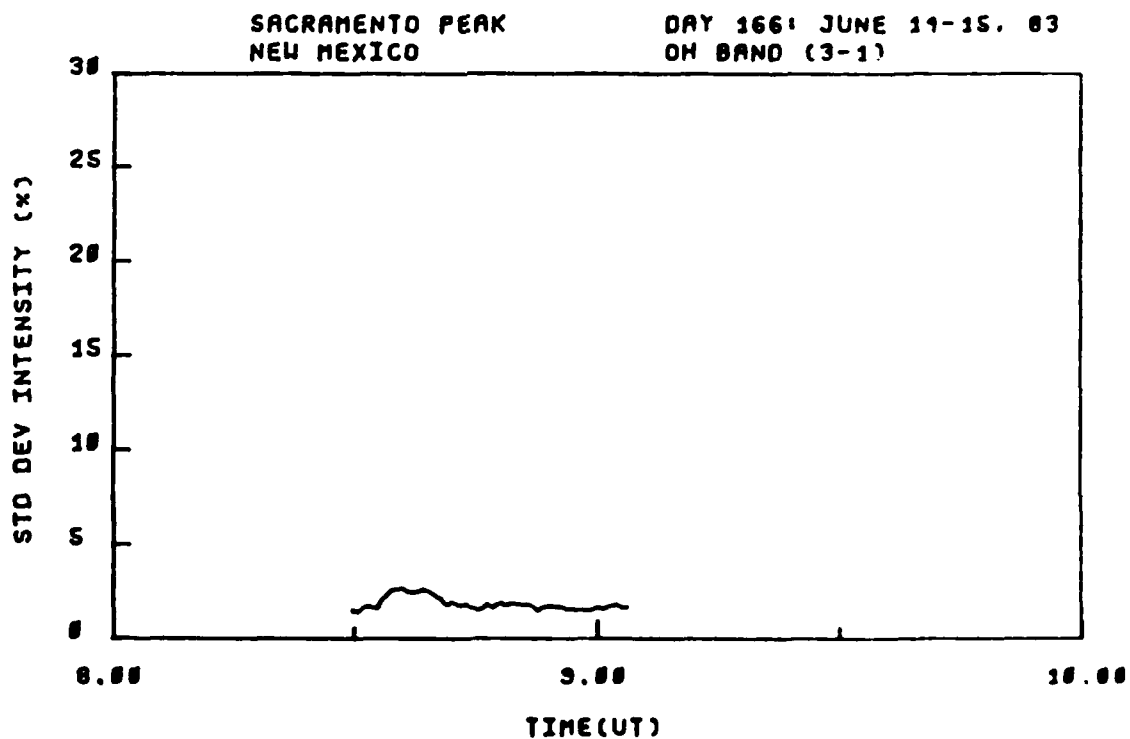
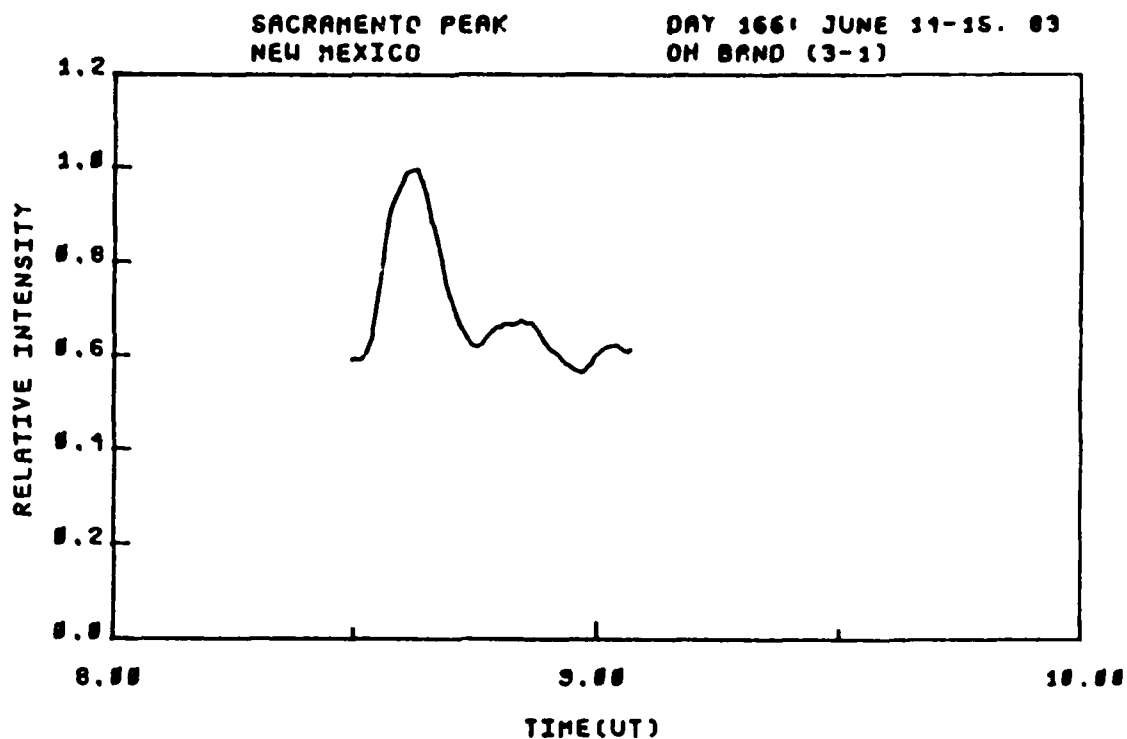


Figure C-40. OH (3,1) band relative intensity and standard deviation, viewing angle = 15.5° El. 340° Az., day 166, 8:30-9:15 hrs. UT.

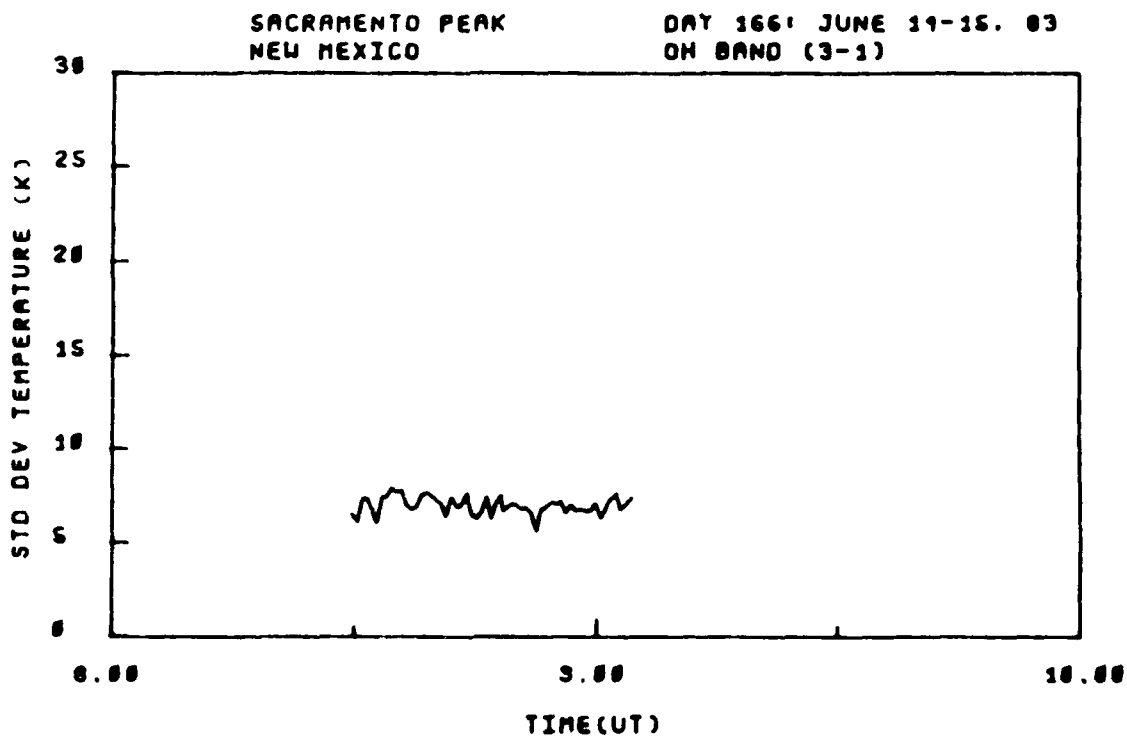
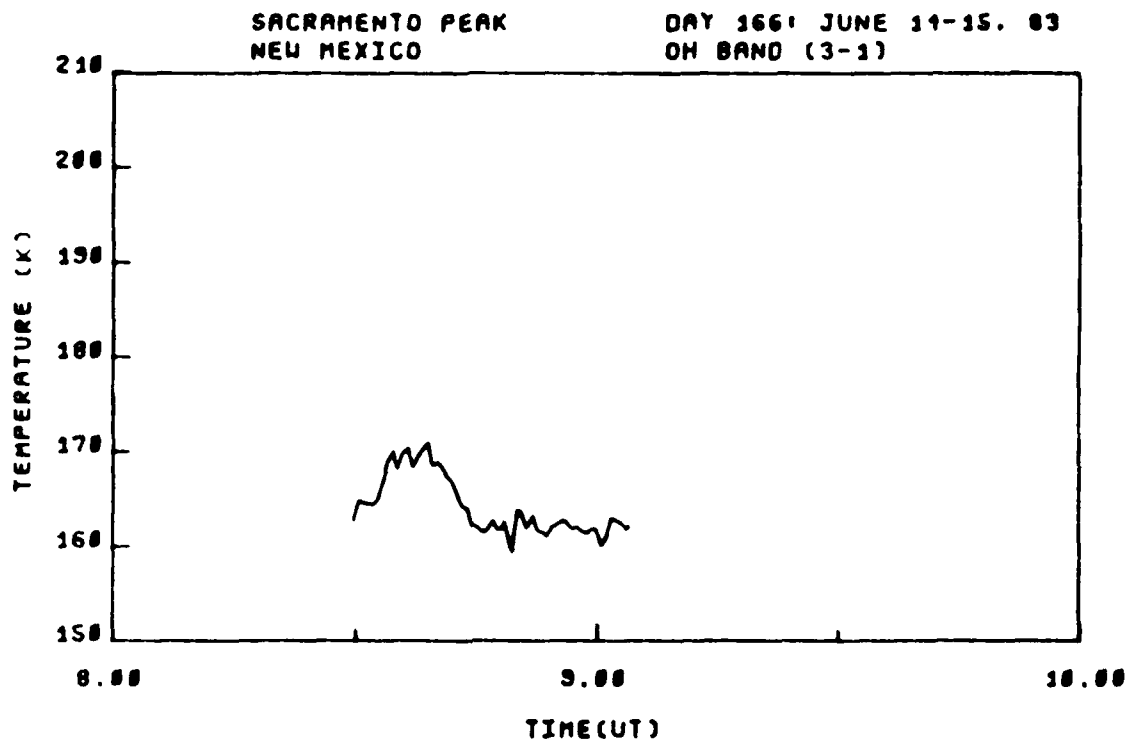


Figure C-41. OH (3,1) band rotational temperature and standard deviation, viewing angle = 15.5° El. 340° Az., day 166, 8:30-9:15 hrs. UT.

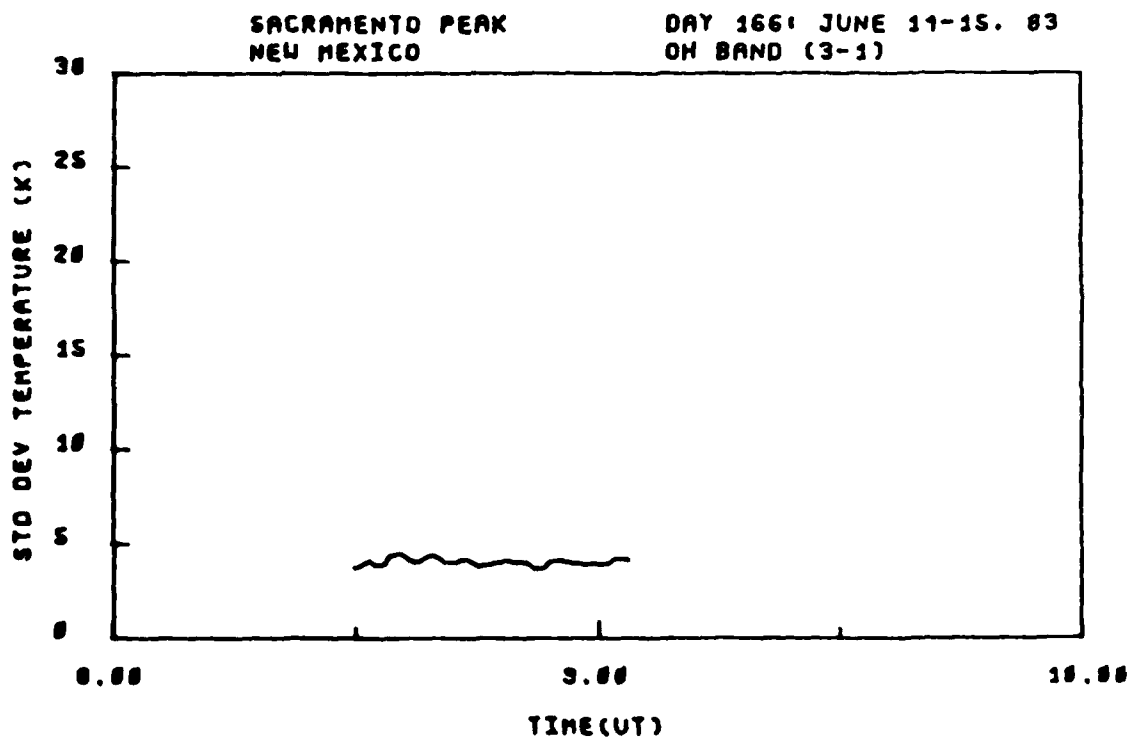
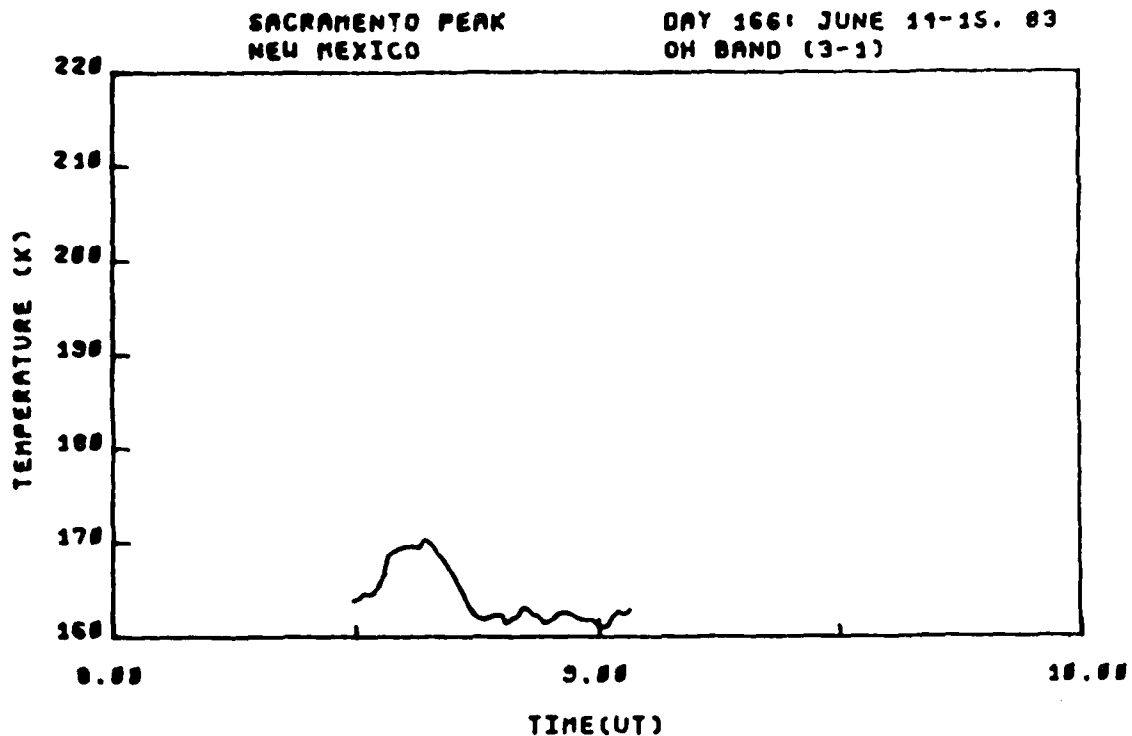


Figure C-42. OH (3,1) band smoothed rotational temperature and standard deviation, viewing angle = 15.5° El. 340° Az., day 166, 8:30-9:15 hrs. UT.

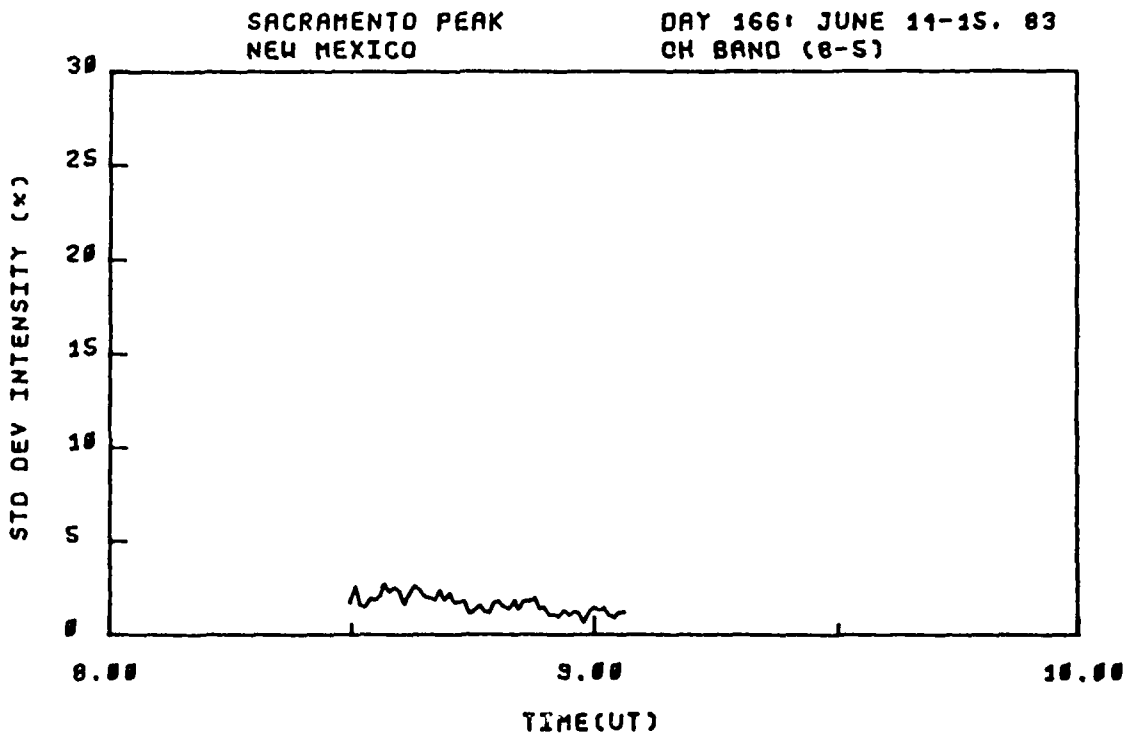
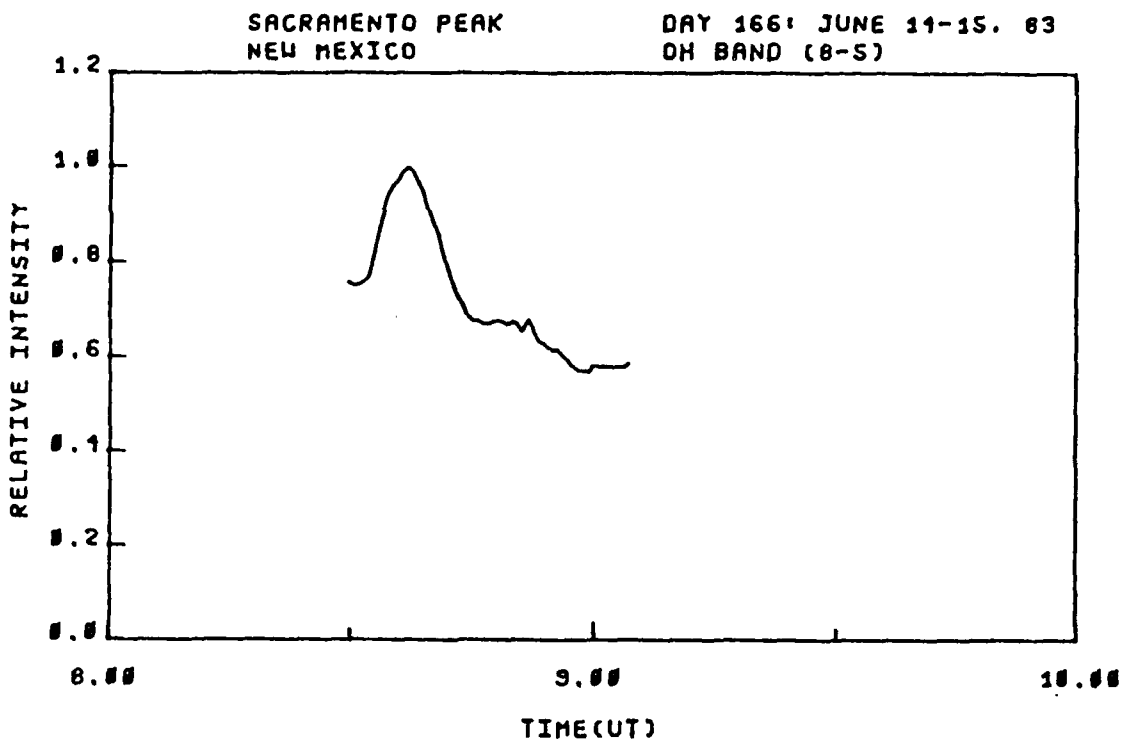


Figure C-43. OH (8,5) band relative intensity and standard deviation, viewing angle = 15.5° El. 340° Az., day 166, 8:30-9:15 hrs. UT.

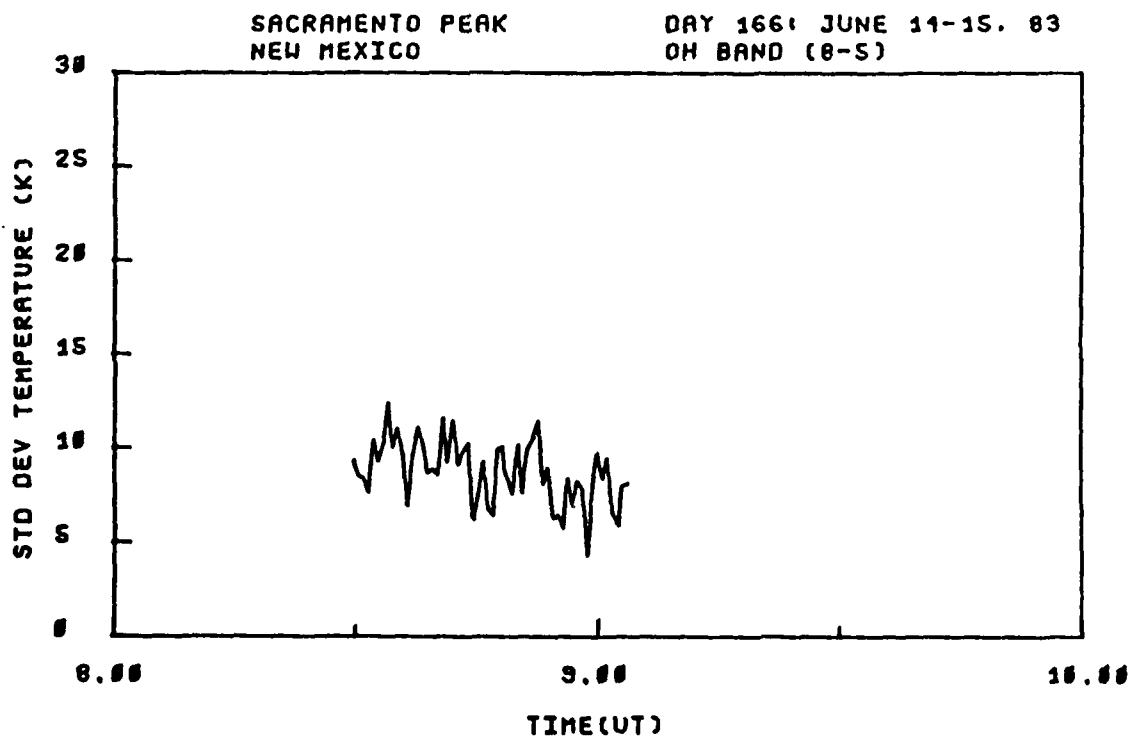
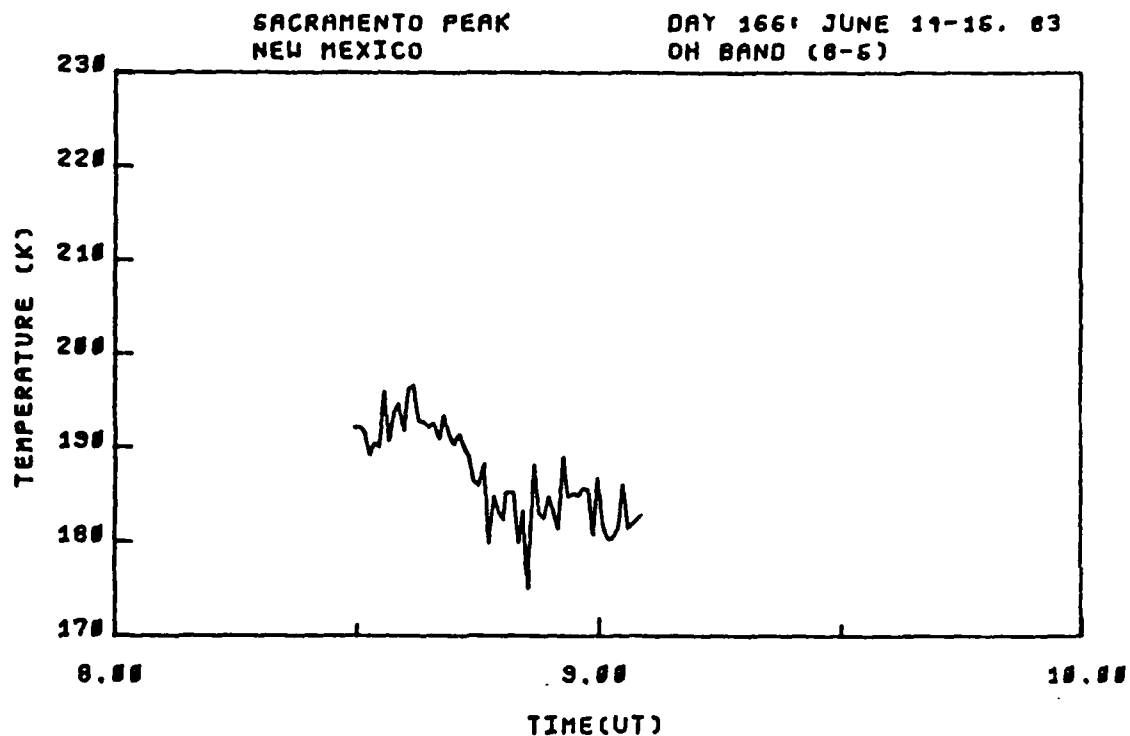


Figure C-44. OH (8,5) band rotational temperature and standard deviation, viewing angle = 15.5° El. 340° Az., day 166, 8:30-9:15 hrs. UT.

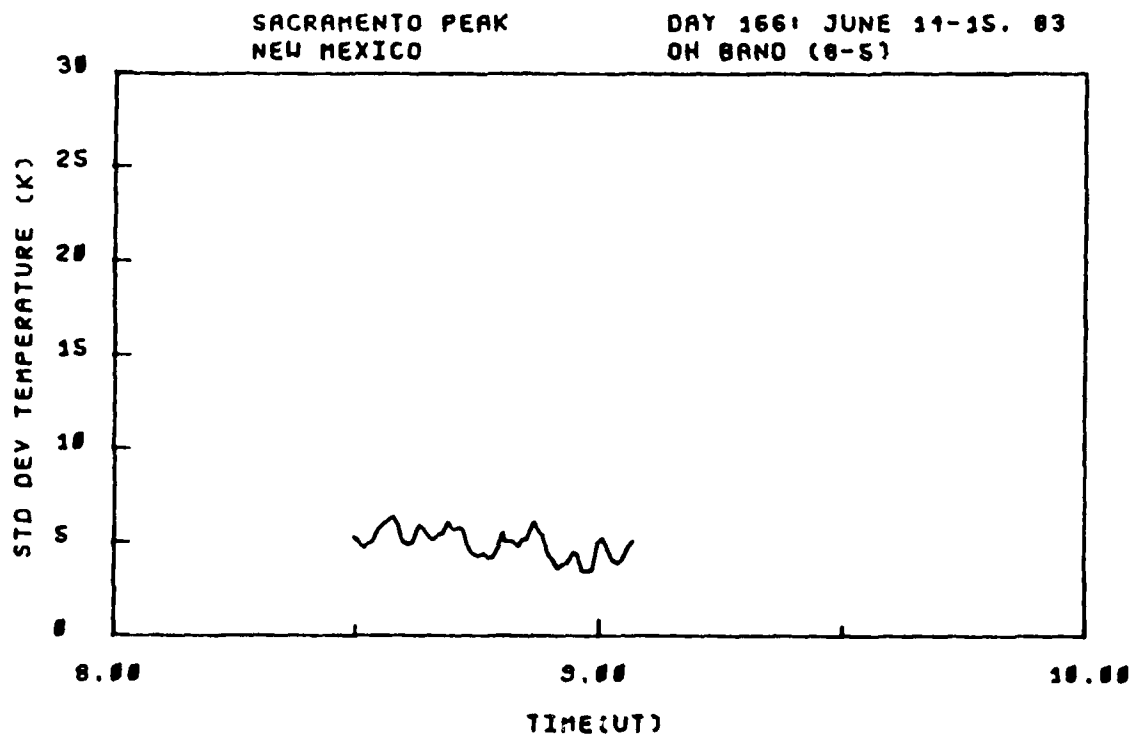
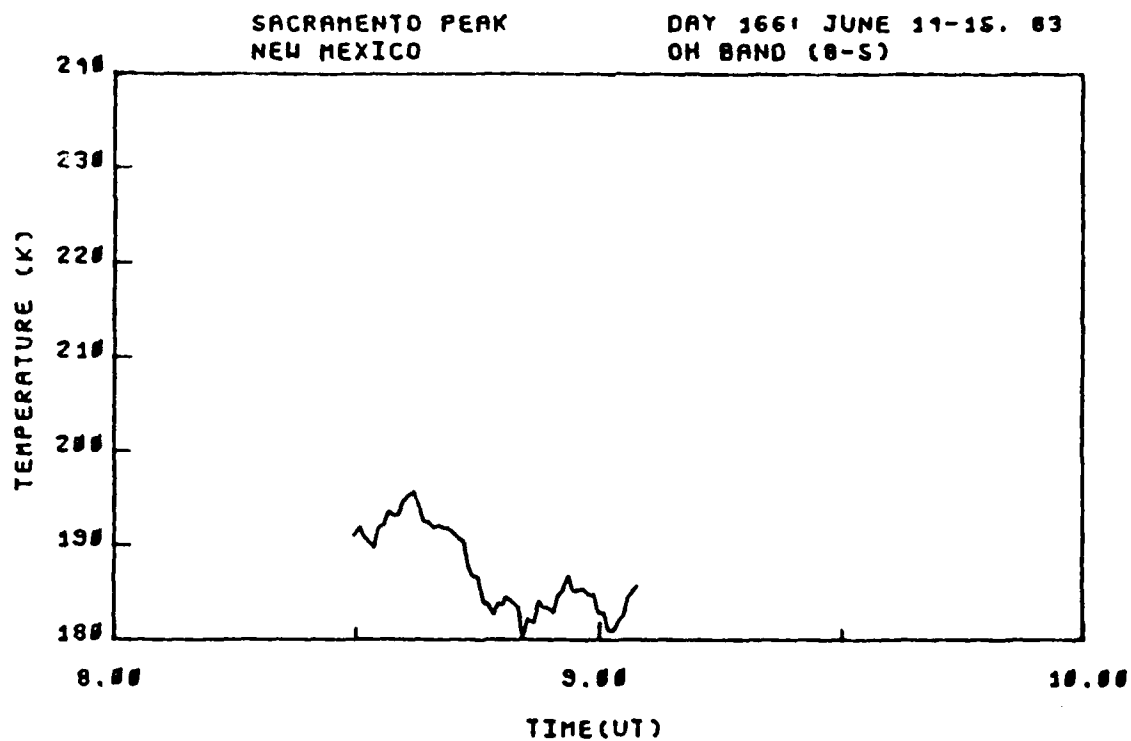


Figure C-45. OH (8,5) band smoothed rotational temperature and standard deviation, viewing angle = 15.5° El. 340° Az., day 166, 8:30-9:15 hrs. UT.

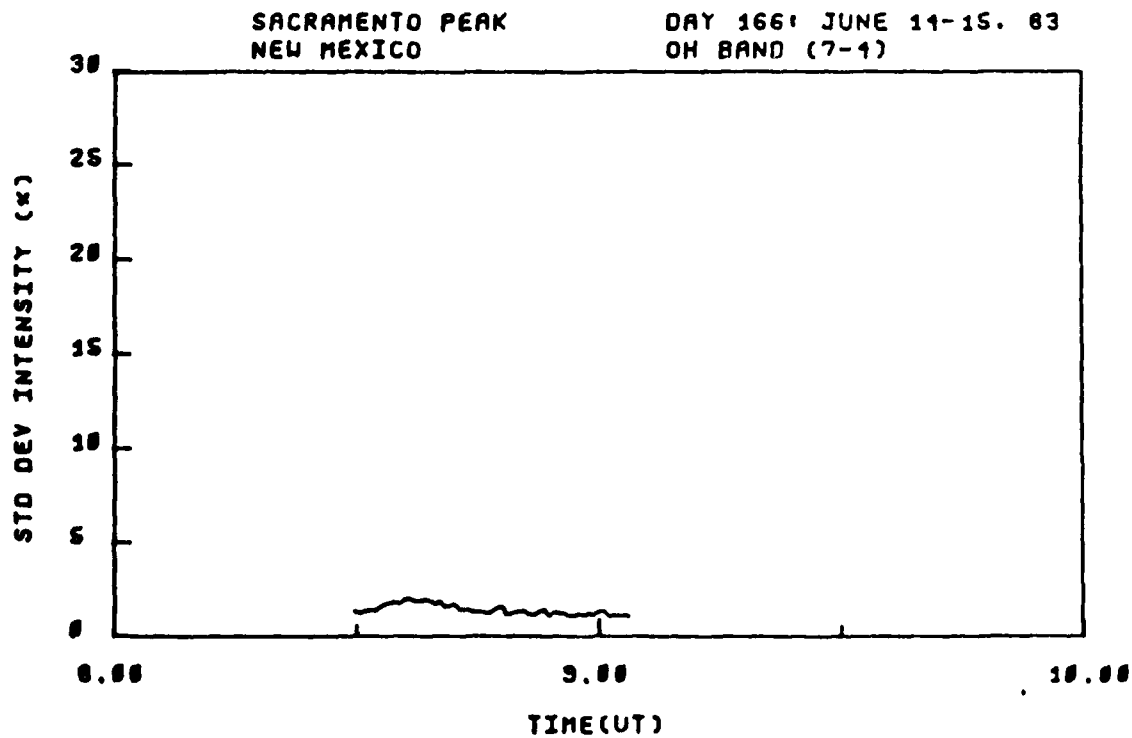
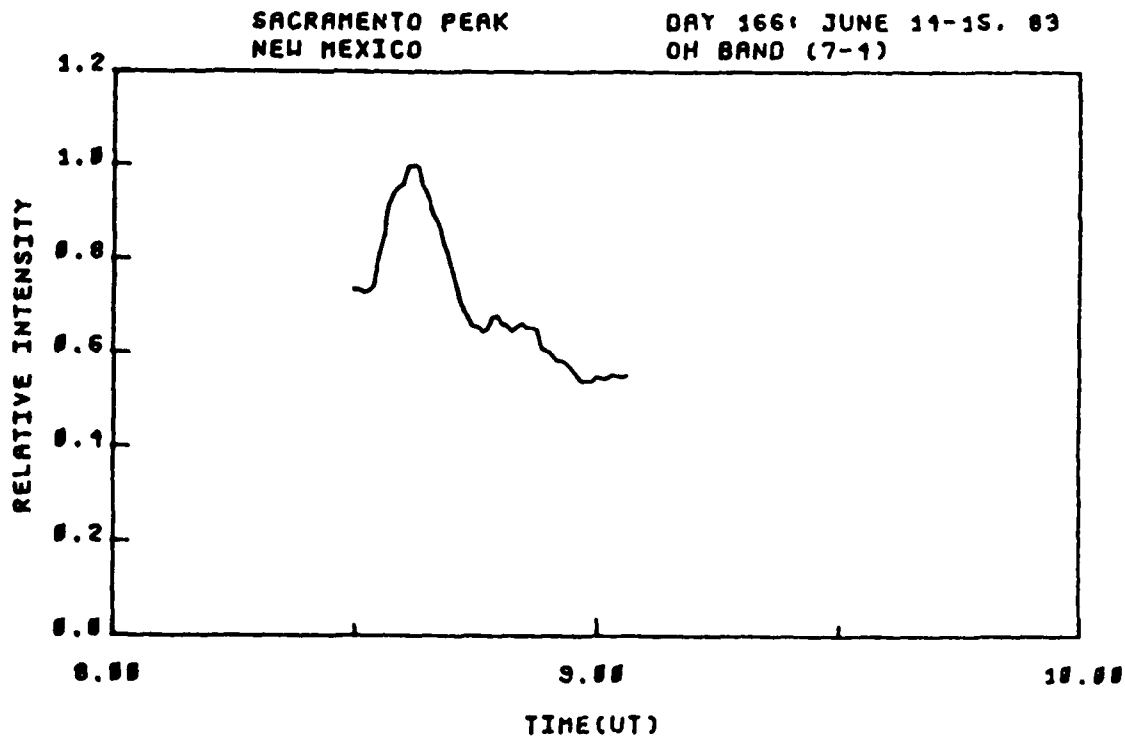


Figure C-46. OH (7,4) band relative intensity and standard deviation, viewing angle = 15.5° El. 340° Az., day 166, 8:30-9:15 hrs. UT.

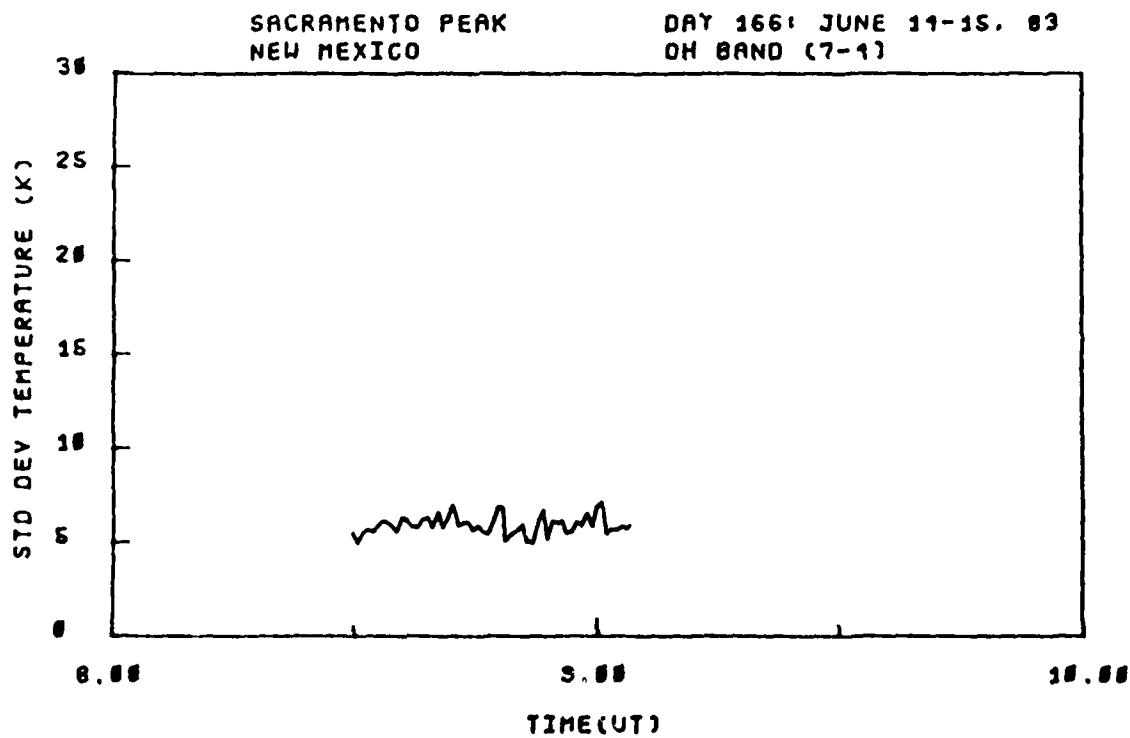
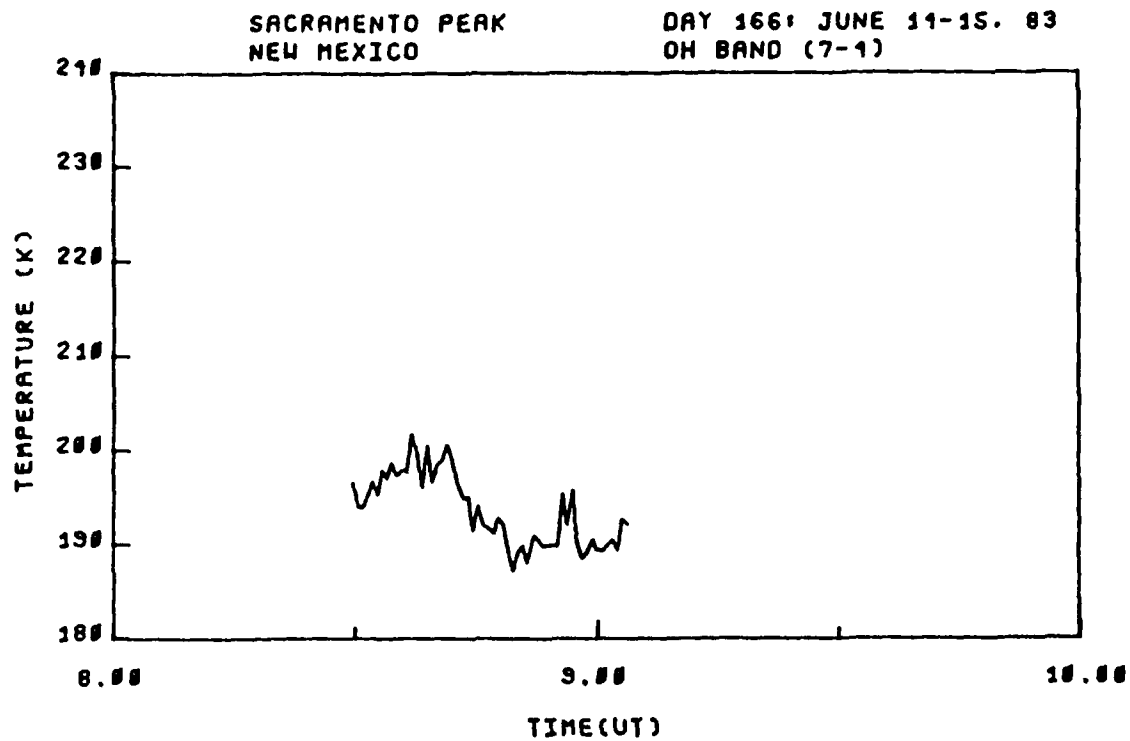


Figure C-47. OH (7,4) band rotational temperature and standard deviation, viewing angle = 15.5° El. 340° Az., day 166, 8:30-9:15 hrs. UT.

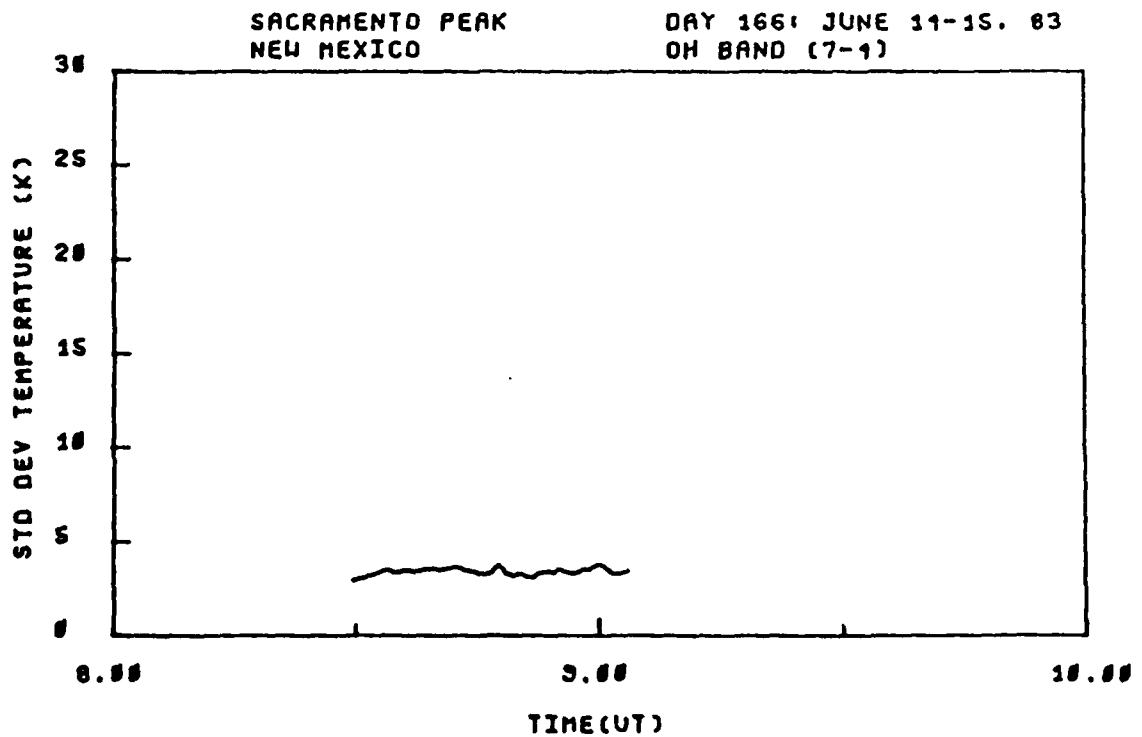
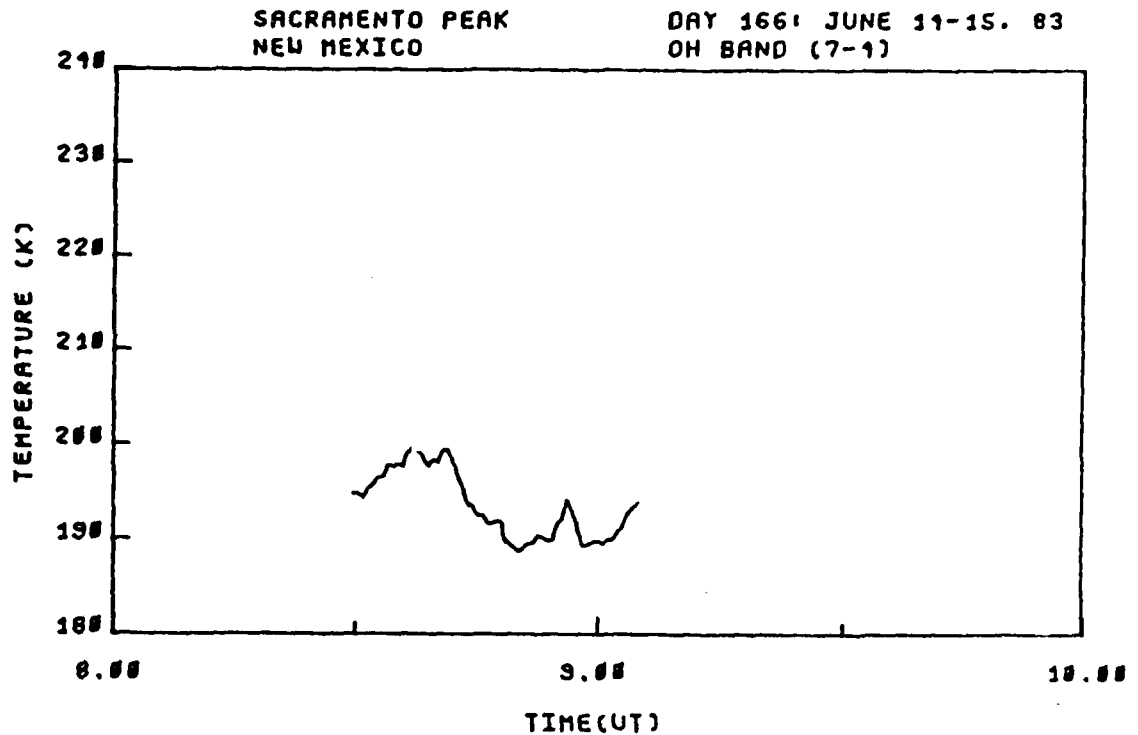


Figure C-48. OH (7,4) band smoothed rotational temperature and standard deviation, viewing angle = 15.5° El. 340° Az., day 166, 8:30-9:15 hrs. UT.

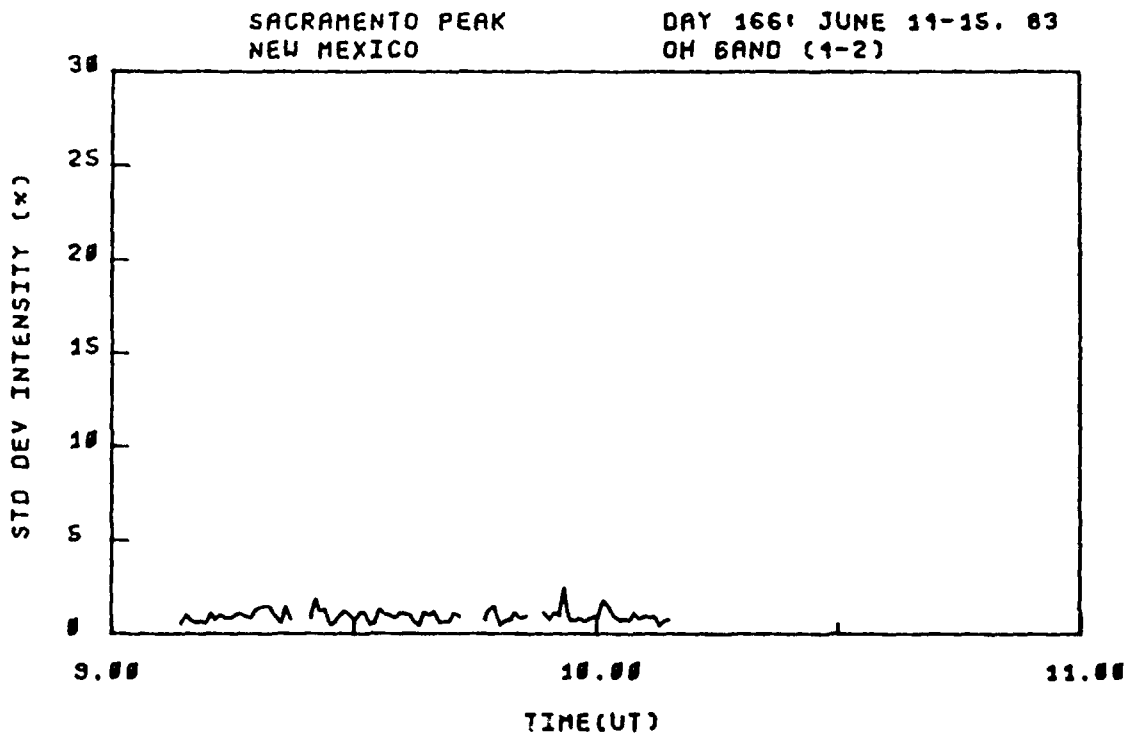
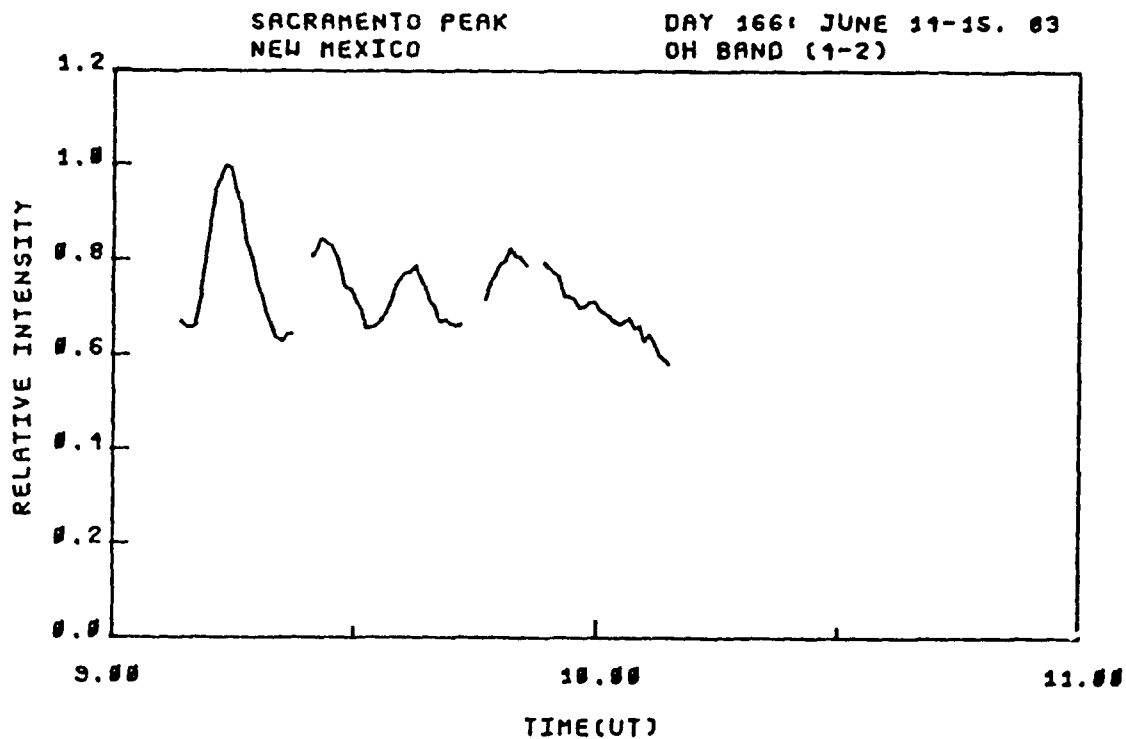


Figure C-49. OH (4,2) band relative intensity and standard deviation, viewing angle = 15.5° El. 309° Az., day 166, 9:15-10:15 hrs. UT.

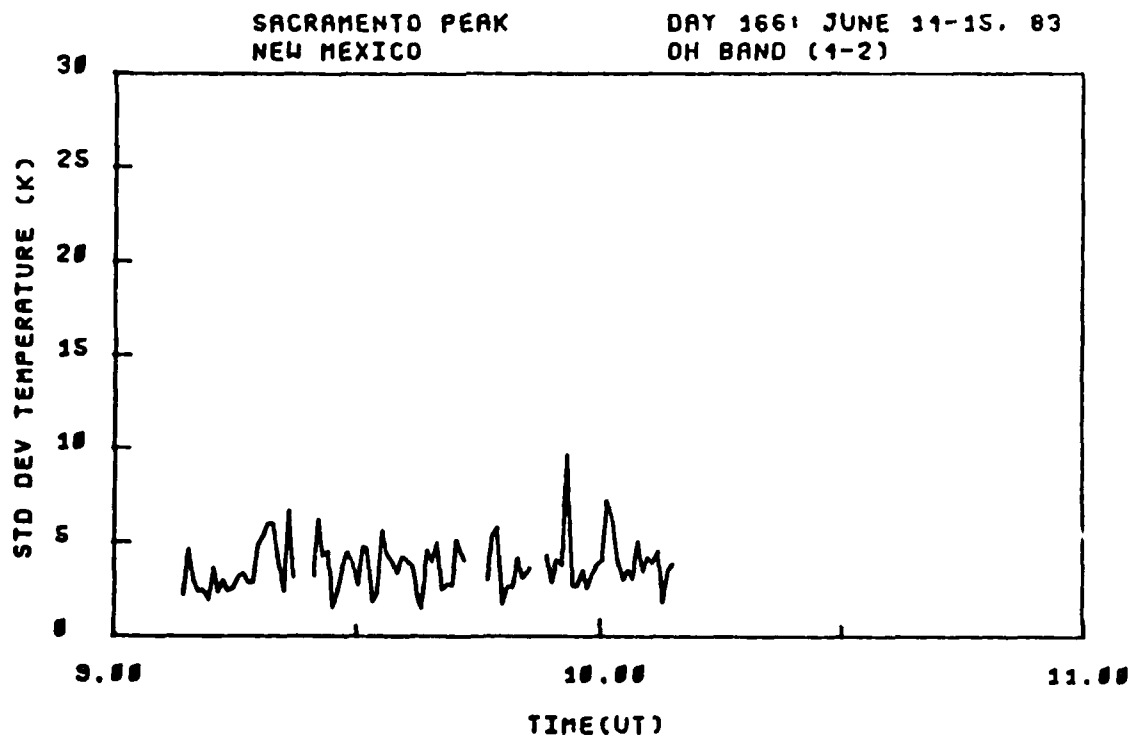
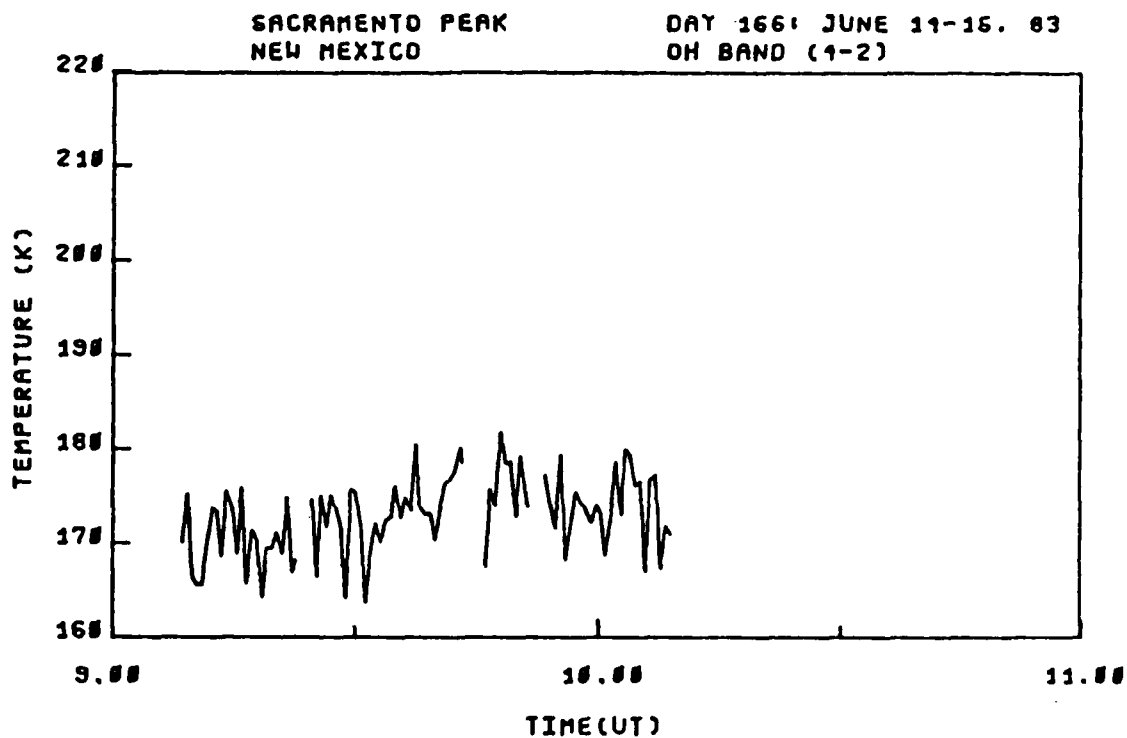


Figure C-50. OH (4,2) band rotational temperature and standard deviation, viewing angle = 15.5° El. 309° Az., day 166, 9:15-10:15 hrs. UT.

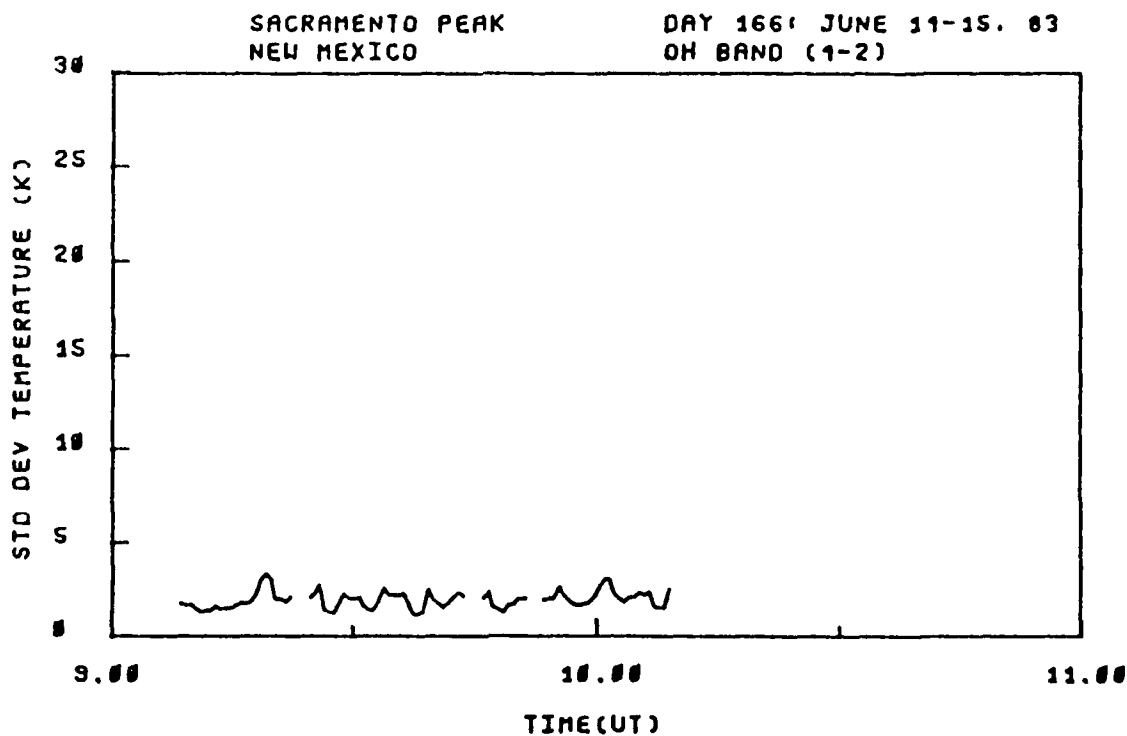
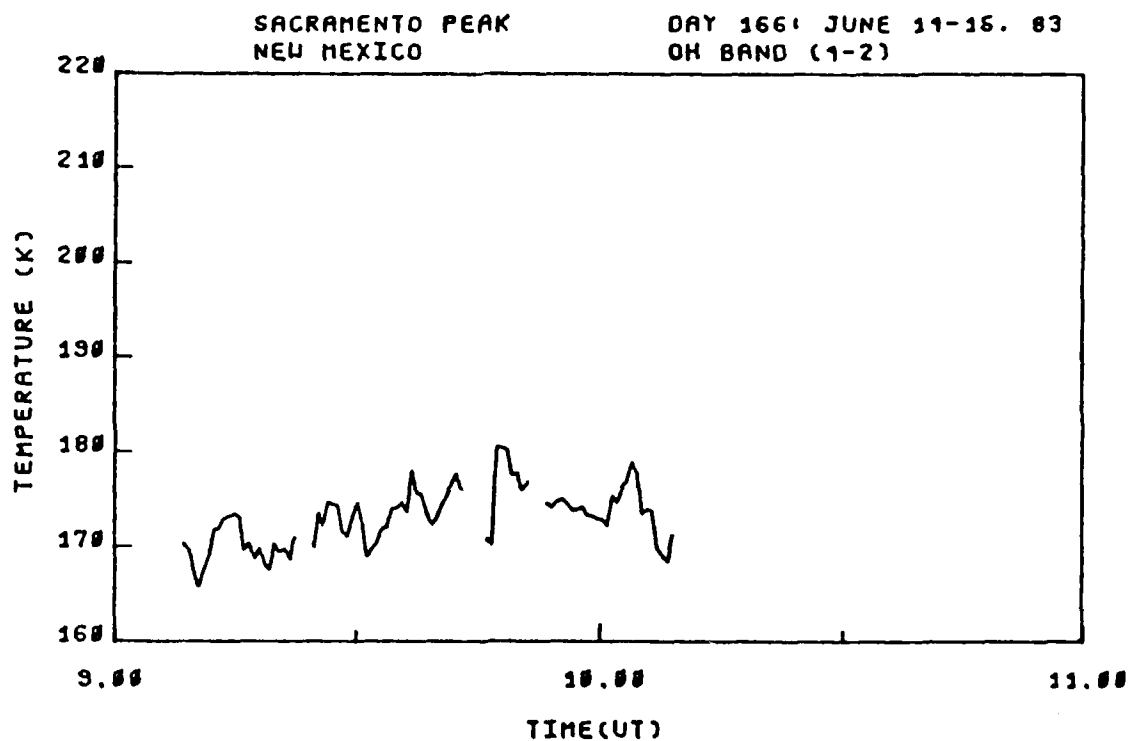


Figure C-51. OH (4,2) band smoothed rotational temperature and standard deviation, viewing angle = 15.5° El. 309° Az., day 166, 9:15-10:15 hrs. UT.

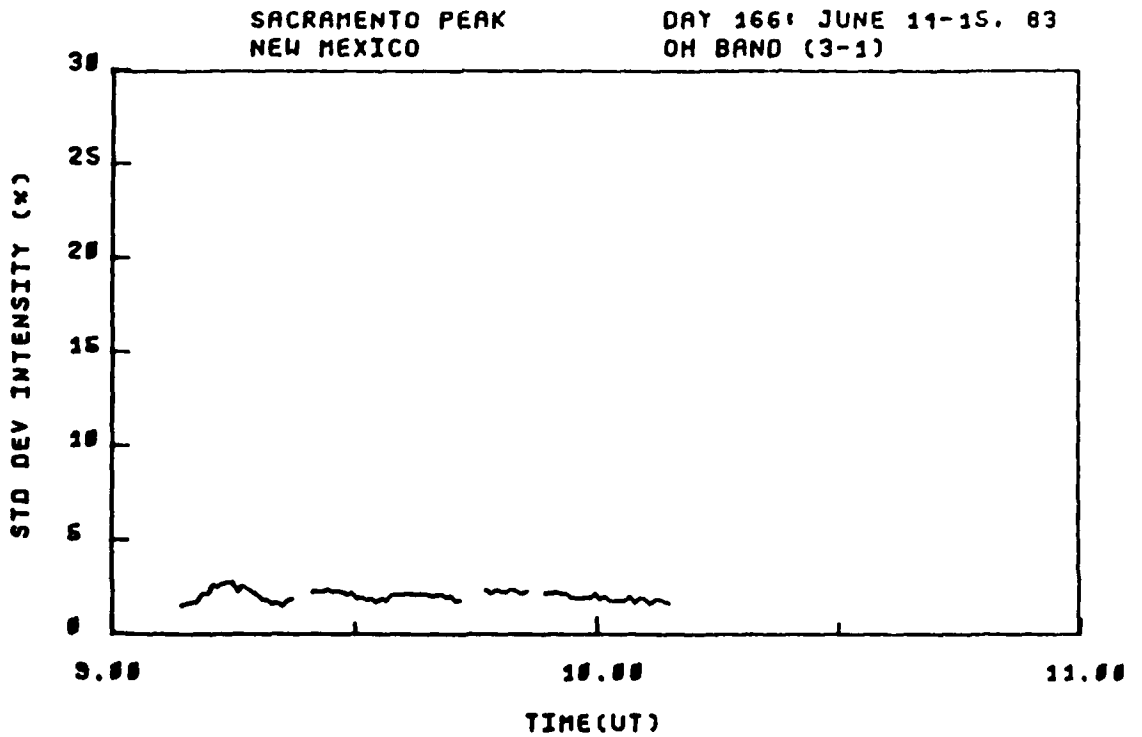
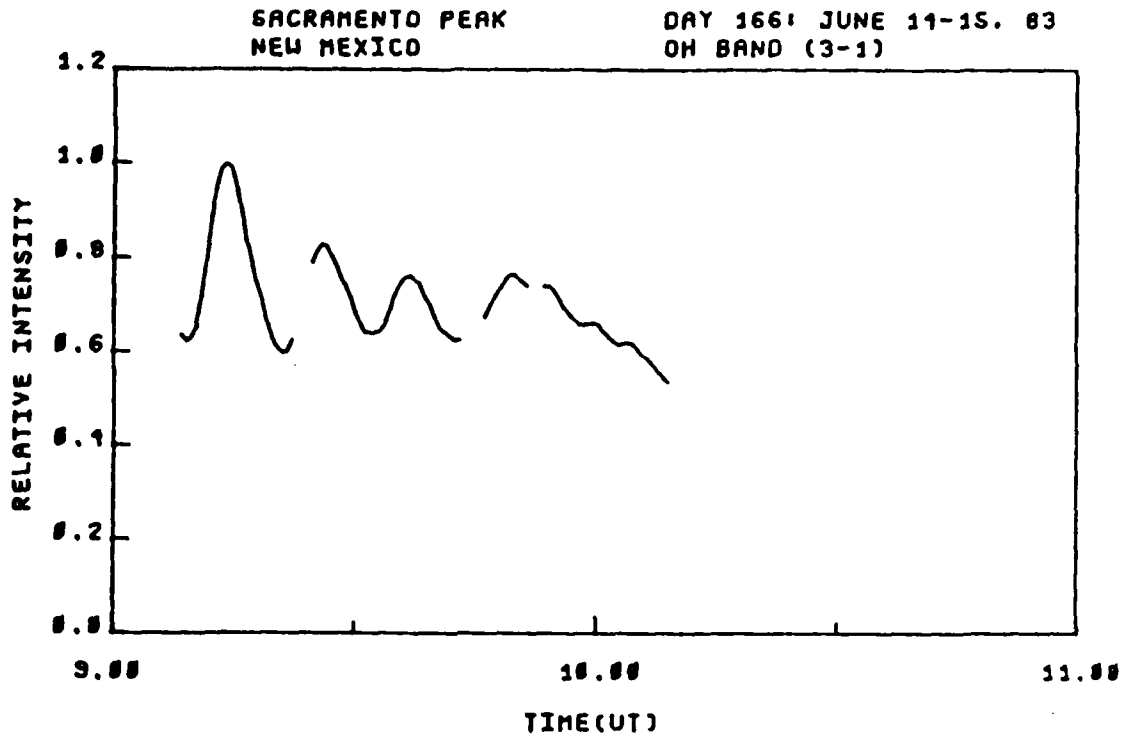


Figure C-52. OH (3,1) band relative intensity and standard deviation, viewing angle = 15.5° El. 309° Az., day 166, 9:15-10:15 hrs. UT.

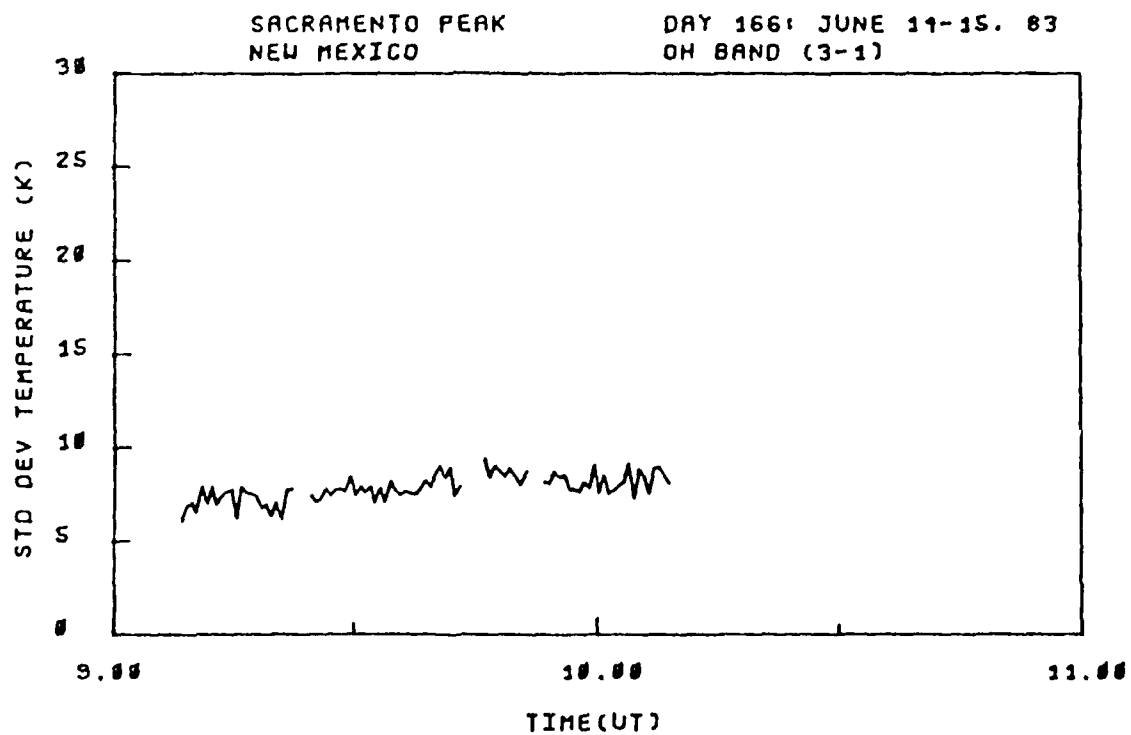
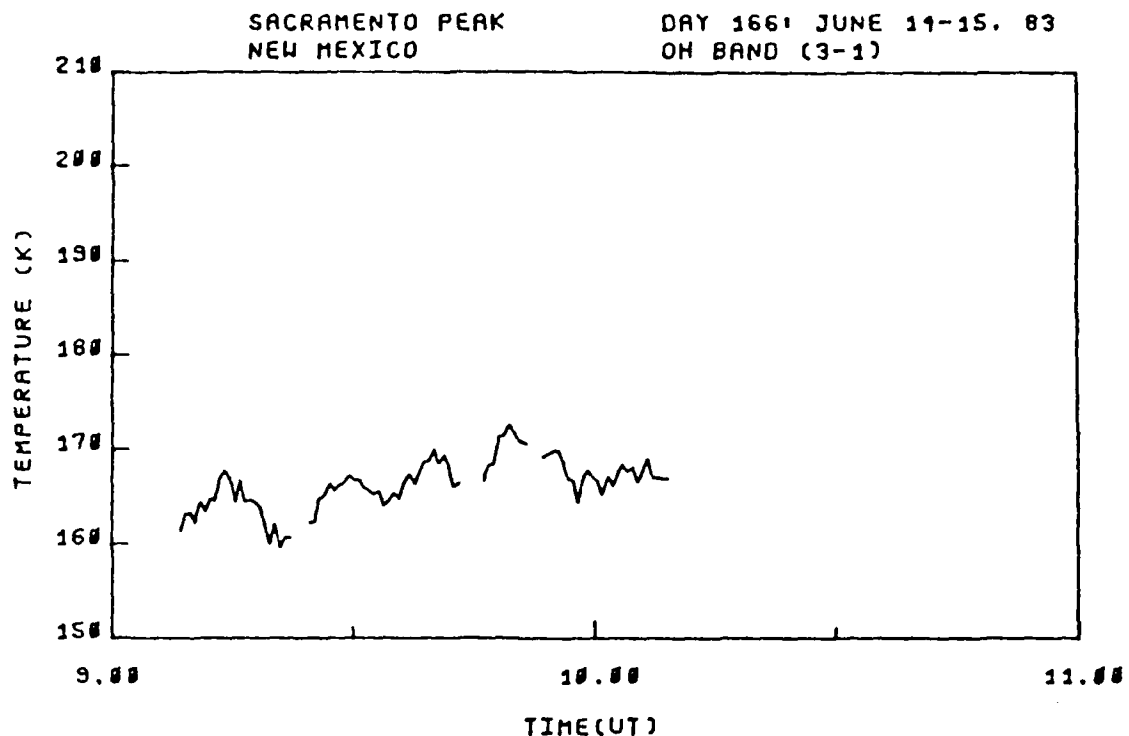


Figure C-53. OH (3,1) band rotational temperature and standard deviation, viewing angle = 15.5° El. 309° Az., day 166, 9:15-10:15 hrs. UT.

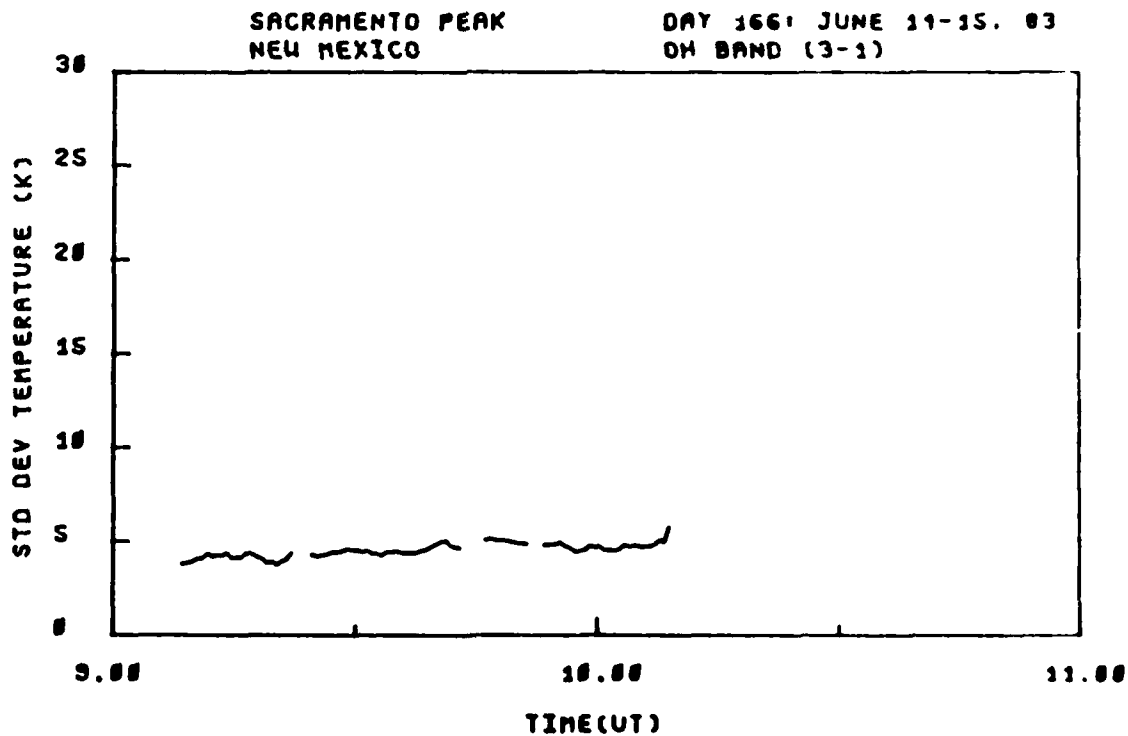
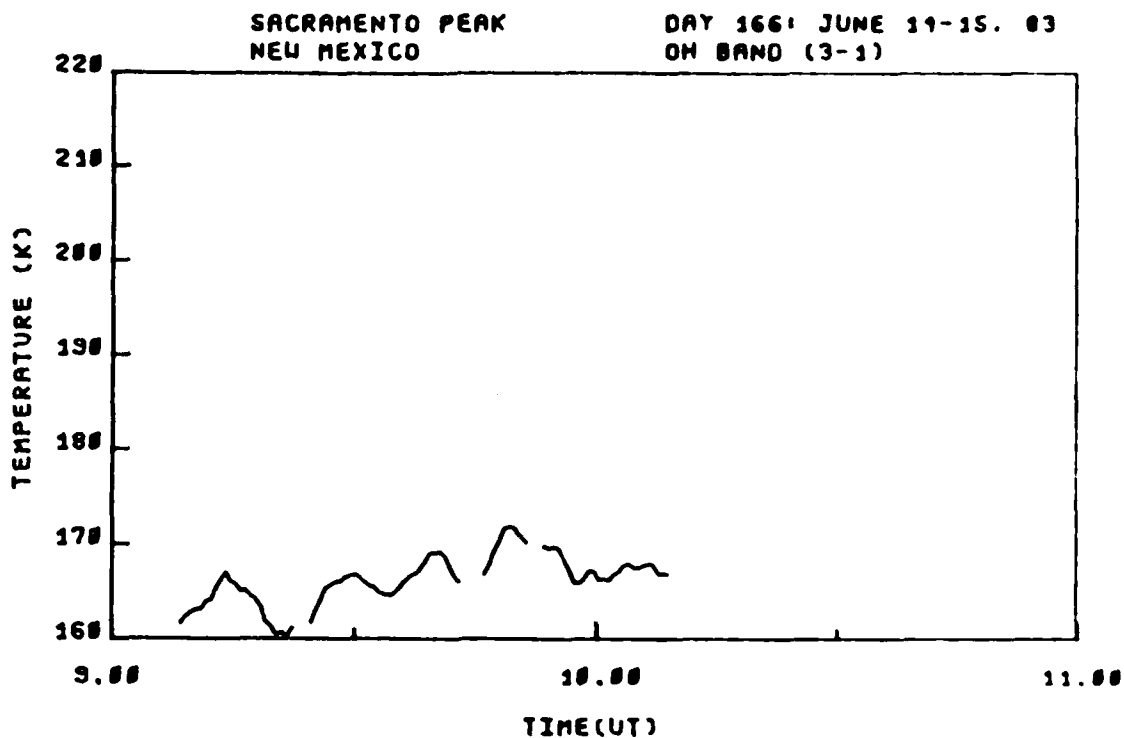


Figure C-54. OH (3,1) band smoothed rotational temperature and standard deviation, viewing angle = 15.5° El. 309° Az., day 166, 9:15-10:15 hrs. UT.

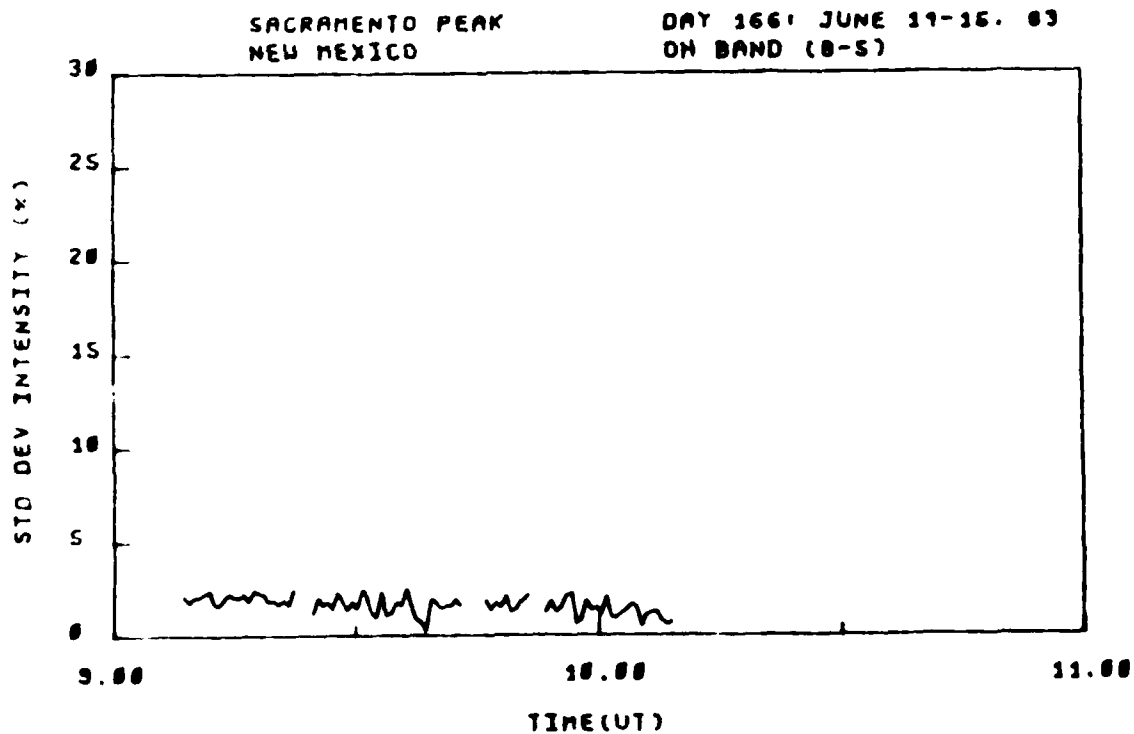
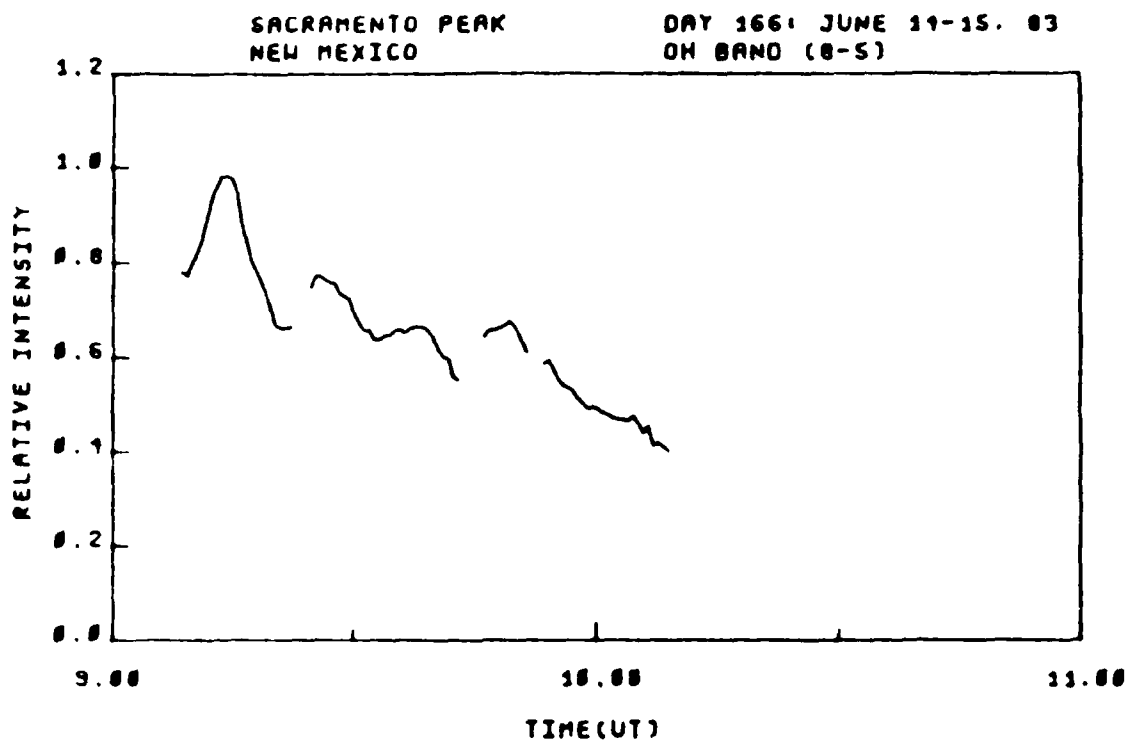


Figure C-55. OH (8,5) band relative intensity and standard deviation, viewing angle = 15.5° El. 309° Az., day 166, 9:15-10:15 hrs. UT.

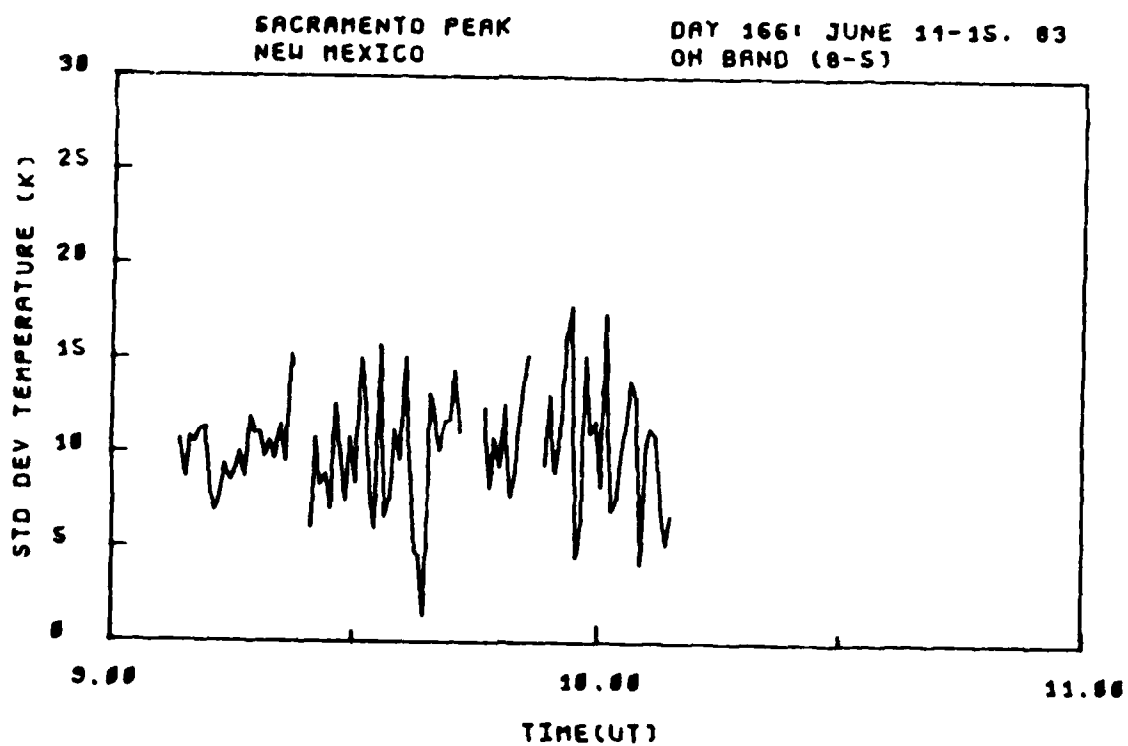
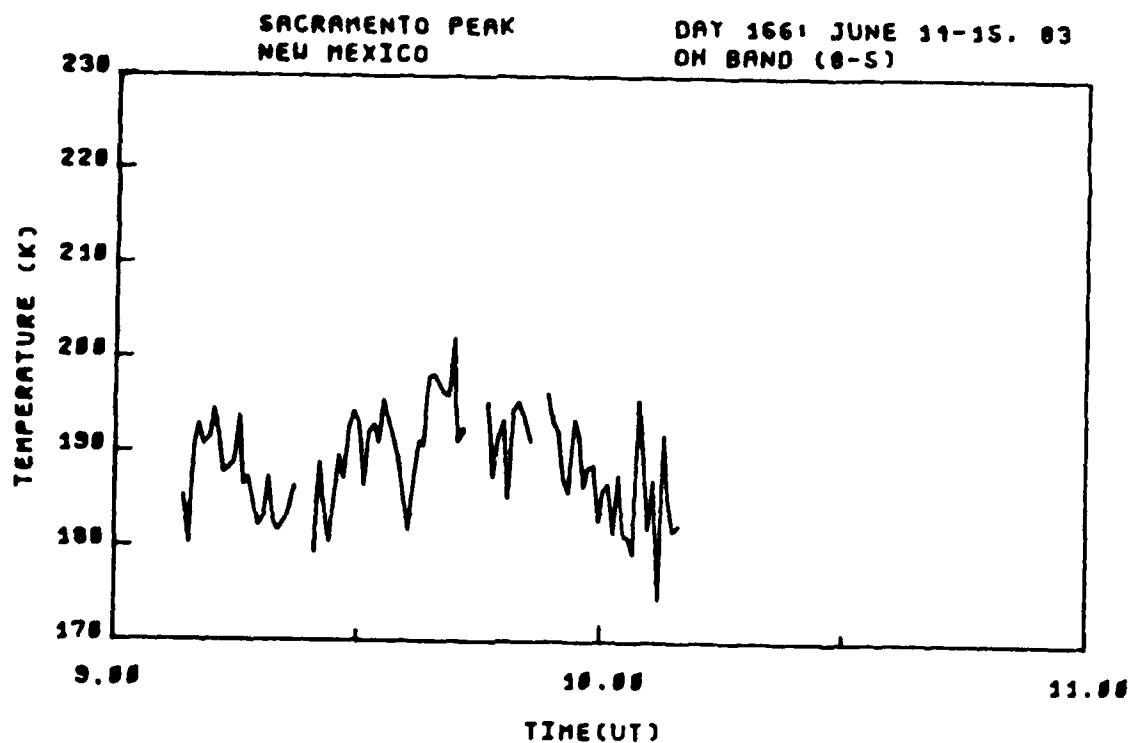


Figure C-56. OH (8,5) band rotational temperature and standard deviation, viewing angle = 15.5° El. 309° Az., day 166, 9:15-10:15 hrs. UT.

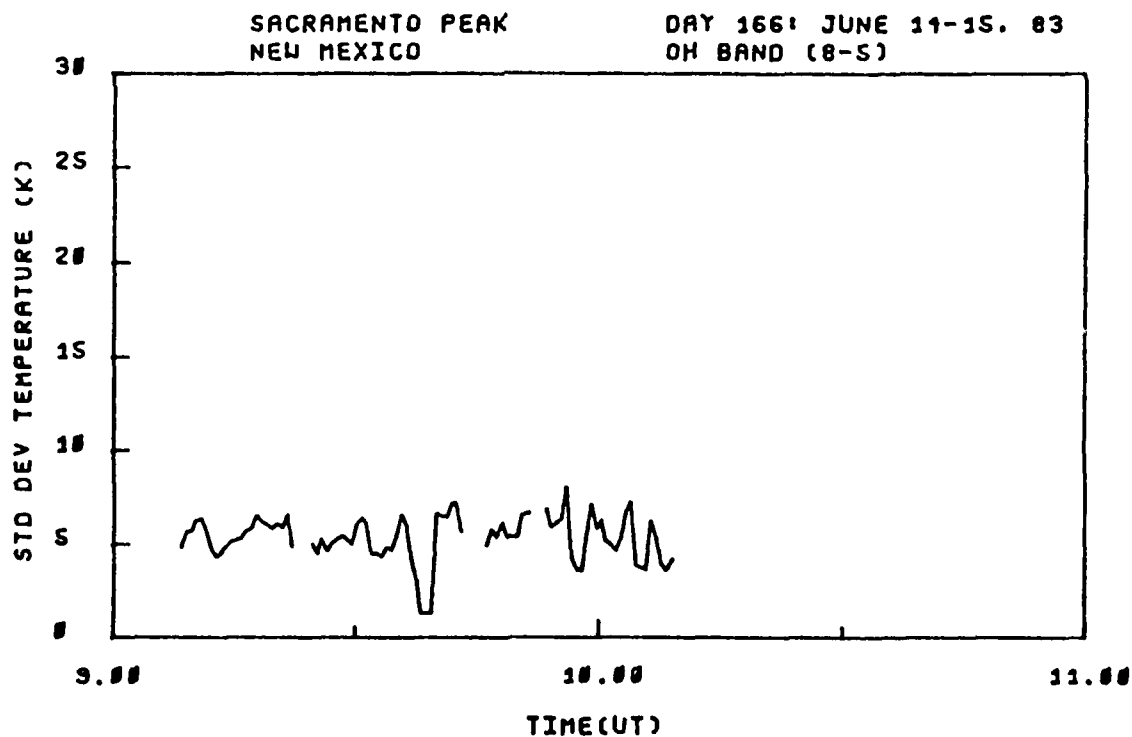
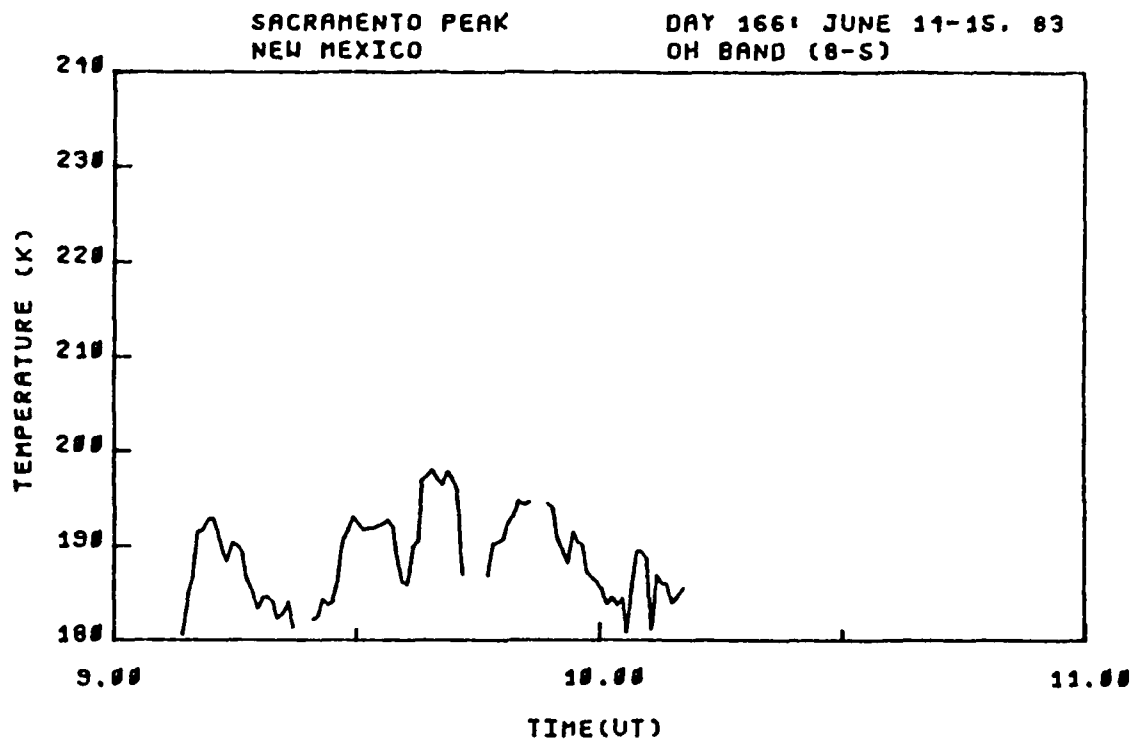


Figure C-57. OH (8,5) band smoothed rotational temperature and standard deviation, viewing angle = 15.5° El. 309° Az., day 166, 9:15-10:15 hrs. UT.

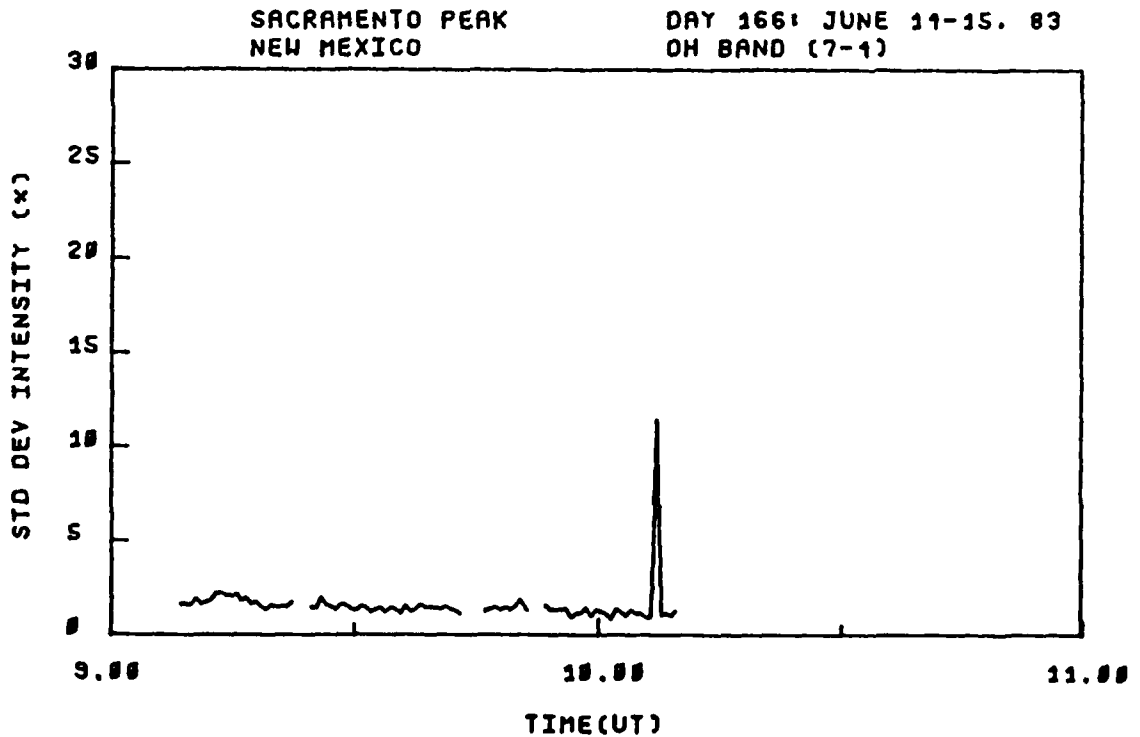
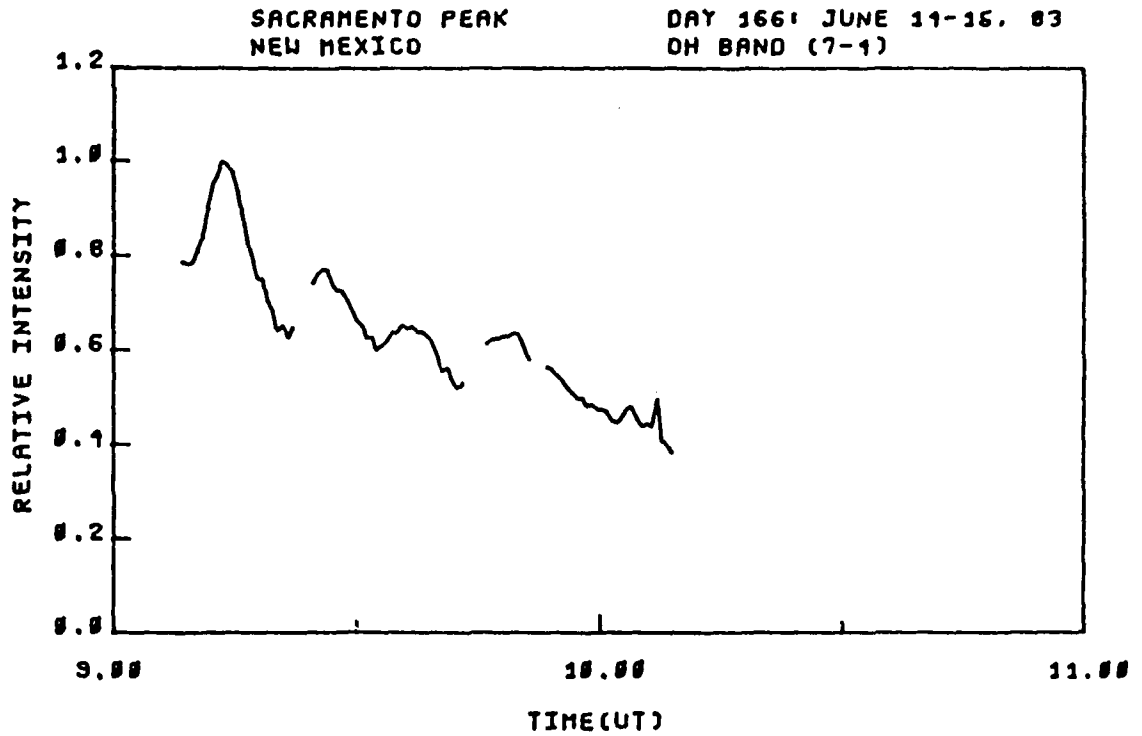


Figure C-58. OH (7,4) band relative intensity and standard deviation, viewing angle = 15.5° El. 309° Az., day 166, 9:15-10:15 hrs. UT.

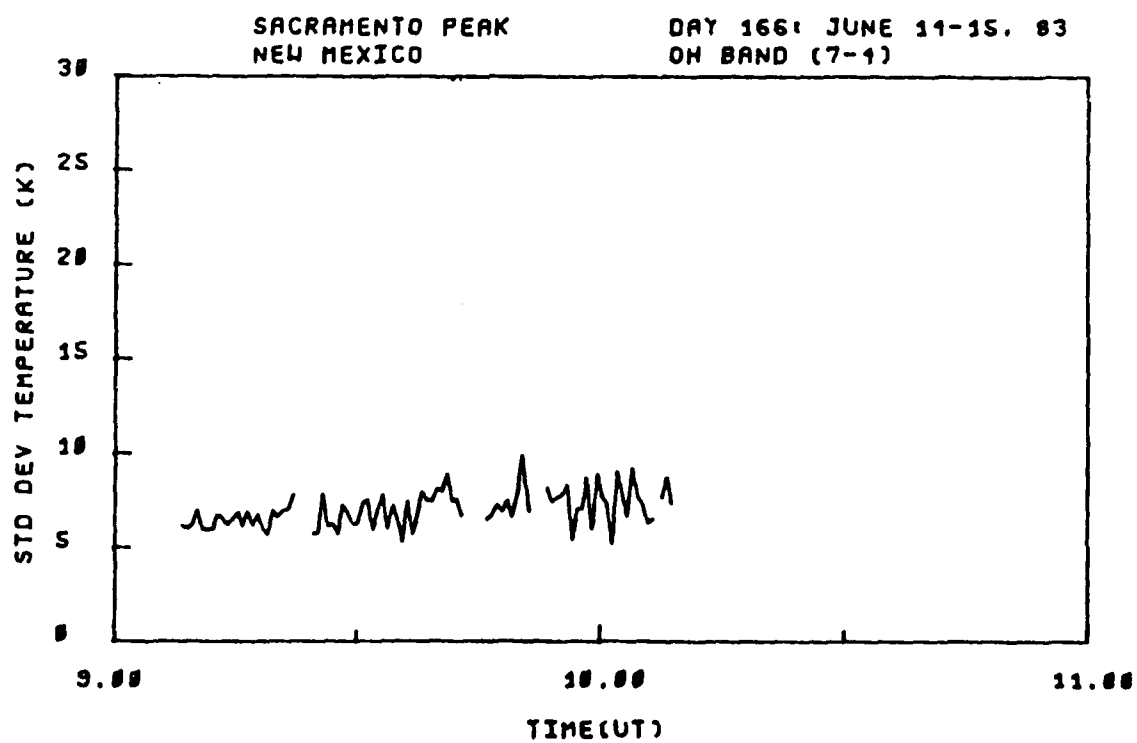
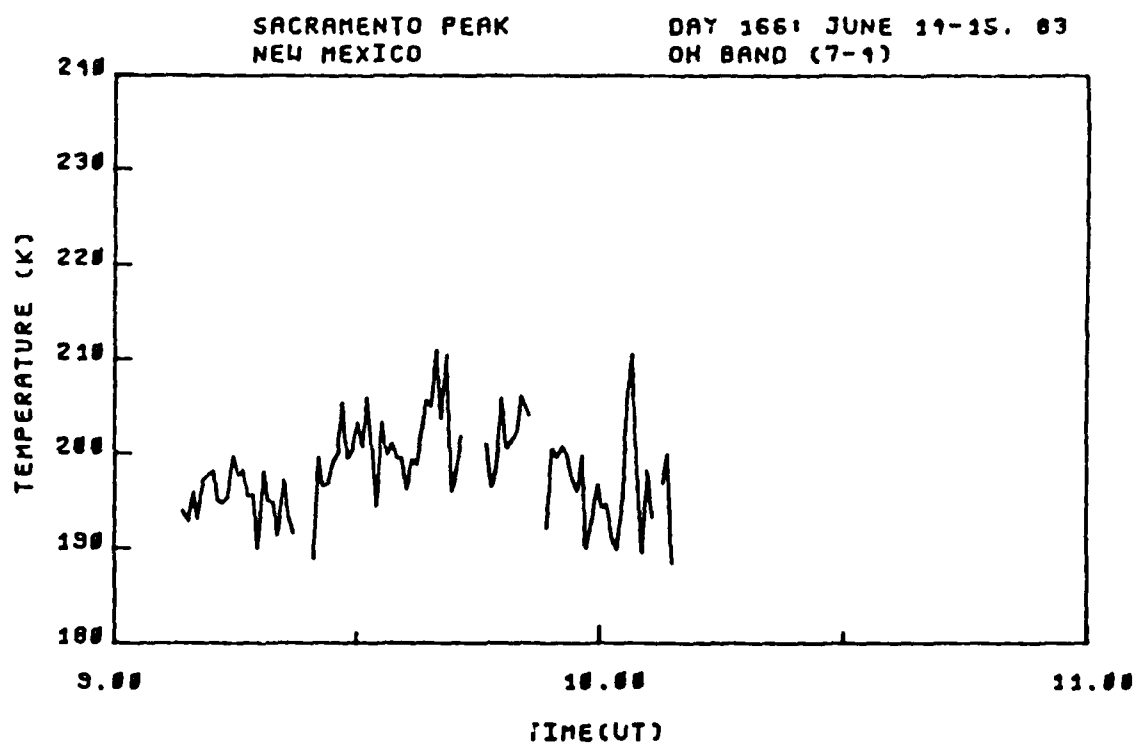


Figure C-59. OH (7,4) band rotational temperature and standard deviation, viewing angle = 15.5° El. 309° Az., day 166, 9:15-10:15 hrs. UT.

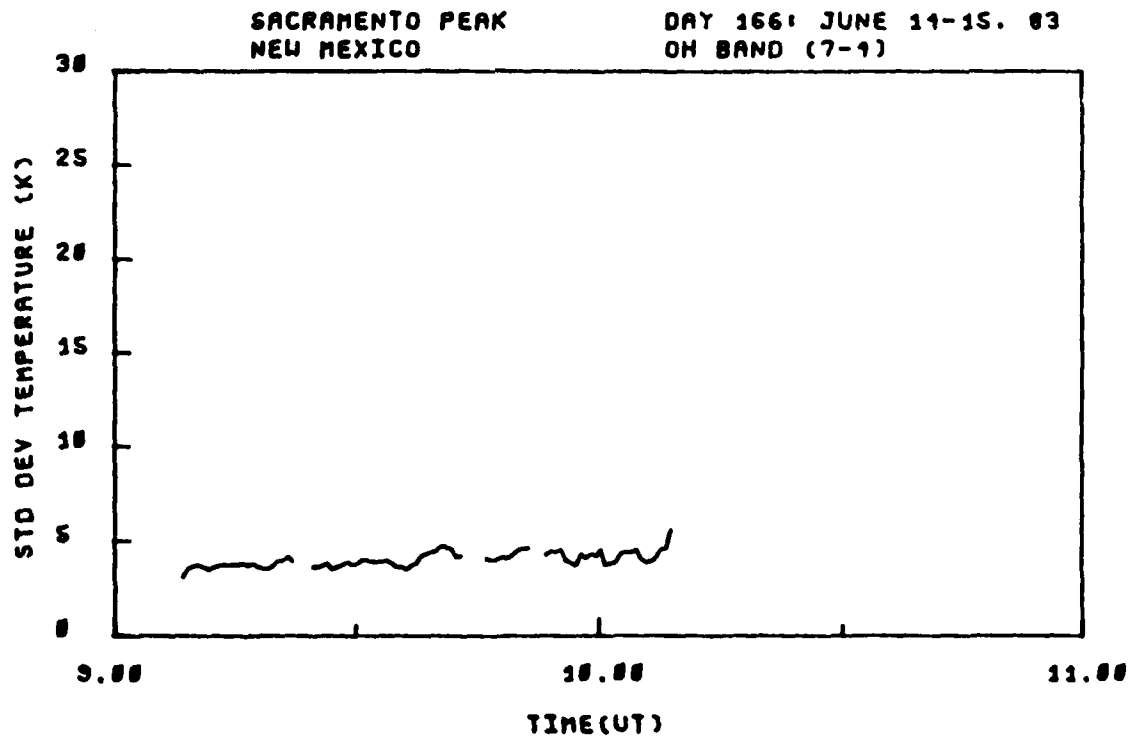
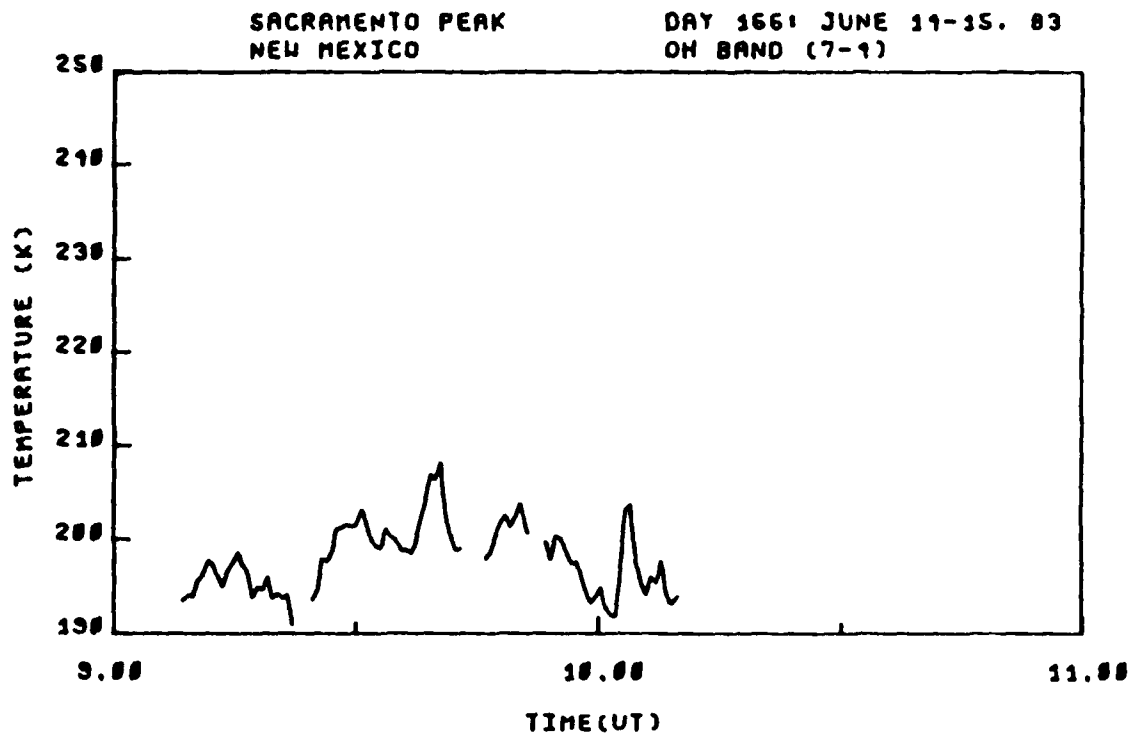


Figure C-60. OH (7,4) band smoothed rotational temperature and standard deviation, viewing angle = 15.5° El. 309° Az., day 166, 9:15-10:15 hrs. UT.

END

7-87

DTIC